Beate Klinger, Dipl.-Ing.

A contribution to GRACE time-variable gravity field recovery: Improved Level-1B data pre-processing methodologies

DOCTORAL THESIS

to achieve the university degree of
Doktorin der technischen Wissenschaften
submitted to

Graz University of Technology

Supervisor

Univ.-Prof. Dr.-Ing. Torsten Mayer-Gürr
Institute of Geodesy
Working Group Theoretical Geodesy and Satellite Geodesy

Graz, March 2018

Affidavit

I declare that I have authored this thesis independently, that I have not used other than the declared sources/resources, and that I have explicitly indicated all material which has been quoted either literally or by content from the sources used. The text document uploaded to TUGRAZonline is identical to the present doctoral thesis.

Date	Signature

Abstract

The observation of temporal variations within the Earth's gravity field has become an invaluable source of information for climate research, providing fundamental insights into the dynamic system Earth. The Gravity Recovery And Climate Experiment (GRACE) satellite mission observed these changes by making use of inter-satellite ranging measurements between two co-planar satellites. GRACE provided information about the Earth's static and time-variable gravity field with unprecedented accuracy for more than 15 years. Currently, no other technique is capable of providing the same resolution, both in space and time. However, the derived gravity field solutions are not matching the baseline accuracy predicted prior to launch. Possible contributors to the error budget are errors within the instrument observation data.

The goal of this work was to improve GRACE derived temporal gravity field models by introducing Level-1B data pre-processing methodologies as part of the ITSG-Grace gravity field processing. For this purpose, three major pre-processing steps are introduced: (1) general data screening strategies to detect outliers within the instrument data, (2) the improvement of the Level-1B attitude data product based on the sensor fusion approach, i.e. combination of star camera and angular accelerometer data, and (3) the Level-1B accelerometer data calibration based on the estimation of biases and a fully-populated scale factor matrix.

The analysis of the improved attitude data, shows that the sensor fusion results in a significant reduction of the high-frequency attitude noise, causing a smoothing of the pointing variations and geometric corrections of the ranging measurements. The temporal evolution of the estimated calibration parameters shows a clear temperature-dependency for both biases and scale factors, confirming the accelerometers' temperature sensitivity. Especially for later mission periods, when the temperature control was switched-off, temperature-induced accelerometer perturbations need to be modeled to avoid a degradation of the monthly gravity field solutions. Using the proposed calibration approach, the estimates of the C20 coefficients significantly improve. In terms of monthly gravity field solutions, the pre-processing methodologies manifest themselves as a step-wise reduction of the error-level.

In general, the results obtained within this work suggest that a detailed analysis of the instrument data can significantly contribute to the overall accuracy of the recovered gravity field solutions. Especially for later GRACE mission periods, the importance and potential of Level-1B data pre-processing methodologies was demonstrated on the basis of the ITSG-Grace processing chain. The results of the presented analysis not only contribute to the improvement of current GRACE gravity field solutions, but also provide information highly valuable for future gravity field missions, such as GRACE-FO. In view of the GRACE-FO mission - a quasi-replica of GRACE - a profound understanding of possible error sources and disturbance prevalent within the GRACE instrument data is essential for meeting the envisaged accuracies.

Kurzfassung

Die Beobachtung von zeitlichen Variationen innerhalb des Erdschwerefelds gewährt grundlegende Einblicke in das System Erde und liefert damit eine wichtige Datengrundlage für die Klimaforschung. Die Gravity Recovery And Climate Experiment (GRACE) Satellitenmission ermöglicht die Beobachtung des zeitvariablen Erdschwerefeldes mit Hilfe von relativen Abstandsmessungen zwischen den beiden GRACE Zwillingssatelliten. Damit hat GRACE in den vergangenen 15 Jahren einen unverzichtbaren Beitrag zur Schwerefeldmodellierung geliefert. Bis dato gibt es kein anderes Beobachtungskonzept, welches die gleiche räumliche und zeitliche Auflösung bereitstellt. Allerdings erreichen die GRACE Schwerefeldlösungen nicht die aus Simulationsstudien prognostizierte Genauigkeit. Eine mögliche Ursache für diese Diskrepanz sind nicht detektierte Fehler bzw. Ausreißer in den Instrumentendaten.

Ziel dieser Arbeit war es die monatlichen GRACE Schwerefeldlösungen, basierend auf Methoden zur Level-1B Datenvorprozessierung, zu verbessern. Dazu wurden innerhalb des ITSG-Grace Prozessierungsschemas drei wesentliche Erweiterungen implementiert: (1) Datenscreening Methoden zur Detektion von Ausreißern innerhalb der Instrumentendaten, (2) Sensor Fusion: Verbesserung der Level-1B Attitudedaten basierend auf der Kombination von Sternenkamera- und Akzelerometerdaten, und (3) Kalibrierung der Level-1B Akzelerometerdaten mittels Schätzung von Bias-Parametern und einer vollbesetzte Skalierungsmatrix.

Die Analyse der kombinierten Attitudedaten zeigt, dass durch die Sensor Fusion das hochfrequente Rauschen der Attitudedaten deutlich reduziert werden kann. Daraus ergeben sich auch eine Reduktion der Pointing-Variationen, sowie eine Glättung der geometrischen Ranging-Korrekturen. Die geschätzten Kalibrierungsparameter (Bias, Skalierungsfaktoren) zeigen eine deutliche Temperaturabhängigkeit und bestätigen damit die Sensitivität der Akzelerometer gegenüber Temperaturschwankungen. Speziell für spätere GRACE Zeiträume ohne aktive Temperaturkontrolle müssen temperaturabhängige Störsignale in den Akzelerometerdaten berücksichtigt werden, um eine Verschlechterung der abgeleiteten Schwerefeldmodelle zu vermeiden. Der vorgestellte Kalibrierungsansatz führt zudem zu einer signifikanten Verbesserung der geschätzten C20 Koeffizienten. Insgesamt führen die einzelnen Methoden zur Datenvorprozessierung zu einer schrittweisen Verbesserung der Schwerefeldlösungen.

Im Allgemeinen kann eine detaillierte Analyse der Instrumentendaten wesentlich zur Reduktion des Rauschniveaus der Schwerefeldlösungen beitragen. Anhand der ITSG-Grace Schwerefeldprozessierung konnte die Wichtigkeit und das Potential der Datenvorprozessierung gezeigt werden. Die erzielten Ergebnisse führen nicht nur zu einer Verbesserung der monatlichen GRACE Schwerefeldmodelle, sondern liefern auch wichtige Erkenntnisse für zukünftige Schwerefeldmissionen, wie GRACE-FO. Für die Nachfolgemission GRACE-FO ist ein genaues Verständnis von möglichen Fehlerquellen innerhalb der GRACE Instrumentendaten essentiell um die geforderten Genauigkeiten erreichen zu können.

Acknowledgement

First of all, I would like to thank my supervisor Univ.-Prof. Torsten Mayer-Gürr. By proposing the research topic, he gave me the opportunity to work on my PhD thesis and to become part of the GRACE research community. The freedom of letting me work independently and steering my thoughts into the right direction every once a while, gave me the right guidance throughout the past years. Thank you for sharing your knowledge and supporting me!

My gratitude also goes to Prof. Dr. Frank Flechtner (Technical University of Berlin, GFZ Potsdam) for being my external reviewer and co-examiner, but also for his willingness to share his knowledge, experience and expertise in the field of GRACE.

This research would not have been possible without numerous discussions with various members of the GRACE Science Team. Especially, I want to thank Tamara Bandikova (JPL) for the collaborations and the sharing of valuable insights.

Further, I would like to thank all my colleagues from the Working Group Theoretical Geodesy and Satellite Geodesy for the enjoyable working environment, their constructive feedback, and their "sportive" distraction from work. Special thanks go to my former and current room mates Christian, Norbert and Saniya.

This thesis would not have been possible either without the support and help from my parents, friends and family. In particular, I am very grateful to my fiancé Daniel for his unlimited encouragement, patience, loyalty and love.

Contents

1 Introduction

1.1 Motivation

The Earth's gravity field is an important indicator of mass variations within the dynamic system of our planet. Primary sources of mass re-distributions and mass variations are climate-relevant geophysical and anthropogenic processes. Therefore, the observation of mass changes from time-variable gravity has become an important topic within global climate research. Observing variations in the Earth's gravity field provides a unique and invaluable source of information for various environmental and geophysical research areas, since these observations provide fundamental insights into the global water cycle, polar and mountain ice mass loss, changes in ocean surface currents, sea level rise, groundwater depletion, and many other processes. Hence, satellite gravimetry can substantially contribute to an improved understanding of the dynamic system Earth and the underlying geophysical processes. This becomes of utmost importance for both understanding and counteracting global climate change and climate warming.

In the past two decades, dedicated satellite missions to observe the Earth's gravity field, such as the ESA mission GOCE (Gravity field and steady-state Ocean Circulation Explorer; ESA, 1999), the German minisatellite mission CHAMP (CHAllenging Minisatellite Payload; Reigber et al., 1999), and the US-German mission GRACE (Gravity Recovery And Climate Experiment; Tapley et al., 2004) have been realized. In the context of global climate monitoring, the GRACE mission holds a special status within this group.

The GRACE mission provided information about the Earth's static and time-variable gravity field with unprecedented accuracy for more than 15 years (2002-2017), and can be therefore considered as the most successful gravity field mission so far. Each spacecraft carries a science payload consisting of a K-Band mircrowave ranging (KBR) system, GPS receiver, star cameras, and accelerometer, providing the primary observations needed for gravity field recovery. Due to its unique orbital configuration and measurement principle, relying on inter-satellite ranging measurements, GRACE provides observations with a high spatial and temporal resolution. This allows, in addition to the determination of the Earth's static gravity field, for the recovery of monthly gravity field models (every ~ 30 days). Since its launch in 2002, GRACE has enabled almost continuous monitoring of the time-variable gravity field, providing an invaluable time series for climate research. The importance of this mission is underlined by a substantial number of related scientific publications (> 3000), and numerous contributions to IPCC (Inter governmental Panel on Climate Change) assessment reports (e.g., IPCC (2013)).

The most recent global mean and time-variable GRACE gravity field models were published by e.g., Bettadpur (2012), Dahle et al. (2013), Mayer-Gürr et al. (2014), Meyer et al. (2016), and Mayer-Gürr et al. (2016b). Although the accuracy of GRACE gravity field

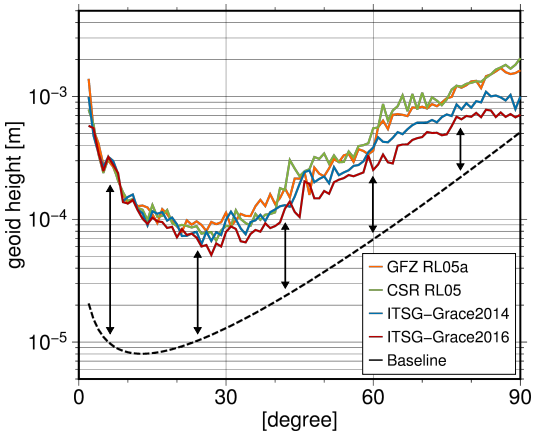

Fig. 1.1.: Illustration of the GRACE baseline offset: Difference degree amplitudes of the GFZ RL05a (orange), CSR RL05 (green), the ITSG-Grace2014 (blue), and the ITSG-Grace2016 (red) monthly gravity field solution for December 2008. The difference degree amplitudes are computed w.r.t. to the GOCO05s.

solutions has increased considerably during the last years, there still remains an offset between the error-level of present gravity field solutions and the GRACE baseline accuracy (cf. Fig. 1.1), i.e. the predicted accuracy from pre-launch simulations (Kim and Tapley, 2002). Therefore, even after more than 15 years of mission operation, efforts are ongoing to identify the remaining error sources. The accuracy of the GRACE-derived gravity field models is primarily limited by the inter-satellite ranging measurement noise, accelerometer errors, attitude errors, orbit errors, and temporal aliasing caused by unmodeled high-frequency variations in the gravity signal. Hence, not only aliasing effects due to under-sampling in space and time, and imperfections of the background models, but also errors and disturbances within the instrument data are a limiting factor. A prominent example for the latter are temperature variations due to reduced battery capacity (coming along with increased mission duration), which directly affect the instruments, causing thermal distortions. To avoid a degradation of the monthly gravity field solutions, the effects of thermal variations on the accelerometer (and other instruments) need to be taken into account during gravity field recovery (Klinger and Mayer-Gürr, 2016). This also implies that improvements within the instrument data processing and instrument data calibration can substantially contribute to the overall accuracy of current gravity field solutions. In recent years, many investigations with respect to sensor errors and disturbances have been carried out (e.g., Frommknecht, 2008; Flury et al., 2008; Bandikova et al., 2012; Peterseim et al., 2012; Bandikova and Flury, 2014; Klinger and Mayer-Gürr, 2014; Inácio et al., 2015; Harvey, 2016; Klinger and Mayer-Gürr, 2016; Harvey et al., 2016; Goswami and Flury, 2016). However, not all error sources and perturbations acting upon satellite instruments and sensors are resolved yet.

The GRACE-FO mission, successor to GRACE, is scheduled for launch in spring 2018 (Flechtner et al., 2017). GRACE-FO is a quasi-replica of GRACE, and pursues the primary objectives of the original GRACE mission by extending the time series of highly-accurate monthly Earth gravity field models. Therefore, a profound understanding of possible error sources and disturbances prevalent within the GRACE instrument data is not only essential for the improvement of current gravity field models, but especially for future gravity field missions, such as GRACE-FO, where even higher accuracies should be achieved.

What all the different approaches for gravity field recovery and involved processing centers have in common, is the data basis used for the GRACE gravity field recovery. In principal, all analysis centers use the so-called Level-1B data products, a publicly-available and pre-processed instrument data set provided by JPL, as input for their algorithms. Therefore, this work is dedicated to the analysis and pre-processing of GRACE Level-1B data products. The primary objective of this thesis is to provide a comprehensive overview on how improved modeling and Level-1B data pre-processing methodologies, as part of the ITSG-Grace gravity field processing chain, can contribute to the aforementioned goals. Thereby, the main focus is on general data screening strategies, the attitude improvement based on a sensor fusion approach (combination of star camera and accelerometer data), and the pre-processing and calibration of the accelerometer data.

1.2 Outline of the thesis

Following the introduction, Chapter 2 gives an overview of the GRACE mission (Section 2.1), summarizing the mission design (Section 2.2), instrument payload (Section 2.3), and available data products (Section 2.4 and Section 2.5). Furthermore, the end-of-lifetime issues affecting the science instrument operation and mission duration (Section 2.6), and the future GRACE-FO mission (Section 2.7) are briefly discussed.

The basic concepts are introduced in Chapter 3. This includes the basic formulae used to describe the equation of motion (Section 3.1), the Earth's gravity field (Section 3.2), and non-gravitational accelerations (Section 3.3). The concept of variational equations, applied for gravity field recovery, the basic principles of least squares adjustment, and VCE are introduced in Section 3.2, 3.5 and 3.6, respectively.

Chapter 4 provides an overview of the processing chain used for the recovery of the latest ITSG-Grace2016 gravity field models (Klinger et al., 2016; Mayer-Gürr et al., 2016a; Mayer-Gürr et al., 2016b). It gives details on the input data (Section 4.1), and the processing chain itself (Section 4.2), with a focus on the data pre-processing (Section 4.3). The Section on "Level-1B data pre-processing" also includes the principles of data resampling and data screening, applied prior to the actual gravity field recovery. Finally, the software package, used for the ITSG-Grace gravity field recovery, is shortly introduced (Section 4.4).

In Chapter 5, the measurement principles, characteristics, measurement accuracies, and data products of two fundamental GRACE instruments, namely: (1) the star camera (Section 5.1), and (2) the accelerometer (Section 5.2), are discussed. A profound knowledge of the instrument characteristics is the basis for any further methodologies, results, or analysis presented within this thesis. The star camera is the main instrument used for attitude determination during science operation. The precise attitude determination is important not only for the in-orbit maintenance of the inter-satellite pointing, which is a fundamental prerequisite for KBR ranging, but also for the post-processing of the inter-satellite ranging observations, and the accelerometer measurements, which are both needed for gravity field recovery. The main purpose of the accelerometer is to measure the linear non-gravitational accelerations, needed to separate the non-gravitational forces from the gravitational ones. Furthermore, it provides additional information in terms of angular accelerations, providing relative attitude information, which can be exploited for the purpose of sensor fusion.

Chapter 6 describes in detail the characteristics of the GRACE attitude determination (Section 6.1), possible shortcomings of the current attitude determination process (Section 6.2), and how an improved attitude determination (sensor fusion; Section 6.3) can be realized on the basis of Level-1B data products. The sensor fusion approach, based on the combination of star camera and angular accelerometer data, is explained in detail. As part of the presented analysis, the effects on the attitude data (Section 6.3.4), the ranging observations (Section 6.3.5), and the accelerometer observations (Section 6.3.6) are discussed. Additionally, a short outlook on further option for attitude processing (Section 6.4), concerning GRACE and GRACE-FO, is given.

Chapter 7 summarizes the basics and results of the accelerometer data calibration, including details on the calibration approach itself (Section 7.1), and the estimated calibration parameters: (1) biases - parameterized in terms of Uniform Cubic Basis Splines (Section 7.2), and (2) scale factors - represented by a fully-populated scale factor matrix (Section 7.3). As in the previous Chapter, a short outlook on further options for accelerometer data processing (Section 7.4) is given.

The results, i.e. the effects of the Level-1B pre-processing methodologies on the recovered gravity field solutions, are analyzed in Chapter 8. This primarily includes analysis with resepct to the sensor fusion approach (Section 8.2), and the data screening and accelerometer data calibration (Section 8.3). In particular, the effect of the accelerometer data calibration on the estimated C20 coefficients is discussed in detail (Section 8.3.1), representing one of the major findings of this work.

The final Chapter 9 shortly summarizes the achieved results, and provides a brief outlook (Section 9.2) for future research possibilities and activities in the context of GRACE and GRACE-FO data processing for the purpose of gravity field recovery.

GRACE

2

2.1 Mission overview

GRACE (**G**ravity **R**ecovery and **C**limate **E**xperiment) is a joint scientific satellite mission between the National Aeronautics and Space Administration (NASA) in the United States and the German Aerospace Center (DLR). It has been proposed jointly by the Center for Space Research (CSR) at the University of Texas at Austin, the German Research Centre for Geosciences (GFZ), the Jet Propulsion Laboratory (JPL), the Space Systems/Loral (SSL), the DLR, and the Astrium GmbH in 1996, and was selected as the second mission in NASA's Earth System Science Pathfinder (ESSP) program in 1997 (Tapley et al., 2004). The GRACE mission consists of two identical satellites, GRACE-A and GRACE-B, following each other in the same orbital track, linked by a highly accurate inter-satellite K-Band microwave ranging system. The satellite constellation is depicted in Figure 2.1. GRACE was successfully launched on board a Rockot launch vehicle from the Russian spaceport Plesetsk on March 17, 2002. The twin satellites were placed in a near-circular and near-polar orbit with an initial altitude of about 500 km and a nominal along-track separation of 220 km. Since then, the orbit naturally decayed to an altitude of about 320 km at the end of science mission. After more than 15 years of missions operation, GRACE has ended science operations in October 2017 due to an age-related battery issue on GRACE-B. On December 24, 2017 GRACE-B re-entered the Earth's atmosphere and burned up upon re-entry. GRACE-A is currently in the decommissioning phase with an expected atmospheric re-entry in early March 2018 (personal communication with Frank Flechtner (GFZ)).

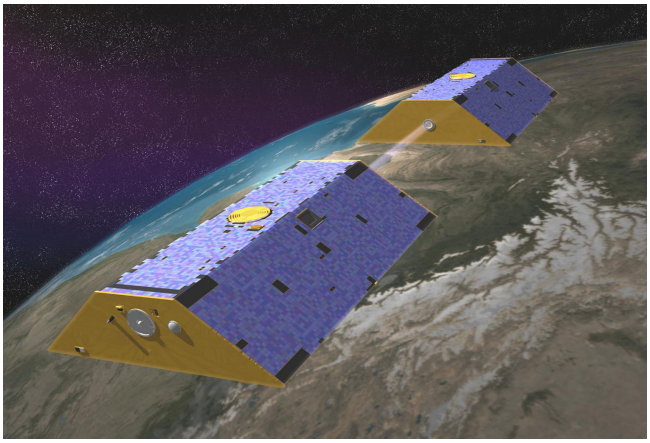

Fig. 2.1.: Illustration of the GRACE twin satellites in orbit. Source: NASA/JPL.

2.1.1 Science objectives

The primary science objective of the GRACE mission is to obtain accurate global models for the mean and the time-variable components of the Earth's gravity field (Stanton et al., 1998). To provide accurate information about the Earth's gravity field, each satellite is equipped with a science payload consisting of a K-Band microwave ranging (KBR) system measuring the inter-satellite distance with micrometer accuracy, a Global Positioning System (GPS) receiver for position determination and radio occultation measurements, star cameras (SCA) for precise attitude determination, and an accelerometer (ACC) measuring the non-gravitational forces acting upon the satellites. Details on the KBR measurement principle and the different instruments on board the GRACE satellites are given in Section 2.2 and 2.3.

GRACE provided information about the Earth's static and time-variable gravity field for more than 15 years, and can be considered as the most successful gravity field mission so far. As the gravity field is an important indicator of mass variations within the dynamic system Earth, the observation of mass changes from time-variable gravity has become an important topic within the scientific community, especially with regard to global climate research (e.g., Fifth Assessment Report of the Intergovernmental Panel on Climate Change (IPCC-AR5; IPCC, 2013). The precise knowledge of the gravity field and its variations provides a unique and invaluable source of information for various environmental and geophysical research areas, enabling fundamental insights into the global water cycle, polar and mountain ice mass loss, changes in ocean surface currents, sea level rise, groundwater depletion, and many other processes.

The secondary science objective of the GRACE mission is to obtain globally distributed vertical temperature and humidity profiles of the atmosphere using the GPS radio occultation technique. Together with other missions, the GRACE radio occultation data enables advances in various fields of atmospheric and climate sciences, including weather modeling and forecasting (Wickert et al., 2009).

2.2 Mission design - Measurement principle

The GRACE measurement principle is based on the Satellite-to-Satellite Tracking (SST) measurement technique, which makes use of satellites to track other satellites (cf. Fig. 2.2). Basically, two types of SST are distinguished: (1) High-low Satellite-to-Satellite Tracking (hl-SST), and (2) Low-low Satellite-to-Satellite Tracking (ll-SST).

High-low Satellite-to-Satellite Tracking: The orbit of a Low Earth Orbit (LEO) satellite is determined using several high altitude satellites with accurately known orbits, such as GNSS (Global Navigation Satellite System) satellites. Details on the GNSS signals, measurement principle and data processing can be found in e.g., Hofmann-Wellenhof et al. (2008).

Low-low Satellite-to-Satellite Tracking: Two satellites are placed in the same orbit with a separation up to a few hundreds of kilometers. Irregularities in the Earth's gravity field cause changes in the relative distance between the two satellites, which can be measured by an on-board ranging system.

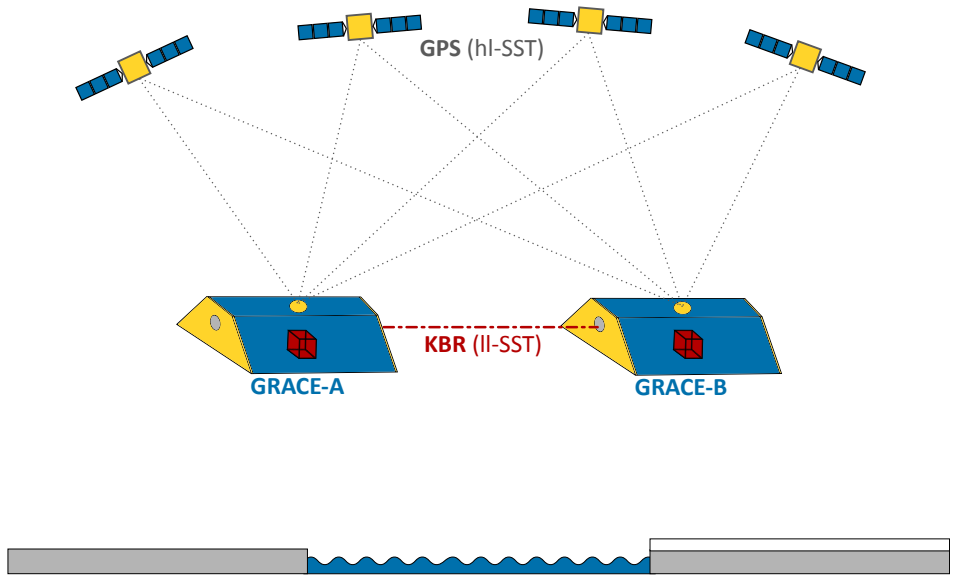

Fig. 2.2.: GRACE measurement principle: hl-SST and ll-SST

The dual-satellite mission GRACE combines both techniques to determine the Earth's gravity field from (1) continuous GPS orbit tracking data (hl-SST), and (2) inter-satellite tracking data (ll-SST: ranges, range-rates, range-accelerations) measured by the onboard KBR system (cf. Section 2.2.1).

To enable ll-SST, the two GRACE satellites (GRACE-A and GRACE-B) are placed in a near-circular (e $<$ 0.005) and near-polar (i $= 89.0°$) orbit, with an initial altitude of 500 km and a nominal along-track separation of 220 ± 50 km. This orbital configuration guarantees a sufficient spatial coverage over any typical 30-day span, which is the nominal interval for GRACE monthly gravity field solutions. Over the mission lifetime, the orbit altitude decays from almost 500 km at the beginning of the mission, to approximately 300 km at the end of the mission. Besides the altitude decay, the orientation of the orbital plane relative to the Sun (β' angle) changes with a period of 322 days (cf. Appendix D.2).

As the satellite pair orbits the Earth, both GRACE satellites experience gravitational perturbations due to the inhomogeneous mass distribution and re-distribution (e.g., exchange of mass between land, ocean, and atmosphere) within the system Earth. Since both satellites are flying in a co-planar orbit separated by 170 km to 270 km, the leading and trailing satellite are sensing slightly different perturbations, resulting in continuous inter-satellite distance variations. These range changes are measured very accurately by the GRACE KBR system (cf. Section 2.3). In addition to the gravitational perturbations, the satellites also experience perturbations due to non-gravitational forces, such as atmospheric drag, solar radiation pressure, and albedo (cf. Section 3.3). For this reason, the GRACE satellites are equipped with high-sensitive accelerometers, which directly measure the non-gravitational accelerations acting upon the spacecraft. This ensures that the differential range changes due to the non-gravitational accelerations are accurately removed (from the GRACE inter-satellite tracking measurements). More details on the SuperSTAR accelerometers on-board GRACE

are provided in Section 5.2. Each GRACE satellite also carries a geodetic GPS receiver to enable continuous Precise Orbit Determination (POD) and the spatial registration of the inter-satellite ranging data.

The combination of GPS hl-SST, KBR ll-SST and accelerometry enables the recovery of highly-accurate temporal gravity field models. Compared to other gravity field missions, such as CHAMP or GOCE, the differential KBR measurements contribute to an improvement of the long and medium wavelength, and allow to observe temporal variations within the Earth's gravity field.

2.2.1 K-band inter-satellite ranging

The KBR Assembly, providing dual one-way range measurements with micrometer-level accuracy, is the key science instrument of the GRACE mission. It measures the changes in the separation distance between the two GRACE satellites using phase tracking of K-band (24 GHz) and Ka-band (32 GHz) signals sent between the two satellites. Figure 2.3 illustrates the concept of the KBR system according to Thomas (1999) and Kim and Tapley (2002).

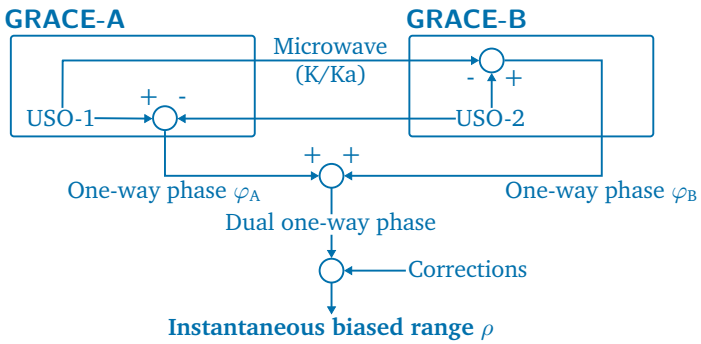

Fig. 2.3.: Schematic overview of the KBR system: operating principle of the dual one-way ranging system according to Thomas (1999) and Kim and Tapley (2002).

The KBR Assembly is identical for both satellites and consists of a single horn antenna, an Ultra-Stable Oscillator (USO), frequency convertors, and an Internal Processing Unit (IPU) (cf. Section 2.3.1). The KBR-horn is mounted at the front panel of each satellite (cf. Fig. 2.5), and is used for both transmission and reception of the microwave signal. Both satellites transmit a dual microwave signal, consisting of a carrier signal modulated on a 24 GHz K-Band and a 32 GHz Ka-Band frequency. The onboard USO, a Quartz crystal resonator, generates these highly-stable microwave signals (Asmar, 1997). The onboard signal processing is done by the IPU and provides for each of the satellite the one-way phase measurements, which represent the difference between the receiver's reference phase and the received phase. During on-ground processing, the one-way phase measurements are combined to the dual one-way phase measurement and corrected for systematic effects. To obtain the instantaneous biased range, the dual one-way phase measurement is multiplied by the wavelength (cf. Fig. 2.3).

The dual one way range $R(t)$, representing the range between the two satellites' centers of mass (CoMs) at a certain time epoch t, is obtained by (Kim and Tapley, 2002)

$$R(t) = \rho(t) + \Delta\rho_{TOF} + \Delta\rho_{Iono} + \Delta\rho_{AOC} + B + \Delta\rho_{err}. \tag{2.1}$$

Therein, $\rho(t)$ denotes the instantaneous biased range at the time epoch t. The light-time correction $\Delta\rho_{TOF}$ accounts for the satellites motion during the signal time of flight (TOF). The ionospheric correction $\Delta\rho_{Iono}$ accounts for the ionospheric delay. The correction for the antenna center offset $\Delta\rho_{AOC}$, which is often denoted as antenna offset correction (AOC), represents the distance between the KBR antenna phase center and the center of mass (CoM) (cf. Section 6.1). The range bias B results from the unknown phase ambiguity values in the one-way phases. And $\Delta\rho_{err}$ represents the measurement noise. The range rates and range accelerations are obtained by numerical differentiation of the range measurements. More details on the KBR can be found in e.g., Thomas (1999), Kim (2000), and Kim and Tapley (2002).

2.2.2 In-orbit constellation - Formation keeping

Since the inter-satellite ranging is carried out between the two KBR horn antennas, which are mounted at the front panel of each satellite, the leading satellite is always turned by $180°$ around its z-axis. The KBR measurement principle requires the KBR antenna phase centers to be aligned with the Line-Of-Sight (LOS) within a few milliradians. In order to ensure a LOS orientation of the KBR microwave link, the formation-flying requires a pitch angle offset between $0.4°$ and $2.2°$, depending on the altitude and separation (Kirschner et al., 2001). During nominal altitude and separation, both satellites fly with a $\pm 1°$ pitch angle offset to enable precise inter-satellite pointing between the two satellites (cf. Fig. 2.4). The importance of the precise satellite alignment is further discussed in Section 6.1.1.

The x-axis (along-track) of the body-fixed Science Reference Frame (SRF) is pointing towards the KBR antenna horn, i.e. it is approximately tangential to the satellite orbit except for the pitch angle offset. The z-axis (radial) is nadir pointing, and the y-axis (cross-track) completes the right handed triad. These somewhat vague definitions of the SRF axes are introduced here for an easier comprehension within this thesis; the exact definitions of the GRACE reference frames can be found in e.g., Case et al. (2010) and Bettadpur (2010). An overview of the most important frames is also provided in Appendix A.

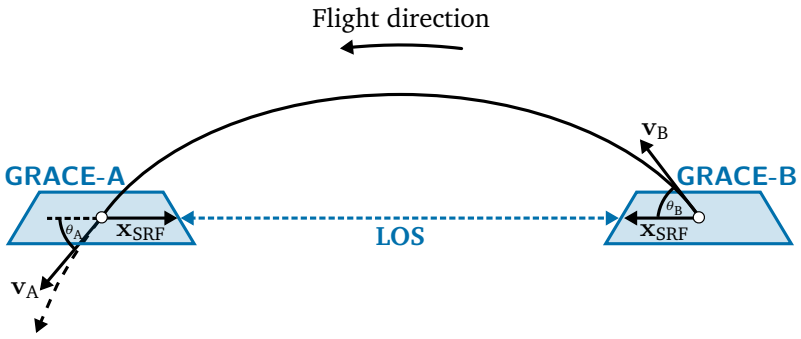

Fig. 2.4.: In-orbit constellation of the GRACE satellites: orientation of the leading and trailing satellite relative to the orbit trajectory, with a pitch angle offset (θ_A, θ_B) enabling KBR inter-satellite ranging.

2.3 Payload

The two co-orbiting twin satellites GRACE-A and GRACE-B are identical, except for ground and inter-satellite communication frequencies. Both GRACE satellites have a prismatic body (3.1 x 1.9 x 0.7 m) with a fully fueled mass of about 487.2 kg. Because of their dimensions, the GRACE satellites belong to the category of small satellites. The description of the GRACE payload is based on the GRACE Launch Press Kit (NASA, 2002) and the GRACE mission pages of GFZ[1] and CSR[2].

2.3.1 Science Instrument System (SIS)

In order to provide accurate information about the Earth's gravity field, the GRACE satellites are equipped with a broad variety of instruments and sensors. The measurements of these instruments and sensors are either directly linked to the Earth's gravity field, or they are needed to liberate the direct measurements from biasing signals in order to enable the recovery of the gravity field information solely. The key science instrument on board GRACE is the KBR Assembly, measuring the inter-satellite distance change (cf. Section 2.2.1). A schematic overview of the GRACE satellites and the science instruments onboard is shown in Figure 2.5. In the following, the different components of the Science Instrument System (SIS) are shortly described and summarized. The SIS includes all elements of the KBR system, the GPS receivers, and associated sensors such as the star cameras and accelerometers. It also coordinates the integration activities of all sensors, assuring their compatibility with each other and the satellite.

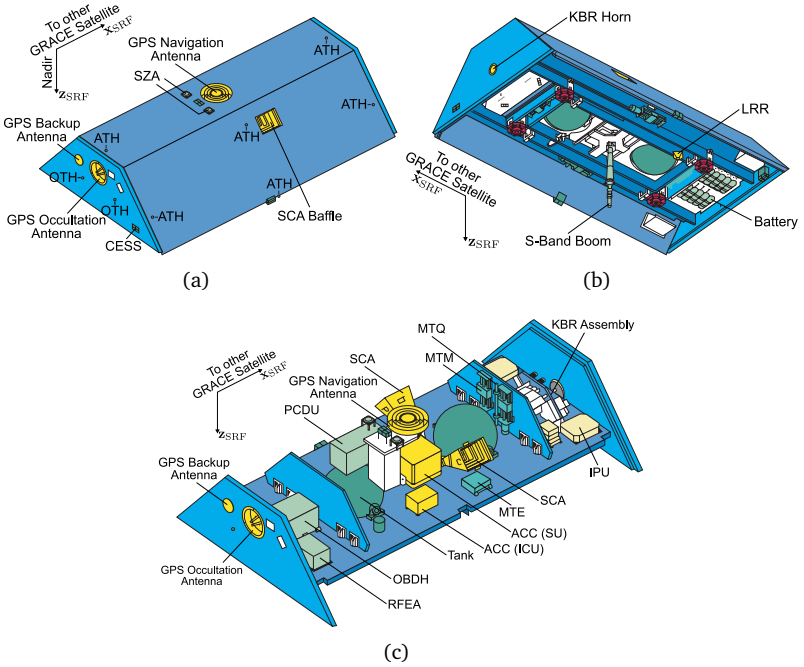

Fig. 2.5.: GRACE instrumentation: (a) front view, (b) bottom view, and (c) internal view of a GRACE satellite. Source: GRACE Launch Press Kit (NASA, 2002).

[1] https://www.gfz-potsdam.de/en/grace/
[2] http://www2.csr.utexas.edu/grace/spacecraft/

As primarily the accelerometer and star cameras are analyzed within this thesis, they are introduced within this Section, but are discussed in more detail in subsequent Sections (cf. Section 5.2 and 5.1).

K-Band Ranging Assembly (KBR): The KBR measures the dual one-way range change between the two GRACE satellites with a precision of about 1 μm/s. The hardware consists of the components listed below:

USO	The USO serves as frequency and clock reference for the satellites.
KBR-Horn	The KBR-Horn transmits and receives K-Band (24 GHz) and Ka-Band (32 GHz) carrier signals between the two satellites.
Sampler	The Sampler downconverts and samples the incoming K- and Ka-Band carrier phase.
IPU	The IPU provides the digital signal processing functions for the K-/Ka-Band signals, and for the GPS signals. Additionally, it is responsible for the data processing of the star camera attitude quaternions.

Global Positioning System Receiver Assembly (GPS): The GPS Receiver Assembly consists of two omnidirectional navigation antennas (primary and backup) and one high-gain helix occultation antenna, which track GPS signals for: (1) POD with cm-accuracy, (2) time-tagging of science data, (3) satellite position and clock determination for on-board operations, and (4) atmospheric and ionospheric profiling.

SuperSTAR Accelerometer (ACC): The SuperSTAR Accelerometer, manufactured by Office National d'Études et de Recherches Aérospatiales (ONERA), measures the non-gravitational accelerations acting on the GRACE satellites. The ACC consists of a Sensor Unit (SU), an Interface Control Unit (ICU), and a harness. The SU consists of a metallic proof mass located inside a slightly larger sensor cage, mounted in the CoM of the satellite. The ICU supplies power to the SU, and performs the filtering and digital signal processing functions for the accelerometer. The ACC measurements are essential for gravity field recovery (separation of gravitational and non-gravitational forces), or can be used to determine upper atmospheric density variations. A more detailed description of the ACC is provided in Section 5.2.

Star Camera Assembly (SCA): The Star Camera Assembly, manufactured by the Technical University of Denmark (DTU), consists of two star camera heads, and determines the attitude of the GRACE satellites with respect to the inertial frame. The SCA measurements are used for the precise orientation of the satellite within the AOCS, and for the correct interpretation of the ACC measurements. A more detailed description of the SCA is provided in Section 5.1.

Laser Retro Reflector (LRR): The Laser Retro Reflector, provided by GFZ, is a passive payload consisting of 4 prisms. The LRR enables the tracking of the GRACE satellites by terrestrial Satellite Laser Ranging (SLR) stations for orbit determination and control.

2.3.2 Satellite System (SAT)

All science instruments (cf. Section 2.3.1), the fuel tanks, batteries and other satellite sub-systems are mounted on a Carbon-Fiber Reinforced Plastic (CFRP) platform in the interior of the satellite (cf. Fig. 2.5). In the following, the individual sub-systems of the Satellite System (SAT) are described in more detail.

Spacecraft Housekeeping & Data Handling System:

OBDH	The Onboard Data Handler (OBDH), the central processor and memory onboard the satellites, is needed for science and housekeeping data management and spacecraft health functions.
RFEA	The Radio-Frequency Electronics Assembly (RFEA) prepares the OBDH data for the S-Band transmission to the ground data system.
S-Band Boom	The S-Band Boom is the primary system used for ground communication.
SZA (TX/RX)	The S-Band Zenith Transmitter (TX) and Receiver (RX) Antenna form the backup system for ground communication.
PCDU	The Power Conditioning, Distribution and Control Unit (PCDU) is responsible for the generation, storage, conditioning and distribution of electrical power, which is generated by solar arrays.
Battery	The Nickle-Hydrogen (NiH) battery (with 16 Ah capacity) provides power storage.
Solar cells	Electrical energy is generated by solar arrays on the top and side panels of the satellites.

Mass Trim System (MTM & MTE): The Mass Trim Mechanism (MTM), and the associated Mass Trim Electronics (MTE) ensure that the spacecraft center of gravity coincides with the center of the ACC proof-mass. This ensures that the ACC only measures the non-gravitational forces.

Attitude and Orbit Control System (AOCS):

SCA	The Star Camera Assembly is the primary sensor within the AOCS.
CESS	The Coarse Earth/Sun Sensor is an additional sensor providing coarse attitude determination.
MAG	The Förster magnetometer is an additional sensor measuring the Earth's magnetic field. It provides coarse attitude determination based on the satellite position (GPS) and an Earth magnetic field model.
Gyro	The Gyroscope is an additional sensor providing 3-axis attitude rate information.
Actuators	Six Magneto-Torquers (MTQ) and a set of 10 mN thrusters (ATH) are used for attitude control.
Orbit Control	Two 40 mN thrusters (OTH) are used for orbit maneuvering and control.

Thermal Control: The Thermal Control sub-system consists of 64 independent heater circuits, 45 resistors and 30 thermistors, which are used for in-flight temperature housekeeping, monitoring and heater control, as well as for on-ground verification testing.

2.4 Data levels

All available GRACE data products are distributed and archived by a distributed Science Data System (SDS). The system development, science data processing, archiving, distribution, and product verification are shared between the JPL, CSR and GFZ (Case et al., 2010). The GRACE Level-0 to Level-2 SDS data products are defined as follows (Case et al., 2010):

Level-0: The Level-0 data products contain the raw science instrument and housekeeping data, which is received from the GRACE satellites, collected and decommutated by the Raw Data Center (RDC) of the Mission Operation System (MOS), which is part of the DLR, and located in Neustrelitz, Germany. The DLR is not only responsible for the data reception, but also for the mission control of the GRACE satellites.

Level-1A: The Level-1A data products are the result of a non-destructive processing applied to the Level-0 data, i.e. the binary encoded measurements are converted to engineering units. The Level-1A data products also contain editing and quality control flags, as well as ancillary data products needed for the further Level-1A to Level-1B processing.

Level-1B: The Level-1B data products contain the final and publicly available science instrument and housekeeping data products, and are derived from the Level-1A data products. During Level-1A to Level-1B data processing the data are correctly time-tagged, resampled and converted to a common reference frame, i.e the original data cannot be reconstructed.

The processing of Level-1 data products (cf. Fig. 2.6) is done primarily at the JPL. For a detailed description of the Level-1 processing, see Case et al. (2010). All Level-1B data products are archived at JPL's Physical Oceanography Distributed Active Archive Center (PODAAC)[3] and at GFZ's Information System and Data Center (ISDC)[4].

Level-2: The Level-2 data products contain the static and time-variable (monthly) gravity field models in a spherical harmonic representation (cf. Section 3.2), derived from the Level-1B data products. Additionally, the Level-2 data products also include ancillary data products (e.g., mean atmospheric and oceanic mass variations), which are necessary to interpret time variabilities within the gravity field solutions.

The Level-1B to Level-2 data processing, as shown in Figure 2.6, is performed independently by different analysis centers (ACs) inside and outside the GRACE SDS. The individual gravity field solutions differ considerably, since each AC adopts independent processing standards and analysis methods. Temporal gravity field models are provided by e.g., CSR (Bettadpur, 2012), JPL (Watkins and Yuan, 2014), GFZ (Dahle et al., 2013), Le Centre national d'études spatiales/Le Groupe de Recherche de Géodésie Spatiale (CNES/GRGS) (Biancale et al., 2014), Astronomical Institute of the University of Bern (AIUB) (Meyer et al., 2016), Institute of Geodesy (IfG) of the Graz University of Technology (Mayer-Gürr et al., 2016b), and others. The official Level-2 products (CSR, JPL, GFZ) are archived at JPL's PODAAC and at GFZ's ISDC, whereas all other Level-2 products can be accessed via the International Centre for Global Earth Models (ICGEM) website[5]. The ICGEM is a service at GFZ coordi-

[3] `ftp://podaac.jpl.nasa.gov/allData/grace/`
[4] `ftp://rz-vm152.gfz-potsdam.de/grace/`
[5] `http://icgem.gfz-potsdam.de/series`

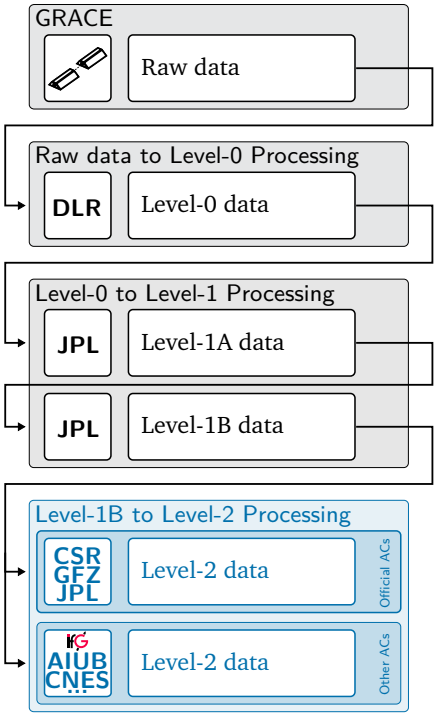

Fig. 2.6.: GRACE data products: Illustration of the Level-0 to Level-2 data processing scheme.

nated by the International Gravity Field Service (IGFS) of the International Association of Geodesy (IAG).

2.5 Level-1B data products

The analysis and results presented within this thesis are based on the GRACE Release 02 (RL02) Level-1B data products listed in Table 2.1. Besides, pre-processed Level-1B data products (cf. Section 6 and 7), and kinematic orbits derived by the raw acceleration approach (Zehentner and Mayer-Gürr, 2015) are used as input for the gravity field recovery. Details on the ITSG gravity field processing are given in Section 4.

Tab. 2.1.: Overview of used GRACE Level-1B science instrument and housekeeping data products.

Science data product	**Description**
ACC1B	Accelerometer Data Product
GNV1B	GPS Navigation Data Format Record
KBR1B	KBR Data Format Record
SCA1B	Star Camera Data Product
Housekeeping data product	**Description**
AHK1B	Accelerometer Housekeeping Data Product
MAS1B	Spacecraft Mass Data Format Record
THR1B	Thrusters Data Format Record
TNK1B	Cold Gas Tank Data Format Record
VKB1B	Vector Product (KBR antenna phase center offset)
SOE	Sequence of Events file

In general, two types of GRACE Level-1B data products are distinguished: (1) science data products, and (2) housekeeping data products. The former are the data products primarily used by the scientific community, as they provide the key observations of the instruments on-board GRACE. The latter give additional information in terms of internal satellite and/or telemetry data. A detailed description of the official Level-1B data products is given in the GRACE Level 1B Data Product User Handbook (Case et al., 2010).

In this section, the GRACE Level-1B RL02 science and housekeeping data products, used and/or analyzed within this thesis, are introduced. The main characteristics and the content of the individual data products are described concisely.

2.5.1 Science data products

All GRACE Level-1B science data products refers to the satellite body-fixed Science Reference Frame (SRF; cf. Appendix A). The data is sampled with a rate of 5 seconds, except the ACC1B data (1 second) and the GNV1B data (60 seconds).

K-Band ranging data (KBR1B)

The KBR1B data product provides the dual-one-way ranging data (biased range, range rate, range acceleration), the light time correction, and the geometric correction (cf. Section 2.2.1). The ranging data, contained within the KRB1B data product, needs to be corrected for these two effects, but is already corrected for ionospheric effects (cf. Eq. (2.1)). In addition, the signal-to-noise ratio (SNR) numbers of the K-/Ka-Band for GRACE-A and GRACE-B are provided, giving information about the signal strength and ranging measurement quality.

Accelerometer data (ACC1B)

The ACC1B data product provides the linear and angular acceleration components (along-track, cross-track, radial) of the accelerometer proof mass. Since the accelerometer has an unknown scale and bias in each direction, the accelerations contained in the ACC1B data product include an instrument scale and bias offset. A general recommendation for the initial estimates of the scale and bias to apply to the ACC1B data is made in the GRACE Technical Note TN-02 (Bettadpur, 2009). The data calibration applied within the ITSG-Grace gravity field recovery is extensively discussed in Section 7.

Star camera data (SCA1B)

The SCA1B data product provides attitude quaternions, describing the orientation of the GRACE spacecrafts with respect to the inertial frame.

The representation of attitude in terms of quaternions is commonly used within spacecraft dynamics and 3D computer graphics, since it consumes relatively little memory capacity (e.g., compared to rotation matrices), and is numerically stable. For details on quaternions, see Appendix C.

Orbit data (GNV1B)

The GNV1B data product provides the navigation solution for the GRACE spacecrafts in terms of satellite positions and velocities with respect to the International Terrestrial Reference Frame (ITRF). Additionally, formal errors for both positions and velocities are provided.

In addition to the above described contents all Level-1B science data products also contain instrument-specific quality flags, providing additional information on the data quality.

2.5.2 Housekeeping data products

Besides the GRACE science data products, ancillary housekeeping data products are provided (cf. Tab. 2.1). Housekeeping data products consist of internal satellite data and/or telemetry data, which is needed for the maintenance of the satellite instruments or the attitude and altitude control. The Level-1B housekeeping data products contain additional information about the instrument health, output of additional on-board sensors (e.g., temperature), or calibration data. Hence, it is a supplementary source of information to monitor the GRACE satellites and thus helps analyzing the GRACE science data.

Accelerometer housekeeping data (AHK1B)

The AHK1B data product provides accelerometer housekeeping data, including displacements of the capacitive sensors, temperatures from various sensors located within the accelerometer, and voltages. Figure 2.7(a) shows the accelerometer core-temperature of both GRACE satellites during science mission (April 2002 to June 2017), derived from the AHK1B data product. As obvious from Figure 2.7(a), between September 2016 and May 2017 no temperature data is available for GRACE-B, since the accelerometer was permanently shut-off in this period (cf. Section 2.6).

Since the accelerometers need a thermally stable environment, they are directly affected by temperature variations (Klinger and Mayer-Gürr, 2016). Detailed investigations concerning the observed temperature variations and their impact on Level-1B accelerometer measurements can be found in Section 7.

Mass data (MAS1B)

The MAS1B data product contains the spacecraft mass in kilograms, derived from both fuel tank observations and thruster usage. Due to fuel consumption, the spacecraft mass is not constant and continuously decreased from 487.2 kg at launch, to approximately 460 kg at the end of mission. Figure 2.7(b) shows the satellite mass of GRACE-A and GRACE-B, based on fuel tank observations, from April 2002 till June 2017. Both mass values, based on fuel tank observations and thruster usage (not shown here), show unexplained jumps and discontinuities from February 2015 onward.

Since the MAS1B data product is used within the accelerometer data modeling (cf. Section 3.3), it directly influences the magnitude of the derived non-gravitational accelerations (cf. Eqs. (3.17), (3.19), (3.26), and (3.30)), and operates as a kind of scaling factor.

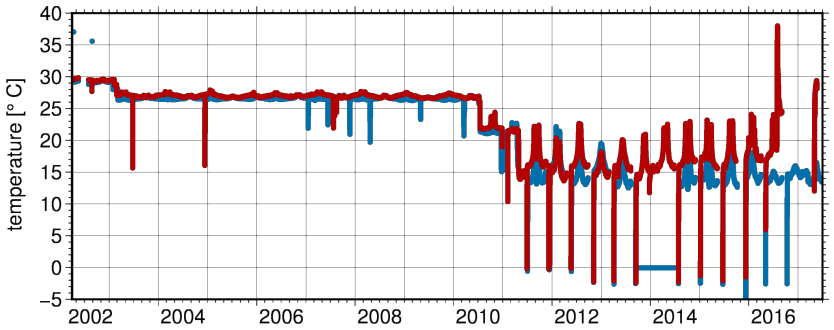

(a) AHK1B

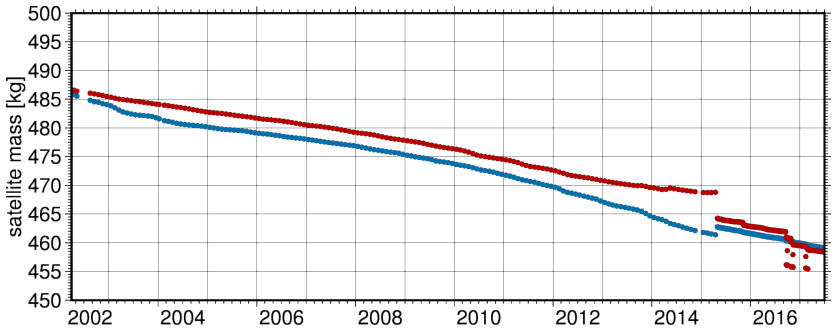

(b) MAS1B

Fig. 2.7.: Temporal evolution of (a) the accelerometer core-temperature, and (b) the satellite mass for GRACE-A (blue) and GRACE-B (red) for the whole GRACE science mission (April 2002 to June 2017). The temperature values in (a) are derived from the AHK1B data product. The satellite mass values in (b) are derived from the MAS1B data product. Note that here the mass values based on fuel tank observations are shown.

Thruster data (THR1B)

The THR1B data product contains the thruster activation data of the on-board cold-gas thrusters (7 pairs in total), separately for each spacecraft. The cold-gas thrusters are needed for orbit and attitude control (cf. Section 2.3.2), and are nominally operated in pairs. For each cold-gas thruster all thruster firing events are logged, including the exact activation time, and the duration of each thruster activation. On average, there are about 600 thruster events per day, primarily needed for attitude maintenance. Note that these number deviates for early and late periods of the GRACE mission. Figure 2.8 shows the spatial distribution of the occurring thruster events and the overall on-time of thrusters for GRACE-A for two month (January 2007, January 2015), representing different orbit constellations. Evidently, the thrusters are activated longer along the geomagnetic equator. This is because the magnetic torquers cannot sufficiently control the attitude (about the roll axis) within this region. In high latitudes, the thrusters are needed to control the attitude (about the yaw axis).

Except for the orbit maintenance thrusters (1 pair), all other thrusters should enforce a torque upon the spacecraft, and therefore should not be visible as linear accelerations. However, due to a possible angle misalignment between the thruster pairs, or small differences in the thrusting force or thrusting time, linear accelerations due to thruster events become visible within the accelerometer data, and have to be considered during the ACC1B data calibration (cf. Section 7).

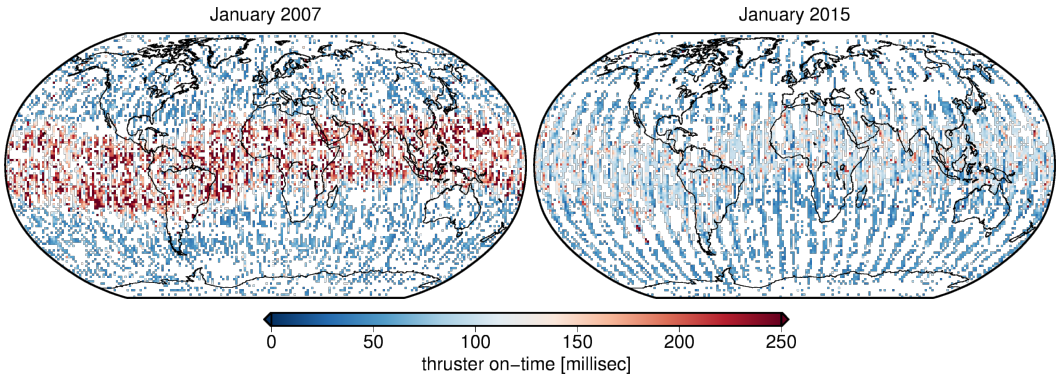

Fig. 2.8.: Spatial distribution of thruster activations for GRACE-A over one month: January 2007 (left) and January 2015 (right). The color indicates the overall thruster on-time, i.e. the sum of all attitude thrusters (6 pairs in total). The thruster events for orbit maintenance are excluded here.

KBR antenna phase center vector (VKB1B)

The VKB1B data product contains the vector offset of the KBR phase center, i.e. the vector from the satellites CoM to the KBR antenna phase center (phC). The x-, y-, and z-components of the vector are given with respect to the SRF. The values of the phC vector were updated once within the GRACE mission, and are also given within the SOE.

Sequence of Events file (SOE)

The SOE file records all relevant satellite events and state changes of satellite sensors, i.e. it contains a sensor and event time series describing their changes of state. These changes may affect the Level-1B science data quality. The ancillary SOE file (GRACE Technical Note TN-01) and the GRACE Technical Note TN-03 (Kruizinga, 2004), which provides a detailed description and format information on the SOE file, can be downloaded - like all other Level-1B data products - from JPL's PODAAC or GFZ's ISDC. For details on the SOE file structure, the reader is referred to Case et al. (2010) and Kruizinga (2004).

The following satellite events and state changes are taken into account during data screening within the Level-1B data pre-processing: (1) orbit maneuvers (yaw turns), (2) disabling of heater circuits, (3) KBR calibration maneuvers, and (4) CoM calibration maneuvers (cf. Section 4.3.2).

2.6 End-of-lifetime issues

After exceeding the nominal mission duration of 5 years and with further increasing lifetime, GRACE is facing additional challenges due to the following reasons:

- Reduced battery capacity,
- Propellant consumption (for orbit and attitude control),
- Orbit decay.

The first two challenges are primarily affecting GRACE-B, because of an age-related battery issue and one worse performing star camera. In order to extend the mission as long as possible, special operations were adopted to handle the constraints due to the reduced battery capacity, and due to the limited fuel availability (Herman et al., 2012; Herman and Steinhoff, 2012).

To ensure that the better star camera is used as primary input for attitude control, especially during Moon or Sun intrusions, satellite swap maneuvers are regularly performed since 2014 (cf. Section 4.3.2). Thus, the satellite swap maneuvers indirectly help to save fuel.

However, the most severe effects on the science instruments arise from the power constraints, which directly affect and/or interrupt the instrument operation periods (cf. Tab. 2.2). Therefore, the reduced battery capacity, the resulting countermeasures to prolong the mission, and their inevitable effects on the science data are discussed in more detail in the following.

2.6.1 Battery capacity

As already mentioned, the major challenge for the nominal operation of the satellites, and the onboard science instruments is posed by the degradation of the NiH batteries, which are comprised of 20 cells packaged in the common pressure vessel (CPV) configuration. The age-related battery degradation limits the available battery capacity, and thus the availability of power-supply in certain orbital configurations (Herman et al., 2012).

As a result of reduced battery capacity, active thermal control was switched-off in April 2011 (Tapley et al., 2015). Since then, temperature variations directly affect the on board instruments. To avoid a degradation of the monthly gravity field solutions, the effects of thermal variations on the accelerometer measurements have to be modeled during gravity field recovery (cf. Section 7.2.1).

To further extend the batteries' lifetime, the KBR and ACC are shut down for approximately 40-50 days during each 161-day β' cycle, i.e. data are not collected during these time periods (Tapley et al., 2015). The β' angle represents the angle between the orbital plane and the Earth-Sun line (cf. Appendix D.2). Every 161 days, at $\beta' = 0°$ crossings, the Sun is in the orbital plane of the satellites. During these periods, the spacecraft spend nearly half their revolution time in the Earth's shadow, and thus rely on their batteries for power. As a consequence, the GRACE instruments are periodically shut down for small β' angles. In between, when the satellite is in full-sun orbit ($\beta' > 70°$), all science measurements are

Tab. 2.2.: Chronology of GRACE power constraints due to degraded battery capacity.

Date	Power constraint	Affected satellite
Since April 2011	Active thermal control stopped	GRACE-A, GRACE-B
Since April 2011	KBR, ACC shut down for small β' angles	GRACE-A, GRACE-B
Since April 2011	Yaw turns for battery discharge & charge	GRACE-A, GRACE-B
Since January 2016	Excess power release by heaters	GRACE-A, GRACE-B
October 2016-May 2017	Permanent shut-down of the ACC	GRACE-B only
Since January 2017	Partial KBR ranging data collection	GRACE-A, GRACE-B

available (Herman et al., 2012). In addition, yaw turns (cf. Section 4.3.2) are performed on a regular basis in order to guarantee an optimal level of battery over-charge, since too much or too little overcharge is a major threat to the batteries lifetime (Herman et al., 2012).

Increased occurrences of battery cell failures on GRACE-B, made additional operational limitations necessary. Since January 2016, the heaters on-board GRACE-B are additionally activated to release excess power if necessary, i.e. avoiding a battery overcharge. Between October 2016 and May 2017, the GRACE-B accelerometer was permanently powered-off. Since all other science measurements are periodically available, GRACE-B accelerometer data is synthesized (Bandikova et al., 2017) to allow gravity field recovery during this period (cf. Section 5.2.3). From early 2017 onward, the KBR ranging data collection is limited to full sun orbit periods (partial KBR operation) in order to reduce the load on the batteries (Save, 2016).

2.7 GRACE-FO

The GRACE-FO (**G**ravity **R**ecovery **A**nd **C**limate **E**xperiment **F**ollow-**O**n) mission is the successor to the GRACE mission, and carries on the work of its predecessor (Flechtner et al., 2017; Flechtner et al., 2016). GRACE-FO is, as GRACE, implemented under US-German partnership. The GRACE-FO satellites will be launched on a Space-X Falcon-9 (rideshare with 5 Iridium-Next satellites) from the Vandenberg Air Force Base in California within the launch period in spring 2018.

The primary objective of the GRACE-FO mission is to continue and extend the GRACE time series of high-resolution global monthly Earth gravity field models with a minimal data gap between both missions. For this, evolved versions of the GRACE microwave ranging instrument, GPS receiver, and accelerometer will be used. Additionally, lessons learnt from GRACE are taken into account for the mission design, i.e. the GRACE-FO attitude control is based on three star camera heads instead of two in the case of GRACE. The use of three star camera heads allows for a more robust attitude determination, especially in phases of Sun or Moon blindings. A secondary objective is to demonstrate the effectiveness of a Laser Ranging Interferometer (LRI) in improving the inter-satellite ranging performance. The LRI serves as a technical demonstration to asses if precision laser interferometry can help to improve the spatial and temporal resolution of the derived gravity field models, which is of particular importance for future next-generation gravity missions (NGGM). Additionally, the GRACE radio occultation measurements should be continued (Flechtner et al., 2016; Sheard et al., 2012).

In contrast to GRACE, the GRACE-FO Level-1A data products (cf. Section 2.4) will be publicly available to all processing centers, in addition to the pre-processed Level-1B data products.

For more details on the GRACE-FO mission, and its instrumentation, the reader is referred to e.g., Flechtner et al. (2017), Flechtner et al. (2016), Sheard et al. (2012), and Christophe et al. (2015).

3 Basic concepts

3.1 Equation of motion

According to Newton's second law of motion (1686)

> *"The rate of change of momentum of a body is directly proportional to the force applied and is in the direction of the applied force."*,

the (perturbed) motion of a satellite in an inertial system under the influence of a force can be described by the equation of motion

$$\ddot{\mathbf{r}} = \frac{\mathbf{F}}{m} = \mathbf{f}(t, \mathbf{r}, \dot{\mathbf{r}}). \tag{3.1}$$

Herein, $\mathbf{f}$ denotes the mass-specific force function depending on the time t, the position of the satellite $\mathbf{r}$, and its velocity $\dot{\mathbf{r}}$, respectively. Subsequently, italics are used for scalar variables, bold lowercase letters for vectors, and bold uppercase letters for matrices.

The overall acceleration of the satellite $\ddot{\mathbf{r}}$ is the sum of the acceleration due to gravitational forces $\ddot{\mathbf{r}}_{\mathrm{G}}$, and the acceleration due to non-gravitational forces $\ddot{\mathbf{r}}_{\mathrm{NG}}$:

$$\ddot{\mathbf{r}} = \ddot{\mathbf{r}}_{\mathrm{G}} + \ddot{\mathbf{r}}_{\mathrm{NG}}. \tag{3.2}$$

The primary gravitational force is caused by the Earth's gravity field (cf. Section 3.2). To a minor extent, third bodies, tidal effects, relativistic effects, and other non-gravitational perturbing forces (cf. Fig. 3.1) also affect the satellite.

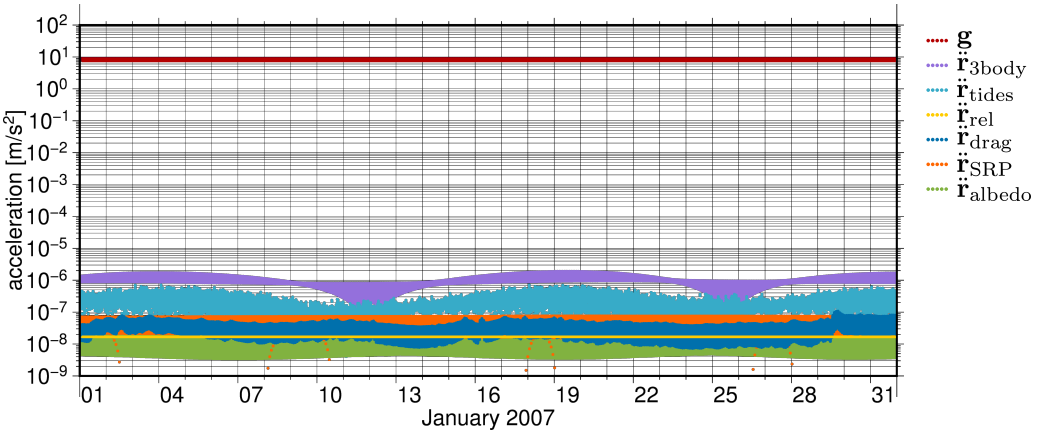

Fig. 3.1.: Modeled gravitational and non-gravitational accelerations of GRACE-A for one month (January 2007). It should be noted that the magnitude of the non-gravitational accelerations due to atmospheric drag ($\ddot{\mathbf{r}}_{\mathrm{drag}}$) strongly depends on the orbit altitude ($\sim$ 475 km in January 2007).

Thus, the total acceleration experienced by the satellite $\ddot{\mathbf{r}}$ is the sum of the following constituents:

$$\ddot{\mathbf{r}} = \mathbf{g} + \ddot{\mathbf{r}}_{\text{3body}} + \ddot{\mathbf{r}}_{\text{tides}} + \ddot{\mathbf{r}}_{\text{rel}} + \ddot{\mathbf{r}}_{\text{drag}} + \ddot{\mathbf{r}}_{\text{SRP}} + \ddot{\mathbf{r}}_{\text{albedo}}, \tag{3.3}$$

with

$\mathbf{g}$	Earth's gravity field	$\ddot{\mathbf{r}}_{\text{G}}$
$\ddot{\mathbf{r}}_{\text{3body}}$	3^{rd} body tides (Sun, Moon, other planets)	
$\ddot{\mathbf{r}}_{\text{tides}}$	solid Earth tides, Earth pole tides, ocean tides, ocean pole tides, atmospheric tides	
$\ddot{\mathbf{r}}_{\text{rel}}$	general relativistic perturbations	
$\ddot{\mathbf{r}}_{\text{drag}}$	atmospheric drag	$\ddot{\mathbf{r}}_{\text{NG}}$
$\ddot{\mathbf{r}}_{\text{SRP}}$	solar radiation pressure (SRP)	
$\ddot{\mathbf{r}}_{\text{albedo}}$	Earth radiation pressure (albedo)	

In the following, only the representation of the Earth's gravity field (cf. Section 3.2), and the non-gravitational accelerations acting upon LEOs (cf. Section 3.3) are discussed in more detail. A detailed description of the other gravitational forces (e.g., solid Earth tides, Earth pole tide, ocean tide, ocean pole tide, etc.) can be found e.g., in the International Earth Rotation and Reference System Service (IERS) conventions (Petit and Luzum, 2010).

3.2 Earth's gravity field

According to Newton's universal law of gravitation (1687), the gravitational force between two bodies with masses m and M at a distance l from each other is given by

$$\mathbf{F} = G\frac{mM}{l^2}\frac{\mathbf{l}}{l}, \tag{3.4}$$

with G being the gravitational constant ($G = 6.67408 \times 10^{-11}$ m^{3}kg^{-1}s^{-2}, Mohr et al. (2016)). Combining Equation (3.4) with Newton's second law of motion (cf. Eq. (3.1)), the gravitational acceleration of the body with mass m with respect to the CoM of the two bodies is obtained by

$$\ddot{\mathbf{r}} = \frac{GM}{l^2}\frac{\mathbf{l}}{l}. \tag{3.5}$$

For m being negligibly small compared to M, Equation (3.5) is consistent with a coordinate system whose origin is at the CoM of M. Then, the gravitational acceleration $\ddot{\mathbf{r}}$ describes the force exerted on an object (e.g., artificial satellite) with unity mass by a central body of mass M (e.g., Earth) at a distance l. Instead of using the vector representation, the gravitational acceleration in Equation (3.5) can be represented as the gradient of a scalar function ($\ddot{\mathbf{r}} = \nabla V$), yielding the gravitational potential

$$V = \frac{GM}{l}. \tag{3.6}$$

As the Earth's gravity field is determined by an inhomogeneous mass and density distribution inside the system Earth, the gravitational potential cannot be computed by integrating Equation (3.6) over the Earth surface. However, the gravitational potential of the Earth V,

representing a harmonic function outside the Earth's surface and thus satisfying Laplace's equation, can be expressed as a series of spherical harmonics (Kaula, 1966; Heiskanen and Moritz, 1967):

$$V(r,\theta,\lambda) = \frac{GM}{R}\sum_{n=0}^{\infty}\sum_{m=0}^{n}\left(\frac{R}{r}\right)^{n+1}(c_{nm}C_{nm}(\theta,\lambda) + s_{nm}S_{nm}(\theta,\lambda)). \tag{3.7}$$

Therein, the spherical (geocentric) coordinates r, θ, λ denote the radius, co-latitude and longitude w.r.t. the Earth fixed reference system, respectively. The constants R and GM are the Earth's reference radius, and the gravitational parameter of the Earth ($GM = 3.9860044150 \times 10^{14}$ m^{3}s^{-2}), defined as the product of the gravitational constant G and the mass of the Earth M. c_{nm} and s_{nm} are the normalized spherical harmonic coefficients of degree n and order m, describing the global structure and irregularities of the Earth's gravity field in the spectral domain. C_{nm} and S_{nm} are the normalized base functions - or surface spherical harmonics - defined as

$$C_{nm}(\theta,\lambda) = \cos(m\lambda)\bar{P}_{nm}(\cos\theta), \tag{3.8}$$

$$S_{nm}(\theta,\lambda) = \sin(m\lambda)\bar{P}_{nm}(\cos\theta), \tag{3.9}$$

with the 4π-normalized associated Legendre functions of the first kind $\bar{P}_{nm}$.

Based on the formulation as a series of spherical harmonics in Equation (3.7), numerical values for the spherical harmonic coefficients c_{nm} and s_{nm} can be determined. In practice, the series in Equation (3.7) is truncated at a maximum degree n_{max}, defining the spatial resolution of the gravity field. The process of coefficient determination, denoted as "gravity field recovery", from GRACE observations is described in Section 3.4.

The acceleration due to the gravity field of the Earth $\mathbf{g}$ is defined by the gradient of the gravitational potential V

$$\mathbf{g}(r,\theta,\lambda) = \nabla V(r,\theta,\lambda). \tag{3.10}$$

3.2.1 Degree amplitudes

In order to analyze and compare different models of the Earth's gravity field in the spectral domain, degree variances or amplitudes are commonly used to evaluate the accuracy of the gravity field models.

The signal degree amplitudes are defined as the square root of the signal degree variances

$$\sigma_n = \sqrt{\sigma_n^2} = \sqrt{\sum_{m=0}^{n}(c_{nm}^2 + s_{nm}^2)}. \tag{3.11}$$

Based on Equation (3.11), the difference degree amplitudes are given by

$$\Delta\sigma_n = \sqrt{\sum_{m=0}^{n}(\Delta c_{nm}^2 + \Delta s_{nm}^2)}, \tag{3.12}$$

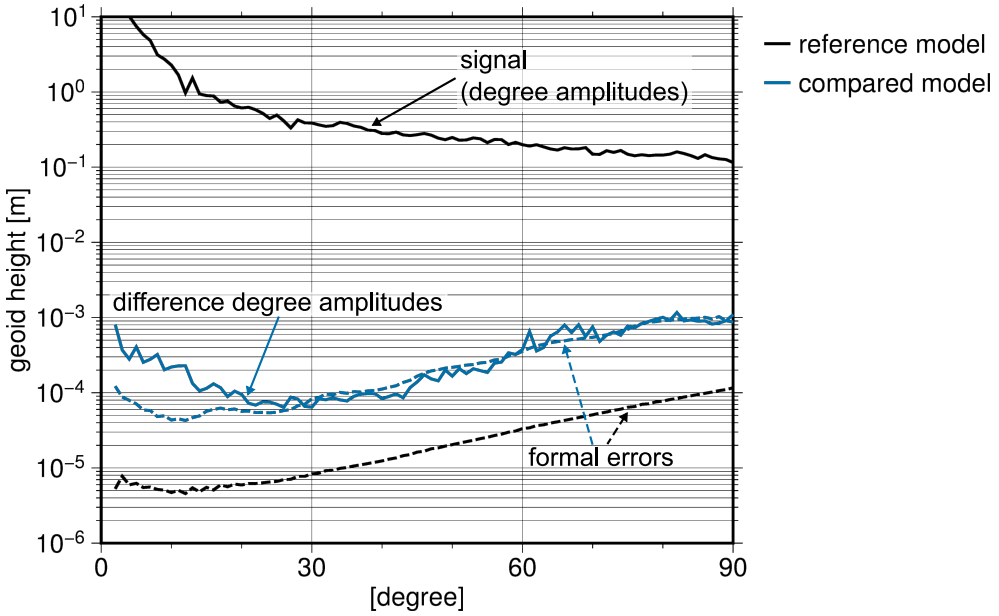

Fig. 3.2.: Concept of degree amplitudes: Comparison of an arbitrary gravity field model (blue) with a reference model (black) by means of signal (degree amplitudes), difference degree amplitudes, and error degree amplitudes.

where $\Delta c_{nm} = c_{nm} - c'_{nm}$ and $\Delta s_{nm} = s_{nm} - s'_{nm}$ denote coefficient differences w.r.t. another model (c'_{nm}, s'_{nm}). Hence, the difference degree amplitudes can be used as a measure of consistency between two gravity field solutions (cf. Fig. 3.2).

The error degree amplitudes or formal errors, follow Equation (3.11), with the spherical harmonic coefficients being replaced by their error estimates ($\hat{\sigma}(c_{nm})$, $\hat{\sigma}(s_{nm})$)

$$\hat{\sigma}_n^2 = \sqrt{\sum_{m=0}^{n} (\hat{\sigma}^2(c_{nm}) + \hat{\sigma}^2(s_{nm}))}. \tag{3.13}$$

Figure 3.2 illustrates the concept of degree amplitudes by comparing an arbitrary gravity field model with a reference model by means of degree amplitudes.

3.2.2 Equivalent water height

The Earth's gravity field underlies time-dependent changes due to mass re-distributions within the system compartments. Since most of the gravity changes are caused by changes in water storage, these mass variations can be interpreted as a thin layer of water thickness changes near the Earth's surface (Wahr et al., 1998). Thus, another method to analyze gravity field models in the spatial domain, is to represent differences or temporal changes in the spherical harmonic coefficients Δc_{nm} and Δs_{nm} in terms of changes of the equivalent water height (EWH). It is common to use a static gravity field model (e.g., GOCO05s) as reference, to represent the changes in the spherical harmonic coefficients of temporal mean gravity field models (e.g., ITSG-Grace2016).

The height changes of equivalent water columns can be related to temporal changes in the Earth's gravity field as (Wahr et al., 1998)

$$\Delta EWH(\theta,\lambda) = \frac{M}{4\pi R^2 \rho_w} \sum_{n=1}^{\infty} \sum_{m=0}^{n} \frac{1+k'_n}{2n+1} (\Delta c_{nm} C_{nm}(\theta,\lambda) + \Delta s_{nm} S_{nm}(\theta,\lambda)), \tag{3.14}$$

where ρ_w denotes the average density of water (~ 1025 kg/m^3). k'_n are the degree-dependent load Love numbers, representing the contribution of the indirect loading effect due to mass re-distributions.

3.2.3 Gaussian filter

GRACE derived monthly gravity field models, represented in terms of spherical harmonic coefficients, contain different types of errors. A part of these errors is caused by correlated and high-frequency noise due to anisotropic spatial sampling of the mission, instrumental noise (KBR, GPS, ACC, SCA), and temporal aliasing caused by the incomplete reduction of short-term mass variations by models (e.g., Dobslaw et al., 2017). In the spatial domain, these errors in the spherical harmonic coefficients manifest themselves as typical north-south "striping patterns". In order to reduce the noise (or striping), smoothing filters need to be applied to GRACE derived monthly gravity field solutions. In the spectral domain, this can be done by applying a filter matrix $\mathbf{W}$ to the spherical harmonic coefficients to derive smoothed coefficients:

$$\mathbf{x}^s = \mathbf{W}\mathbf{x} = \mathbf{W} \begin{bmatrix} c_{nm} \\ s_{nm} \end{bmatrix}. \tag{3.15}$$

Alternatively, the GRACE solutions can be filtered by convolving a filter kernel in the spatial domain. In general, two types of filters are distinguished: (1) isotropic and (2) anisotropic filters. Isotropic filters are degree-dependent in the spectral domain, i.e. $\mathbf{W}$ in Equation (3.15) becomes a diagonal matrix, and independent of direction in the spatial domain. The most common isotropic filter applied to GRACE monthly gravity field solutions is the Gaussian smoothing filter (Jekeli, 1981) (cf. Section 8). It acts as a spatial low-pass filter on the spherical harmonic coefficients with the resulting solutions being essentially spatially averaged over the filter-defined smoothing radius (cf. Fig. 3.3). In contrast, anisotropic filters (e.g., DDK filter (Kusche et al., 2009)) are degree and order dependent in the spectral domain and location dependent in the spatial domain. For more details on filters, the reader is referred to e.g., Wahr et al. (1998), Jekeli (1981), Kusche (2007), and Kusche et al. (2009).

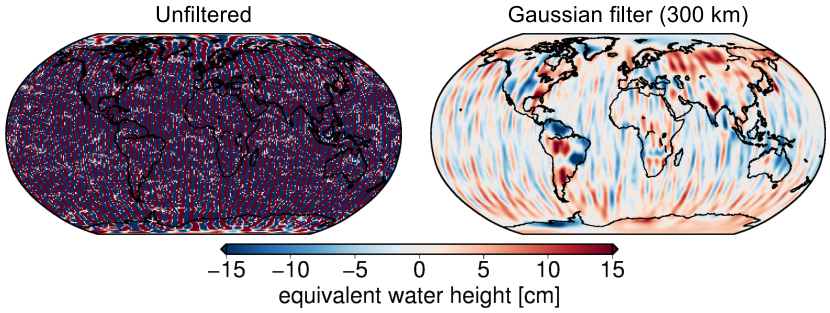

Fig. 3.3.: Unfiltered (left) and Gaussian filtered (right) EWHs for April 2014 (ITSG-Grace2016). The EWHs are given in cm, with the static GOCO05s, trend, annual and semiannual signals removed.

3.3 Non-gravitational accelerations

The non-gravitational accelerations acting upon low altitude satellites, such as GRACE, are caused by atmospheric drag, solar radiation pressure and Earth radiation pressure:

$$\ddot{\mathbf{r}}_{\mathrm{NG}} = \ddot{\mathbf{r}}_{\mathrm{drag}} + \ddot{\mathbf{r}}_{\mathrm{SRP}} + \ddot{\mathbf{r}}_{\mathrm{albedo}}. \tag{3.16}$$

These non-gravitational accelerations are significantly smaller than the major gravitational accelerations caused by the Earth's gravity field (cf. Fig. 3.1). For LEOs, the non-conservative accelerations are dominated by atmospheric drag and solar radiation pressure; the magnitudes of the individual compartments are mainly depending on the satellite's current position with respect to the Earth and Sun, its attitude, velocity, shape, mass, cross-surface area and surface properties. In along-track direction, the main contribution to the non-conservative acceleration is caused by atmospheric drag (cf. Section 3.3.1), pointing always in opposite direction of the satellites motion causing a permanent de-acceleration of the satellite. Whereas, in cross-track and radial direction, the accelerations are composed of different components, with the magnitudes strongly depending on the orbital configuration (cf. Section 7.1.4, cf. Fig. 7.5).

GRACE Macro Model: The GRACE Macro Model, a 9-plate model, represents the satellites complex geometry by flat surface elements, and is given in the GRACE Product Specification Document (Bettadpur, 2010). It contains the surface properties and geometry of the GRACE satellites; which are identical for both spacecraft. For more details on the GRACE Macro Model, see Appendix B.

The individual forces (atmospheric drag, SRP, albedo), and the basic equations used for the modeling of the non-gravitational accelerations are described in the following. To model the non-gravitational accelerations realistically, the geometry and surface properties of the two GRACE satellites have to be taken into account. Therefore, the described formulae for acceleration modeling refer to the individual surface elements of the GRACE Macro Model. To obtain the total non-gravitational acceleration acting upon the satellite, the individual contributions of atmospheric drag, SRP, and albedo for each of the 9 surface elements have to be added (cf. Section 3.3.4).

3.3.1 Atmospheric drag

Atmospheric drag is the force acting on the satellite's surface caused by its interaction with the surrounding atmosphere; it represents the predominant non-gravitational perturbation acting on LEOs. The atmospheric drag is always directed opposite to the velocity of the satellite motion, hence de-accelerating the satellite. Lift and binormal forces, acting perpendicular to the satellite's relative velocity causing minor perturbations, can be neglected (Montenbruck and Gill, 2001).

The acceleration due to atmospheric drag is obtained by

$$\ddot{\mathbf{r}}_{\mathrm{drag},i} = -\frac{1}{2} c_D \frac{A_i}{m} \rho(\mathbf{r}) \dot{\mathbf{r}} |\dot{\mathbf{r}}|, \tag{3.17}$$

with its magnitude depending on the drag coefficient c_D, the atmospheric density ρ at the satellite's position $\mathbf{r}$, the relative velocity of the satellite with respect to the atmosphere $\dot{\mathbf{r}}$, the cross-sectional area A of the surface element i, and the satellite mass m. The drag coefficient c_D is a dimensionless quantity, describing the interaction of the satellite's surface material with the atmosphere; for GRACE a constant value of 2.4 is approximated. For the relative velocity of the satellite it is assumed that the atmosphere co-rotates with the Earth (Montenbruck and Gill, 2001), and both vertical and horizontal winds are neglected. The cross-sectional area A_i is provided by the GRACE Macro Model (cf. Appendix B). For a more realistic drag modeling, the satellite-specific mass m is not assumed to be constant, but derived from the MAS1B data product (cf. Section 2.5.2). The MAS1B data product contains the total satellite mass in kilograms, based on thruster firings and/or gas tank readings.

There exist several atmospheric models, such as the Drag Temperature Model 2013 (DTM2013; Bruinsma, 2014), the Jacchia-Bowman 2008 (JB2008; Bowman et al., 2008), and the NRLMSISE-00 (Picone et al., 2002), which deliver two fundamental quantities: (1) the atmospheric density, and (2) the ambient air temperature. Here, the DTM2013 and JB2008 models are used to obtain atmospheric density values ρ (cf. Section 3.3.5). For GRACE, the atmospheric drag modeling seems to be a limiting factor in accelerometer modeling, especially for later time periods with a constantly decreasing satellite altitude. Therefore, this topic is discussed further in Section 7.1.4.

In general, accurate modeling of the atmospheric drag is difficult for several reasons: (1) the density of the upper atmosphere and its variations are not very accurately known, (2) drag modeling requires a detailed knowledge of the interaction of the satellite's different surfaces with the surrounding atmosphere, and (3) the varying attitude and altitude of the satellite have to be taken into account (Montenbruck and Gill, 2001). Hence, especially the numerical values used for the density ρ, and the drag coefficient c_D in Equation (3.17) are a major source of uncertainty in modeling the accelerations due to atmospheric drag.

3.3.2 Solar radiation pressure

Solar radiation pressure is the force acting on the satellite's surface caused by its interaction with the incident sunlight, i.e. the absorption and/or reflection of photons (cf. Fig. 3.5). Aside from the gravitational forces and the atmospheric drag, the solar radiation pressure has a significant influence on LEOs.

In a first step, the size of the incoming solar radiation pressure acting on a sunlit surface is modeled according to

$$P_{\odot} = \nu \cdot \frac{1AU^2}{r_{\odot}^2} \frac{\Phi}{c}. \tag{3.18}$$

The solar radiation pressure $P_{\odot}$ is determined by the incident solar flux Φ divided by the velocity of light c. In a distance of 1 Astronomical Unit (1 AU = 149 597 870 700 m) from the Sun - in the vicinity of the Earth - the solar flux has a value of $\Phi \sim 1367$ W/m^2 (McCarthy, 1996). For realistic SRP modeling, the varying distance of the satellite from the Sun $r_{\odot}$ is taken into account by applying the inverse square law, i.e. the solar radiation pressure increases with a decreasing Sun-satellite distance. The shadow function ν determines the eclipse conditions, whether the satellite is in Earth's umbra ($\nu = 0$), penumbra ($0 < \nu < 1$), or in full sunlight ($\nu = 1$). Therefore, it directly influences the magnitude of the solar

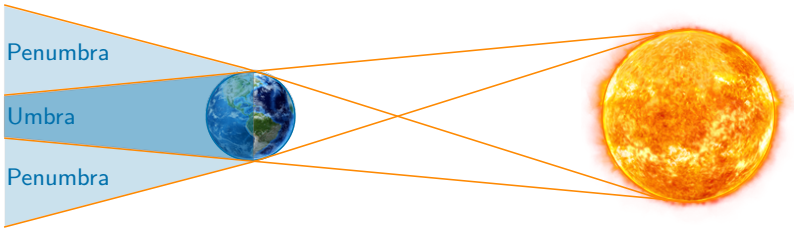

Fig. 3.4.: Conical shadow model according to Montenbruck and Gill (2001)

radiation pressure. For the shadow function a simple conical shadow model (Montenbruck and Gill (2001); cf. Fig. 3.4) is used, which computes the eclipse conditions for both the Earth and the Moon.

In a second step, the actual acceleration on the individual surface element i due to solar radiation pressure is obtained by

$$\ddot{\mathbf{r}}_{\mathrm{SRP},i} = P_{\odot}\frac{A_i}{m}\cos(\theta_i)\,[(\varepsilon_{\mathrm{abs},i})\mathbf{e}_{\odot} - (2\varepsilon_{\mathrm{refl},i}\cos(\theta_i))\mathbf{n}_i - (\frac{2}{3}\varepsilon_{\mathrm{diff},i})\mathbf{n}_i], \tag{3.19}$$

with

$$\cos(\theta_i) = -\mathbf{n}_i^T \cdot \mathbf{e}_{\odot}. \tag{3.20}$$

In Equation (3.19), A_i denotes the cross-section area of surface element i, m denotes the satellite mass, $\mathbf{e}_{\odot}$ denotes the unit vector pointing from the satellite to the Sun, and $\mathbf{n}_i$ denotes the unit normal vector of the surface element i. The cosine of the angle between the surface normal vector $\mathbf{n}_i$ and the direction to the Sun $\mathbf{e}_{\odot}$ is represented by $\cos(\theta_i)$. If $\cos(\theta_i)$ is negative, the surface element i is not illuminated by the Sun, and thus the acceleration due to solar radiation pressure becomes zero. Otherwise, one part of the incoming solar radiation is absorbed, and the other part is reflected. Basically, three types of radiation pressure forces occur simultaneously: (1) absorption, (2) specular reflection, and (3) diffuse reflection (cf. Fig. 3.5). The corresponding absorptivity and reflectivty coefficients ε of the individual surface elements i satisfy the following condition

$$\varepsilon_{\mathrm{abs},i} + \varepsilon_{\mathrm{refl},i} + \varepsilon_{\mathrm{diff},i} = 1. \tag{3.21}$$

For GRACE SRP modeling, the cross-section area A_i, the unit normal vector $\mathbf{n}_i$ and the reflectivity coefficients $\varepsilon_{\mathrm{abs},i}, \varepsilon_{\mathrm{refl},i}, \varepsilon_{\mathrm{diff},i}$ are derived from the GRACE Macro Model (cf. Appendix B). The satellite mass is derived from the MAS1B data product (cf. Section 2.5.2).

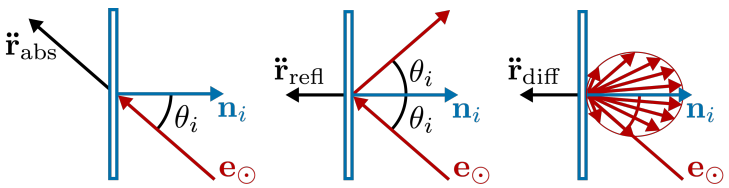

(a) absorption (b) specular reflection (c) diffuse reflection

Fig. 3.5.: Three basic types of radiation pressure forces: (a) absorption, (b) specular reflection, and (c) diffuse reflection. Interaction between incoming radiation (red) and satellite surface element (blue), and the resulting radiation pressure force vectors (black).

3.3.3 Earth radiation pressure - Albedo

The Earth radiation pressure (albedo) is the force acting on the satellite's surface caused by its interaction with the radiation re-emitted by the Earth. Compared to the direct solar radiation pressure, the albedo only causes a small perturbation on the satellite ($\sim 10 - 35\%$ of the acceleration due to solar radiation pressure (Knocke et al., 1988); cf. Fig. 3.1), which acts strongest in radial direction. In connection with Earth's albedo, two components are distinguished: (1) the shortwave visible radiation, and (2) the longwave infrared (IR) radiation. The shortwave radiation results from the portion of incoming shortwave solar radiation, which is reflected back to space by the Earth's surface or clouds. Therefore, the shortwave albedo is only emitted by the daylight side of the Earth and may vary significantly depending on surface characteristics and cloud coverage. Whereas, the longwave part of the re-emitted radiation results from the portion of direct solar radiation, that has been absorbed by the Earth's surface and is re-emitted to space as IR radiation. Hence, the longwave albedo always acts on the spacecraft. The total acceleration due to albedo, acting on one satellite surface element i, is given by the sum of all shortwave ($\ddot{\mathbf{r}}_{\text{albedo(VIS)},i}$) and longwave ($\ddot{\mathbf{r}}_{\text{albedo(IR)},i}$) accelerations:

$$\ddot{\mathbf{r}}_{\text{albedo},i} = \ddot{\mathbf{r}}_{\text{albedo(VIS)},i} + \ddot{\mathbf{r}}_{\text{albedo(IR)},i}. \tag{3.22}$$

Subsequently, the modeling of the perturbing accelerations caused by shortwave and longwave albedo are described in more detail.

Shortwave albedo (visible)

The incoming shortwave albedo acting on a satellite surface i is determined according to

$$P^{\text{Vis}}_{\otimes,k} = \frac{1}{\pi r^2_{\text{sat},k}} \cos(\alpha_k)\delta_k P_{\odot,k} \cos(\phi_k)\Delta\Omega_k, \tag{3.23}$$

with

$$\cos(\phi_k) = \mathbf{n}_k \cdot \mathbf{e}^{\odot}_{\otimes,k}, \tag{3.24}$$

$$\cos(\alpha_k) = \mathbf{n}_k \cdot \mathbf{e}_{\otimes,k}. \tag{3.25}$$

In Equation (3.23), the amount of shortwave Earth radiation pressure $P^{\text{Vis}}_{\otimes,k}$ received by the satellite depends, firstly, on the incoming solar radiation pressure $P_{\odot,k}$ arriving at the Earth's surface element k, the surface element area $\Delta\Omega_k$, and the angle of the incident solar radiation $\cos(\phi_k)$ (i.e., the angle between the surface element normal vector and the direction to the Sun). Assuming a Lambertian reflection - a perfectly diffuse reflection with the reflection being independent of the incident angle of the incoming radiation (cf. Fig. 3.6) - the incoming radiation pressure $P^{\text{Vis}}_{\otimes,k}$ depends, secondly, on the mean reflectivity δ_k of the surface element k, the angle of the reflected radiation $\cos(\alpha_k)$ (i.e., the angle between the surface element normal vector and the Earth-satellite direction), and the distance to the satellite $r_{\text{sat},k}$; with the pressure decreasing proportional to the square of the distance from the reflecting source. To determine the shortwave albedo, a surface model of the Earth, which describes the reflectivity properties of the Earth's surface, is needed. For this purpose, the CERES (Clouds and Earth's Radiant Energy System) model (Wielicki and Barkstrom,

1996) is used. The CERES model is a mean global surface albedo model providing mean reflectivity values δ_k for each surface element k on a global grid (cf. Section 3.3.5).

The resulting acceleration due to shortwave albedo (from one surface element k on one satellite surface element i) is derived in the same way as for the solar radiation pressure (cf. Eq. (3.19)), yielding

$$\ddot{\mathbf{r}}_{\text{albedo(VIS)},i,k} = P^{\text{Vis}}_{\otimes,k} \frac{A_i}{m} \cos(\theta_i) \left[(\varepsilon_{\text{abs},i})\mathbf{e}_{\otimes,k} - (2\varepsilon_{\text{refl},i}\cos(\theta_i))\mathbf{n}_i - (\frac{2}{3}\varepsilon_{\text{diff},i})\mathbf{n}_i\right], \tag{3.26}$$

with

$$\cos(\theta_i) = -\mathbf{n}_i^T \cdot \mathbf{e}_{\otimes,k}. \tag{3.27}$$

By summing up all Earth's surface elements k, which are visible to the satellite, the acceleration for one surface element of the satellite i is obtained by

$$\ddot{\mathbf{r}}_{\text{albedo(VIS)},i} = \sum_k \ddot{\mathbf{r}}_{\text{albedo(VIS)},i,k}. \tag{3.28}$$

Longwave albedo (IR)

The acceleration due to the second constituent of the Earth albedo, the longwave albedo, is basically derived in the same way as for the shortwave albedo (cf. Eqs. (3.23), (3.25), (3.26), and (3.27)). The incoming longwave albedo acting on a satellite surface i is determined according to

$$P^{\text{IR}}_{\otimes,k} = \frac{1}{4\pi r^2_{\text{sat},k}} \cos(\alpha_k)\varepsilon_k \Delta\Omega_k. \tag{3.29}$$

Compared to Equation (3.23), the IR radiation pressure $P^{\text{IR}}_{\otimes,k}$ received by the satellite is independent of the incoming solar radiation (at the Earth's surface), and only depends on the mean emissivity ε_k of the surface element k, the angle between the surface element k and the satellite $\cos(\alpha_k)$ (cf. Eq. (3.25), cf. Fig. 3.6), and the distance to the satellite $r_{\text{sat},k}$. As the IR radiation is a near isotropic re-emission of the direct solar radiation absorbed by the Earth, the factor $\frac{1}{\pi r^2_{\text{sat},k}}$ in Equation (3.23), representing the irradiated Earth cross-section, is replaced by $\frac{1}{4\pi r^2_{\text{sat},k}}$, representing the total radiating Earth surface. To determine the longwave albedo, the mean emissivity values ε_k for each Earth surface element k are again derived from the CERES model (Wielicki and Barkstrom (1996); cf. Section 3.3.5), representing a mean global surface albedo model.

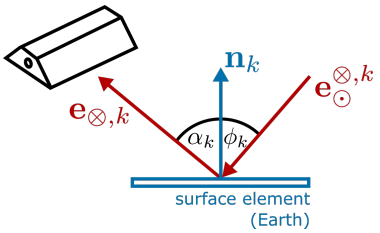

Fig. 3.6.: Albedo surface model: incident ($\mathbf{e}^{\otimes,k}_{\odot}$) and reflected ($\mathbf{e}_{\otimes,k}$) radiation

The acceleration due to longwave albedo (from one surface element k on one satellite surface element i) is given by (cf. Eq. (3.26))

$$\ddot{\mathbf{r}}_{\text{albedo(IR)},i,k} = P^{\text{IR}}_{\otimes,k}\frac{A_i}{m}\cos(\theta_i)\,[(\varepsilon_{\text{abs},i})\mathbf{e}_{\otimes,k} - (2\varepsilon_{\text{refl},i}\cos(\theta_i))\mathbf{n}_i - (\frac{2}{3}\varepsilon_{\text{diff},i})\mathbf{n}_i]. \tag{3.30}$$

The sum over all Earth's surface elements k gives the total acceleration for one surface element i of the satellite

$$\ddot{\mathbf{r}}_{\text{albedo(IR)},i} = \sum_k \ddot{\mathbf{r}}_{\text{albedo(IR)},i,k}. \tag{3.31}$$

3.3.4 Total non-gravitational accelerations

The total non-gravitational acceleration acting on the satellite due to atmospheric drag, solar radiation pressure and albedo is given by the sum over all compartments and surface elements i:

$$\ddot{\mathbf{r}}_{\text{NG}} = \sum_i \ddot{\mathbf{r}}_{\text{drag},i} + \sum_i \ddot{\mathbf{r}}_{\text{SRP},i} + \sum_i \ddot{\mathbf{r}}_{\text{albedo},i}. \tag{3.32}$$

For more details on the formulae used for the non-gravitational acceleration modeling, the reader is referred to Montenbruck and Gill (2001) and Frommknecht (2008).

3.3.5 Atmospheric density & Albedo models

Table 3.1 summarizes the individual models and constants used for the modeling of the non-gravitational surface forces acting on the GRACE satellites (cf. Sections 3.3.1, 3.3.2, and 3.3.3). The surface elements of the satellites, including geometry and surface properties, are modeled according to the GRACE Macro Model (Bettadpur, 2010, cf. Appendix B).

Tab. 3.1.: Models and constants used for the modeling of the non-gravitational forces.

	Model	**Constants**
Atmospheric drag	DTM2013 [a]	drag coefficient ($c_D = 2.4$)
	JB2008 [b]	drag coefficient ($c_D = 2.4$)
Solar radiation pressure	- [c]	solar flux at 1 AU ($\Phi \approx 1367$ W/m^2)
Earth albedo	CERES [d]	-

[a] Drag Temperature Model 2013 (Bruinsma, 2014)

[b] Jacchia-Bowman 2008 (Bowman et al., 2008)

[c] Shadow function modeled according to Montenbruck and Gill (2001)

[d] Clouds and the Earth's Radiant Energy System (Wielicki and Barkstrom (1996); Rodríguez-Solano et al. (2009))

DTM2013 and JB2008 Model: Both models, DTM2013 and JB2008, are used to obtain the atmospheric densities along the GRACE orbits, which are needed for the modeling of the atmospheric drag (cf. Section 3.3.1). Note that the JB2008 is only used from June 20, 2015 onward, as the DTM2013 is currently not available for subsequent time periods (cf. Fig. 3.7).

Figure 3.7 illustrates the temporal evolution of the atmospheric densities from April 2002 to June 2017, derived from the DTM2013 and JB08 model.

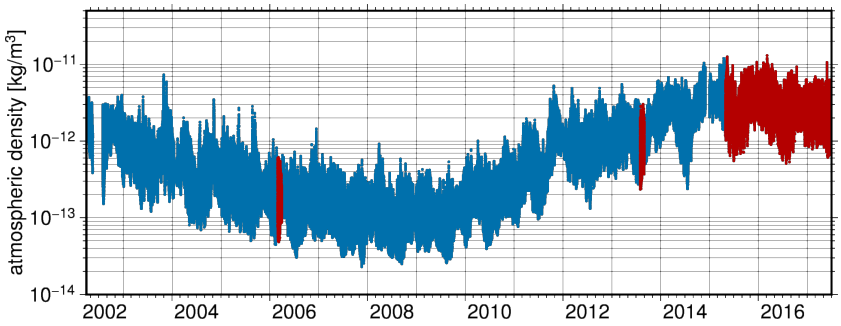

Fig. 3.7.: Temporal evolution of the atmospheric density for GRACE-A from April 2002 to June 2017 derived from DTM2013 (blue) and JB2008 (red) models. Note that the atmospheric densities are displayed on a logarithmic scale.

CERES Model: The reflectivity and emissivity coefficients needed for albedo modeling (cf. Section 3.3.3) are derived from CERES data (Wielicki and Barkstrom, 1996). Based on the monthly means of the CERES data, a model containing mean reflectivity and emmisivity values for each month of the year (on a $2.5° \times 2.5°$ grid) is derived (Rodríguez-Solano et al. (2009), cf. Fig. 3.8). This simplification is justified as the impact on the modeled non-gravitational accelerations is very small (not shown here).

Figure 3.8 exemplarily shows the mean reflectivity values and the mean emissivity values of the Earth's surface for the month of July, derived from CERES data.

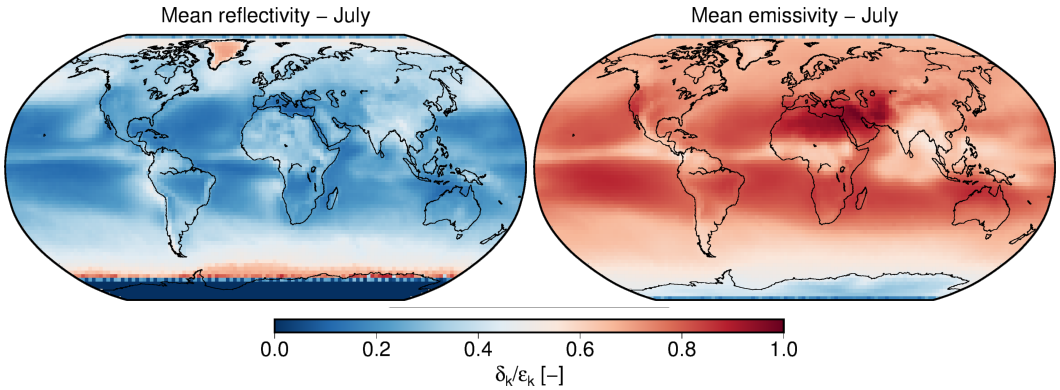

Fig. 3.8.: CERES model: Mean reflectivity (left) and emmissivity (right) for the month of July derived from 10 years (2000-2009) of CERES data (Rodríguez-Solano et al., 2009; Wielicki and Barkstrom, 1996)

3.4 Gravity field determination

There exist several methods and concepts to derive the Earth's gravity field and its temporal variations from satellite observations (Johannessen et al., 2003). Within this thesis, the main focus is put on the gravity field recovery from GRACE data, i.e. the exploitation of the concept of ll-SST and hl-SST for the estimation of temporal gravity field models.

The GRACE mission (cf. Section 2) enables the determination of the Earth's static and temporal gravity field with unprecedented accuracy. Therefore, it allows to monitor mass variations within the system Earth. The primary observable of GRACE is the (biased) range (ρ) between the two satellites, which is continuously measured by the on-board KBR system tracking the relative motion of the two satellites. The corresponding range rate ($\dot{\rho}$) and range acceleration ($\ddot{\rho}$) are numerically derived by differentiation (Thomas, 1999; Kim, 2000). For a successful recovery of the Earth's gravity field, one of the primary observation quantities (range, range rates, range accelerations) needs to be be connected to the gravitational potential V (cf. Section 3.2) or any other functional of the gravitational potential. Generally, various approaches exist to derive global mean and time-variable gravity field models (i.e., spherical harmonic coefficients) from GRACE. The most common and successful approaches are: (1) the classical variational equation approach (Reigber, 1989; Tapley et al., 2004), (2) the celestial mechanics approach (Beutler et al., 2010), (3) the integral equation approach (Schneider, 1968; Mayer-Gürr, 2006), and (4) the acceleration approach (Rummel, 1979). All four approaches are based on Newton's equation of motion (cf. Eq. (3.1)). Variants of the classical variational equation approach are used by the official processing centers (CSR, JPL, GFZ) to produce the official releases of static and monthly GRACE gravity field solutions. The most recent GRACE-derived gravity field models were published by e.g., Bettadpur (2012), Dahle et al. (2013), Meyer et al. (2016), and Mayer-Gürr et al. (2016b). All methods feature solutions with comparable quality. However, differences occur due to different error characteristics of the used primary observation quantity and the propagation of the observation errors through the processing chain.

Here, the focus is on the variational equation approach, which has been successfully utilized to derive the latest ITSG-Grace releases, including the ITSG-Grace2014 (Mayer-Gürr et al., 2014) and the ITSG-Grace2016 (Klinger et al., 2016; Mayer-Gürr et al., 2016a) release. Previous releases, such as the ITG-Grace03 (Mayer-Gürr, 2007) and ITG-Grace2010 (Mayer-Gürr et al., 2010), were based on the integral equation approach (Mayer-Gürr, 2006). Compared to other common approaches, the particular characteristics of the integral equation approach are the use of short-arcs to avoid the accumulation of modeling errors, and the consideration of correlated errors between the observations.

The basic principles of the variational equation approach are presented in the following. For a detailed description of the variational equations, the reader is referred to e.g., Montenbruck and Gill (2001) and Bettadpur and McCullough (2017).

3.4.1 Variational equations

Integration of the equation of motion (cf. Eq. (3.1)), which represents a second order differential equation, yields

$$\dot{\mathbf{r}}(t) = \dot{\mathbf{r}}_0 + \int_{t_0}^{t} \mathbf{f}(t', \mathbf{r}(t'))dt', \tag{3.33}$$

$$\mathbf{r}(t) = \mathbf{r}_0 + \dot{\mathbf{r}}_0 t + \int_{t_0}^{t} (t - t') \cdot \mathbf{f}(t', \mathbf{r}(t'))dt'. \tag{3.34}$$

Equation (3.34) represents an initial value problem. The position $\mathbf{r}(t)$ at any epoch t is only dependent on six initial parameters, i.e. the position and velocity of the satellite at the beginning of the integration. The relation to the unknown spherical harmonic coefficients (c_{nm}, s_{nm}) is given implicitly through the force function $\mathbf{f}$. The variable $t' \in [t_0, t]$ denotes the variable of integration.

The position and velocity of a satellite at a epoch t are given by the state vector

$$\mathbf{y}(t) = \begin{bmatrix} \mathbf{r}(t) \\ \dot{\mathbf{r}}(t) \end{bmatrix}. \tag{3.35}$$

The initial state $\mathbf{y}(t_0) = [\mathbf{r}_0 \ \dot{\mathbf{r}}_0]^\intercal$ is defined by the position and velocity of the first epoch t_0. Any change of these initial values results in a change of all positions and velocities at any later epoch t along the orbital arc. This relation is described by the state transition matrix, i.e. by the partial derivatives with respect to the initial state (Montenbruck and Gill, 2001):

$$\mathbf{\Phi}(t, t_0) = \left(\frac{\partial \mathbf{y}(t)}{\partial \mathbf{y}(t_0)} \right)_{6\times 6}. \tag{3.36}$$

Aside from the initial state, the orbit also depends on two types of parameters: (1) the force model parameters $\mathbf{p} = [c_{nm}, s_{nm}, \dots]^\intercal$ - determining the different forces acting on the satellite, and (2) the measurement model parameters $\mathbf{q}$ - including e.g., bias values, misalignments. These dependencies are described by the sensitivity matrices, i.e. by the partial derivatives with respect to the force model and measurement model parameters:

$$\mathbf{S}_\mathbf{p}(t) = \left(\frac{\partial \mathbf{y}(t)}{\partial \mathbf{p}} \right)_{(6\times n_p)}, \tag{3.37}$$

$$\mathbf{S}_\mathbf{q}(t) = \left(\frac{\partial \mathbf{y}(t)}{\partial \mathbf{q}} \right)_{(6\times n_q)}. \tag{3.38}$$

In simplified notation, the variational equations are given by

$$\underbrace{\begin{bmatrix} \mathbf{r}(t) \\ \dot{\mathbf{r}}(t) \end{bmatrix}}_{\mathbf{y}(t)} = \underbrace{\begin{bmatrix} \frac{\partial \mathbf{r}(t)}{\partial \mathbf{p}} \\ \frac{\partial \dot{\mathbf{r}}(t)}{\partial \mathbf{p}} \end{bmatrix}}_{\mathbf{S}_\mathbf{p}} \underbrace{\begin{bmatrix} \frac{\partial \mathbf{r}(t)}{\partial \mathbf{q}} \\ \frac{\partial \dot{\mathbf{r}}(t)}{\partial \mathbf{q}} \end{bmatrix}}_{\mathbf{S}_\mathbf{q}} \underbrace{\begin{bmatrix} \frac{\partial \mathbf{r}(t)}{\partial \mathbf{r}_0} & \frac{\partial \mathbf{r}(t)}{\partial \dot{\mathbf{r}}_0} \\ \frac{\partial \dot{\mathbf{r}}(t)}{\partial \mathbf{r}_0} & \frac{\partial \dot{\mathbf{r}}(t)}{\partial \dot{\mathbf{r}}_0} \end{bmatrix}}_{\mathbf{\Phi}} \underbrace{\begin{bmatrix} \mathbf{p} \\ \mathbf{q} \\ \mathbf{r}_0 \\ \dot{\mathbf{r}}_0 \end{bmatrix}}_{\mathbf{x}}, \tag{3.39}$$

where $\mathbf{y}(t)$ denotes the state vector, $\mathbf{A} = [S_\mathbf{p}\ \mathbf{S}_\mathbf{p}\ \mathbf{\Phi}]$ denotes the design matrix - representing the partial derivatives of the state with respect to the parameters, and $\mathbf{x} = [\mathbf{p}\ \mathbf{q}\ \mathbf{r}_0\ \dot{\mathbf{r}}_0]^\intercal$ denotes the vector of unknown parameters. However, the partial derivatives in Equation (3.39) are complicated by the fact that the specific force function $\mathbf{f}$, appearing in the equations for both position and velocity, is again dependent on the position $\mathbf{r}(t)$.

For details on numerical integration methods, the set up of the differential equations for the state transition matrix and sensitivity matrix, and methods for solving a system of variational equations, the reader is referred to Montenbruck and Gill (2001).

The observation equations for all other types of observations (e.g., KBR observations, SLR, etc.) can be derived from the variational equations and realized as simple matrix multiplication (cf. Eq. (3.39)). In the case of GRACE, the observation equations are composed of positions and KBR range rate observations. To derive the observation equation for KBR range rate observations ($\dot{\rho}$), the relative velocity vector $\dot{\mathbf{r}}_{\text{AB}}$ is projected along the LOS $\mathbf{e}_{\text{AB}}$ between the two GRACE satellites:

$$\dot{\rho}(t) = \mathbf{e}_{\text{AB}}(t) \cdot \dot{\mathbf{r}}_{\text{AB}}(t), \tag{3.40}$$

$$\mathbf{A}_{\dot{\rho}} = \frac{\partial \dot{\rho}}{\partial \mathbf{x}} = \frac{\partial \dot{\rho}}{\partial \dot{\mathbf{r}}} \frac{\partial \dot{\mathbf{r}}}{\partial \mathbf{x}}. \tag{3.41}$$

Following from Equation (3.39), a system of linearised observation equations can be established trough

$$\mathbf{l} = \mathbf{A}\mathbf{x} + \mathbf{e}, \tag{3.42}$$

where $\mathbf{l} = (\mathbf{r}, \dot{\rho})^\intercal$ represents the reduced observations, composed of satellite positions and KBR range rate observations. The unknown parameters are represented by the vector $\mathbf{x}$, denoting the spherical harmonic coefficients, initial values and other force and measurement model parameters, respectively. The design matrix $\mathbf{A}$ is composed of the partial derivatives with respect to the unknown parameters, as shown in Equation (3.39). The vector $\mathbf{e}$ denotes the error vector. The system of equations is solved by a least squares adjustment (LSA; cf. Section 3.5). For GRACE, every day of a month represents a partial system of observation equations, which are block-wise accumulated to build the whole system of observation equations. From this follows, that for each day a set of initial conditions are adjusted. In order to account for different observation accuracies separate variance factors are estimated for individual arcs, which represent a shorter sub-daily period of e.g., 3 hours, by means of a variance component estimation (VCE; cf. Section 3.6) procedure (Koch and Kusche, 2001).

3.5 Least squares adjustment

In the field of satellite geodesy, Least Squares Adjustments (LSAs) are commonly used to determine the best linear unbiased estimate (BLUE; e.g., Koch (1999), Meissl (1982), and Niemeier (2008)) of parameters from an overdetermined system of observation equations.

Within this thesis, the principles of LSA are applied to estimate: (1) improved attitude quaternions based on the sensor fusion approach (cf. Section 6), (2) calibration parameters for the GRACE accelerometer data (cf. Section 7), and (3) monthly sets of spherical harmonic coefficients from GRACE observations (cf. Section 3.4).

In a LSA, the unknown parameters are estimated from the observations based on a functional and a stochastic model. The relation between observations and unknown parameters can be expressed as system of equations in the form of

$$\mathbf{l} = \mathbf{A}\mathbf{x} + \mathbf{e} \quad \text{with} \quad \Sigma(\mathbf{l}) = \sigma_0^2 \mathbf{P}^{-1}, \tag{3.43}$$

where $\mathbf{l}$ denotes the observations (number of observations $n >$ number of unknowns u), $\mathbf{x}$ denotes the unknown parameters, and the design matrix $\mathbf{A}$ contains the partial derivatives of the functional model w.r.t. the unknown parameters ($\mathbf{A} = \partial \boldsymbol{f}(\mathbf{x})/\partial \mathbf{x}$). The stochastic model describes the observation errors, and is characterized by the variance covariance matrix of the observations $\Sigma(\mathbf{l})$. This matrix is derived from the inverse of the weight matrix $\mathbf{P}$, containing the accuracies of the observations, and the a priori variance factor σ_0^2. By adding the residual vector $\mathbf{e}$, random errors in the observations are taken into account. Thus, a consistent system of observation equations is obtained. Equation (3.43) represents the general formulation of a Gauß-Markov Model.

In most cases, the observation equations are non-linear. Therefore, the functional model $\boldsymbol{f}(\mathbf{x})$, describing the relationship between $\mathbf{l}$ and $\mathbf{x}$, has to be linearized. The linearization is achieved by a first-order Taylor series approximation with respect to the unknown parameters $\mathbf{x}$:

$$\mathbf{l} - \mathbf{l}_0 = \left.\frac{\partial \boldsymbol{f}(\mathbf{x})}{\partial \mathbf{x}}\right|_{x_0} (\mathbf{x} - \mathbf{x}_0) + \mathbf{e}, \tag{3.44}$$

evaluated at the approximate values of the unknown parameters $\mathbf{x}_0$. In Equation (3.44), the right-hand term $\mathbf{l} - \mathbf{l}_0$ denotes the residual parameters, and the term $\mathbf{x} - \mathbf{x}_0$ denotes the residual parameters. Hereinafter, a linear or linearized system of equations is assumed. Hence, in the case of a linearized system, the parameter vector $\mathbf{x} := \mathbf{x} - \mathbf{x}_0$ represents residual parameters and the observations vector $\mathbf{l} := \mathbf{l} - \mathbf{l}_0$ represents residual observations.

By minimizing the squared residuals in the L_2-norm

$$\mathbf{e}^\intercal \mathbf{P} \mathbf{e} \rightarrow \text{MIN!}, \tag{3.45}$$

the overdetermined system of equations in Equation (3.43) can be solved in a least squares sense

$$\hat{\mathbf{x}} = \left(\mathbf{A}^\intercal \mathbf{P} \mathbf{A}\right)^{-1} \mathbf{A}^\intercal \mathbf{P} \mathbf{l}. \tag{3.46}$$

Therein, $\hat{\mathbf{x}}$ denotes the statistical estimate of the parameter vector $\mathbf{x}$, or the improvements to the approximate values $\mathbf{x}_0$. Equation (3.46) can be rewritten as

$$\hat{\mathbf{x}} = \mathbf{N}^{-1}\mathbf{n} \;\text{ with }\; \mathbf{N} = \mathbf{A}^\intercal \mathbf{P} \mathbf{A} \;\text{ and }\; \mathbf{n} = \mathbf{A}^\intercal \mathbf{P} \mathbf{l}, \tag{3.47}$$

with the normal equation matrix $\mathbf{N}$ and the right-hand side vector $\mathbf{n}$.

The a posteriori variance factor

$$\hat{\sigma}_0^2 = \frac{\hat{\mathbf{e}}^\intercal \mathbf{P} \hat{\mathbf{e}}}{n-u} \quad \text{with} \quad \hat{\mathbf{e}} = \mathbf{l} - \hat{\mathbf{l}} = \mathbf{l} - \mathbf{A}\hat{\mathbf{x}}, \tag{3.48}$$

is an estimator for the common variance level of the observations. Therefore, it can be used as a plausibility check for the a priori assumptions made (cf. Eq. (3.43)). In reality, the accuracies of the observations are usually not exactly known and often more than one set of observations (e.g., k observation groups $\mathbf{l}_k$ with different accuracies) is used. In that case, the variance factors can be approximated in an iterative LSA analyzing the post-fit residuals $\hat{\mathbf{e}}$ (e.g., by means of VCE, cf. Section 3.6).

The stochastic behavior of the estimated parameters $\hat{\mathbf{x}}$ is represented by the variance covariance matrix, defined as

$$\Sigma(\hat{\mathbf{x}}) = \hat{\sigma}_0^2 \mathbf{N}^{-1}. \tag{3.49}$$

3.6 Variance component estimation

VCE enables the estimation of different levels of accuracies for multiple inhomogeneous observation groups. If different types of observations (e.g., quaternions and angular accelerations, range rates and positions) and thus different levels of accuracies are combined within one LSA, the proper relative weighting between the observation groups becomes essential. Instead of relying on the a priori assumed accuracies, the relative weighting of the observation groups is estimated iteratively from the observations themselves. For this purpose, the method of VCE has been established. The following formulations are based on the approach described by Koch and Kusche (2001).

Within the gravity field processing chain (cf. Section 4), the concept of VCE is applied at different phases: (1) within the sensor fusion approach for the relative weighting of different types of observations and for the outlier detection based on the estimated variances (cf. Sections 6.3.1 and 6.3.3), and (2) within the gravity field recovery for the proper relative weighting of the observation groups within individual arcs.

The total normal equation system

$$\mathbf{N}\hat{\mathbf{x}} = \mathbf{n}, \tag{3.50}$$

is accumulated by the weighted sum of the individual normal equations

$$\begin{aligned} \mathbf{N} &= \sum_k \frac{1}{\hat{\sigma}_k^2} \mathbf{N}_k = \sum_k \frac{1}{\hat{\sigma}_k^2} \mathbf{A}_k^\intercal \mathbf{P}_k \mathbf{A}_k, \\ \mathbf{n} &= \sum_k \frac{1}{\hat{\sigma}_k^2} \mathbf{n}_k = \sum_k \frac{1}{\hat{\sigma}_k^2} \mathbf{A}_k^\intercal \mathbf{P}_k \mathbf{l}_k, \end{aligned} \tag{3.51}$$

where the index k denotes the k^{th} group of observations. The unknown variance component estimates $\hat{\sigma}_k^2$ can be obtained by the best invariant quadratic unbiased estimation (Förstner, 1979). Thus, the variance component of one observations group k is given by

$$\hat{\sigma}_k^2 = \frac{\Omega_k}{r_k}. \tag{3.52}$$

Therein, Ω_k denotes the square sum of the residuals

$$\Omega_k = \hat{\mathbf{e}}_k^\intercal \mathbf{P}_k \hat{\mathbf{e}}_k = \hat{\mathbf{x}}^\intercal \mathbf{N}_k \hat{\mathbf{x}} - 2\mathbf{n}_k^\intercal \hat{\mathbf{x}} + \mathbf{l}_k^\intercal \mathbf{P}_k \mathbf{l}_k, \tag{3.53}$$

and r_k the partial redundancy, i.e. the contribution of the observations and the prior information to the overall redundancy. The partial redundancy is obtained from

$$r_k = m_k - \frac{1}{\hat{\sigma}_k^2} \text{trace}(\mathbf{N}_k \mathbf{N}^{-1}), \tag{3.54}$$

where m_k denotes the number of observations within one observation group. The total redundancy $\sum_k r_k = m - n$ is equal to the sum of the partial redundancies.

To allow for an estimation of the variance components, the estimated solution $\hat{\mathbf{x}}$ of the LSA and the variance components $\hat{\sigma}_k^2$ themselves are needed (cf. Eqs. (3.52), (3.53) and (3.54)). Therefore, both, the solution of the normal equation system and variance component estimation are done iteratively. Starting from approximate values, the estimation of the variance components is iterated until convergence. Here, a threshold value for the relative change in the a posteriori variance factor (cf. Eq. (3.48)) is used as convergence criterion, as it is an estimator for the common variance level of the different observation groups. For more details on the principles of VCE, the reader is referred to Koch and Kusche (2001).

3.6.1 Robust estimation of variance components

In order to consider outliers within the observation groups, a robust estimator, such as the robust Huber M-estimator, can be used in combination with VCE.

A robust parameter estimation is an estimation which is insensitive to outliers in the observations. Hence, the method of LSA does not belong to the robust estimators, since minimizing the sum of squares of the residuals leads to a blurring of the outliers (Koch, 1999). By robust estimators, observations which may be distorted by outliers can be identified and thus down-weighted within the LSA. In order to be robust, the adjustment is performed iteratively with variable weights:

$$\hat{w}_i := w(\hat{e}_i) := \frac{\Psi(\hat{e}_i)}{\hat{e}_i}, \tag{3.55}$$

with Ψ denoting the influence function.

Within this thesis, the concept of VCE in combination with a slightly modified robust Huber M-estimator is applied to the sensor fusion approach (cf. Section 6). The combination of VCE (observation group weighting) with individual data weighting (M-estimation) enables not only a relative weighting of the different inhomogeneous observation groups (quaternions, angular accelerations), but also the simultaneous detection of large outliers or spurious data within the individual observation groups.

Subsequently, the robust Huber M-estimator, the Danish method, and the estimator used within this thesis are shortly introduced. The formulations are based on the principles of robust parameter estimation described by Koch (1999).

Robust Huber M-estimator

To derive the robust Huber M-estimator, a probability density function is chosen, which in the middle consists of the normal distribution and at the tails of the Laplace distribution, a special form of the exponential distribution (Koch, 1999). Thus, the Huber distribution (Huber, 1981) assumes the observations to be normally distributed within an interval $[-c\sigma, c\sigma]$, and following the Laplace distribution outside this interval. By this, outliers can be considered by decreasing the influence of observations outside the predefined interval. The weights proposed by Huber (1981) can be expressed as

$$\hat{w}_i = \begin{cases} 1 & \text{for } |\hat{e}_i| \leq c\sigma \\ \dfrac{c\sigma}{|\hat{e}_i|} & \text{for } |\hat{e}_i| > c\sigma, \end{cases} \tag{3.56}$$

where the index i denotes the observation epoch, and c denotes a constant whose value depends on the amount of outliers in the data (Huber, 1981). Commonly, c is chosen in an interval between 1.5 and 3. The robust weights w_i will decrease if the standardized residual $|\hat{e}_i|$ is outside the defined interval. In Huber's robust M-estimation, the observations are iteratively re-weighted by the weights derived according to Equation (3.56), i.e. no outliers are removed but the weights of the outliers will decrease until convergence.

Danish method

Instead of the weights proposed by Huber (1981), the Danish method (Krarup et al., 1980; Kubik et al., 1985), which is also frequently applied, uses

$$\hat{w}_i = \begin{cases} 1 & \text{for } |\hat{e}_i| \leq 2\sigma \\ e^{-k\hat{e}_i^2} & \text{for } |\hat{e}_i| > 2\sigma, \end{cases} \tag{3.57}$$

where k denotes a constant. For more details on robust estimators, the reader is referred to e.g., Koch (1999).

Modified Huber M-estimator

In order to allow for an outlier detection within the sensor fusion approach (cf. Section 6), the concept of VCE (cf. Section 3.6) is extended by robust estimation. For this purpose, the VCE is combined with a slightly modified version of the Huber M-estimator, which is based on a combination of the Huber M-estimator with the Danish method (cf. Eq. (3.56) and (3.57)). The robust variances can be written as

$$\hat{\sigma}_i = \begin{cases} \hat{\sigma}_k & \text{for } \hat{\sigma}_i\sqrt{\Omega_i/r_i} \leq c\hat{\sigma}_k \\ \hat{\sigma}_k \cdot \left(\dfrac{\hat{\sigma}_i\sqrt{\Omega_i/r_i}}{c\hat{\sigma}_k}\right)^{1.5} & \text{for } \hat{\sigma}_i\sqrt{\Omega_i/r_i} > c\hat{\sigma}_k. \end{cases} \tag{3.58}$$

Therein, $\hat{\sigma}_i$ denotes the empirical variance at observation epoch i (within one observation group k), and $\hat{\sigma}_k$ denotes the variance component of the observation group k derived by means of VCE. The constant is set to $c = 2.5$. In contrast to Equation (3.56), the formula is

extended by the exponent 1.5. This modification allows for a more rigorous outlier detection within the observation groups, and thus guarantees that not only large blunders, but also smaller outliers are identified, and are down-weighted accordingly. If the empirical variance differs significantly from the value of the variance component, a new weight based on both the empirical variance and the variance component is assigned to the observation. The decision on the significance of the difference is based on the modified Huber-M-estimator. In a first step, the variance components are estimated according to Equation (3.52). In a second step, the variance components (of suspicious observations, i.e. possible outliers) are re-weighted by Equation (3.58). Both steps are done iteratively, using least squares methodology.

This approach offers the following advantages: (1) there is no need for an a priori outlier detection to remove bad or spurious observations, and (2) arcs with a small number of observations can still be solved, since no observations are removed beforehand. The only drawback of this method is that enough observations are needed in order to allow for a reliable outlier detection.

4 Gravity field processing - ITSG-Grace2016

The ITSG-Grace2016 release[1] (Mayer-Gürr et al., 2016b), successor to the ITSG-Grace2014 release (Mayer-Gürr et al., 2014), comprises the latest GRACE only gravity field models computed at the Institute of Geodesy (IfG) at the Graz University of Technology. Aside from unconstrained monthly gravity field models, it also provides Kalman smoothed daily solutions (e.g., Kurtenbach, 2011; Kvas et al., 2016). The current release covers the whole GRACE time span, from April 2002 to June 2017. The ITSG-Grace2016 time series is the working groups' contribution to the European Space Agency (ESA) Climate Change Initiative (CCI); since the temporal gravity field models are used as input for operational ice mass balance products.

The following Sections give a - very general - overview of the gravity field processing chain used to derive the monthly ITSG-Grace2016 gravity field models, with an emphasis on the GRACE Level-1B data pre-processing. Section 4.1 shortly summarizes the data products used as input for the GRACE gravity field recovery and/or for data pre-processing purposes. Section 4.2 provides a general overview of the ITSG-Grace processing chain, i.e. the process of deriving spherical harmonic coefficients from GRACE observations based on the variational equation approach (cf. Section 3.4). Whereas, Section 4.3 outlines details of the Level-1B data pre-processing methodologies, which are part of the ITSG-Grace2016 processing chain. This also includes the introduction of some strategies for data resampling and data screening. Section 4.4 introduces the GROOPS software package, used for the ITSG gravity field recovery.

4.1 Input data

The ITSG-Grace2016 monthly gravity field models are computed from GRACE Level-1B RL02 data products (cf. Section 2.5), including the inter-satellite range-rates derived from the K-Band link between the two satellites, attitude data from the star cameras, non-gravitational accelerations measured by the accelerometer, and orbit information.

In addition to the official Level-1B orbit data products (cf. Section 2.5), kinematic orbits computed at the IfG (Zehentner and Mayer-Gürr, 2015) are also part of the input data. Prior to the actual gravity field recovery, the Level-1B data products are pre-processed (cf. Section 4.3). From this an improved attitude data product and a calibrated accelerometer data product are derived (cf. Sections 4.3, 6, and 7), which replace the official Level-1B star camera and accelerometer data product (SCA1B, ACC1B) in the further recovery process.

[1] Available for download at: `ifg.tugraz.at/ITSG-Grace2016`

4.2 Processing chain

The gravity field recovery from GRACE data is complex, and cannot be explained in full detail here. Therefore, Figure 4.1 explains schematically the processing chain of the ITSG-Grace2016 release. Based on the GRACE Level-1B input data and background models, the monthly gravity field models are estimated in terms of spherical harmonic coefficients by an iterative LSA using variational equations.

In a first step (1 in Fig 4.1), the GRACE Level-1B input data is pre-processed. The data pre-processing includes data resampling to a common sampling interval of 5 seconds (cf. Section 4.3.1), data screening (cf. Section 4.3.2), combination of angular accelerometer and star camera data (cf. Section 6), and accelerometer data calibration (cf. Section 7). The pre-processed GRACE Level-1B data serves as input for the gravity field recovery. In a second step (2 in Fig 4.1), the observations equations are set-up and the LSA is solved iteratively. An essential part is to integrate the variational equations and fit them to the kinematic orbits. Details on the numerical orbit integration can be found in Ellmer and Mayer-Gürr (2017b). Another important aspect is the observation weighting and noise modeling (Behzadpour et al., 2017), which is done by applying the principles of VCE. As output (3 in Fig 4.1) one gets the estimated spherical harmonic coefficients, representing an unconstrained GRACE-only global monthly gravity field model of the Earth.

Details on the ITSG-Grace2016 processing chain can be found in e.g., Mayer-Gürr et al. (2016a), Mayer-Gürr et al. (2016b), and Klinger et al. (2016).

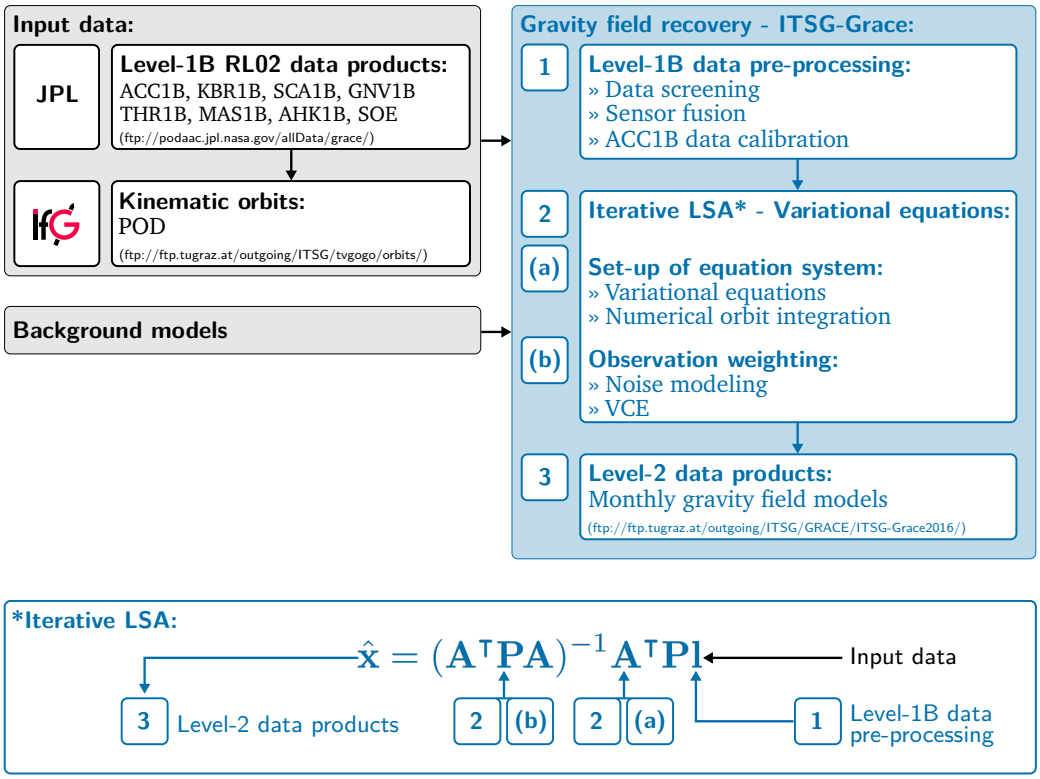

Fig. 4.1.: Schematic overview of the ITSG-Grace processing chain: gravity field recovery based on ITSG-Grace2016 processing standards.

4.3 Level-1B data pre-processing

The GRACE Level-1B data processing is part of the ITSG-Grace processing chain and can be seen as an a priori processing of the official GRACE Level-1B RL02 data products, before they are used as input for the actual recovery of the gravity field models (cf. Fig. 4.1). This Section gives a general overview of the GRACE Level-1B data pre-processing step. Additionally, Section 4.3.1 and 4.3.2 will introduce the most important aspects of data resampling and data screening. The necessity of resampling and screening the input data prior to the actual data pre-processing, depicted in Figure 4.2, is one aspect all pre-processing steps have in common. The latter is of particular importance to identify anomalous data before being used as input for data pre-processing and thus gravity field recovery.

Figure 4.2 shows a flowchart of the GRACE Level-1B data pre-processing: starting from the input data the individual sub-modules, data streams, derived output data and mutual dependencies between the modules are shown. The sub-modules represent the different pre-processing methodologies applied to the GRACE Level-1B data products. The processing chain to obtain pre-processed Level-1B data products can be roughly divided into three individual modules or steps. These steps include: (1) the combination of accelerometer and star camera data to derive an improved attitude data product (sensor fusion), (2) the modeling of non-gravitational accelerations, and (3) the accelerometer data calibration. The input data are the GRACE Level-1B RL02 science and housekeeping data products. The resulting output data includes an improved attitude data product, modeled accelerometer data, and a priori calibrated accelerometer data.

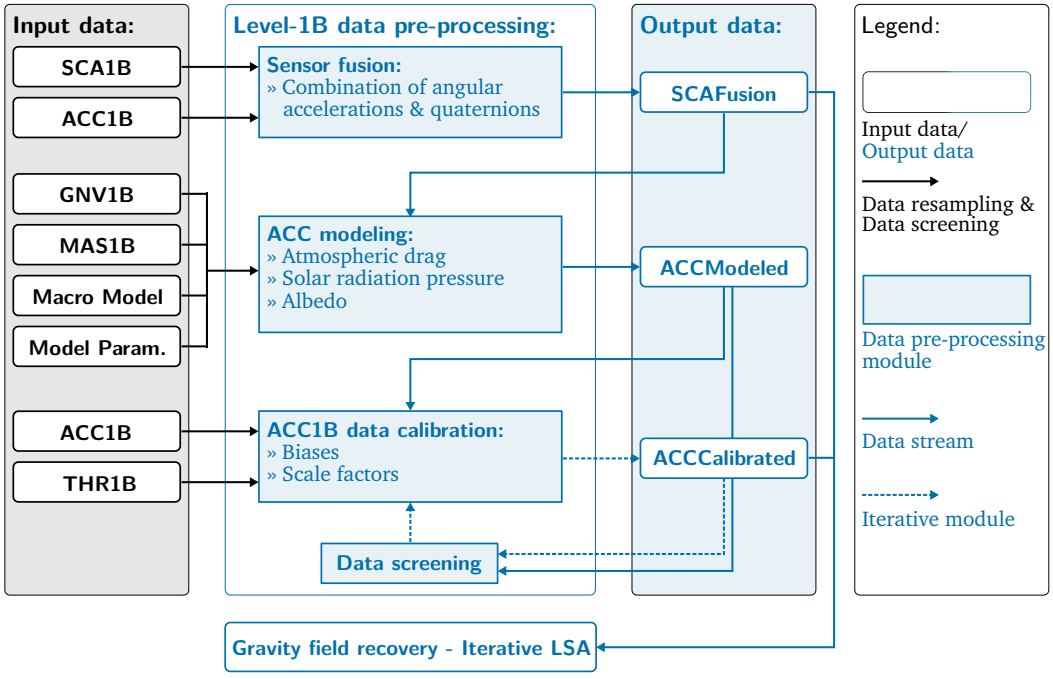

Fig. 4.2.: Schematic overview of the GRACE Level-1B data pre-processing: flowchart of the data stream among the individual sub-modules.

The schematic overview given in Figure 4.2 serves as an introduction to subsequent Sections, discussing the individual pre-processing methodologies in-depth. Details on the characteristics of the improved attitude determination and accelerometer data modeling and calibration, are given in Section 6 and Section 7, respectively. The characteristics of the GRACE attitude determination, star camera and accelerometer data are discussed separately within Section 5. The effects and benefits of the presented pre-processing methodologies on the recovered temporal gravity field solutions are then further analyzed in Section 8.

4.3.1 Data resampling

The Level-1B science data products are resampled in order to guarantee a common sampling interval of 5 seconds, and to interpolate small data gaps (up to a maximum predefined time interval). Table 4.1 gives an overview of the resampling method used for the interpolation of accelerometer, orbit and star camera data. Data gaps within the Level-1B KBR ranging data are not interpolated.

Tab. 4.1.: Level-1B data resampling.

Data product	Max. data gap	Resampling method	LSA*
ACC1B	10 sec	polynomial interpolation (degree = 1)	no
GNV1B	10 min	polynomial interpolation (degree = 3)	yes
SCA1B	10 min	polynomial interpolation (degree = 1)	no

*yes: LSA, no: degree+1 surrounding data points used for interpolation

The Level-1B housekeeping data products (cf. Section 2.5.2) are not edited, but used as given. Note that not all Level-1B housekeeping data products are uniformly sampled (Case et al., 2010).

4.3.2 Data screening

The purpose of data screening prior to the actual data pre-processing is to automatically detect large blunders and outliers within the Level-1B science data products, as well as to identify periods of possibly anomalous data quality. Therefore, the data screening is divided into three independent steps: (1) threshold-based outlier detection tailored to the (accuracy) characteristics of the different science data products, (2) identification of periods with reduced data quality based on the information contained in the SOE, and (3) detection of periods around yaw turns with non-nominal attitude characteristics.

Figure 4.3 shows time periods (on a monthly basis), in which data was screened out within the GRACE data pre-processing due to specific satellite events (2, 3). Details on the individual events highlighted in Figure 4.3, are given in the subsequent paragraphs.

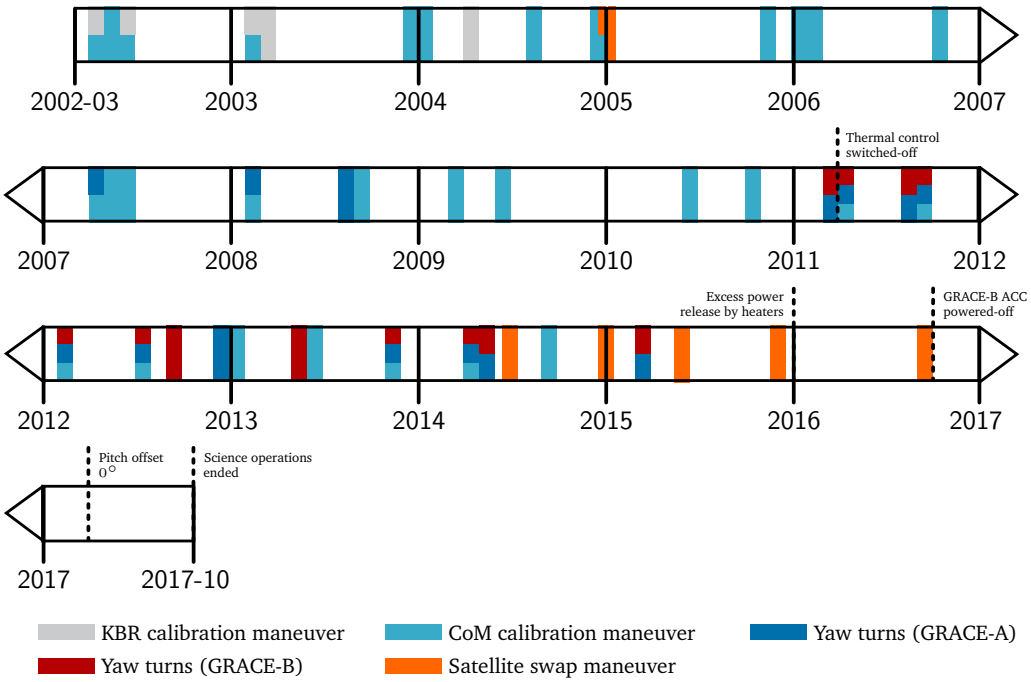

Fig. 4.3.: GRACE data screening: time periods with screened data from April 2002 to October 2017.

Threshold-based outlier detection

Within the Level-1B data pre-processing, a fully automated threshold-based outlier detection is done in order to minimize the amount of blunders and large outliers within the Level-1B data products. The thresholds are defined empirically according to the accuracy characteristics of the individual data products (cf. Sections 5.1 and 5.2). Depending on the instrument-type and the data products available, one (or more) of the following three methods is applied:

$$\text{(1) median-based:} \quad |x^i - \tilde{x}| \geq threshold, \tag{4.1}$$

$$\text{(2) absolute value:} \quad |x^i| \geq threshold, \tag{4.2}$$

$$\text{(3) reference data:} \quad |x^i - x^i_{\text{ref}}| \geq threshold. \tag{4.3}$$

Therein, x^i denotes arbitrary data derived from Level-1B data products at an epoch i, x^i_{ref} denotes reference data at the same epoch i, and $\tilde{x}$ represents the median value of the data set. Methods (1) and (2) are chosen for data screening of Level-1B data products with no reference data available, i.e. the outlier detection is based on the data itself. Blunders within the data are identified by means of extreme values (1) or by deviations to the median value (2). With additional reference data available, outliers are identified by analyzing the differences between the data sets (3). If the differences exceed a predefined threshold, the corresponding epochs are removed. For all three methods an arbitrary margin can be defined to additionally remove epochs before and after the identified outliers.

Table 4.2 summarizes the threshold values and margins used for outlier detection within the Level-1B data pre-processing.

Tab. 4.2.: Level-1B data screening: Threshold-based outlier detection.

Data product	Data type	Threshold	Margin
ACC1B	angular accelerations	$\lvert a_y^i \rvert \leq 0.005$	300 sec
		$\lvert a_z^i \rvert \leq 0.005$	300 sec
ACC1B	angular accelerations	$\lvert a_x^i - \tilde{a}_x \rvert \leq 8 \cdot 10^{-4}$	300 sec
		$\lvert a_y^i - \tilde{a}_y \rvert \leq 8 \cdot 10^{-4}$	300 sec
		$\lvert a_z^i - \tilde{a}_z \rvert \leq 8 \cdot 10^{-4}$	300 sec
ACC1B	linear accelerations	$\lvert a_x^i - \tilde{a}_x \rvert \leq 10^{-5}$	600 sec
		$\lvert a_y^i - \tilde{a}_y \rvert \leq 10^{-5}$	600 sec
		$\lvert a_z^i - \tilde{a}_z \rvert \leq 10^{-5}$	600 sec
ACCCalib, ACCModeled	linear acceleration	$\lvert a^i_{x,\text{calib}} - a^i_{\text{x,modeled}} \rvert \leq 10^{-6}$	150 sec
		$\lvert a^i_{y,\text{calib}} - a^i_{\text{y,modeled}} \rvert \leq 10^{-6}$	150 sec
		$\lvert a^i_{z,\text{calib}} - a^i_{\text{z,modeled}} \rvert \leq 10^{-6}$	150 sec
KBR1B, AOCFusion*	antenna offset correction (range)	$\lvert \text{AOC}^i_\rho - \text{AOC}^i_{\rho,\text{fusion}} \rvert \leq 10^{-4}$	150 sec
KBR1B, AOCFusion*	antenna offset correction (range rate)	$\lvert \text{AOC}^i_{\dot{\rho}} - \text{AOC}^i_{\dot{\rho},\text{fusion}} \rvert \leq 10^{-5}$	150 sec

*Details see Section 6.1.1

Sequence of Events file (SOE)

Based on the SOE file (cf. Section 2.5.2), time periods, in which GRACE-A and/or GRACE-B perform CoM calibration maneuvers and/or KBR calibration maneuvers, are identified and excluded from the gravity field recovery. The exclusion is done precautionary, since the Level-1B data quality might be reduced during these maneuvers.

CoM calibration maneuvers: The CoM of each satellite changes during the mission, mainly due to fuel consumption and the imbalance between the two fuel tanks. Therefore, CoM calibration maneuvers are executed on a regular basis every few months (cf. Fig. 4.3). This ensures that the proof mass of the accelerometer is positioned within 100 μm of the CoM of the satellite. During these dedicated CoM calibration maneuvers, the CoM offset is determined, and reset to zero to avoid a contamination of the non-gravitational acceleration measurements by rotational accelerations and gravity gradients (Wang et al., 2010).

KBR calibration maneuvers: KBR calibration maneuvers are needed to precisely determine the location of the KBR phase center with respect to the CoM. This information is essential to determine the geometric correction of the KBR ranging measurements (cf. Section 6.1.1). As shown in Figure 4.3, KBR calibration maneuvers were performed solely in the early years of the mission.

For the CoM and KBR calibration, the satellites execute a number of pre-defined sequences of maneuvers to calibrate the COM position and K-Band boresight. For details on the calibration procedures, the reader is referred to e.g., Wang (2003) and Wang et al. (2010).

Yaw turns

A yaw turn, or yaw slew, is defined as a counterclockwise rotation of the spacecraft about its radial axis. In the case of GRACE, yaw turns are executed during satellite swap maneuvers, when leading and trailing satellite change position, or for battery management purposes. Figure 4.4 (a) illustrates the accommodation of the body-fixed SRF within the GRACE spacecraft and the corresponding definition of roll, pitch and yaw angles. The concept of a $\pm 90°$ yaw turn of GRACE-B in top view is depicted in Figure 4.4 (b).

Satellite swap: During a satellite swap maneuver the GRACE satellites exchange position using an eccentricity-inclination vector separation (Kirschner et al., 2004). After half the nominal mission lifetime ($\sim$ 2.5 years after launch, cf. Fig. 4.3), the first satellite swap maneuver was executed to switch the GRACE formation. The switch in satellite positions mainly aimed at balancing the surface erosion of the on-board K-Band horns. Since 2014, satellite swap maneuvers are executed approximately every 161 days (cf. Fig. 4.3) to keep the better star camera as primary camera for attitude control on both satellites (Bandikova, 2015). Thus, the satellite swaps help to save fuel, especially on GRACE-B, by staying on the better performing star camera.

Yaw turns - battery management: With increasing mission lifetime, GRACE is facing additional challenges due to the degradation of the on-board batteries; this applies in particular to GRACE-B (cf. Section 2.6). Due to battery degradation and multiple cell failures, the available capacity of the operational cells is severely limited. To prolong the mission despite these considerable power constraints special operations are needed. In order to avoid too little and too much overcharge of the batteries, which is a major threat to the batteries lifetime, yaw turns are executed to guarantee an optimal level of over-charge (Herman et al., 2012).

During full-sun orbit ($\beta' > 70°$; cf. Appendix D.2), when the Sun is visible to the satellite at all time and primarily illuminates the side panels, the solar panels are turned away from the Sun by making a $-90°$ yaw maneuver. This results in an artificial eclipse, i.e. the Sun illuminates the rear side of the satellite. After a short stay at this $-90°$ offset, the satellite is slewed back to its nominal orientation by making an additional $+90°$ yaw maneuver. By these $\pm 90°$ yaw turns, the battery on-board GRACE is forced to discharge and re-charge with a high current rate, which facilitates rapid cell recovery (Herman et al., 2012).

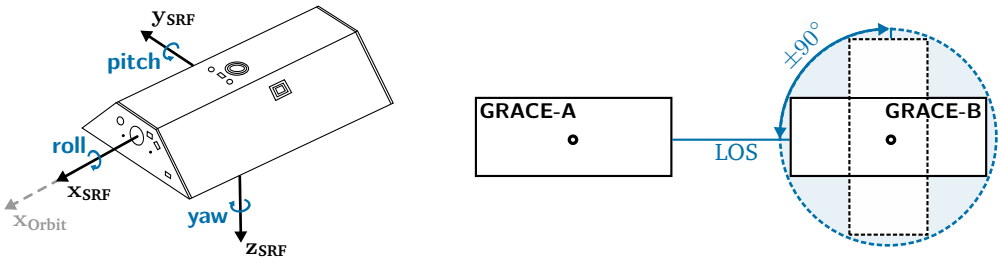

(a) (b)

Fig. 4.4.: Left (a): Accommodation of the SRF within the GRACE spacecraft and definition of roll, pitch, yaw angles. Right (b): top view of a $\pm 90°$ yaw turn of GRACE-B

During most time of the yaw turn maneuvers, no KBR data is available, since the satellites are not in LOS anymore, and the inter-satellite link is lost (cf. Fig. 4.4). However, close to the beginning and end of such yaw turn maneuvers the KBR is still tracking and thus providing KBR measurements. To avoid a degradation of the recovered gravity field models due to anomalous KBR data, the available KBR data with yaw angles exceeding a 100 mrad threshold ($\pm$ 10 min margin) is excluded from processing (cf. Figs. 4.5(b) and 4.5(c)). This ensures that data significantly exceeding the attitude control deadbands over long time periods is removed, but epochs just slightly exceeding the deadbands are not screened. The GRACE roll and pitch deadbands are fixed to 3 mrad and 4 mrad. The value of the yaw deadband was changed several times during mission operations, and was lastly fixed to 5.4 and 5.2 mrad for GRACE-A and GRACE-B, respectively (cf. Section 6; Herman and Steinhoff, 2012). Large movements such as yaw turns can be identified by analyzing the inter-satellite pointing variations in terms of roll, pitch, and yaw rotation angles; which can be derived from the GRACE star camera (SCAFusion), orbit (GNV1B) and KBR antenna phase center offset (VKB1B) data. The roll, pitch, and yaw angles are defined as the angular deviation of the KBR antenna phC from the LOS, i.e. inter-satellite pointing variations are represented as a rotation between the KBR-Frame and LOS-Frame (cf. Section 6.1.2, cf. Appendix A and D.1). Further details on the characteristics of the inter-satellite pointing and attitude control are discussed in Section 6.1.1.

Figure 4.5(a) shows yaw pointing variations of GRACE-A for the time period of one month, plotted along the orbit. The yaw pointing angle time series clearly reflects the presence of satellite events (CoM calibration maneuver, yaw turn maneuvers) within the shown period. Apart from these satellite events, the AOCS successfully keeps the yaw pointing variations within the specified deadband of 5.4 mrad. Figures 4.5(b) and 4.5(c) illustrate the results of the applied data screening for two individual yaw turn maneuvers.

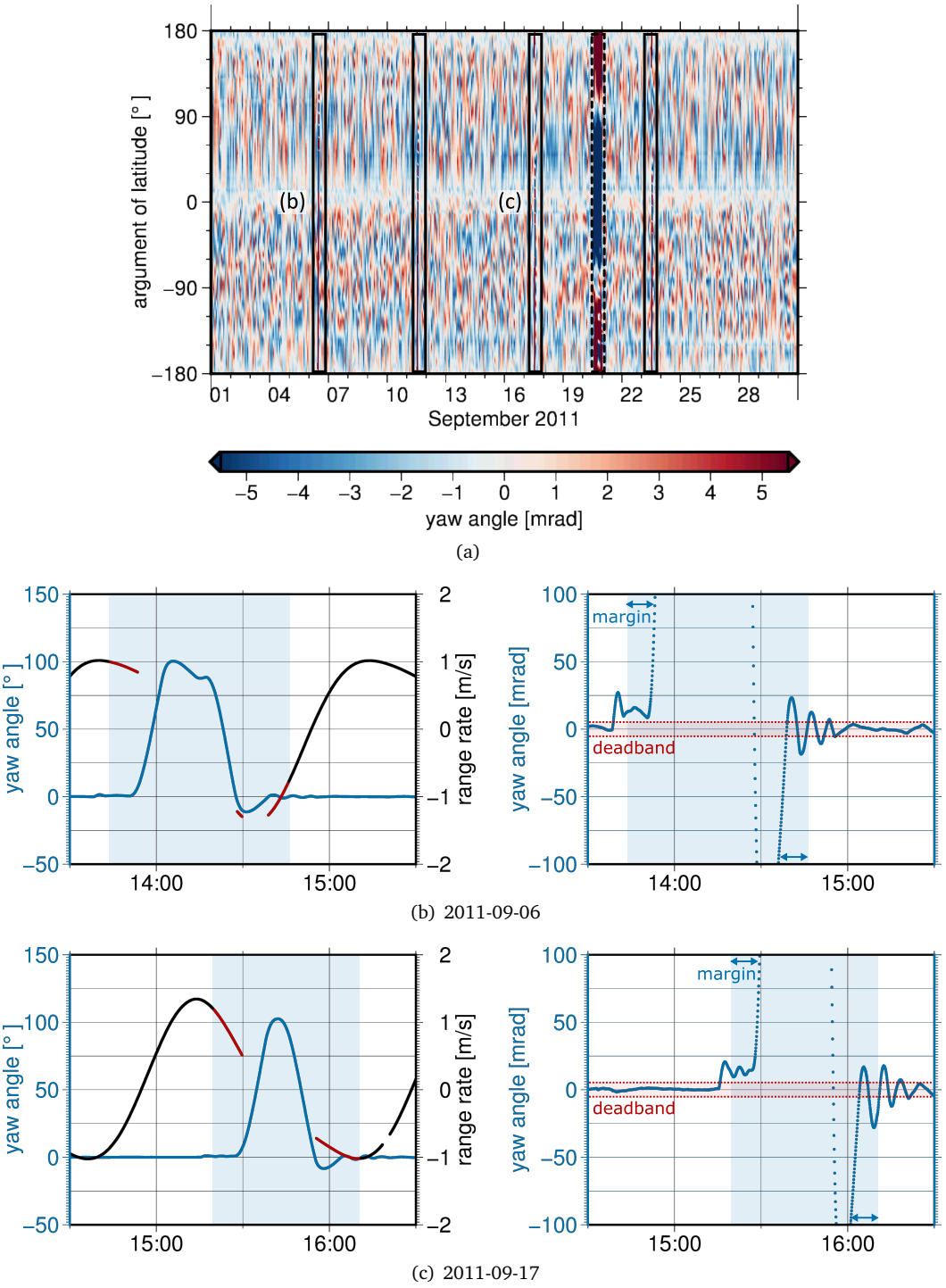

Fig. 4.5.: (a) Yaw angle variations of GRACE-A for one month (September 2011) plotted along the orbit. Yaw turns for battery management and CoM calibration maneuvers are marked in black and black-dashed boxes, respectively. (b,c) Time series of yaw pointing angles (blue) for a time-span of 2 hours during yaw turn maneuvers on 2011-09-06 and 2011-09-17. Left: The KBR range rates are shown in black, with the KBR data screened shown in red. No KBR data is available for the time period highlighted in lightblue. Right: Zoom-in of the yaw angles, showing small scale variations. Yaw angles exceeding the 100 mrad threshold (± 10 minutes) are excluded from processing. The yaw deadband limits are highlighted by red-dashed lines. Note that the scaling for figures on the left and right is different.

4.4 GROOPS

The gravity field processing chain for the recovery of the ITSG-Grace2016 release (cf. Section 4.2), including the instrument data pre-processing and calibration methodologies developed within this thesis, is implemented completely within the Gravity Recovery Object Oriented Programming System (GROOPS).

GROOPS is an independent scientific software package dedicated to all kinds of applications related to gravity field recovery, as well as to applications related to GNSS processing. Besides, the software offers a wide variety of tools for data handling, conversion and visualization in general. Originally, the software was developed by Prof. Dr.-Ing. Mayer-Gürr at the Institute of Geodesy and Geoinformation at the University of Bonn in Germany. Since 2011, the Working Group for Theoretical Geodesy and Satellite Geodesy at the IfG at the Graz University of Technology maintains and further develops the GROOPS software package. Therefore, the software is in a permanent process of development and improvement. At the moment, the GROOPS software comprises approximately 400 individual C++ routines. A Graphical User Interface (GUI) facilitates the handling of the software by offering pull-down menus that represent the main programs in a logical way. The GUI is based on Extensible Markup Language (XML).

The main field of application is the gravity field recovery from various satellite missions, such as GRACE, Champ, GOCE or Swarm. The highly modular design of the GROOPS software offers not only flexibility for different processing scenarios, but also enables a detailed control over all relevant processing options. Furthermore, it offers a powerful environment for automating mission-specific processing chains, as done for the latest ITSG-Grace2016 release. A detailed description of all available GROOPS programs is out of the scope of this work. Therefore, only schematic overviews of the ITSG-Grace2016 processing chain, and the GRACE instrument data pre-processing in particular (cf. Fig. 4.1 and Fig. 4.2), are given. Within this work, a variety of C++ routines for GRACE instrument and housekeeping data handling and data pre-processing have been developed. All analysis and results presented are based on GROOPS.

5 Instrument characteristics

In order to recover the Earth's gravity field from GRACE observations, a broad variety of closely collaborating instruments and sensors is needed. Some instrument or sensor measurements are directly linked to the Earth's gravity field, whereas others are needed to liberate these direct measurements from biasing or disturbing signals to allow for the recovery of the gravity field information.

In Section 2.3, the instruments and sensors on-board GRACE are briefly introduced and discussed. For GRACE, the KBR assembly is considered as the key-instrument, since it enables ll-SST tracking between the two twin satellites. However, for the data pre-processing methodologies, introduced within this thesis (cf. Section 4.3, 6, and 7), the star camera assembly (SCA) and the accelerometer (ACC) are of major importance. A detailed understanding of both instruments is essential for any results and analysis presented and discussed within subsequent Sections. Therefore, Sections 5.1 and 5.2 are dedicated to the on-board SCA and ACC, introducing the measurement principle and the accuracy characteristics of both instruments. Additionally, the SCA and ACC Level-1B data products (SCA1B, ACC1B) are discussed in more detail.

5.1 Star Camera

A star camera or star tracker allows artificial satellites and other space probes to orient themselves within space by determining their absolute 3-axis attitude from star observations. Without this absolute attitude information, scientific measurements from satellites often become worthless. Thus, star cameras can be considered as essential parts of the payload, specifically in the case of GRACE (cf. Section 6). Basically, a star tracker is a digital camera connected to a mirco-processor (Liebe, 2002). By taking pictures of the stars in its field of view (FoV) on a charged coupled device (CCD) array, stars can be located and identified. Based on these observations the attitude of the satellite can be determined (cf. Section 5.1.1).

The star camera assembly (SCA) on-board GRACE, as for CHAMP and GOCE, was developed and built by the DTU (Jørgensen and Pickles, 1998). As shown in Figure 5.1, the SCA consists of two star camera head units (star cameras), two baffles, and a data processing unit. The baffles protect the star camera head units from light intrusions, i.e. reduce the effect of stray light from the Sun, Moon or Earth. For GRACE, the data processing unit is integrated into the IPU, where SCA, KBR and GPS data are processed together. The SCA is part of the AOCS, and is the key attitude determination sensor onboard GRACE, providing accurate information about the satellite's orientation with respect to the inertial frame. Moreover, this attitude information is needed for the correct interpretation of the ACC measurements.

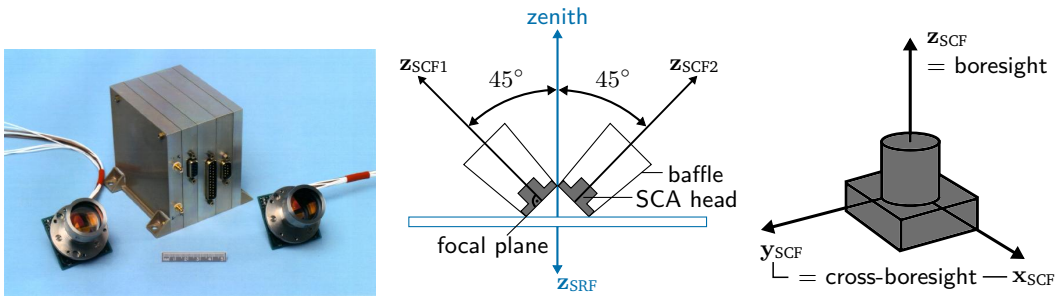

(a) (b) (c)

Fig. 5.1.: (a) CHAMP SCA: 2 SCA heads and data processing unit (Source: Jørgensen and Pickles (1998)), (b) Mounting of the GRACE star camera head units, (c) Illustration of an individual star camera head.

On-board the GRACE satellites, the two star camera head units are rigidly attached to the accelerometer and view the sky at a $\pm 45°$ angle with respect to the zenith direction, pointing towards the port and starboard panel of the spacecraft (cf. Fig. 5.1(b) and Fig. B.1). Each star camera head unit provides attitude information in terms of quaternions, representing the attitude of the star camera frame (SCF) with respect to the inertial frame. The SCF is a sensor frame, with one axis beeing aligned with the boresight or optical axis of the star camera (cf. Figs. 5.1(b) and 5.1(c), cf. Appendix A).

5.1.1 Measurement principle

The GRACE SCA comprises the following two main parts: (1) two star camera head units - each an optical system with a wide angle lense and a low light CCD array, and (2) a data processing unit (part of the IPU), including a micro-processor, and software with an internally stored star catalog (Jørgensen and Pickles, 1998, cf. Fig. 5.1(a)). GRACE uses ESA's Hipparcos star catalog [1], containing information about the position of the stars in the celestial sphere, to identify individual stars within the sensed images. Figure 5.2 shows the layout of a modern autonomous star camera according to Liebe (2002).

Each star camera views a small area of the surrounding starry sky and takes a digital image of the stars in its FoV ($18° \times 16°$). The brightest stars within the FoV are detected (centroiding), and the digital image is matched against the internal star catalog by comparing the measured star coordinates with the known positions of the stars. Based on the sensed star patterns, stars can be located and identified by automatically performed pattern recognition algorithms. Thereby, each star camera unit is able to determine what direction it is pointing, and the attitude of the spacecraft to which it is attached can be determined as well. In the case of GRACE, the attitude output of the two star cameras is provided in terms of attitude quaternions (cf. Appendix C), representing the orientation of the SCF with respect to the inertial frame. A more detailed description of the measurement principle of autonomous star cameras, as used for GRACE, can be found in e.g., Jørgensen and Pickles (1998), Liebe (2002), and Bandikova (2015).

[1] `https://www.cosmos.esa.int/web/hipparcos/catalogues`

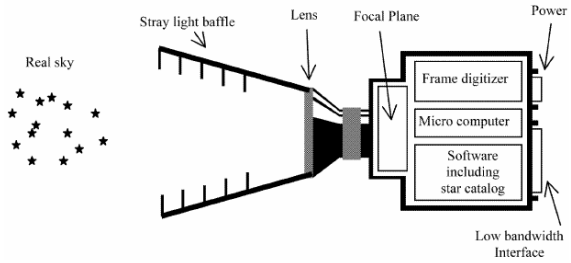

Fig. 5.2.: Layout of an autonomous star camera. Source: Liebe (2002).

For GRACE, each satellite is equipped with a SCA, consisting of two simultaneously operating star cameras, looking at different parts of the sky. The mounting geometry (cf. Fig. 5.1(b)) guarantees redundancy, and thus ensures a continuous attitude determination by at least one of the two star cameras. Due to the orbital configuration of GRACE, both sensors are repeatedly blinded by either the Sun or the Moon (cf. Fig. 5.4), i.e. the Sun or the Moon moves into the FoV. During these Sun or Moon intrusions, the second camera proceeds to measure the attitude.

5.1.2 Measurement accuracy

Due to the sensor construction geometry, star cameras are characterized by an anisotropic measurement accuracy, i.e. not all rotations about the three axis can be determined with the same accuracy. Star cameras are more sensitive to rotations about the cross-boresight axes than about the boresight axis (Liebe, 2002). The latter is perpendicular to the focal plane and points in direction of the FoV (cf. Fig. 5.1). From that follows, that rotations about the boresight axis result in rotations of the stars around the center of the FoV, i.e. stars close to the center show much smaller displacements than stars at the edge. Whereas, rotations around the cross-boresight axes result in a translation of all stars in the FoV, causing a uniform displacement across the whole image. Therefore, rotations around the cross-boresight axes can be determined more accurately by the optical system.

The performance of a star camera depends on several different factors: (1) the sensitivity to starlight, (2) the FoV, (3) the accuracy of star centroiding, (4) the star detection threshold, (5) the number of stars in the FoV, (6) the internal star catalog, and (7) the calibration (Liebe, 2002). Detailed discussions of the individual accuracy components can be found in e.g., Liebe (2002), Jørgensen and Pickles (1998), and Jørgensen (2000).

For GRACE, the nominal accuracy requirements of the star cameras are defined with $30\ \mu$rad and $240\ \mu$rad for the rotation about the cross-boresight axes ($\mathbf{x}_{\mathrm{SCF}}, \mathbf{y}_{\mathrm{SCF}}$) and boresight axis ($\mathbf{z}_{\mathrm{SCF}}$), respectively (Stanton et al., 1998). From that follows, that rotations about the cross-boresight axes can be determined with a factor 8 better than the rotation about the boresight axis. However, no error model describing the star camera noise is available. From the Power Spectral Density (PSD) in Figure 5.3(a) and 5.3(b), showing the rotation angles about the SCF axes (derived from SCA1A data), the anisotropic accuracy characteristics become evident. The rotations about the cross-boresight axis (x,y) are characterized by a smaller noise compared to the boresight axis (z). At high frequencies, between 0.02 Hz and 0.5 Hz, the PSD becomes white noise. Here, the noise levels meet the nominal accuracy requirements. All three axes, show strong per revolution signals (1-per-revolution, 2-per-

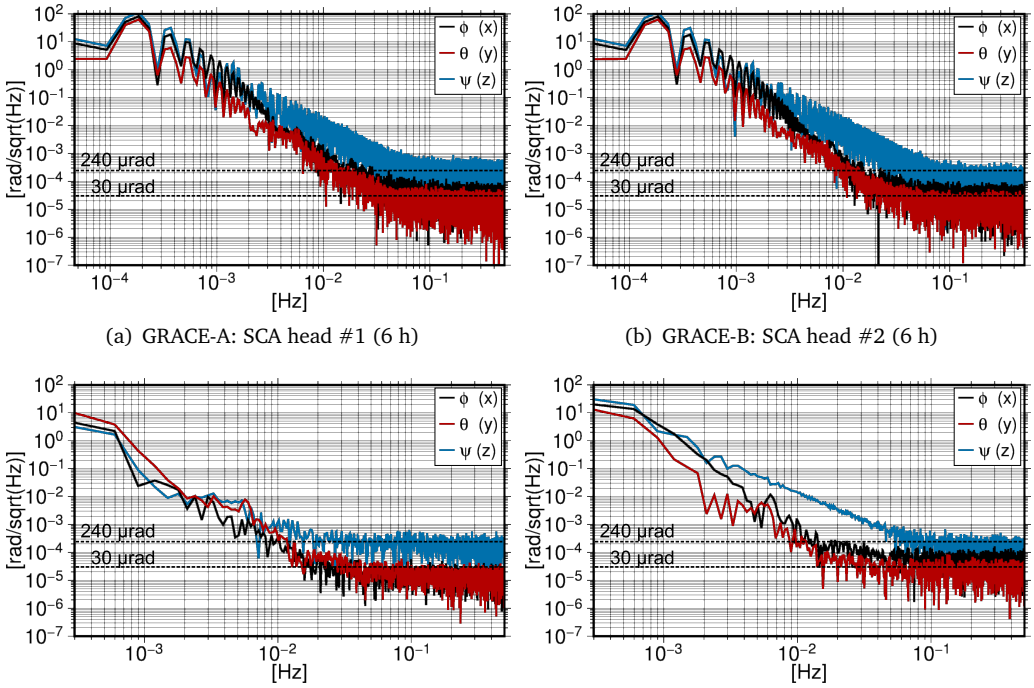

(a) GRACE-A: SCA head #1 (6 h)

(b) GRACE-B: SCA head #2 (6 h)

(c) GRACE-A: SCA head #1 (1 h)

(d) GRACE-A: SCA head #2 (1 h)

Fig. 5.3.: Noise characteristics of the GRACE star cameras: PSD of the roll, pitch, and yaw rotation angles about the SCF cross-boresight (x, y) and boresight (z) axis, derived from the SCA1A data product. Here 6 h intervals (with no data gaps) for (a) the star camera head #1 of GRACE-A and (b) the star camera head #2 of GRACE-B on 2008-12-01 are shown. Additionally, 1 h intervals (with no data gaps) for (c) the star camera head #1 and (d) head #2 of GRACE-A on 2008-12-01 are shown. The Level-1A data products, used for the analysis shown here, were kindly provided by the CSR.

revolution, 3-per-revolution, etc.), caused by the orbital constellation. However, the noise characteristics are not the same for the in total four star cameras (cf. Fig. 5.3) and are not constant over time, i.e. change over the mission lifetime (Bandikova, 2015; Inácio et al., 2015). Since, the thesis focuses on Level-1B data pre-processing, no further accuracy analysis of the SCA1A data are presented or discussed here.

For further data processing, the attitude information provided by the individual star cameras needs to be related to the common SRF. Because of the anisotropic noise characteristics, the rotation from SCF to SRF is affected by an unfavorable noise propagation of the less accurate component (c.f. Siemes, 2011). Due to the mounting geometry of the two star cameras, the combination of both star cameras can prevent the noise propagation induced by the reference frame transformation. By correctly combining both star cameras, full accuracy about all three axes can be achieved. Therefore, the GRACE SCA1B data product contains a combined attitude solution (cf. Section 5.1.3).

5.1.3 GRACE SCA1B RL02 data product

The GRACE SCA1B (RL02) data product provides the attitude of the GRACE satellites in terms of attitude quaternions (cf. Appendix C), which represent the orientation of the satellites SRF with respect to the inertial frame. The SCA1B data product is obtained from the SCA1A data

products during Level-1A to Level-1B processing (Wu et al., 2006). The original attitude quaternions of both star camera heads are combined by a weighted sum, if valid data from both heads is available. However, as shown by Bandikova and Flury (2014), the combination is not done correctly due to an implementation error in the processing scheme. Therefore, the combined solution within the SCA1B data product shows a significantly higher noise level than expected and does not carry the full accuracy about all three axes. By correctly combining the two star camera heads, i.e. taking the anisotropic noise characteristics into account, the noise could be reduced by a factor of 3-4 and full accuracy about all three axis can be achieved (Bandikova and Flury, 2014). The shortcomings of the current attitude processing are further discussed in Section 6.2.

Data availability

The SCA1B data product contains a combined solution only in periods when valid data from both star camera heads is available, otherwise single star camera head solutions are provided. Figure 5.4 shows the SCA1B identification number (ID) for one year of data for GRACE-A and GRACE-B, respectively. The SCA1B ID contains information about the data combination, i.e. whether the SCA1A data of one star camera head or both heads were combined to derive the SCA1B data product. Due to the orbital configuration of GRACE, the two star cameras are repeatedly blinded by either the Sun or the Moon, causing star camera data outages.

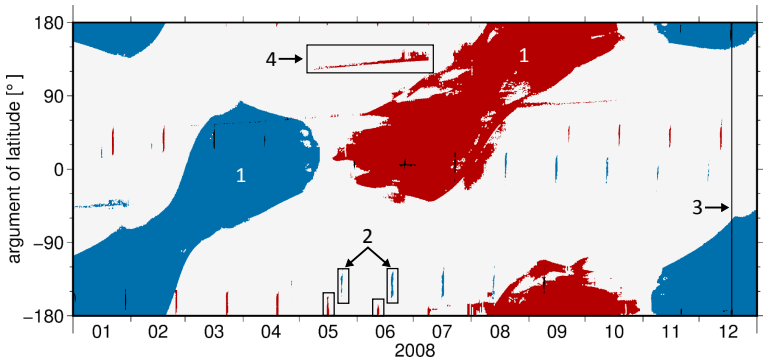

(a) GRACE-A

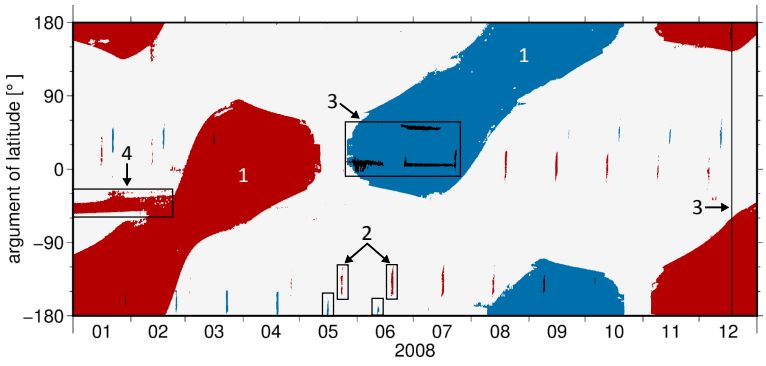

(b) GRACE-B

Fig. 5.4.: SCA1B data combination information of (a) GRACE-A and (b) GRACE-B for one year (2008). Blue = Star camera #1, Red = Star camera #2, Light gray = Combination of star camera #1 + #2, Black = no data available. SCA outages: 1 = Sun intrusions, 2 = Moon intrusions, 3 = data gap, 4 = SCA outage not related to Sun or Moon blinding.

These regular star camera outages are a common issue to both GRACE satellites, causing a reduced availability of the combined solution, which also influence the SCA1B data accuracy. Other outages, not related to Sun or Moon intrusions, might be causes by stray light due to an increased Earth Albedo (cf. Fig. 5.4; Witkowski and Massmann, 2012).

Noise characteristics

To analyze the performance of the SCA1B data product, the quaternions and the corresponding angular accelerations are analyzed in the time and frequency domain. For details on the derivation of angular accelerations from quaternion representation, see Appendix C.

Figure 5.5 shows time series of the attitude quaternion elements contained in the SCA1B data product for a sample 6 h interval, and the corresponding PSD derived from this sample data set for both GRACE-A and GRACE-B, respectively. The time series of the quaternions show a sinusoidal behavior, with an oscillation period twice the revolution period (≈ 3 h). Thus, the PSD shows a strong signal at half the orbit frequency, at about $9 \cdot 10^{-5}$ Hz (not perfectly resolved due to the limited interval length). At high frequencies, between 0.01 Hz and 0.1 Hz, the PSD becomes white noise. The noise level of all for quaternion components lies around 5-e5 (≈ 11 arcs), for both GRACE-A and GRACE-B. According to the attitude requirements, the simulated noise level is in the range of $9 - 11$ arcsec ($4.4 - 5.3 \cdot 10^{-5}$) (Frommknecht, 2008), which principally agrees with the real data shown here. But, all four quaternions are characterized by a rather homogeneous high-frequency noise, which is attributed to the combination error during the Level-1A to Level-1B data processing.

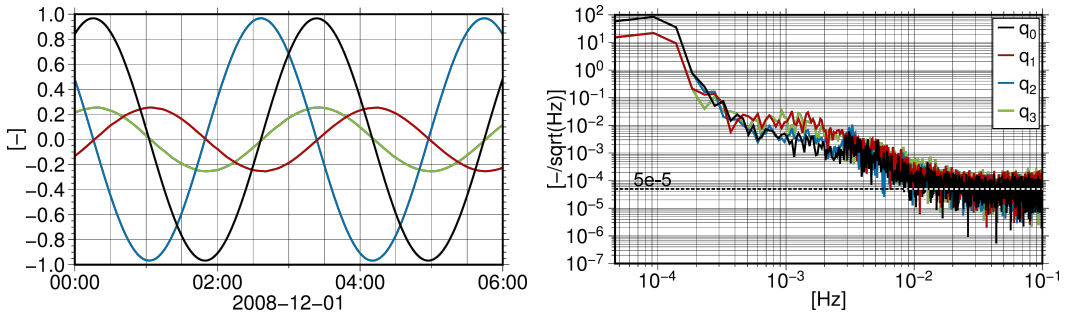

(a) GRACE-A

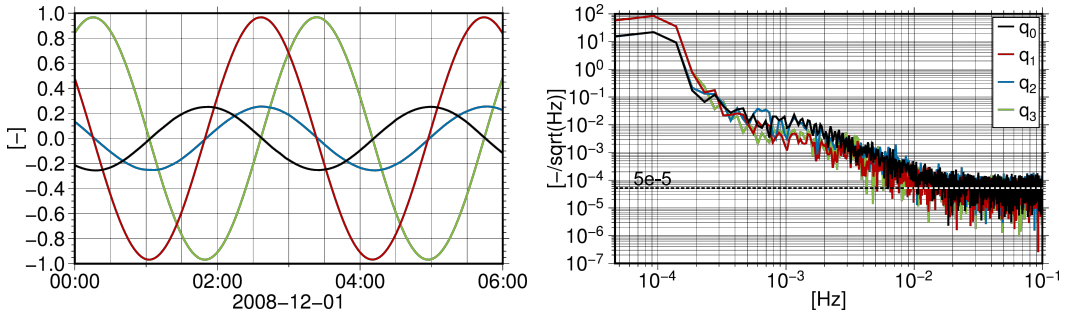

(b) GRACE-B

Fig. 5.5.: GRACE SCA1B data product: Left: Time series of the SCA1B attitude quaternions of GRACE-A (a) and GRACE-B (b) for a 6 h interval on 2008-12-01; Right: PSD of the SCA1B attitude quaternions for GRACE-A (a) and GRACE-B (b) for the same 6 h sample interval on 2008-12-01.

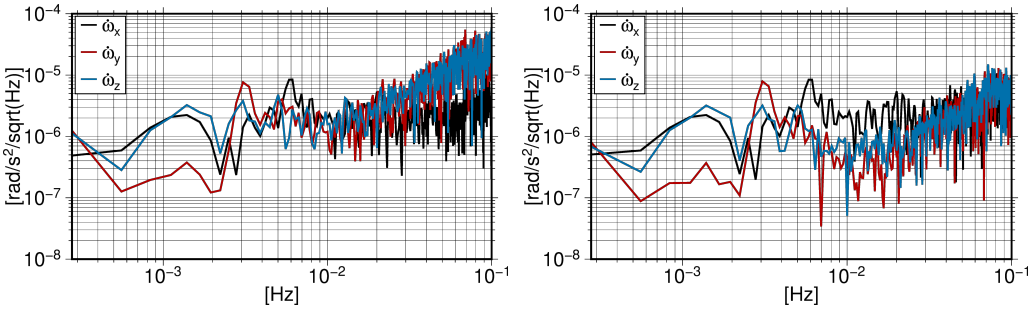

(a) SCA1B (b) SCA1B Repro (Correct combination)

Fig. 5.6.: PSD of the angular accelerations $\dot{\omega}_x$ (black), $\dot{\omega}_y$ (red), $\dot{\omega}_z$ (blue) derived from the SCA1B data product (a), and from a correctly combined re-processed attitude data product (Level-1A to Level-1B processing according to Wu et al. (2006)) (b). To show the effect of not taking into account the anisotropic noise characteristics of the star cameras during data combination, the PSD is derived from a 1 h interval on 2008-12-01, where both star camera heads provided valid attitude data without gaps. The Level-1A data products, used for the analysis shown here, were kindly provided by the CSR.

Another method to asses the performance of the SCA1B data product, is to analyze the angular accelerations derived from the attitude quaternions. Figure 5.6 shows the PSD of the angular accelerations derived from the original SCA1B (RL02) data product, and from a correctly combined re-processed Level-1B attitude product (according to Wu et al. (2006)). A time interval of 1 h is shown, where both star camera heads simultaneously provide valid attitude data without gaps. For the angular accelerations derived from the SCA1B data product (cf. Fig. 5.6(a)), the noise level of the angular accelerations about the x-axis is significantly smaller than that of the y- and z-axis. Due to the mounting geometry of the star camera heads, one would expect approximately the same noise level for all three axes. In case of correct data combination, taking into account the anisotropic noise characteristics (cf. Fig. 5.6(b)), the noise level of the angular accelerations about the y- and z-axis can be reduced significantly. The reduced noise between $5 \cdot 10^{-3}$ Hz and 10^{-1} Hz is the result of the correct weighting of the boresight and cross-boresight axes (cf. Bandikova et al., 2016). Thus, it can be concluded from Figures 5.6(a) and 5.6(b), that the SCA1B data product does not contain the full accuracy about all three axes due to the error in the Level-1A to Level-1B data processing.

5.2 Accelerometer

An accelerometer, located at a satellites COM, allows to measure the accelerations due to the non-gravitational forces acting on it. The SuperSTAR accelerometer onboard each GRACE satellite is a servo-controlled three-axis electrostatic accelerometer manufactured by the Office National d'Études et de Recherches Aérospatiales (ONERA) in France (Touboul et al., 1999). It provides the satellites linear accelerations along three axes, and the angular accelerations about the same three axes. The SuperSTAR accelerometer is the successor of the STAR accelerometer, a quasi-identical instrument which was used on-board the CHAMP mission. Because of the low-vibration design of the GRACE satellites, the high temperature stability, and other improvements (e.g., smaller acceleration bias and bias fluctuations), the SuperSTAR resolution is improved by a factor 10 - compared to its predecessor STAR.

The main purpose of the accelerometers is to measure the non-gravitational forces, including atmospheric drag, solar radiation pressure and Earth albedo (cf. Section 3.3), acting upon the spacecraft. For the recovery of the Earth's gravity field, the non-gravitational forces are needed to separate them from the gravitational forces. Furthermore, the accelerometer also provides additional information in terms of angular accelerations, which can be used e.g., for the purpose of attitude determination (cf. Section 6).

5.2.1 Measurement principle

The sensor unit of the SuperSTAR accelerometer, depicted in Figure 5.7, consists of a parallelepipedic proof mass, located inside a slightly lager sensor cage, which is mounted in the CoM of the satellite. The proof mass is a gold-coated titan cube ($40 \times 40 \times 10$ mm^2), with a mass of 70 g. The asymmetry of the configuration, i.e. a not cubic proof mass, is required to perform an electrostatic levitation of the proof mass during ground testing under normal gravity (Touboul et al., 2004).

In principle, the accelerometer comprises two main parts: (1) the position detector - detecting the position of the proof mass inside the sensor cage, and (2) the servo-mechanism - keeping the proof mass in its nominal position. To allow for electrostatic position detection and control, the gold-coated walls of the sensor cage are equipped with electrodes, which serve both as capacitive sensors to derive the instantaneous proof mass position, and as actuators to apply low frequency actuation voltages to keep the proof mass motionless at the center of the electrodes cage. Measurements of the electrostatic forces and torques, which are generated by the electrodes in order to maintain the mass motionless with respect to the sensor cage, provide the six outputs of the accelerometer (linear acceleration vector, angular acceleration vector). The measured electrostatic force is proportional to the acceleration exerted upon the satellite by the non-gravitational forces.

More details on the accelerometer and its measurement principle can be found in e.g., Touboul et al. (1999), Touboul et al. (2004), and Frommknecht (2008).

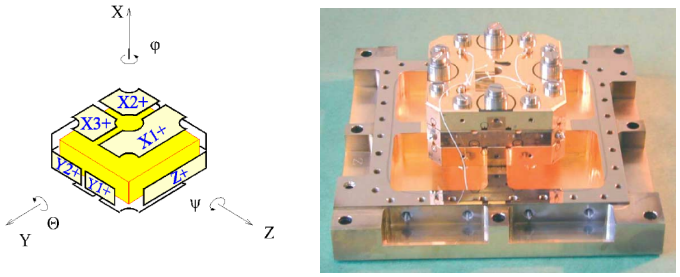

(a) (b)

Fig. 5.7.: SuperSTAR accelerometer: (a) accelerometer model (Image courtesy of ONERA), (b) sensor head inside three gold coated plated rigidly fixed to the instrument reference frame (Source: Touboul et al. (2004)).

Disturbing forces

The measurements of the GRACE accelerometers are perturbed by different types of disturbances, including electric, magnetic, thermal, and pressure disturbances resulting from internal parasitic forces (Touboul et al., 2004). As a consequence, the accelerometer senses in addition to the surface accelerations also satellite-induced disturbing accelerations, such as accelerations due to temperature variations (Klinger and Mayer-Gürr, 2016), thruster firings (Frommknecht, 2008), magnetic torquer induced accelerations (twangs and spikes) (Hudson, 2003; Fackler, 2004; Peterseim et al., 2012; Peterseim, 2014) and others. The effect of twangs and spikes is reduced by low-pass filtering the 1 Hz accelerometer data during Level-1A to Level-1B processing, but it is not corrected sufficiently (Peterseim, 2014). Since, the influences due to these effects onto the recovered gravity field are expected to be small, and already pre-processed Level-1B data products are used for gravity field recovery, they are neglected in the analysis presented within this thesis. Under the assumption of thruster misalignments, force imbalances or differences in reaction time, the accelerations due to thruster firings represent actual linear accelerations, and thus need to be measured by the accelerometer. Hence, their presence within the acceleration time series is justified. Since the GRACE accelerometers principally have or had a thermally controlled environment, which should keep the temperature variations below 0.1 K per revolution (Stanton et al., 1998), accelerations due to temperature variations were not expected to have a large influence on the gravity field recovery. In order to achieve the required thermal stability both satellites are equipped with an active thermal control, i.e. heaters keeping the temperature of parts of the satellite or instruments within a specified temperature range. As a result of reduced battery capacity, the active thermal control was permanently switched-off in April 2011 (Tapley et al., 2015). Since then, temperature variations, resulting from the orbital geometry, directly affect the on-board accelerometers. To avoid a degradation of the recovered gravity field solutions, these temperature variations have to be taken into account during Level-1B data pre-processing and gravity field recovery (cf. Section 7 and Section 8).

In case the accelerometer is not precisely located at the satellite's CoM, i.e. the accelerometer is displaced relative to the CoM, the measured linear accelerations contain additional signal due to the satellite's angular motion and due to gravitational forces (Kim, 2000). In order to meet the requirements of the GRACE mission (Stanton et al., 1998), the proof mass has to be positioned very precisely at the CoM (or center of gravity) of the satellite to avoid accelerations offsets and measurement disturbances. To minimize these effects, the offset is corrected by the Mass Trim System (cf. Section 2.3.2), by regularly performing CoM calibration maneuvers.

In general, it is not trivial to differ distinctly between sensor errors, noise and disturbances induced by the satellite environment. In order to reduce their impact on the recovered gravity field solutions, known sources of disturbances or errors should be modeled within the data pre-processing and gravity field recovery, if applicable.

Measurement model

The linear accelerations measured by the accelerometer are the sum of the non-gravitational accelerations corrupted by unknown scale factors, biases, disturbing forces and random noise. Under the assumptions that the accelerometer is located at the CoM, and that other

disturbing forces can be neglected, a simplified measurement model is given by (Stanton et al., 1998):

$$\mathbf{\Gamma} = \mathbf{c}_0 + \mathbf{c}_1\mathbf{a}_d + \mathbf{c}_2\mathbf{a}_d^2 + \mathbf{c}_3\mathbf{a}_d^3 + \mathbf{noise}, \tag{5.1}$$

where $\mathbf{\Gamma}$ denotes the accelerometer output, $\mathbf{a}_d$ denotes the true non-gravitational accelerations expressed in the accelerometer coordinates, $\mathbf{c}_0$ denotes the bias vector, and $\mathbf{c}_1, \mathbf{c}_2, \mathbf{c}_3$ correspond to the linear, quadratic and cubic scaling factors. According to the SuperSTAR error specifications (Stanton et al., 1998), the noise is specified according to Equations (5.2) to (5.4), and the bias is expected to be $< 2{\cdot}10^{-6}\mathrm{m/s^2}$ for the sensitive axes, and $< 50{\cdot}10^{-6}\mathrm{m/s^2}$ for the less-sensitive axis. The linear scaling factors for both sensitive and less-sensitive axes are assumed to be 1 ± 0.02. Higher order scaling factors are assumed to be negligible.

Accelerometer and Science Reference Frame

The original accelerometer measurements refer to the Accelerometer Frame (AF), whereas the acceleration vector given in the ACC1B data product refers to the SRF. The SRF is defined to have its origin at the CoM of the satellite, the axes are directed parallel to the measurement axes of the accelerometer (cf. Fig. 5.8) (Bettadpur, 2010). According to Case et al. (2010), the $\mathbf{x}_{SRF}$ axis (along-track) is pointing towards the K-Band antenna horn, i.e. it is pointing towards the other satellite. It is approximately tangential to the satellite orbit, except of a pitch angle offset ensuring precise inter-satellite pointing (cf. Section 2.2.2). The $\mathbf{z}_{SRF}$ axis (radial) is nadir pointing, and the $\mathbf{y}_{SRF}$ axis (cross-track) completes the right handed triad. The exact definitions of the GRACE reference frames can be found in Appendix A, or in e.g., Case et al. (2010) and Bettadpur (2010).

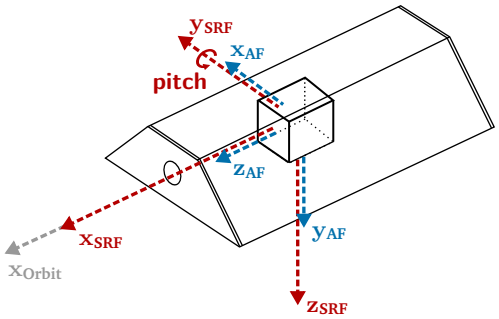

Fig. 5.8.: Accommodation of the Accelerometer Frame (AF) (blue) and the Science Reference Frame (SRF) (red) within the GRACE spacecraft.

5.2.2 Accuracy characteristics

Before the launch of GRACE, the performance of the SuperSTAR accelerometers was analyzed by pre-launch simulations (Stanton et al., 1998; Hudson, 2003). Afterwards, various studies further analyzed the noise characteristics of the real Level-1A and Level-1B accelerometer data (Fackler, 2004; Flury et al., 2008; Frommknecht, 2008; Peterseim et al., 2012; Peterseim, 2014). Table 5.1 summarizes the pre-launch specifications of the SuperSTAR accelerometer, including the measurement range and measurement accuracy of the linear and angular accelerations, as defined by Stanton et al. (1998), Hudson (2003) and ONERA (personal communication).

Tab. 5.1.: Specifications of the SuperSTAR accelerometer, derived from Stanton et al. (1998), Hudson (2003) and ONERA

Axis (SRF)	Range	Accuracy
a_x	$\pm 5 \cdot 10^{-5}$ m/s^2	$1 \cdot 10^{-10}$ m/s$^2/\sqrt{\text{Hz}}$
a_y	$\pm 5 \cdot 10^{-4}$ m/s^2	$1 \cdot 10^{-9}$ m/s$^2/\sqrt{\text{Hz}}$
a_z	$\pm 5 \cdot 10^{-5}$ m/s^2	$1 \cdot 10^{-10}$ m/s$^2/\sqrt{\text{Hz}}$
$\dot{\omega}_x$	$\pm 1 \cdot 10^{-2}$ rad/s^2	$5 \cdot 10^{-6}$ rad/s$^2/\sqrt{\text{Hz}}$
$\dot{\omega}_y$	$\pm 1 \cdot 10^{-3}$ rad/s^2	$2 \cdot 10^{-7}$ rad/s$^2/\sqrt{\text{Hz}}$
$\dot{\omega}_z$	$\pm 1 \cdot 10^{-2}$ rad/s^2	$5 \cdot 10^{-6}$ rad/s$^2/\sqrt{\text{Hz}}$

Linear accelerometer

The SuperSTAR accelerometer has two high-sensitive axes, the radial and along-track axes, and one less-sensitive axis, the cross-track axis (w.r.t. the SRF). The cross-track axis has a reduced sensitivity due to the non-cubic shape of the proof mass, which allows for a levitation of the proof mass during ground testing under normal gravity conditions on Earth (Touboul et al., 2004). Within the high frequency band (frequencies above 30 mHz), the linear acceleration can be determined with an accuracy of 10^{-10}ms$^{-2}/\sqrt{\text{Hz}}$ for the high-sensitive axes, and with 10^{-9}ms$^{-2}/\sqrt{\text{Hz}}$ for the less-sensitive axis (Flury et al., 2008).

The accelerometer performance mainly depends on the accuracy of the proof mass motion sensing and control, on the measurement accuracy of the generated electrostatic forces of the suspension, and on proof mass motion disturbances that are generated by environment fluctuations (e.g., magnetic, electric, thermal) or by any residual stiffness that links the test mass to the accelerometer cage (Touboul et al., 2004). For the linear accelerations, an estimate of the noise is provided by error models defined by Stanton et al. (1998):

$$noise_{a_x}(f) = 1 \cdot 10^{-10} \left[1 + (0.005/f)\right]^{0.5} \text{ms}^{-2}/\sqrt{\text{Hz}}, \tag{5.2}$$

$$noise_{a_y}(f) = 1 \cdot 10^{-9} \left[1 + (0.1/f)\right]^{0.5} \text{ms}^{-2}/\sqrt{\text{Hz}}, \tag{5.3}$$

$$noise_{a_z}(f) = 1 \cdot 10^{-10} \left[1 + (0.005/f)\right]^{0.5} \text{ms}^{-2}/\sqrt{\text{Hz}}, \tag{5.4}$$

with the frequency f expressed in Hz. The noise in Equations (5.2) to (5.4) is specified as the sum of white position and acceleration noise with an additional $1/f$ component below a corner frequency f_0, with $f_0 = 0.1$ Hz for the less-sensitive axis and $f_0 = 0.005$ Hz for the sensitive axes. During Level-1A to Level-1B data processing, the Level-1A linear accelerations are low-pass filtered in order to reduce the high-frequent measurement noise (Wu et al., 2006). Following from this, the linear accelerations provided within the ACC1B data product represent a smoothed version of the Level-1A accelerometer (ACC1A) data product. Since the AF should coincide with the SRF, expect for the axis definition, the accelerometer noise characteristics (below the 0.035 Hz cut-off frequency used for filtering) given in Equations (5.2) to (5.4) should be transferable to the ACC1B data product.

Thorough investigations of the ACC1A data product already have been carried out in the past by e.g., Hudson (2003), Fackler (2004), Flury et al. (2008), Frommknecht (2008), Peterseim et al. (2012), and Peterseim (2014). Here, only the ACC1B data product is analyzed and compared with the findings of the previous investigations.

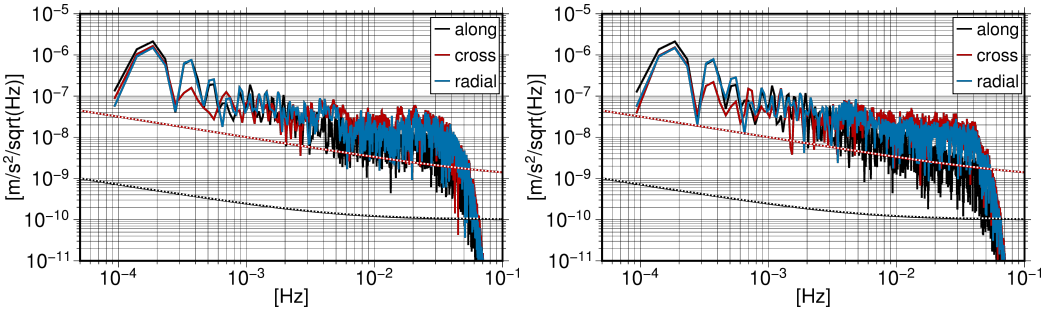

(a) GRACE-A (b) GRACE-B

Fig. 5.9.: Noise characteristics of the ACC1B linear accelerations: PSD of the linear accelerations $\mathbf{a}_x$ (black), $\mathbf{a}_y$ (red), $\mathbf{a}_z$ (blue) derived from a 6 h interval of the ACC1B data product on 2008-12-01, for GRACE-A (a) and GRACE-B (b). The sensor error model for the high-sensitive (black-dashed line) and less-sensitive (red-dashed line) axes is shown as well. Note that here the bias was reduced according to GRACE TN-02 (Bettadpur, 2010).

Figure 5.9 shows the accelerometer error models for the high-sensitive and less-sensitive axes, and the PSD derived from the ACC1B data product for a 6 h sample interval for both GRACE-A and GRACE-B, respectively. According to the investigations carried out by Frommknecht (2008), the performance of the sensitive axes (along-track, radial) is about 5 times worse than predicted by the instrument specifications. Whereas, the performance of the less-sensitive axis (cross-track) seemingly agrees with the specifications. Investigations by Flury et al. (2008) showed that the pre-launch noise specifications are met only during periods with the heater circuits being inactive. According to Figure 5.9, the noise levels of the Level-1B along-track and radial accelerations are significantly higher than expected from the sensor model. The main causes for the high noise levels were found to be thruster activations, magnetic torquer induced accelerations (twangs and spikes), and heater activations and de-activations (Fackler, 2004; Flury et al., 2008; Frommknecht, 2008; Peterseim et al., 2012; Peterseim, 2014). The linear acceleration in all three directions (along-track, cross-track, radial) show strong once- and twice-per-revolution signals. Compared to the motion of the satellite relative to the Earth, the non-gravitational forces experienced by the satellite are almost the same from one revolution to the other. Therefore, the measured linear accelerations are periodic with the orbit frequency. In terms of signal magnitude, the along-track component is expected to be strongest followed by the cross-track and radial component. However, the magnitude strongly depends on the orbit altitude and orbit constellation, i.e. the current β' angle. Additionally, thruster firing, which are primarily present in the cross-track and radial axes (cf. Fig. 5.11), contribute to the signal magnitude. At frequencies higher than 0.035 Hz, the drop of the signal is caused by the low-pass filter applied during Level-1A to Level-1B data processing.

Angular accelerometer

The angular accelerations are characterized by an anisotropic accuracy, with one sensitive axis (cross-track), and two less-sensitive axes (along-track, radial) - vice versa to the linear accelerations. For the angular accelerations, an estimate of the noise of the angular accelerations with respect to the AF can be provided from the instrument error budget (personal communication with Bernard Foulon (ONERA)). Since the AF should coincide with the SRF, expect for the axis definition, the noise characteristics should be transferable to the angular

accelerations provided within the ACC1B data product. From the initial design description document, the performance of the angular accelerations, i.e. the noise of the ϕ, θ, ψ rotation about the x-, y-, and z- axis (in the SRF), in the [10^{-4} Hz; $4 \cdot 10^{-2}$ Hz] frequency bandwidth, is specified by:

$$noise_{\dot{\omega}_x} = 5 \cdot 10^{-6} \left[1 + (0.010/f)\right]^{0.5} \text{rads}^{-2}/\sqrt{\text{Hz}}, \tag{5.5}$$

$$noise_{\dot{\omega}_y} = 2 \cdot 10^{-7} \left[1 + (0.005/f)\right]^{0.5} \text{rads}^{-2}/\sqrt{\text{Hz}}, \tag{5.6}$$

$$noise_{\dot{\omega}_z} = 5 \cdot 10^{-6} \left[1 + (0.010/f)\right]^{0.5} \text{rads}^{-2}/\sqrt{\text{Hz}}, \tag{5.7}$$

with the frequency f expressed in Hz.

The bias estimated from the error budget is defined by:

$$bias_{\dot{\omega}_x} = 2.2 \cdot 10^{-3} \text{ rads}^{-2}, \tag{5.8}$$

$$bias_{\dot{\omega}_y} = 7.7 \cdot 10^{-5} \text{ rads}^{-2}, \tag{5.9}$$

$$bias_{\dot{\omega}_z} = 2.2 \cdot 10^{-3} \text{ rads}^{-2}. \tag{5.10}$$

Figure 5.10 shows the error models for the angular accelerations, and the PSD derived from the SCA1B data product for a 6 h sample interval for both GRACE-A and GRACE-B, respectively. The noise levels of the angular accelerations, representing rotations about the along-track, cross-track and radial axis, are approximately equal (cross-track) or even below (along-track, radial) the specifications. The PSD of all three components is almost flat, apart from signal peaks at once- and twice-per-revolution. The angular accelerations about the cross-track axis also shows a signal peak at about $3 \cdot 10^{-3}$ Hz, which is probably caused by the on-board magnetic torquers, since the rotation about the cross-track axis is almost entirely controlled by the magnetic torquers (not shown here; Frommknecht, 2008). The presence of thruster events, mainly visible in the rotations about the along-track and radial axis (cf. Fig. 5.12), possibly influences the signal amplitude. Additionally, magnetic torquer induced signals and temperature variations, might also affect the signal.

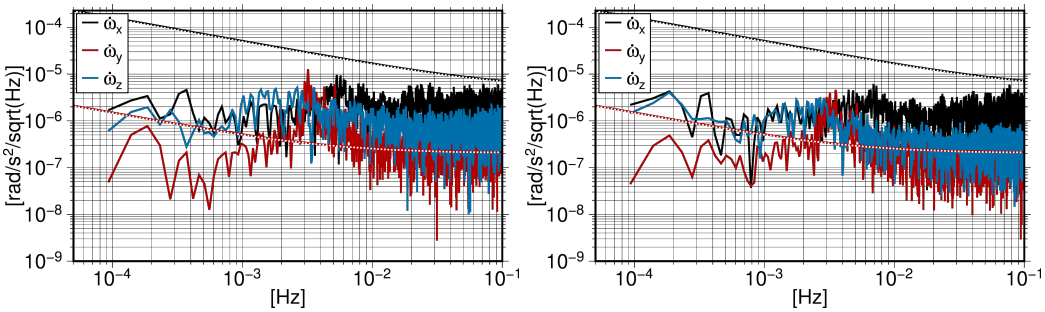

(a) GRACE-A (b) GRACE-B

Fig. 5.10.: Noise characteristics of the ACC1B angular accelerations: PSD of the angular accelerations $\dot{\omega}_x$ (black), $\dot{\omega}_y$ (red), $\dot{\omega}_z$ (blue) derived from a 6 h interval of the ACC1B data product on 2008-12-01, for GRACE-A (a) and GRACE-B (b). The sensor error model for the high-sensitive (black-dashed line) and less-sensitive (red-dashed line) axes is shown as well. Note that here a constant bias was reduced.

5.2.3 GRACE ACC1B & AHK1B RL02 data product

Bias and scale factors

The ACC1B data product contains the linear and angular acceleration measurements in along-track, cross-track and radial direction (w.r.t. the SRF). The accelerations contained in the ACC1B data product include an unknown instrument scale and bias offset, i.e. the accelerometer measurements are subject to instrument specific scale factors, biases and random noise.

A general recommendation for the initial estimates of the scale and bias to apply to the linear accelerations (ACC1B data) is made in the GRACE Technical Note TN-02. For details on the estimation, the reader is referred to Bettadpur (2009). As the recommendations are based on analysis of data between launch and March 2009, the recommendations will progressively worsen as the epoch of the data moves further into the future. Further, the scale factors and biases may vary significantly over the satellite's lifetime due to satellite-induced effects (or external influencing factors), such as the activations and de-activations of the onboard heater lines, or temperature variations due to the switched-off thermal control. The topic of bias variations is further discussed in Section 6.3.2 and Section 7.2.

Figures 5.11 and 5.12 exemplary show bias-corrected linear and angular accelerations in along-track, cross-track, and radial direction derived from the ACC1B data product, in the temporal and spatial domain. The left columns show the acceleration time series for a selected 6 h time interval on 2008-12-01, and the right columns show the accelerations along the orbit for one month of data (December 2008). As both GRACE satellites are identical and show a similar behavior for the selected time period, the analysis is confined to one satellite, GRACE-A. The spikes within the time series of the linear and angular ACC1B accelerometer measurements correspond to epochs with thruster firing events, indicated by the black dots.

From Figure 5.11 it becomes obvious, that the along-track accelerations have the largest magnitude (several $1 \cdot 10^{-8}$ m/s^2) of all three axis. Since the atmospheric drag is the major contributor to the along-track accelerations (for LEOs), the accelerations are mostly negative, resulting in a de-acceleration of the satellite. But in general, the magnitude of the linear accelerations strongly depends on the orbital altitude, as well as on the orbital configuration with respect to the Sun (cf. Appendix D.2). For the time interval shown, the β' angle is about $35°$ and the orbit altitude is about 470 km. The peaks of the thruster events visible are smoothed and smeared out (compared to ACC1A data), and mainly affect the cross-track and radial axes. The horizontal stripe-like pattern visible within the linear accelerations plotted along the orbit (between $-30°$ and $90°$), corresponds to eclipses, i.e. the GRACE-A satellite crosses the Earth shadow. The eclipses are also marked within the linear acceleration time series (left column). During eclipses, the accelerations due to solar radiation pressure and due to shortwave Albedo (cf. Section 3.3) become zero, leading to a reduction of the overall accelerations. A detailed analysis of the different non-gravitational acceleration components (atmospheric drag, solar radiation pressure, albedo) is given in Section 7.1.4.

From Figure 5.12, showing the angular accelerations around the along-track, cross-track, and radial axis, it becomes visible that the thruster firing events mainly affect the rotations about the along-track and radial axis. The rotations about these two axes are mainly

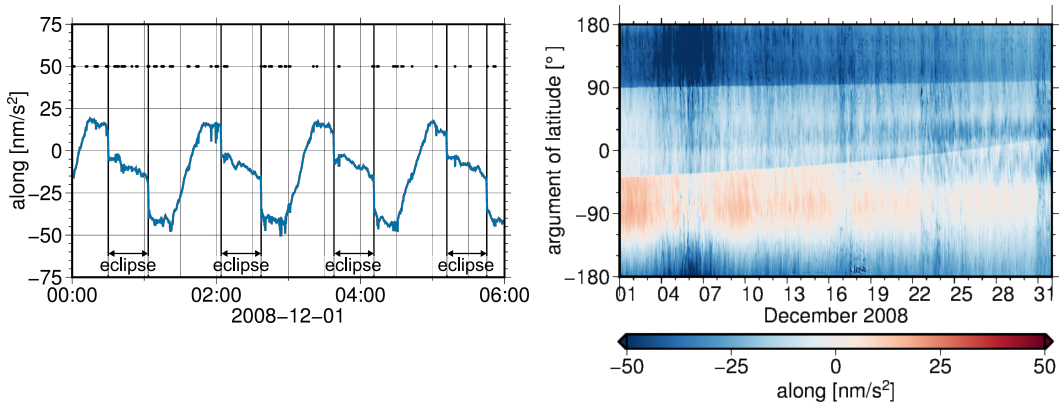

(a) along-track

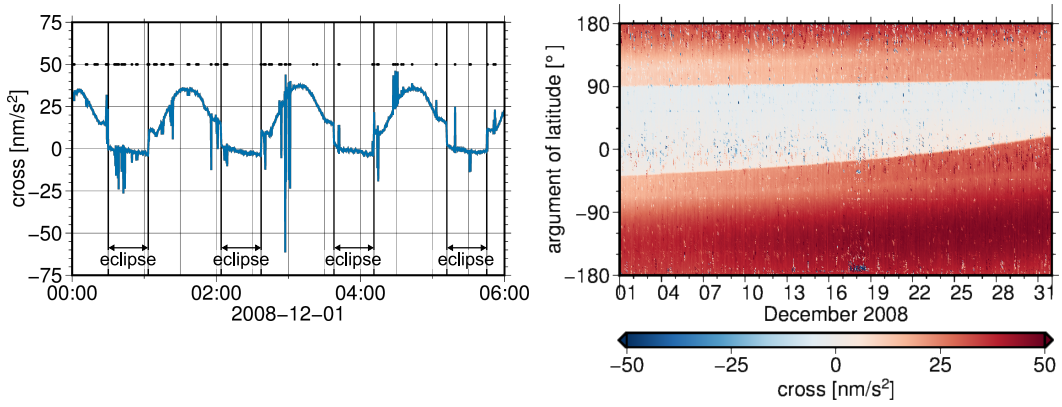

(b) cross-track

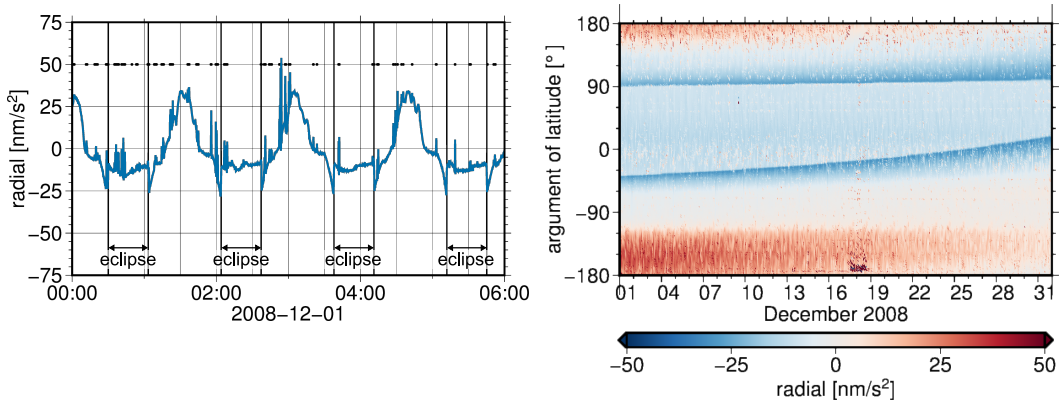

(c) radial

Fig. 5.11.: Linear accelerations in along-track (a), across-track (b), and radial (c) direction for GRACE-A recovered from the Level-1B RL02 data products (ACC1B). The left column shows the linear accelerations (blue) for a selected 6 h interval on 2008-12-01. The black dots indicate epochs with thruster firings. The left column shows the linear accelerations along the orbit for GRACE-A for the whole month (December 2008). Note that here bias-corrected linear accelerations are shown, the accelerations are calibrated according to the initial recommendations in TN-02 (Bettadpur, 2009).

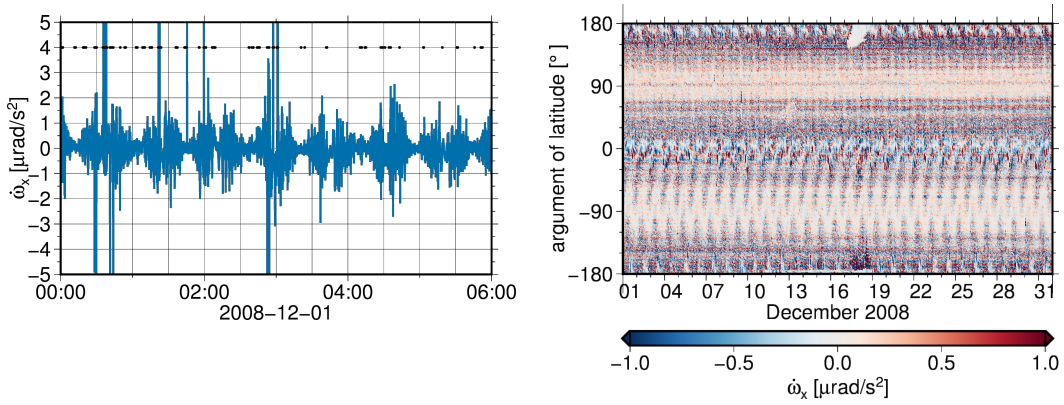

(a) $\dot{\omega}_x$

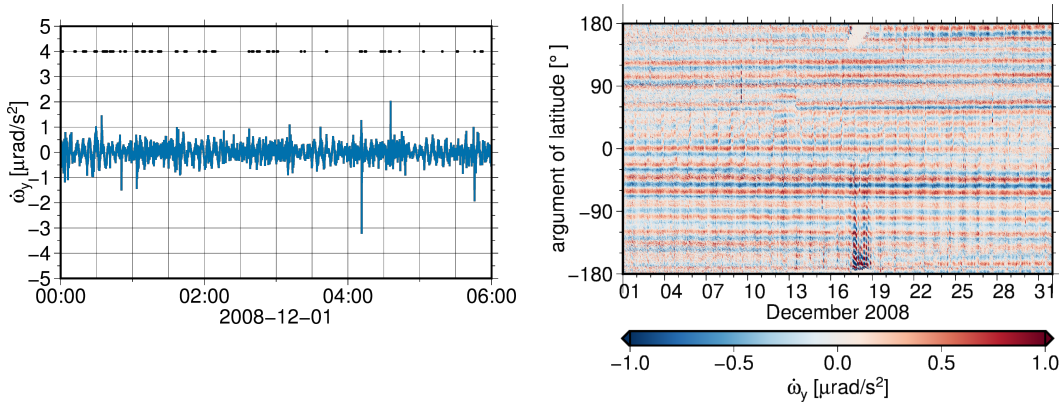

(b) $\dot{\omega}_y$

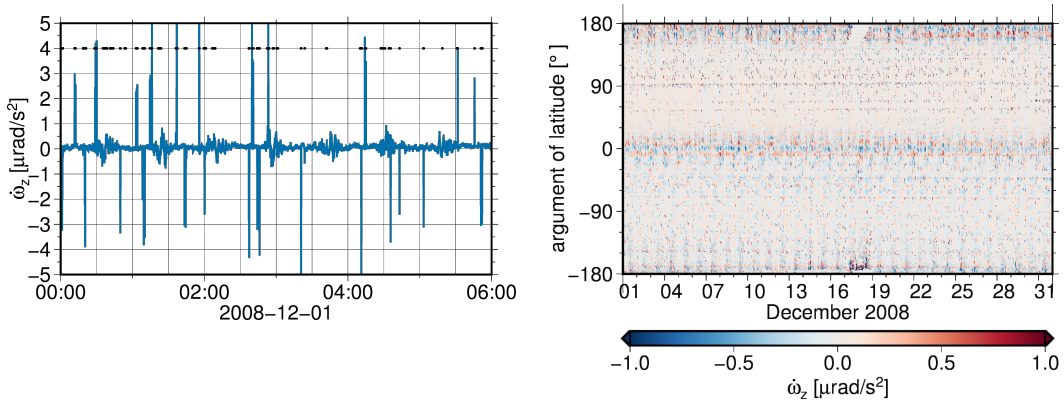

(c) $\dot{\omega}_z$

Fig. 5.12.: Angular accelerations about the along-track (a), across-track (b), and radial (c) axis for GRACE-A recovered from the Level-1B RL02 data products (ACC1B). The left column shows the angular accelerations (blue) for a selected 6 h interval on 2008-12-01. The black dots indicate epochs with thruster firings. The left column shows the angular accelerations along the orbit for GRACE-A for the whole month (December 1008). Note that here bias-corrected angular accelerations are shown.

controlled by the cold-gas thrusters. Whereas, the rotations about the cross-track axis are controlled by the magnetic torquers instead. From the rotations about the cross-track axis (cf. Fig. 5.12(b)), the typical latitude-dependent pointing jitter (pitch variations) also becomes visible (cf. Section 6.1.2). The magnitude of the angular accelerations is largest for the rotations about the along-track axis.

Data availability

In October 2016, the accelerometer on-board GRACE-B was permanently powered-off to reduce the stress on the remaining battery cells (cf. Section 2.6). Since then, no GRACE-B accelerometer data is available (except for May 2017). To allow for gravity field recovery, the GRACE-B accelerometer data needs to be replaced by synthetic accelerometer data, the so-called transplant data (Bandikova et al., 2017).

The synthetic accelerometer transplant data - replacing the missing GRACE-B accelerometer measurements - is recovered from the GRACE-A accelerometer measurements by applying a time and attitude correction. The GRACE accelerometer data transplant is possible because both satellites fly in the same orbit and have a time delay of approximately 25 seconds due to the spacecraft separation. Therefore, the change in the non-gravitational accelerations during this time delay is very small, and both accelerometers should measure approximately the same signal. The time and attitude correction, which is applied to the GRACE-A accelerometer measurements, appropriately accounts for both the variable separation between the two spacecrafts and the orientation differences relative to each other. The inclusion of the modeling of residual linear accelerations due to thruster firings additionally improves the quality of the transplanted data (Bandikova et al., 2017). To further improve the accelerometer transplant solution, the angle of attack difference between the two spacecrafts was removed in April 2017. By removing the pitch offset, i.e. changing the pitch offset from 1° to 0°, the differences in the non-gravitational accelerations due to atmospheric drag can be minimized. However, this also led to increased noise in the KBR range corrections (cf. Section 6.3.5). For a detailed description of the accelerometer data transplant procedure, the reader is referred to e.g., Bandikova et al. (2017) and Kruizinga et al. (2017).

Temperature variations

The AHK1B housekeeping data product (cf. Section 2.5.2) provides information about the onboard temperature variations. From this data it becomes obvious, that since April 2011 the temperature variations are highly correlated to the orbital configuration w.r.t. the Sun (cf. Fig. D.2). This behavior is illustrated in Figure 5.13, showing the GRACE-A core-temperature variations (AHK1B), the β' angle variations, and the illumination of the side panels (starboard, port) by the Sun for the year 2012. Details on the computation of the incident angle $\cos(\theta)$ are given in Section 3.3. If the surface element is not illuminated by the Sun, $\cos(\theta)$ becomes zero. If the incident radiation is perpendicular to the surface normal, $\cos(\theta)$ becomes one. For periods with maximum β' angles, causing a permanent and near-perpendicular illumination of one of the side panels, the temperature increases accordingly (cf. Figs. 5.13(a), 5.13(c), and 5.13(d)). The β' angle maxima occur with a period of ~ 160 days (cf. Appendix D.2), causing temperature variations with the same periodicity.

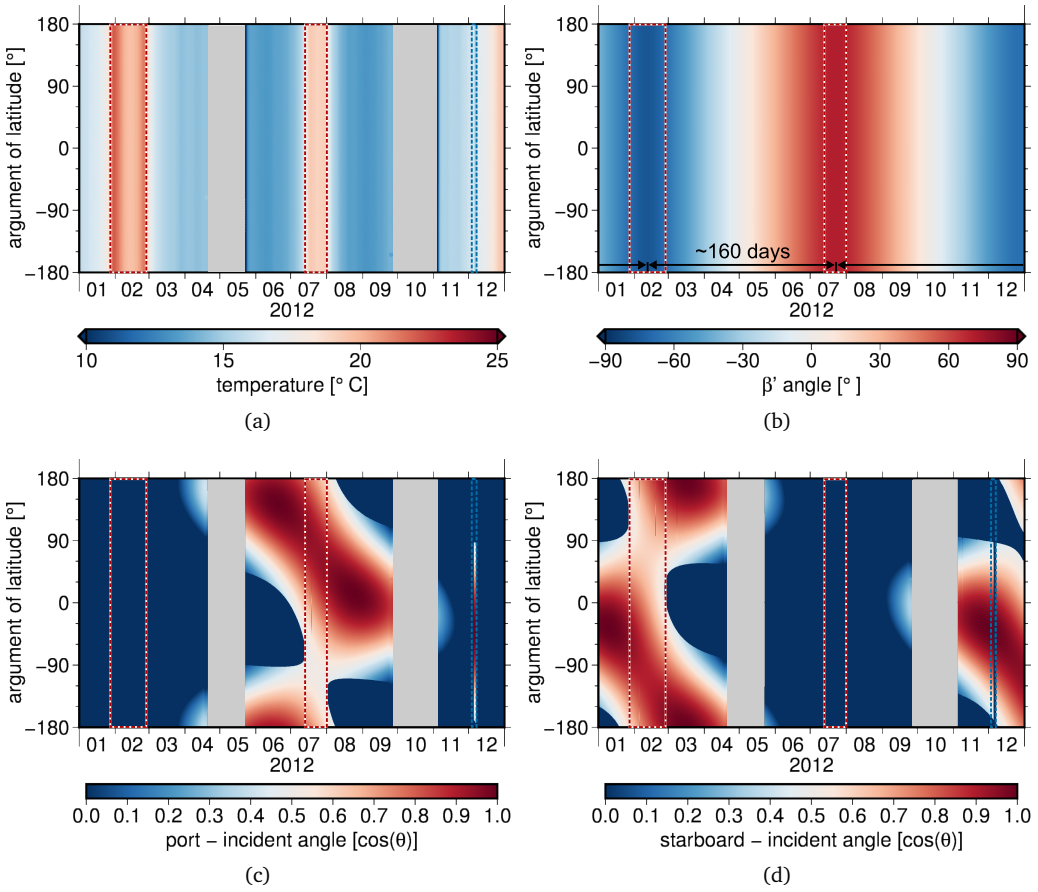

Fig. 5.13.: (a) Accelerometer core temperature variations (AHK1B), (b) β' angle variations, and (c,d) incident angles ($\cos(\theta)$) of solar radiation for the port and starboard panel along the orbit for GRACE-A for the year 2008. The β' angle variations and incident angles are recovered based on Level-1B RL02 data products (GNV1B, SCA1B) and the GRACE Macro Model. Note that gray areas (a,c,d) correspond to data gaps due to the shut-down of KBR and ACC for small β' angles. The red-dashed boxes highlight time periods with temperature maxima, and the blue-dashed box highlights a yaw turn maneuver on 2012-12-07 (cf. Section 4.3.2).

Attitude determination - Sensor fusion

6

For GRACE, the precise knowledge of the satellite's attitude and the associated attitude data processing are not only essential for the realization and maintenance of the precise in-orbit inter-satellite pointing, but also for the fulfillment of the mission goals, i.e. the recovery of accurate temporal gravity field models of the Earth.

One of the main objectives of this work is to improve the official Level-1B RL02 attitude data product by combining Level-1B star camera and angular accelerometer data. This combination approach - hereafter simply denoted as sensor fusion - will be extensively discussed and analyzed within this Chapter. For the presented results and analysis, a detailed understanding of the GRACE star cameras and angular accelerations is essential. Therefore, Sections 5.1 and 5.2 give an overview of the measurement principle and performance characteristics of both instruments.

The following Sections give an overview of the GRACE attitude determination, and outline the sensor fusion approach applied to improve the official Level-1B RL02 attitude data product (SCA1B). Section 6.1 discusses the characteristics of the GRACE attitude determination in more detail, and highlights the importance of the precise inter-satellite pointing for the KBR ranging observations. Besides, the representation of inter-satellite pointing variations in terms of attitude angles is presented. Section 6.2 discusses the shortcomings of the current RL02 attitude data product with respect to the data combination, possible pointing biases, and the benefits of incorporating additional attitude information. Section 6.3 introduces the sensor fusion approach, including details on the data combination. Furthermore, the results and their impact on the KBR ranging and accelerometer are analyzed. Finally, in Section 6.4 further options for the GRACE attitude data processing are outlined.

6.1 Characteristics of the attitude determination

The precise inter-satellite pointing is a fundamental requirement for the realization of the KBR inter-satellite ranging, which represents the primary observation technique of GRACE. Thus, the maintenance of the alignment is one of the major challenges of the mission operations in order to meet the pointing requirements. The spacecraft's attitude is permanently perturbed by both internal and external disturbing torques. The attitude determination and control is performed by the AOCS (cf. Section 2.3.2), which is responsible for the recovery of the orientation of the GRACE spacecrafts from sensor measurements, as well as for maintaining and adjusting the satellite's attitude with the help of the on-board thrusters and torquers. The AOCS also enables the performance of satellite maneuvers under a controlled environment. These maneuvers, including calibration maneuvers, satellite swap maneuvers, and battery-management maneuvers (cf. Section 4.3.2), are fundamental for a successful mission operation, and in the case of GRACE also for an effective mission

prolongation. Depending on the operation mode, the absolute orientation of the spacecraft is determined with respect to the Earth, the Sun, the Earth's magnetic field or the stars (Herman et al., 2004). During science mode (SM), when science data for the gravity field recovery is collected and the precise inter-satellite pointing has to be maintained, the absolute orientation of the GRACE spacecrafts with respect to the inertial frame is sensed by the two star cameras on-board each satellite. The star cameras are the most important attitude determination sensors on-board GRACE, since they provide accurate information about the spacecraft's instantaneous attitude (cf. Section 5.1).

Besides the in-orbit alignment of the GRACE satellite, the precise information on the satellite's attitude is also a key element for the scientific data processing of both KBR ranging and accelerometer observations. Since these observations are directly used as input data for the gravity field recovery (cf. Section 4), any imperfections in the alignment or systematic errors within the attitude data propagate directly to the recovered gravity field models. Thus, any improvements within the on-ground determination of the inter-satellite pointing will contribute to the overall accuracy of the recovered gravity field solutions. The on-ground attitude determination includes not only the Level-1A to Level-1B star camera data processing, but also the derivation of geometric corrections from the star camera observations for the KBR ranging data. In the following, the importance of the precise inter-satellite pointing for the KBR processing is discussed.

Details on the on-board attitude determination and control system, as well as on the differences between on-board and on-ground attitude determination can be found in e.g., Bandikova (2015). This thesis concerns the Level-1B star camera data product, and thus only discusses the on-ground attitude determination during data post-processing.

6.1.1 Inter-satellite pointing - Effects on KBR ranging

As previously mentioned, the precise inter-satellite pointing or exact alignment of the GRACE satellites is an essential prerequisite for the KBR inter-satellite ranging (cf. Sections 2.2.1 and 2.2.2), which provides the primary observations for gravity field recovery. In the case of an ideal alignment, the line joining one satellite's CoM with its KBR antenna phase center (APC) would exactly point to the twin satellite's CoM (cf. illustration of non-ideal alignment in Fig 6.1). During SM, the AOCS maintains the GRACE satellites close to the state of ideal alignment (Arbinger et al., 2003; Herman et al., 2004).

The KBR ranging observations (biased range, range rate, range acceleration) are originally related to the KBR APCs, i.e. the system measures the range between the two antenna phase centers (cf. Fig. 6.1). However, for the purpose of gravity field recovery, the distance between the two satellites' CoMs needs to be obtained.

Antenna Offset Correction

To convert the original ranging observation to a distance between the two satellites' CoM, a geometric correction, often denoted as antenna offset correction (AOC; cf. Eq. (2.1)), has to be added. The AOC directly depends on the inter-satellite alignment (Case et al., 2010), and corrects for both the offset of the KBR antenna phase center from the CoM, and for the imperfect inter-satellite pointing. This dependency is illustrated in Figure 6.1.

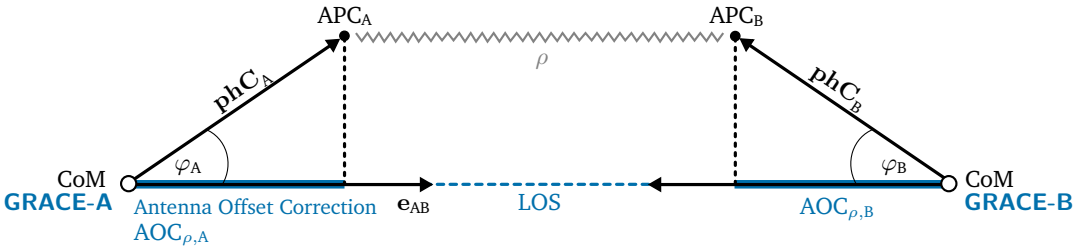

Fig. 6.1.: Illustration of the geometric antenna offset correction (AOC; blue) for the measured range ρ (gray). The components for both GRACE satellites are shown: AOC$_{\rho,A}$ and AOC$_{\rho,B}$.

The total AOC consists of the two components: AOC$_A$ for GRACE-A, and AOC$_B$ for GRACE-B (cf. Fig. 6.1). Geometrically, the AOC for the range (AOC$_\rho$) can be interpreted as the projection of both phC vectors ($\mathbf{phC}_A, \mathbf{phC}_B$) on the LOS

$$\begin{aligned} \text{AOC}_\rho &= \text{AOC}_{\rho,A} + \text{AOC}_{\rho,B} \\ &= \mathbf{phC}_A \cos\varphi_A + \mathbf{phC}_B \cos\varphi_B. \end{aligned} \tag{6.1}$$

Therein, φ denotes the misalignment angle, representing the angle between the phC and LOS vector. During SM, this angle is kept within a threshold of a few milliradians (Herman et al., 2004). The misalignment angle φ directly depends on the pitch (θ), and yaw (ψ) angle. The attitude angles (roll, pitch, yaw) can be computed from GRACE Level-1B data products as described in the subsequent Section (cf. Section 6.1.2). According to the spherical law of cosines, the misalignment angle φ can be expressed by:

$$\cos\varphi = \cos\theta \cdot \cos\psi. \tag{6.2}$$

For each satellite, the correction is calculated by first transforming the phC vector from the SRF to the inertial frame (IRF), and then evaluating the inner product with the LOS vector ($\mathbf{e}_{AB}$), which is given in the IRF, pointing from one CoM to the other satellites CoM. Consequently, the total AOC for the range is obtained by

$$\text{AOC}_\rho = \underbrace{\mathbf{e}_{AB} \cdot (\mathbf{R}^{IRF}_{SRF,A}\mathbf{phC}_A)}_{\text{AOC}_{\rho,A}} - \underbrace{\mathbf{e}_{AB} \cdot (\mathbf{R}^{IRF}_{SRF,B}\mathbf{phC}_B)}_{\text{AOC}_{\rho,B}}, \tag{6.3}$$

where $\mathbf{e}_{AB}$ represents the normalized LOS vector (derived from GNV1B), and $\mathbf{R}^{IRF}_{SRF}$ denotes the rotation matrix from SRF to IRF (given by SCA1B). The phc vector (given by VKB1B) has a length of approximately ~ 1.47 m, i.e. the APC is mounted in a distance of ~ 1.47 m from the satellites COM (cf. Fig. 6.1).

The antenna offset corrections (AOCs) for the range rates (AOC$_{\dot\rho}$) and range accelerations (AOC$_{\ddot\rho}$) represent the time derivatives of the geometric range correction (AOC$_\rho$), and are obtained by numerical differentiation

$$\text{AOC}_{\dot\rho} = \frac{d}{dt}\text{AOC}_\rho, \tag{6.4}$$

$$\text{AOC}_{\ddot\rho} = \frac{d^2}{dt^2}\text{AOC}_\rho = \frac{d}{dt}\text{AOC}_{\dot\rho}. \tag{6.5}$$

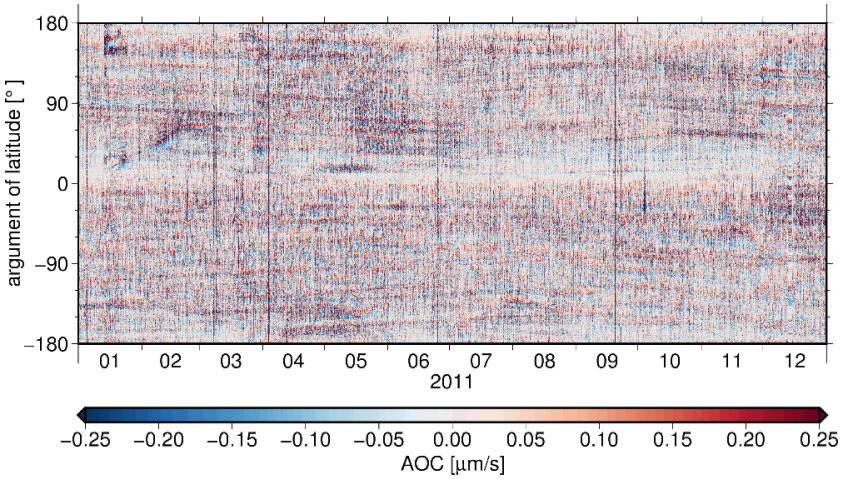

Fig. 6.2.: GRACE KBR AOCs for range rates, derived from the KBR1B data product, plotted along the orbit for the year 2011.

The values for the AOC_{ρ} are in the range of 2.95 m, due to the APC offset from the COM. The values for the $AOC_{\dot{\rho}}$ and $AOC_{\ddot{\rho}}$ are in the range of $\pm 0.5\ \mu m/s$ and $\pm 0.2\ \mu m/s^2$, respectively.

The KBR AOCs for the ranges, range rates and range accelerations are provided within the Level-1B KBR data product (KBR1B; cf. Section 2.5) (Case et al., 2010). During Level-1A to Level-1B processing, precise geometric information is used to compute the geometric correction for the KBR data. Following Equation (6.3), the AOCs for each satellite can be computed based on three inputs: (1) the satellite positions (GNV1B), (2) the CoM-to-APC vector ($\mathbf{phC}$) with respect to the SRF (VKB1B), (3) and the inertial orientation of the satellite (SCA1B).

Figure 6.2 shows AOCs for range rates ($AOC_{\dot{\rho}}$), recovered from the KBR1B data product, for one year (2011). Obviously, the AOCs are subject to systematic effects (e.g., striping pattern), which are a result of systematics contained within the inter-satellite pointing variations (cf. Fig. 6.3). These effects are further discussed in Section 6.1.2. Reproducing the geometric range rate corrections according to Equations (6.3) and (6.5) using the GNV1B orbits, VKB1B phC vector, and SCA1B quaternions, results practically in the same corrections as those contained in the KBR1B data product (not shown here).

Any systematic errors present in the attitude data (SCA1B) and/or phC vector (VKB1B), directly affect the accuracy of the KBR ranging observations through the AOCs. In addition, the attitude data is also needed for the rotation of the accelerometer data product (ACC1B) from the SRF to the IRF. Thus, alignment errors not only directly affect the KBR observations, but also indirectly affect the ACC observations (cf. Section 6.3.6). These two effects on the GRACE observations may in turn affect the accuracy of the recovered gravity field solutions.

6.1.2 Inter-satellite pointing - Attitude angles

The most intuitive and common way to describe the attitude or rotation of a satellite is to use Cardan angles: roll, pitch, and yaw (cf. Appendix D.1). Roll (ϕ), describes the

rotation around the x-axis, which corresponds here to the along-track direction. Yaw (ψ), describes the rotation around the z-axis, corresponding to the radial direction, which is perpendicular to the horizontal plane of the satellite. Pitch (θ), describes the rotation around the cross-track axis, which completes the right-handed system. For GRACE, the inter-satellite pointing variations can be geometrically interpreted as angular deviations of the KBR phC vector from the LOS (cf. Fig. 6.1), expressed in terms of roll, pitch, and yaw rotation angles (cf. Bandikova et al., 2012).

Roll, pitch, yaw

Per definition, the phC vector, joining the CoM with the KBR APC, coincides with the x-axis of the KBR frame (KF), and the LOS coincides with the x-axis of the LOS frame (LOSF) (cf. Appendix A). Therefore, roll, pitch and yaw attitude angles can be derived from the matrix rotating the KF to the LOSF, which is obtained by

$$\mathbf{R}_{\mathrm{KF}}^{\mathrm{LOS}} = \mathbf{R}_{\mathrm{IRF}}^{\mathrm{LOS}} \left(\mathbf{R}_{\mathrm{IRF}}^{\mathrm{KF}}\right)^{\mathsf{T}}. \tag{6.6}$$

The pointing variations represented by Equation (6.6), can be expressed as a sequence of rotations

$$\mathbf{R}_{\mathrm{KF}}^{\mathrm{LOS}} = \mathbf{R}_1(\phi)\mathbf{R}_2(\theta)\mathbf{R}_3(\psi), \tag{6.7}$$

where $\mathbf{R}_i$ $(i = 1, 2, 3)$ represents elementary rotations about the roll (x), pitch (y), and yaw (z)-axis, respectively. Thus, the roll (ϕ), pitch (θ), and yaw (ψ) attitude angles can be directly derived from the elements of the $\mathbf{R}_{\mathrm{KF}}^{\mathrm{LOS}}$ matrix (cf. Eq. (D.1))

$$\begin{aligned} \phi &= \arctan\left(\frac{R_{23}}{R_{33}}\right), \\ \theta &= -\arcsin(R_{13}), \\ \psi &= \arctan\left(\frac{R_{12}}{R_{11}}\right), \end{aligned} \tag{6.8}$$

where R_{ij} denotes the matrix elements, with the indices i, j referring to the rows and columns of the matrix.

Following from Equation (6.6), the recovery of the attitude angles from the GRACE Level-1B data products is done in three subsequent steps: (1) expressing the phC vector in the SRF (VKB1B), (2) rotating the SRF to the IRF (SCA1B), and (3) rotating the IRF to the LOSF (GNV1B). From the resulting rotation matrix $\mathbf{R}_{\mathrm{KF}}^{\mathrm{LOS}}$, representing the rotation from the KF into the LOS frame (cf. Eq. (6.6)), the attitude angles can be derived according to Equation (6.8). In the following, the representation of the underlying $\mathbf{R}_{\mathrm{IRF}}^{\mathrm{KF}}$ and $\mathbf{R}_{\mathrm{IRF}}^{\mathrm{LOS}}$ matrices are explained in more detail.

Based on the inertial orientation of the spacecraft, and the alignment of the phC within the SRF, the matrix rotating the IRF into the KF can be obtained as follows (cf. Appendix A.5)

$$\mathbf{R}_{\mathrm{IRF}}^{\mathrm{KF}_j} = \begin{bmatrix} \mathbf{x}_{\mathrm{KF}_j}^{\mathsf{T}} \\ \mathbf{y}_{\mathrm{KF}_j}^{\mathsf{T}} \\ \mathbf{z}_{\mathrm{KF}_j}^{\mathsf{T}} \end{bmatrix} = \begin{bmatrix} \left(\left(\mathbf{R}_{\mathrm{IRF}}^{\mathrm{SRF}_j}\right)^{\mathsf{T}} \dfrac{\mathbf{phC}}{|\mathbf{phC}|}\right)^{\mathsf{T}} \\ \left(\mathbf{z}_{\mathrm{KF}_j} \times \mathbf{x}_{\mathrm{KF}_j}\right)^{\mathsf{T}} \\ \left(\mathbf{x}_{\mathrm{LOS}_j} \times \mathbf{y}_{\mathrm{SRF}_j}\right)^{\mathsf{T}} \end{bmatrix}, \tag{6.9}$$

where the index $j = \text{A, B}$ refers to GRACE-A or GRACE-B. The vector $\mathbf{phC}$ represents the KBR phC vector with respect to the SRF, provided by the VKB1B data product. The information about the inertial orientation of the GRACE spacecrafts is provided by the SCA1B data product, containing the attitude of the SRF with respect to the IRF in terms of quaternions. Thus, the matrix rotating the SRF to the IRF is given by (cf. Appendix C)

$$\mathbf{R}_{\text{SRF}}^{\text{IRF}} = \begin{bmatrix} q_0^2 + q_1^2 + q_2^2 + q_3^2 & 2(q_1 q_2 - q_0 q_3) & 2(q_1 q_3 + q_0 q_2) \\ 2(q_1 q_2 + q_0 q_3) & q_0^2 - q_1^2 + q_2^2 - q_3^2 & 2(q_2 q_3 - q_0 q_1) \\ 2(q_1 q_3 - q_0 q_2) & 2(q_2 q_3 + q_0 q_1) & q_0^2 - q_1^2 - q_2^2 + q_3^2 \end{bmatrix}. \tag{6.10}$$

In order to derive the instantaneous LOS vector ($\mathbf{x}_{\text{LOS}}$), joining the two satellites COMs, the positions of both satellites witch respect to the IRF (provided by GNV1B) are needed. Based on the inertial positions, the matrix rotating the IRF into the LOSF can be obtained by (cf. Appendix A.6)

$$\mathbf{R}_{\text{IRF}}^{\text{LOS}_j} = \begin{bmatrix} \mathbf{x}_{\text{LOS}_j}^\intercal \\ \mathbf{y}_{\text{LOS}_j}^\intercal \\ \mathbf{z}_{\text{LOS}_j}^\intercal \end{bmatrix} = \begin{bmatrix} \left(\dfrac{\mathbf{r}_i - \mathbf{r}_j}{|\mathbf{r}_i - \mathbf{r}_j|} \right)^\intercal \\ \left(\mathbf{x}_{\text{LOS}_j} \times \dfrac{\mathbf{r}_\text{A}}{|\mathbf{r}_\text{A}|} \right)^\intercal \\ \left(\mathbf{x}_{\text{LOS}_j} \times \mathbf{y}_{\text{LOS}_j} \right)^\intercal \end{bmatrix}, \tag{6.11}$$

where parameters with the indices $i, j = \text{A, B}$ $(i \neq j)$ refer to GRACE-A or GRACE-B, and the vector $\mathbf{r}$ represents the position of one satellite w.r.t. the IRF.

For GRACE, the inter-satellite pointing requirements are defined by deadbands, defining the maximum allowed angular deviation of the phC vector relative to the LOS. Originally, the deadbands were set to 3 mrad for roll and pitch, and 4 mrad for yaw, during SM. The value of the yaw deadband was changed repeatedly during the mission lifetime. In January 2012, it was set to 5.4 mrad and 5.2 mrad for GRACE-A and GRACE-B, respectively (Herman and Steinhoff, 2012). The aim of the AOCS is to keep the variations of the inter-satellite pointing as small as possible by continuously aligning the phC vector with the LOS vector. This keeps the geometric error within the KBR measurements as small as possible.

Figure 6.3 shows inter-satellite pointing variations expressed in terms of roll, pitch, and yaw attitude angles, derived from Level-1B data products for GRACE-A. For the attitude angles, two different representations are shown: (1) a time series of a 6 hour interval ($\sim$ 4 orbital revolutions), and (2) a plot of the attitude angles along the orbit for a time period of one month (December 2008). Since the pointing variations for both satellites show a similar behavior, the analysis is restricted to GRACE-A. From Figure 6.3 it becomes obvious, that the pointing variations are kept within the deadbands, if the non-zero mean values are reduced. Possible reasons for the occurrence of pointing biases are further discussed in Section 6.2.2.

There are systematic effects visible within the roll, pitch, and yaw attitude angles, which are different for all three axes (cf. Figs. 6.3(a), 6.3(b), and 6.3(c)). The most prominent effect is the GRACE associated pointing jitter, which becomes visible within the pitch angle variations, and is related to the attitude sensors and actuators used for the AOCS. The very regular horizontal striping in Figure 6.3(b) is caused by systematic oscillations (around 3.3 mHz) related to the dominant frequency of the magnetic torquer rods (Bandikova,

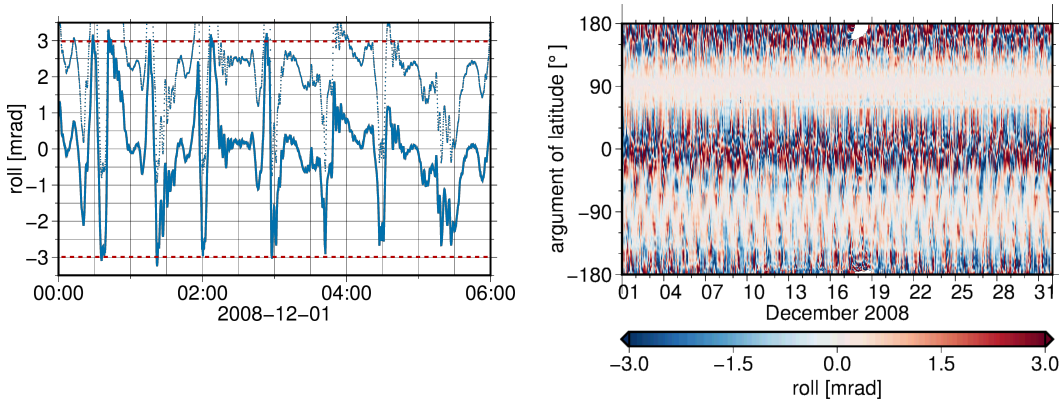

(a) roll (ϕ)

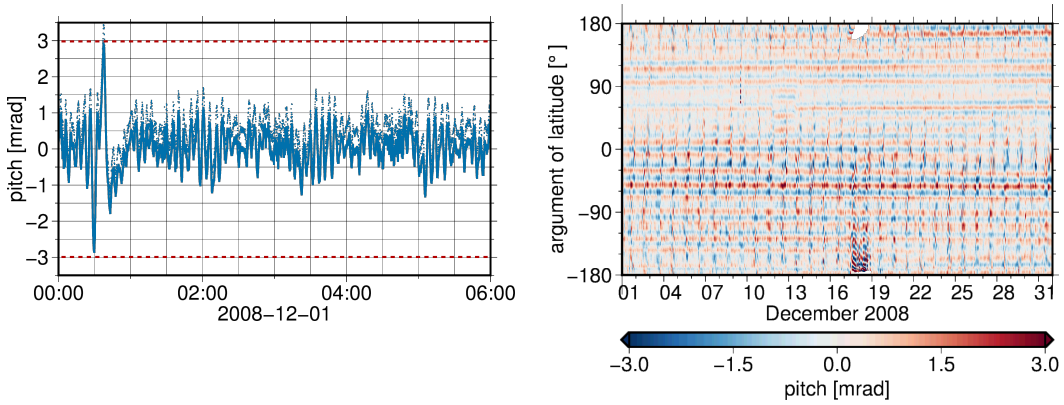

(b) pitch (θ)

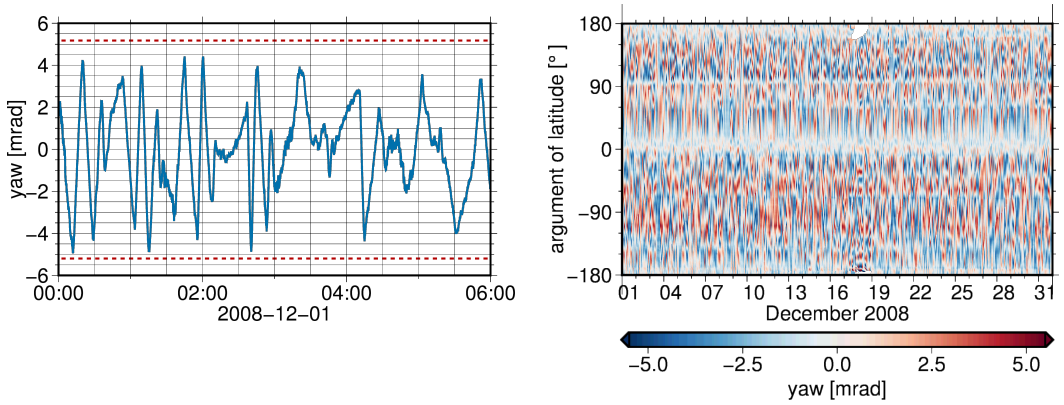

(c) yaw (ψ)

Fig. 6.3.: Roll (a), pitch (b), and yaw (c) attitude angles for GRACE-A recovered from the Level-1B RL02 data products (SCA1B, GNV1B). The left column shows the attitude angles (blue) and the corresponding deadbands (red) for a 6 h interval on 2008-12-01. Note that for the roll and pitch angle the mean value was subtracted (solid line), since the original (dashed line) do not have a zero mean value. The right column shows the attitude angles along the orbit for GRACE-A for the whole month (December 2008).

2015). Consequently, these variations are not caused by geophysical phenomena, but rather by on-board electronics and/or sensors. Additionally, irregular variations at specific geographical locations are reflected in Figure 6.3(b), i.e. stronger variations for the ascending orbit around $-60°$ (cf. Appendix D.3). If long time series of pitch variations are analyzed (cf. Fig. 6.14), different systematics related to star camera head switches or blindings, CoM calibration maneuvers, disabling of supplemental heater lines, etc. become visible as well (Bandikova, 2015). The pointing jitter is not clearly visible within the roll and yaw variations (cf. Fig. 6.3(a) and 6.3(c)). Due to the orientation of the torquer rods w.r.t. to the magnetic field, the roll and yaw alignment is mainly controlled by thruster activations. The attitude control with thrusters is not as smooth as with magnetic torquers. Therefore, the pointing variations become larger, except for regions where the magnetic torquer rods sufficiently control the attitude (roll: over the poles, yaw: equator; cf. Figs. 6.3(a) and 6.3(c)).

6.2 Shortcomings of the attitude determination

6.2.1 SCA1B data product

As shown by Bandikova and Flury (2014), the GRACE SCA1B RL02 data product contains a systematically higher noise level than expected (cf. Fig. 5.6). The high noise level results from a software bug within the Level-1A to Level-1B processing, i.e. the star camera head combination is implemented incorrectly within the JPL processing routines. Due to this software bug, the noise suppression for the weak axes is invalid, resulting in high frequency noise due to the sub-optimal combination of the star camera data. By implementing the correct algorithm within Level-1A to Level-1B processing, the SCA1B data noise is reduced, but no significant improvements were found in the CSR monthly gravity field solutions (Kruizinga et al., 2015).

Harvey (2016) showed that, apart from the incorrect star camera head combination, also the stellar aberration correction was implemented incorrectly. This error is already part of the Level-1A data products, since the on-board software uses Earth Center Fixed coordinates instead of inertial coordinates, resulting in a twice per revolution stellar aberration error with a sidereal day modulation. During nominal spacecraft science operations, the use of corrected SCA1B data products does not seem to have a significant effect on the recovered gravity field solutions (of the official processing centers) (Kruizinga et al., 2017).

Another feature visible within the SCA1B data product, are jumps or discontinuities at transitions from dual star camera operation (combined solution) to single star camera operation (single head solution) and vice versa (cf. Fig. 6.12), due to direct Sun and/or Moon intrusions (Ko et al., 2015; Bandikova, 2015). These jumps are caused by the different performance of the two star camera heads, but remain untreated within the SCA1B RL02 data product.

Apart from these processing errors, changes within the short-term and long-term stability of the alignment, as well as temperature variations, also might cause errors within the SCA1B data products. The current quality of the star cameras also seems to limit the phC (VKB1B) and inter-boresight (QSA) alignment determination.

The studies by e.g., Bandikova and Flury (2014), Inácio et al. (2015), and Harvey (2016) became key impulses for the JPL to initiate a currently ongoing GRACE Level-1B data re-processing campaign (cf. Section 6.2.3), aiming at improving the attitude data processing (RL03 SCA1B).

6.2.2 KBR1B data product - Inter-satellite pointing bias

As shown by Horwath et al. (2011), the inter-satellite pointing angles recovered from Level-1B RL01 data products (SCA1B, GNV1B, VK1B; cf. Section 6.1.2) were characterized by a non-zero mean value, i.e. contain a systematic bias. These pointing biases directly affects the KBR1B AOCs, as the AOC is obtained by a projection of the phC vector (VKB1B) on the LOS. Thus, the length of the AOC directly depends on the pointing angles, i.e. larger angles result in shorter AOC, whereas smaller angles result in a longer AOC (cf. Fig. 6.4). Horwath et al. (2011) demonstrated by his study that the biased AOCs significantly degrade the recovered gravity field solution. As a consequence, JPL re-estimated the calibration parameters related to the star cameras and the KBR APCs in 2011, resulting in improved Level-1B RL02 data products.

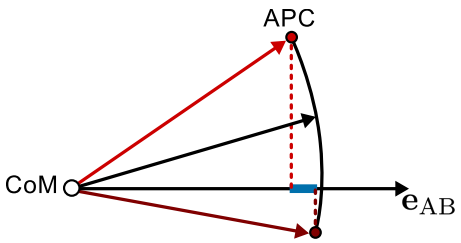

Fig. 6.4.: Illustration of the effect of a pointing bias on the length of the antenna offset correction (AOC).

The bias contained within the pointing angles derived from the Level-1B RL02 data products is significantly reduced (compared to RL01, Bandikova, 2015), but still exists with its sources still remaining unknown (cf. Fig. 6.3). Performing a re-estimation of the star camera and KBR calibration parameters (QSA, QKS, VKB) based on an improved attitude data product (e.g., RL03), might result in improved results further minimizing the pointing bias. Another possibility is to co-estimate the phC vector during gravity field recovery.

6.2.3 Attitude improvement

Theoretically, the GRACE attitude data product (SCA1B) can be improved by incorporating additional attitude information provided by other on-board sensors, such as the accelerometer or the Inertial Measurement Unit (IMU). However, the IMU on-board GRACE-A failed directly after the launch of the satellites, and the IMU on-board GRACE-B is switched-off at almost all times. Therefore, for GRACE only the combination based on star camera and accelerometer data is feasible. Based on this idea, the sensor fusion approach was introduced within the ITSG processing chain, as part of the Level-1B data pre-processing (Klinger and Mayer-Gürr, 2014). The sensor fusion and its impact on the ACC and KBR observations are extensively discussed in Section 6.3. Furthermore, its impact on the recovered gravity field is analyzed in Section 8.2.

Prior to the sensor fusion approach (Klinger and Mayer-Gürr, 2014), the combination of star camera and accelerometer data was already tested by Frommknecht (2008). The combination was performed on the level of angular rates by using low-pass filtered star camera, and high-pass filtered accelerometer data (with a cut-off frequency of $3 \cdot 10^{-2}$ Hz). A similar method was implemented for the combination of GOCE star camera and gradiometer data, based on the combination by means of Wiener filtering (Stummer et al., 2011; Stummer, 2012).

According to Kruizinga et al. (2016), the SDS decided to change the official SCA1B algorithm in order to combine star camera and angular accelerometer data using a Kalman filtering approach (Bandikova et al., 2016; Sakumura et al., 2016). SDS has implemented a similar approach (Precision Attitude Determination) already in 2004 and also observed a reduction in high frequency noise in the SCA1B data product. However, CSR observed degraded gravity fields using the updated SCA1B data product, resulting in a rejection of this approach back then (Kruizinga et al., 2015). The RL03 Level-1B data products, which are currently being re-processed, will include re-processed SCA1B and KBR1B data products. For the KBR1B data products only the derived KBR range corrections (AOCs) will be changed. In addition to the star camera and accelerometer data combination, known processing errors within the current RL02 SCA1B data products should be fixed (cf. Bandikova and Flury, 2014; Harvey, 2016). Additionally, the SCA1B data product will have a higher data sampling (1 Hz instead of 0.2 Hz) (Kruizinga et al., 2016). The re-processed RL03 Level-1B data products are expected to be released at the time when the RL06 gravity products of the official processing centers (CSR, GFZ, JPL) are released. Initial assessments showed that the high frequency noise within the SCA1B RL03 data product is significantly reduced, and an improved attitude reconstruction for single camera operations could be achieved. These improvements result in slightly improved JPL gravity field solutions (Bandikova et al., 2016; Kruizinga et al., 2016; Sakumura et al., 2016). Thus, only minor effects on the gravity field solutions are expected. A complete re-processing of the Level-1B data products (RL04) will be done after the decommissioning of the GRACE mission.

6.3 Improved attitude determination - Sensor fusion

Until recently, the attitude determination and the alignment between the two GRACE satellites during SM were carried out solely by the two star cameras on-board each satellite. Originally, the official Level-1A to Level-1B processing described in Wu et al. (2006) did not envisage the combination of star camera and accelerometer data to derive a combined attitude data product. But, the accelerometer provides in addition to the measured linear accelerations also relative attitude information in terms of angular accelerations (cf. Section 5.2). Therefore, the basic idea is to incorporate this additional information within the attitude estimation. By combining both Level-1B star camera and angular accelerometer data (SCA1B, ACC1B) in a LSA, the attitude estimation can be further improved. This approach, schematically depicted in Figure 6.5, is denoted as sensor fusion approach.

However, some limitations occur, since already pre-processed Level-1B data products are used as input for the senor fusion - the combined attitude estimation. Errors or noise present within the ACC1B and SCA1B data products due to incorrect data processing (cf. Section 6.2)

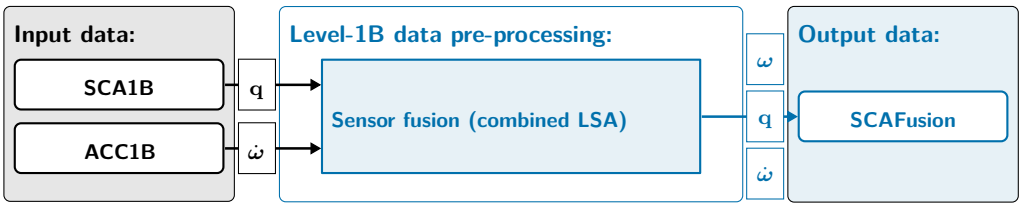

Fig. 6.5.: Schematic overview of the sensor fusion approach: combination of accelerometer (ACC1B) and star camera (SCA1B) data.

cannot be eliminated by combining both data sets. Yet, the high-frequent noise of the SCA1B data product can be reduced significantly (cf. Section 6.3.4 and 6.3.5).

As output of the sensor fusion approach, a combined attitude data product, hereafter denoted as SCAFusion, is derived (cf. Fig. 6.5). Analysis of the combined SCAFusion data product in both the temporal and the frequency domain demonstrate the potential of the sensor fusion approach in reducing the high-frequent attitude noise. Based on the combined SCAFusion data product, the geometric corrections (AOCs; cf. Section 6.1.1) added to the ranging observations of the KBR1B data product can be re-computed. Additionally, the attitude information is also needed to rotate the linear accelerometer measurements from the SRF to the IRF during gravity field recovery. Therefore, also the indirect effects on the GRACE KBR1B and ACC1B data products, used for gravity field recovery, are analyzed in detail (cf. Sections 6.3.5 and 6.3.6).

6.3.1 Sensor fusion approach

In general, the sensor fusion approach is based on the combination of GRACE Level-1B star camera and accelerometer data on the attitude level (quaternions). The SCA1B data product provides information about the satellites orientation w.r.t. inertial frame in terms of attitude quaternions (cf. Section 5.1.3, cf. Appendix C). The ACC1B data product provides angular accelerations, containing relative attitude information in terms of rates of change of the angular velocity (cf. Section 5.2.3). This gives information about the rotation changes about the SRF axes. However, the angular accelerations provided by the ACC1B data product contain an unknown bias and thus need to be calibrated. The rotational part of the satellites motion, represented by the angular velocity and the angular acceleration, can also be derived by numerical differentiation from the inertial attitude provided by the star camera data (cf. Appendix C.2.8). Therefore, the derived star camera angular accelerations can be used for the calibration of the accelerometer data, i.e. for the bias estimation.

The combination benefits from the different noise characteristics of the star camera and angular accelerometer data (cf. Sections 5.1.2 and 5.2.2). This becomes most evident, it the two data sets are compared on the level of angular accelerations (cf. Fig. 6.11). Due to the incorrect combination of the two star camera heads, the noise of the less accurate boresight component unfavorably propagates to $\dot{\omega}_y$ and $\dot{\omega}_z$ in the SRF due to the reference frame transformation (from SCF to SRF)(cf. Fig. 5.6(a)). For this reason the angular accelerations derived from SCA1B data are characterized by two less-sensitive axes w.r.t. the SRF (y, z). Whereas, the ACC1B angular accelerations are characterized nominally by one sensitive axis

w.r.t. the SRF ($\dot{\omega}_y$). But in direct comparison with the angular accelerations derived from SCA1B data, they contribute to both axes ($\dot{\omega}_y, \dot{\omega}_z$, cf. Fig. 6.11).

The combination of both observation types (quaternions, angular accelerations) is achieved by means of a LSA, i.e the ACC1B and SCA1B data products are directly used as input without applying any a priori filtering techniques. Hence, the combination is based solely on the absolute attitude information provided by the SCA1B data product, and the relative attitude information provided by the ACC1B data product. The optimal weighting between the two different observation groups is achieved by means of VCE (cf. Section 3.6) in combination with a robust estimator (cf. Section 3.6.1), under the assumption of uncorrelated observations. Based on the principles of LSA, the system of linearized observation equations, describing the relation between the observations and unknown parameters within the sensor fusion approach, can be formulated as

$$\begin{aligned} \underbrace{\begin{bmatrix} \mathbf{l}_{\text{ACC1B}} \\ \mathbf{l}_{\text{SCA1B}} \end{bmatrix}}_{\mathbf{l}} &= \underbrace{\begin{bmatrix} \mathbf{A}_{\text{ACC1B}} & \mathbf{B}_{\text{ACC1B}} \\ \mathbf{A}_{\text{SCA1B}} & \mathbf{0} \end{bmatrix}}_{\mathbf{A}} \underbrace{\begin{bmatrix} \mathbf{q} \\ \mathbf{b} \end{bmatrix}}_{\mathbf{x}}, \\ &= \begin{bmatrix} \frac{\partial \dot{\boldsymbol{\omega}}}{\partial \mathbf{q}} & \frac{\partial \dot{\boldsymbol{\omega}}}{\partial \mathbf{b}} \\ \mathbf{I} & \mathbf{0} \end{bmatrix} \begin{bmatrix} \mathbf{q} \\ \mathbf{b} \end{bmatrix}, \end{aligned} \tag{6.12}$$

with

$$\begin{aligned} \mathbf{l}_{\text{ACC1B}} &= \dot{\boldsymbol{\omega}}_{\text{ACC1B}} - \dot{\boldsymbol{\omega}}_0(\mathbf{q}_0, \ddot{\mathbf{q}}_0), \\ \mathbf{l}_{\text{SCA1B}} &= \mathbf{q}_{\text{SCA1B}} - \mathbf{q}_0, \\ \mathbf{q}_{\text{Fusion}} &= \mathbf{q}_0 + \mathbf{q}. \end{aligned} \tag{6.13}$$

In Equation (6.12), the observations $\mathbf{l}$ are composed of the SCA1B quaternions ($\mathbf{l}_{\text{SCA1B}}$), and the ACC1B angular accelerations ($\mathbf{l}_{\text{ACC1B}}$). Since the sensor fusion takes place on the level of quaternions, the unknown parameters $\mathbf{x}$ contain the residual quaternions ($\mathbf{q}$), and a bias vector ($\mathbf{b}$) in order to allow for a calibration of the angular accelerations. The sparsely populated design matrix $\mathbf{A}$ consists of four parts, each containing the partial derivatives of the functional models w.r.t. the unknown parameters. Due to the non-linearity of the observation equations, the estimated quaternions $\mathbf{q}_{\text{Fusion}}$, given in the combined SCAFusion data product, are composed of the a priori approximation $\mathbf{q}_0$ (initially derived from the SCA1B data product), and the estimated quaternion improvements $\mathbf{q}$ (cf. Eq. (6.13)). Applying the principles of VCE, the LSA is solved iteratively, i.e. the approximate values ($\mathbf{q}_0, \dot{\boldsymbol{\omega}}_0$) and the VCE weights ($\sigma_q, \sigma_{\dot{\omega}}$) are adjusted step-by-step. The combination of VCE (observation group weighting, cf. Section 3.6) with a robust estimator (individual data weighting, cf. Section 3.6.1), allows not only for a relative weighting of the different inhomogeneous observation groups (quaternions, angular accelerations), but also enables the simultaneous identification and down-weighting of large outliers within the individual observation groups.

For the ITSG-Grace2016 release, an arc length of 30 min was used in order to derive the SCAFusion data product, i.e. the sensor fusion in terms of data combination is done separately for each arc. The arc length can be extended arbitrarily by solving the LSA on the level of normal equations.

6.3.2 Incorporation of ACC1B attitude information

In order to incorporate the attitude information provided by the angular accelerations into the combined LSA (cf. Eq. (6.12)), a relation between the angular accelerations and the quaternions needs to be established. The combination with the information provided by the star camera data takes place on the level of quaternions.

In a first step, the functional relationship between angular rates and quaternions can be established through (Diebel, 2006)

$$\boldsymbol{\omega}(\mathbf{q}, \dot{\mathbf{q}}) := 2\mathbf{W}(\mathbf{q})\dot{\mathbf{q}}, \tag{6.14}$$

where $\boldsymbol{\omega}$ denotes the angular rates, $\mathbf{W}$ denotes the angular rate matrix, and $\dot{\mathbf{q}}$ denotes the quaternion rates, i.e. the first temporal derivative of the unit quaternions. The function given in Equation (6.14), maps a unit quaternion and its temporal derivative to the angular velocity in a body-fixed coordinate system. From Equation (6.14) follows that the angular accelerations, expressed in a body-fixed system (SRF), can be related to the first and second time derivatives of the quaternion parameters by

$$\begin{aligned}\dot{\boldsymbol{\omega}}(\mathbf{q}, \dot{\mathbf{q}}) &:= 2\mathbf{W}(\mathbf{q})\ddot{\mathbf{q}} + 2\mathbf{W}(\dot{\mathbf{q}})\dot{\mathbf{q}} = 2\mathbf{W}(\mathbf{q})\ddot{\mathbf{q}}, \\ &:= 2\underbrace{\begin{bmatrix} -q_1 & +q_0 & +q_3 & -q_2 \\ -q_2 & -q_3 & +q_0 & +q_1 \\ -q_3 & +q_2 & -q_1 & +q_0 \end{bmatrix}}_{\mathbf{W}} \underbrace{\begin{bmatrix} \ddot{q}_0 \\ \ddot{q}_1 \\ \ddot{q}_2 \\ \ddot{q}_3 \end{bmatrix}}_{\ddot{\mathbf{q}}}.\end{aligned} \tag{6.15}$$

Due to its orthogonal structure, the term $2\mathbf{W}(\dot{\mathbf{q}})\dot{\mathbf{q}}$ in Equation (6.15) becomes zero.

By further evaluating Equation (6.15), the angular accelerations about the three SRF axes (x, y, z) can be related to the unit quaternions and its second temporal derivative through

$$\dot{\omega}_x = 2[-q_1\ddot{q}_0 + q_0\ddot{q}_1 + q_3\ddot{q}_2 - q_2\ddot{q}_3], \tag{6.16}$$

$$\dot{\omega}_y = 2[-q_2\ddot{q}_0 - q_3\ddot{q}_1 + q_0\ddot{q}_2 + q_1\ddot{q}_3], \tag{6.17}$$

$$\dot{\omega}_z = 2[-q_3\ddot{q}_0 + q_2\ddot{q}_1 - q_1\ddot{q}_2 + q_0\ddot{q}_3]. \tag{6.18}$$

Second order derivative - unit quaternions

The second order derivatives of the unit quaternions can be approximated by applying a second order difference quotient:

$$i = 0: \quad \ddot{q}^i = \frac{q^{i+2} - 2q^{i+1} + q^i}{\Delta t^2}, \tag{6.19}$$

$$0 < i < N: \quad \ddot{q}^i = \frac{q^{i+1} - 2q^i + q^{i-1}}{\Delta t^2}, \tag{6.20}$$

$$i = N: \quad \ddot{q}^i = \frac{q^{i-2} - 2q^{i-1} + q^i}{\Delta t^2}. \tag{6.21}$$

Therein, the index i denotes the observation epoch within one arc, and Δt denotes the sampling of the data in seconds. To derive the second derivative of the unit quaternion of the first epoch ($i = 0$), the forward difference quotient (cf. Eq. (6.19)) is used. Whereas, for the last epoch ($i = N$), the backward difference quotient (cf. Eq. (6.21)) is used. For all other epochs ($0 < i < N$), the central difference quotient (cf. Eq. (6.20)) is applied in order to derive the second derivative of the unit quaternions. The latter is the general preference from a mathematical point of view, as it provides a more accurate approximation for the second order derivative. In contrast to the one-sided differencing formulas, it incorporates the values from the central quaternion at the current epoch, and from the quaternions on both sides of the current epoch.

Other numerical differentiation methods, including numerical differentiation by polynomial interpolation, were tested. But, the best results in terms of noise (for both the second order quaternion derivatives and the estimated combined quaternions) were achieved when the numerical differentiation is based on either a first-order interpolation polynomial or on the equivalent second-order difference quotients (not shown here). Due to the sinusoidal behavior of the unit quaternions (cf. Fig. 5.5), higher degree polynomials lead to a higher noise and introduce oscillation effects at the edges of the arcs. Here, the difference quotients are preferred, due to their straight-forward representation within the functional model (cf. Eq. (6.22)).

Substituting Equations (6.19), (6.20), and (6.21) into Equation (6.16), relates the angular accelerations to the quaternion elements of adjacent epochs. The resulting equations are exemplarily shown for the angular accelerations around the x-axis:

$$
\begin{aligned}
\dot{\omega}_x^0 &= \frac{2}{\Delta t^2}\,[-q_1^0(q_0^2 - 2q_0^1 + q_0^0) + q_0^0(q_1^2 - 2q_1^1 + q_1^0) \\
&\quad + q_3^0(q_2^2 - 2q_2^1 + q_2^0) - q_2^0(q_3^2 - 2q_3^1 + q_3^0)], \\
\dot{\omega}_x^i &= \frac{2}{\Delta t^2}\,[-q_1^i(q_0^{i+1} - 2q_0^i + q_0^{i-1}) + q_0^i(q_1^{i+1} - 2q_1^i + q_1^{i-1}s) \\
&\quad + q_3^i(q_2^{i+1} - 2q_i^1 + q_2^{i-1}) - q_2^i(q_3^{i+1} - 2q_3^i + q_3^{i-1})], \\
\dot{\omega}_x^N &= \frac{2}{\Delta t^2}\,[-q_1^N(q_0^{N-2} - 2q_0^{N-1} + q_0^N) + q_0^N(q_1^{N-2} - 2q_1^{N-1} + q_1^N) \\
&\quad + q_3^N(q_2^{N-2} - 2q_2^{N-1} + q_2^N) - q_2^N(q_3^{N-2} - 2q_3^{N-1} + q_3^N)].
\end{aligned}
\tag{6.22}
$$

Herein, the superscripts refer to the observation epoch, and the subscripts refer to the SRF-axis or to the quaternion elements. Equivalent formulas can be derived for the angular accelerations about the y- and z-axis (not shown here).

Angular accelerometer bias

The ACC1B angular accelerations contain an unknown bias (cf. Section 5.2.3). Besides a constant bias offset, regular bias variations occur, which are mainly caused by temperature variations related to the switch-off of the active thermal control. Furthermore, sudden bias jumps occur several times a year, which are most likely to be caused by sudden voltage jumps within one of the accelerometer electrodes of the accelerometer sensor unit (Bandikova et al., 2016). To illustrate possible bias variations, Figure 6.6 shows the uncalibrated ACC1B angular accelerations together with the AHK1B core temperatures over the whole GRACE mission period, from April 2002 to June 2017. From this it becomes obvious, that since

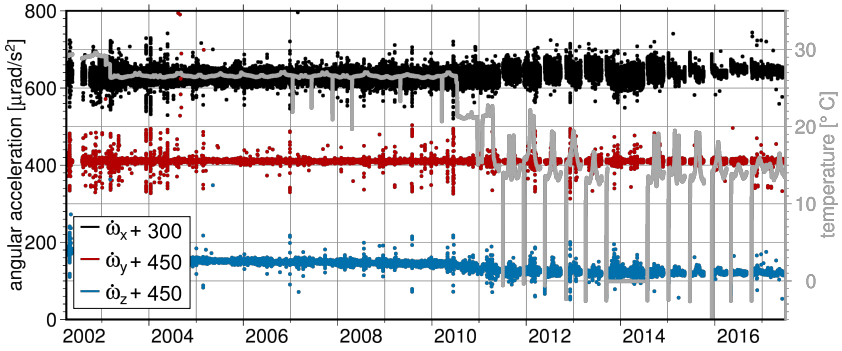

Fig. 6.6.: Temporal evolution of the ACC1B angular accelerations $\dot{\omega}_x$ (black), $\dot{\omega}_y$ (red), $\dot{\omega}_z$ (blue) for GRACE-A compared to the accelerometer core-temperature (gray) for the time period April 2002 to June 2017.

April 2011 temperature-related bias drifts occur with a regular pattern, primarily affecting the angular accelerations about the less-sensitive along-track and radial axes.

To account for the bias and its variations within the ACC1B data, a bias vector is estimated as unknown parameter within the sensor fusion approach (cf. Eq. (6.12)). The uncalibrated ACC1B angular accelerations $\dot{\boldsymbol{\omega}}_{\text{ACC1B}}$ are related to the true angular accelerations $\dot{\boldsymbol{\omega}}_{\text{obs}}$ by

$$\dot{\boldsymbol{\omega}}_{\text{ACC1B}} = \dot{\boldsymbol{\omega}}_{\text{obs}} + \mathbf{b}, \tag{6.23}$$

where $\mathbf{b}$ denotes the bias vector, representing the bias in the angular accelerometer observations. The estimated bias is parameterized by a first order polynomial, accounting for constant bias offsets and linear bias drifts. Non-linear bias drifts are not modeled. This simplified bias modeling is motivated by the used short arc length of 30 min, and the assumption that the occurring temperature-related bias drifts can be successfully approximated by this model.

Figure 6.7 expemplarily shows the uncalibrated ACC1B and the bias-reduced angular accelerations about the radial axis ($\dot{\omega}_z$), as used within the sensor fusion approach. For all three directions, the bias jumps and temperature-dependent bias variations, which become visible as striping patterns, can be reduced successfully by estimating a linear bias.

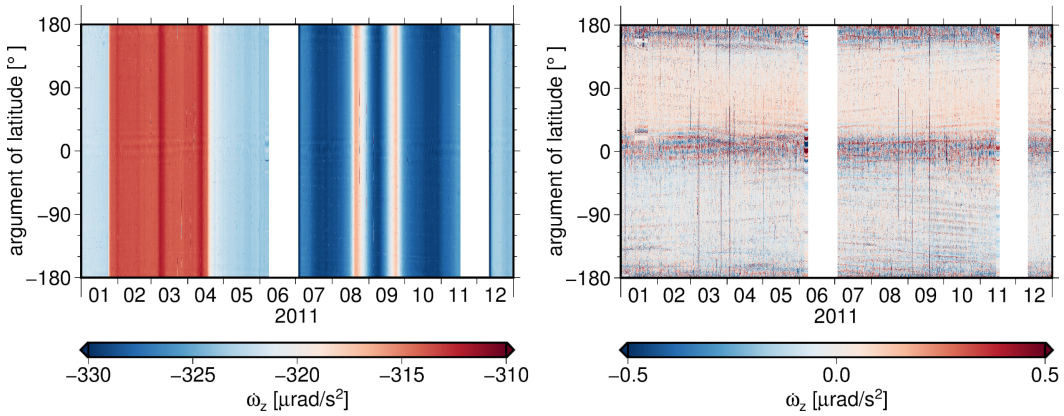

Fig. 6.7.: GRACE-A angular accelerations about the radial axis ($\dot{\omega}_z$) along the orbit for one year (2011). Left: uncalibrated ACC1B angular accelerations, Right: calibrated ACC1B angular accelerations. Note that not the same scaling is used.

Angular accelerometer correction

The accelerometer measures the torque necessary to maintain the proof mass motionless with respect to the electrodes cage. Consequently, the measured angular accelerations are linked to the inertial angular acceleration and rate by the following formulae

$$\dot{\omega}_{\text{obs},x} = \dot{\omega}_x + \frac{I_z - I_y}{I_x}\omega_y\omega_z \approx \dot{\omega}_x - \omega_y\omega_z, \tag{6.24}$$

$$\dot{\omega}_{\text{obs},y} = \dot{\omega}_y + \frac{I_x - I_z}{I_y}\omega_x\omega_z \approx \dot{\omega}_y, \tag{6.25}$$

$$\dot{\omega}_{\text{obs},z} = \dot{\omega}_z + \frac{I_y - I_x}{I_z}\omega_x\omega_y \approx \dot{\omega}_z + \omega_x\omega_y, \tag{6.26}$$

where $\dot{\omega}_{i,\text{obs}}$ denotes the measured angular accelerations (given by ACC1B), $\dot{\omega}_i$ denotes the inertial angular accelerations, and ω_i denotes the inertial angular rates. The index $i = x, y, z$ refers to the axes of the SRF. The moments of inertia of the GRACE accelerometer proof mass are defined as

$$I_x = 1.959 \cdot 10^{-5}\ \text{kg} \cdot \text{m}^2, \tag{6.27}$$

$$I_y = I_z = 1.037 \cdot 10^{-5}\ \text{kg} \cdot \text{m}^2. \tag{6.28}$$

Due to the parallelepiped (non-square) shaped proof mass of the GRACE accelerometer (cf. Section 5.2), the moments of inertia are not equal (cf. Eq. (6.27) and (6.28)). Thus, only the measurement about the y-axis (w.r.t. the SRF) is a pure angular acceleration (cf. Eq. (6.25); personal communication with Bernard Foulon (ONERA)). Therefore, the angular accelerations, contained in the ACC1B data product, need not only to be corrected for a bias (cf. Eq. (6.23)), but also for the effects of the non-square proof mass (cf. Eqs. (6.24) to (6.26)). Due to the Earth pointing attitude of the satellites, the angular rate about the cross-track axis $\omega_y \approx 1.12 \cdot 10^{-3}$ rad/s is not negligible, and should be considered correctly. As a consequence, the ACC1B angular accelerations, which are used as observations within the sensor fusion approach, are corrected for these effects.

6.3.3 VCE - Initial observation weights

In order to enable an iterative LSA, utilizing the principles of VCE togehter with a robust estimator, initial weights for both observation groups are introduced. Table 6.1 summarizes the introduced a priori variance factors of the SCA1B quaternion and the ACC1B angular acceleration observations. To facilitate the VCE, only two observation groups are used. Therefore, fixed scale factors are used to initially scale the angular accelerations with respect to each other.

Tab. 6.1.: Initial VCE variance factors of the ACC1B and SCA1B observations.

Observation (SRF)	Variance factor (σ_0)	Scaling factor
$\dot{\omega}_x$	$5 \cdot 10^{-6}$ rad/s^2	$25 \cdot \dot{\omega}_y$
$\dot{\omega}_y$	$2 \cdot 10^{-7}$ rad/s^2	$1 \cdot \dot{\omega}_y$
$\dot{\omega}_z$	$5 \cdot 10^{-7}$ rad/s^2	$2.5 \cdot \dot{\omega}_y$
q_0, q_1, q_2, q_3	$5 \cdot 10^{-5}$	x

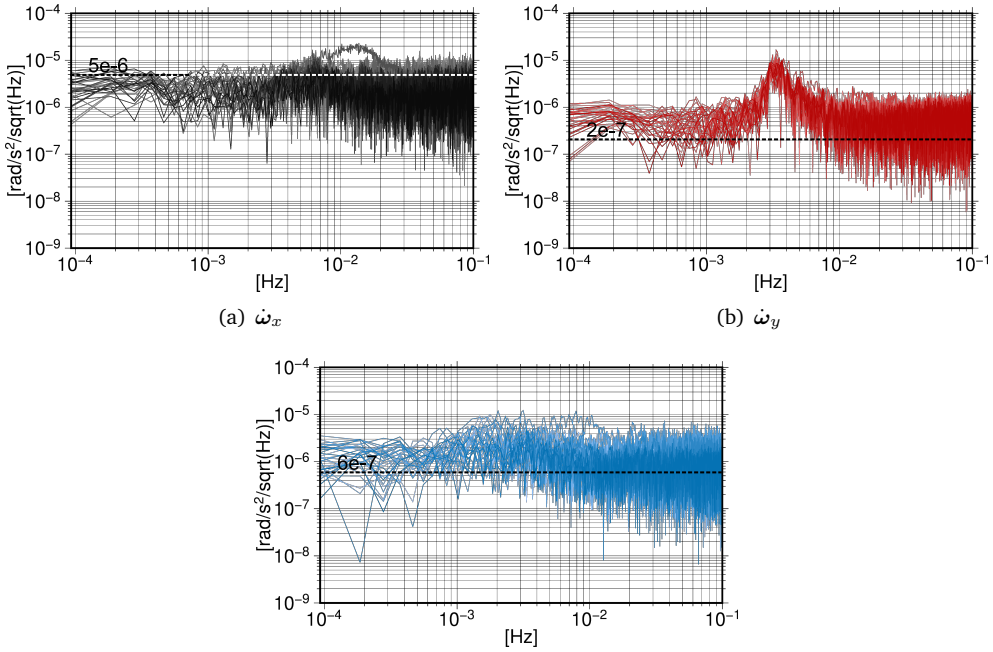

(a) $\dot{\omega}_x$ (b) $\dot{\omega}_y$

(c) $\dot{\omega}_z$

Fig. 6.8.: PSD of the ACC1B angular accelerations: (a) $\dot{\omega}_x$ (black), (b) $\dot{\omega}_y$ (red), and (c) $\dot{\omega}_z$ (blue). PSDs for various 3 h intervals within December 2008 are shown. As reference, the initial variance factors listed in Tab. 6.1 are shown (black dashed line).

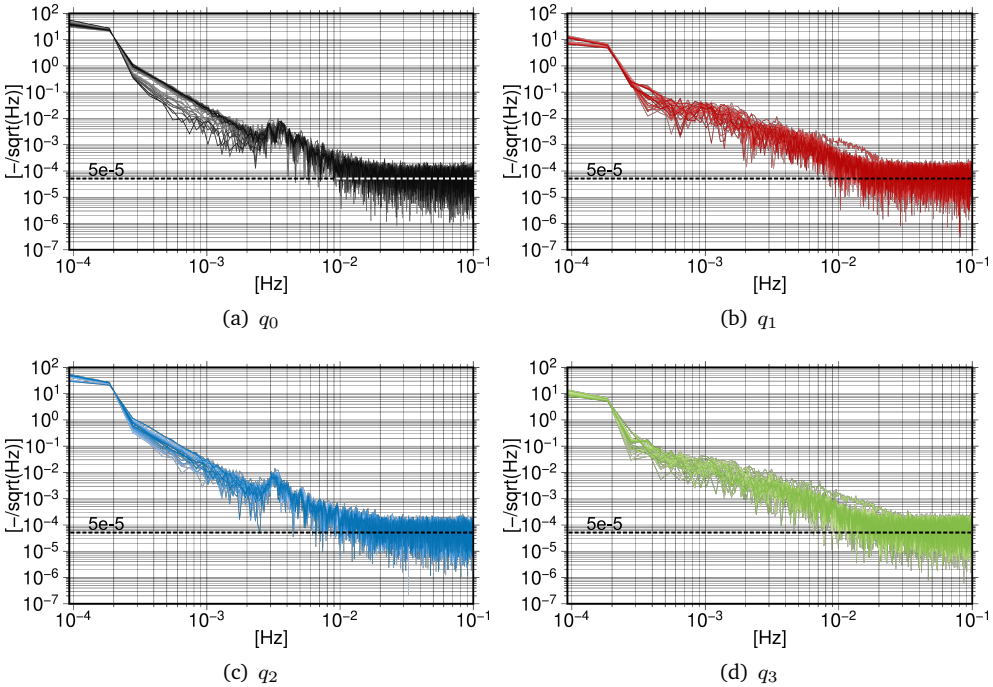

(a) q_0 (b) q_1

(c) q_2 (d) q_3

Fig. 6.9.: PSD of the SCA1B quaternion elements: (a) q_0 (black), (b) q_1 (red), (c) q_2 (blue), and (c) q_3 (green). PSDs for various 3 h intervals within December 2008 are shown. As reference, the initial variance factors listed in Tab. 6.1 are shown (black dashed line).

The combination of heterogeneous data types, as done by the sensor fusion approach, requires a relative weighting among the different observation groups (angular accelerations, quaternions). This was achieved by applying the principles of VCE, in combination with a robust estimator. This enables not only a more realistic weighting of the observation groups, but also the identification or down-weighting of large blunders within the iterative LSA.

In a first approximation, the initial variance factors of the angular accelerations about the along-track and cross-track axis are taken from the GRACE instrument specifications given in Stanton et al. (1998), Hudson (2003) and defined by ONERA. Only, the variance factors of the angular accelerations about the radial axis are adjusted, since they are characterized by a significantly lower noise compared to the specifications. Therefore, the initial accuracies were approximated from the PSD analysis shown in Figure 6.8(c). Since no specifications exist for the star camera observations in terms of quaternions, the accuracies are derived from noise level simulations by Frommknecht (2008). Following from that, together with the PSD analysis shown in Figure 6.9, the same initial variance factors are used for all four quaternion elements (cf. Tab. 6.1). The homogeneous values are owed to the incorrect combination of the star camera heads (cf. Sections 5.1.3 and 6.2).

A comparison of Figures 6.8 and 6.9 with the initial approximations for the variance components of the ACC1B angular accelerations and SCA1B quaternions given in Table 6.1, shows a good agreement between the PSD analysis and the underlying accuracy/noise assumptions.

6.3.4 Improvement of the attitude data product

To allow for an evaluation of the sensor fusion approach, the SCAFusion data product is directly compared with the official RL02 SCA1B data product, generated by JPL. The results of this comparison are shown in Figures 6.10 and 6.11. As expected, the combined attitude solution (SCAFusion) benefits from the different noise characteristics of the star camera (SCA1B) and the angular accelerometer (ACC1B). By applying the sensor fusion, the fused attitude information consists of the low-frequency information provided by the star camera, and the high-frequent information provided by the angular accelerometer (cf. Fig. 6.11).

Quaternions

Figure 6.10 shows a comparison of the SCAFusion and RL02 SCA1B data product in terms of quaternion elements in the time and frequency domain, respectively. In the time domain, the differences in terms of quaternion element differences are small, at a level of $0.5 - 1 \cdot 10^{-3}$. In the frequency domain, the combined quaternions (SCAFusion) are characterized by a reduced noise within the high frequencies, i.e. the high frequencies of the spectrum are damped. At frequencies above $9 \cdot 10^{-3} - 1 \cdot 10^{-2}$ Hz, the noise level is significantly reduced. In general, the same behavior can be observed for the spectra of the angular accelerations, shown in Figure 6.11. Since the results for the other quaternion elements (not shown here) are similar, the analysis is limited to q_0 and q_1.

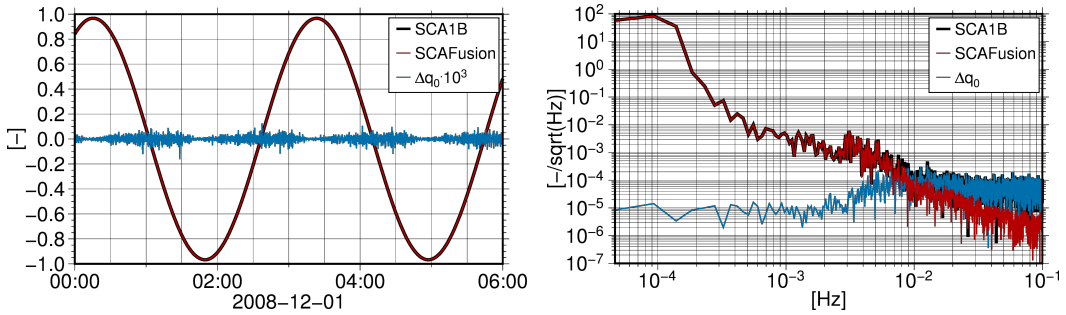

(a) $\mathbf{q}_0$

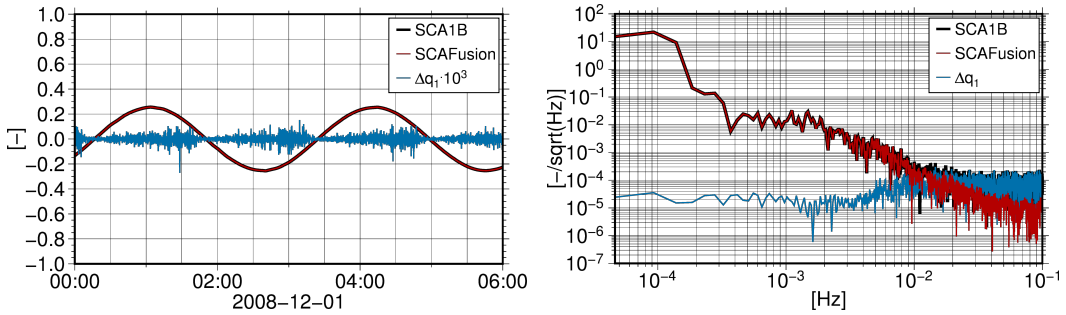

(b) $\mathbf{q}_1$

Fig. 6.10.: Comparison of the GRACE SCA1B (black) and SCAFusion (red) data product: Left: Quaternion time series of GRACE-A for a 6 h interval on 2008-12-01; Right: PSD of the quaternion elements q_0 (a) and q_1 (b) of GRACE-A for the same 6 h interval on 2008-12-01. The differences $\Delta\mathbf{q}$ between the SCA1B and the SCAFusion quaternions are shown in blue. Note that the differences are scaled by a factor 10^3 in the time domain.

Angular accelerations

The effect of the sensor fusion in terms of reducing the high-frequent attitude noise becomes most evident, if the RL02 SCA1B, the RL02 ACC1B, and the SCAFusion data product are compared on the level of angular accelerations. Figure 6.11 shows a comparison of the angular accelerations of all three data products (SCA1B, ACC1B, SCAFusion) in the frequency domain. From this comparison it becomes evident that the fused angular accelerations benefit from the different noise characteristics of the SCA1B and ACC1B data, and show a reduced noise level, especially about the cross-track and radial axes ($\dot{\omega}_y$, $\dot{\omega}_z$). At frequencies higher than $8 \cdot 10^{-3}$ to 10^{-2} Hz, the ACC1B data fully contributes to the spectrum of the combined angular accelerations (cf. Fig. 6.11(b) and 6.11(c)). Within this frequency band, the noise level of $\dot{\omega}_y$ and $\dot{\omega}_z$ is decreased by a factor of $2 - 50$ w.r.t. to the official SCA1B RL02 data. Thus, the sensor fusion primarily helps to reduce the high-frequent star camera noise, which is partly caused by the incorrect combination of the two star camera heads within the Level-1A to Level-1B processing (cf. Fig. 5.6; Bandikova and Flury, 2014).

Summarizing the above, it can be concluded that the combination of the GRACE RL02 Level-1B star camera and accelerometer data (SCA1B, ACC1B) contributes to a reduction of the high-frequent attitude noise. As a consequence, the resulting attitude is smoother than the one derived from original star camera observations (cf. Fig. 6.13).

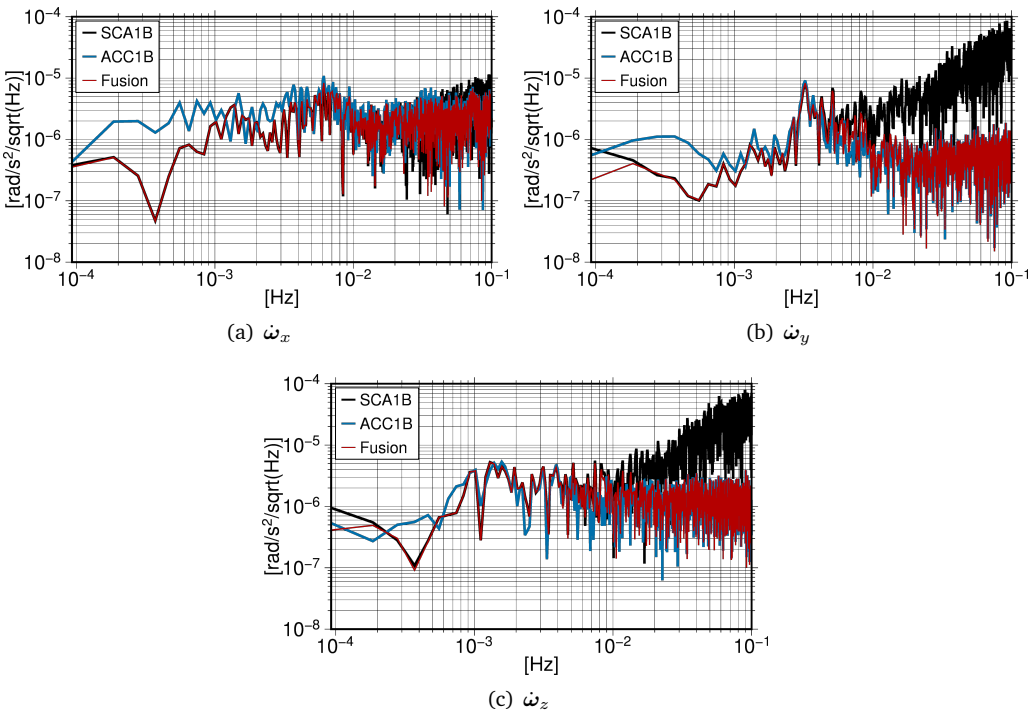

(a) $\dot{\omega}_x$ (b) $\dot{\omega}_y$

(c) $\dot{\omega}_z$

Fig. 6.11.: Comparison of the GRACE SCA1B (black), SCAFusion (red), and ACC1B (blue) data product: PSD of the angular accelerations $\dot{\omega}_x$ (a), $\dot{\omega}_y$ (b), and $\dot{\omega}_z$ (c) about the SRF axes for a 3 h interval on 2008-12-01.

Jumps within the SCA1B data

Due to light intrusions from the Sun or the Moon, there are single camera and dual camera phases, depending on the number of available star camera heads (cf. Fig. 5.4). Since the SCA1B data product is based on the combination of the data from the two star camera heads (cf. Section 5.1.3), discontinuities appear at transitions from dual camera to single camera phases and vice versa (Ko et al., 2015; Bandikova, 2015). The magnitudes of these jumps can reach up to 0.3 mrad and are the consequence of the different performance of the two star camera heads. Therefore, the jumps are pronounced for transitions to or from single star camera phases (e.g., transition to or from star camera head #2 on-board GRACE-B, cf. Fig. 6.12). As can be seen from Figure 6.12, the pitch jumps within the GRACE-B SCA1B data are smoothed out when using the SCAFusion data product.

However, according to Ko et al. (2015), the reduction of the discontinuities within the SCA1B data product do not appear to have a large influence on the CSR gravity field solutions (Ko et al., 2015).

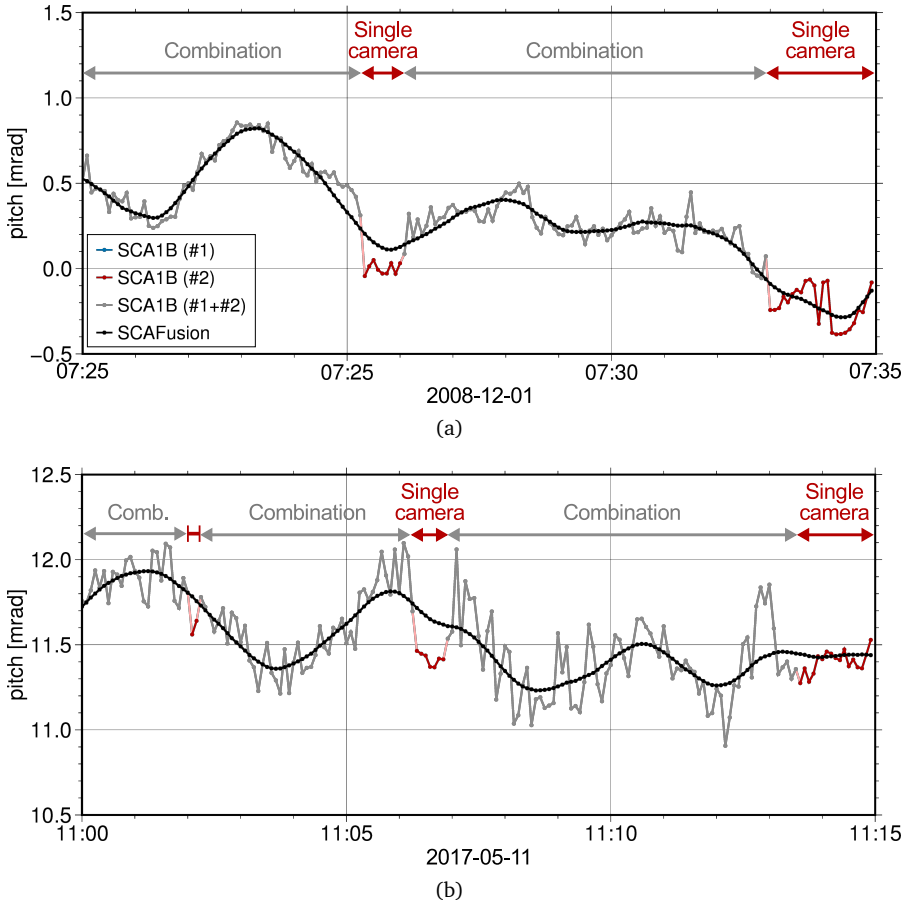

Fig. 6.12.: Jumps within the SCA1B data product: Pitch angles derived from the SCA1B data product (color) and the SCAFusion data product (black) for a 15 min interval on (a) 2008-12-01 and (b) 2017-05-11 for GRACE-B. To highlight the transition form single to dual camera mode, the SCA1B data combination is indicated by the color: Blue = Star camera #1, Red = Star camera #2, Gray = Combination of star camera #1+#2.

6.3.5 Effect on the Antenna Offset Correction

The previous analysis of the combined SCAFusion data product (cf. Section 6.3.4), demonstrated the potential of the sensor fusion approach to reduce the high-frequent noise present in the original RL02 SCA1B data product. In the following, the effect of this attitude noise reduction on other GRACE data products, namely the KBR1B and ACC1B data product, is analyzed. Both data products represent essential satellite observations, which are needed for gravity field recovery (cf. Section 4.2).

The KBR ranging observations need to be corrected for the CoM-offset of the KBR antennas, and the imperfect inter-satellite pointing by adding the AOC (cf. Section 6.1.1). The AOC for ranges, range rates, and range accelerations are directly derived from the satellites attitude and orbit information. Hence, increased noise or errors within the attitude data product directly propagate to the AOCs. To analyze the impact of the sensor fusion, the AOCs are derived from both the SCA1B, and the SCAFusion data product, respectively. Additionally, the inter-satellite pointing angles (roll, pitch, yaw), directly representing the variations of the two satellites orientation, are also recovered from both data products.

Attitude angles - roll, pitch, yaw

Figure 6.13 shows the attitude angles derived from the SCA1B RL02 and SCAFusion data product, in the time and frequency domain. From this, it becomes obvious, that in particular the pitch and the yaw angles are much smoother as compared to the original RL02 SCA1B data product. This reflects the findings of the previous Section, and also agrees with the expected attitude behavior of the satellites. The differences of the pitch and yaw angles ($\Delta\theta, \Delta\psi$) reach up to $0.2 - 0.5$ mrad (during single camera phases). In the frequency spectrum, this becomes visible by a reduced noise within the high frequencies (above $\sim 8 \cdot 10^{-3} - 1 \cdot 10^{-2}$ Hz). Since the sensor fusion mainly helps to reduce the high-frequent noise of the rotations about the cross-track and radial axes, the roll angles show no significant improvement.

By comparing the absolute differences between the pitch angles derived from the SCA1B RL02 and SCAFusion data product along the orbit for one year (2008) (cf. Fig. 6.14), features related to the availability of the combined attitude solution, i.e. whether one or two star camera heads were used to derive the SCA1B data product, become visible (cf. Section 5.1.3, cf. Fig. 5.4). Due to the orbital configuration of GRACE, the two star cameras are repeatedly blinded by either the Sun or the Moon, causing star camera outages. The absolute pitch angle differences in Figure 6.14 are larger for periods with single star camera availability, when the attitude determination is based solely on the worse performing star camera head #1, for both GRACE-A and GRACE-B (cf. Fig. 5.4) (Bandikova, 2015; Harvey, 2016). Whereas, for the better performing star camera head #2, the absolute differences are smaller. From these differences between the SCA1B and SCAFusion data product it follows that the sensor fusion particularly improves the attitude estimation during these periods of Sun and Moon intrusions, blinding the better star camera head. In agreement with Figure 6.13, showing the improvements of the pointing angles in the high frequencies, similar spatial patterns become visible for the absolute yaw angle differences (not shown here).

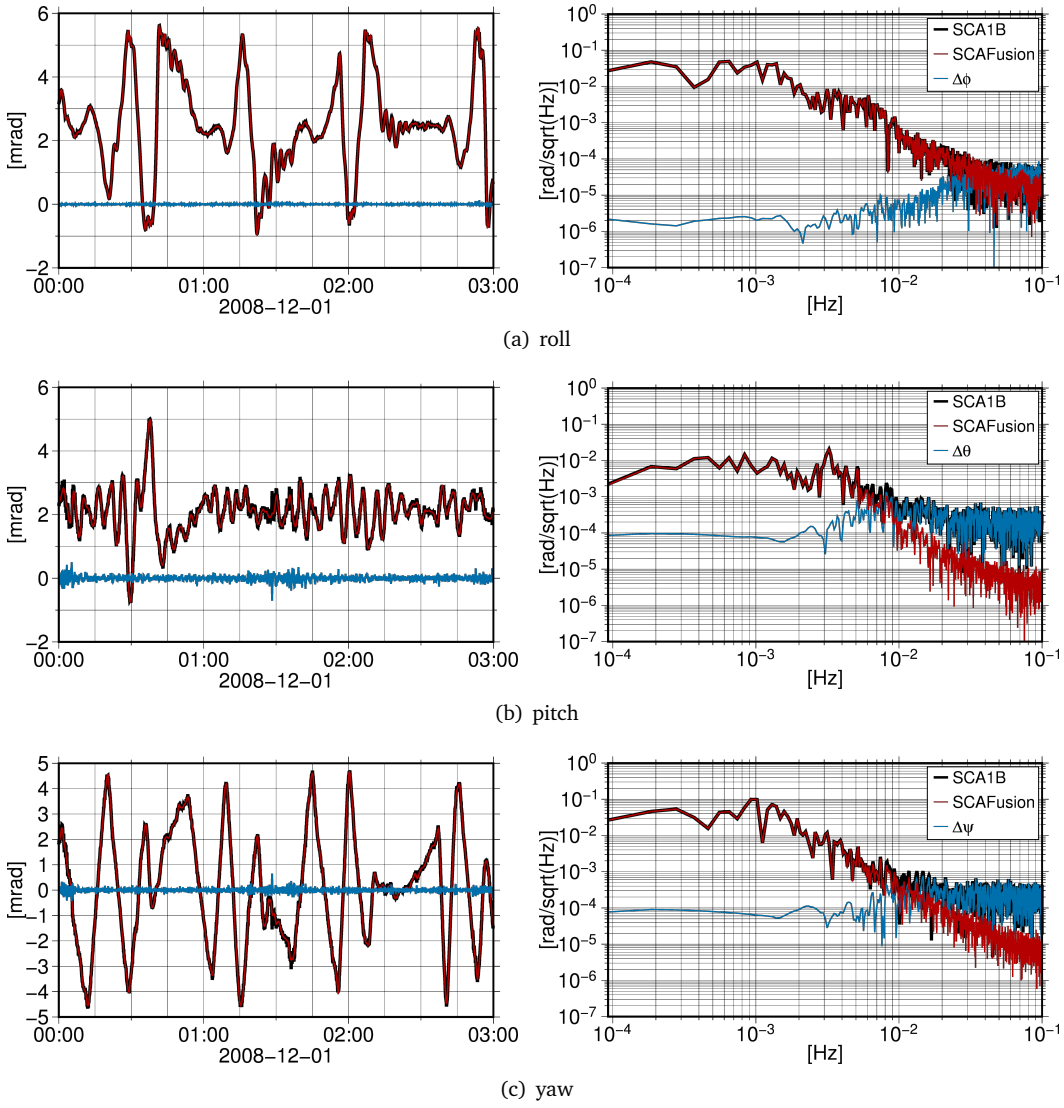

(a) roll

(b) pitch

(c) yaw

Fig. 6.13.: Comparison of the GRACE SCA1B (black) and SCAFusion (red) data product: Left: Time series of the roll (a), pitch (b), and yaw (c) inter-satellite pointing angles for a 3 h interval on 2008-12-01 for GRACE-A; Right: PSD of the roll (a), pitch (b), and yaw (c) inter-satellite pointing angles of GRACE-A derived from the same 3 h interval on 2008-12-01. The differences $\Delta\mathbf{q}$ between the SCA1B and the SCAFusion data products in terms on inter-satellite pointing angles are shown in blue.

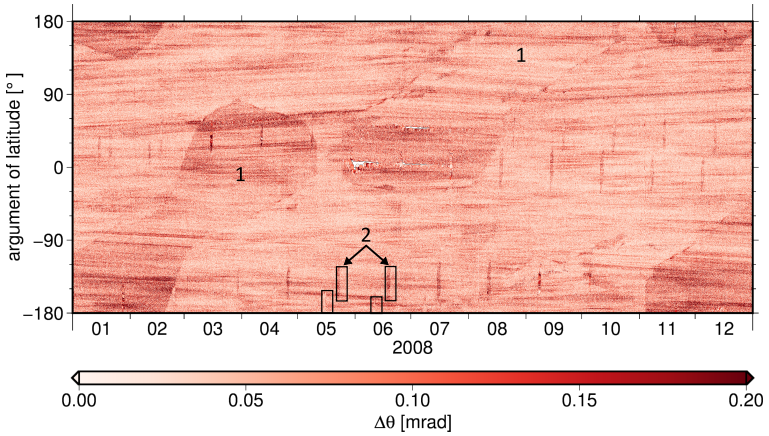

(a) GRACE-A

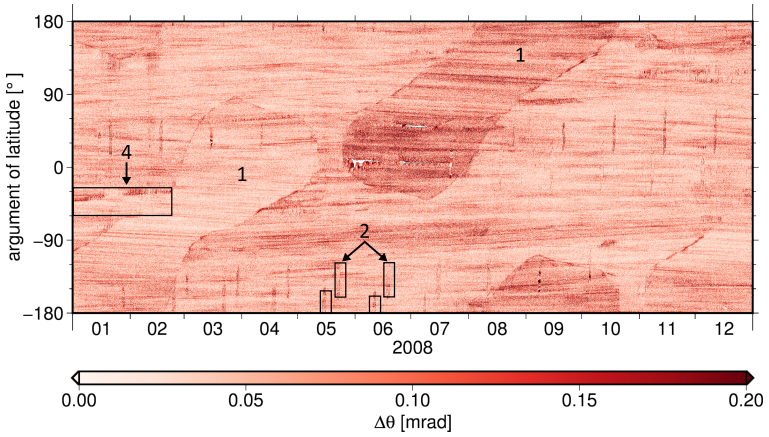

(b) GRACE-B

Fig. 6.14.: Absolute pitch angle differences between the SCA1B and SCAFusion data product for (a) GRACE-A and (b) GRACE-B for one year (2008). SCA outages: 1 = Sun intrusions, 2 = Moon intrusions, 3 = data gap, 4 = SCA outage not related to Sun or Moon blinding (cf. Fig. 5.4).

Antenna Offset Correction (AOC)

The effect of the sensor fusion on the KBR AOCs for range rates is demonstrated in Figures 6.15 and 6.16, showing the KBR range rate corrections for two different month within the GRACE mission period. For the earlier one (December 2008; cf. Fig. 6.15), the sensor fusion results in a smoothed AOC, i.e. significantly reducing the high-frequent attitude noise. This becomes even more pronounced for the later month (May 2017; cf. Fig. 6.16). Since March 29, 2017, the pitch angles were set to $0°$ on both spacecraft to improve the quality of the transplanted GRACE-B ACC1B product (cf. Section 5.2.3). The removal of the pitch offset results in larger AOCs for both spacecraft. Consequently, the noise reduction achieved by the sensor fusion becomes more apparent for this month. The direct comparison of the SCAFusion and SCA1B AOCS for range rates in the spatial domain (cf. Figs. 6.16(b) and 6.16(c)), confirms these findings. The results shown demonstrate the impact of the sensor fusion on the AOC corrections, which in turn directly affect the KBR ranging observations used for gravity field recovery. The effect of a changed satellite alignment, i.e. change of the pitch offset, is further discussed in Section 8.2.

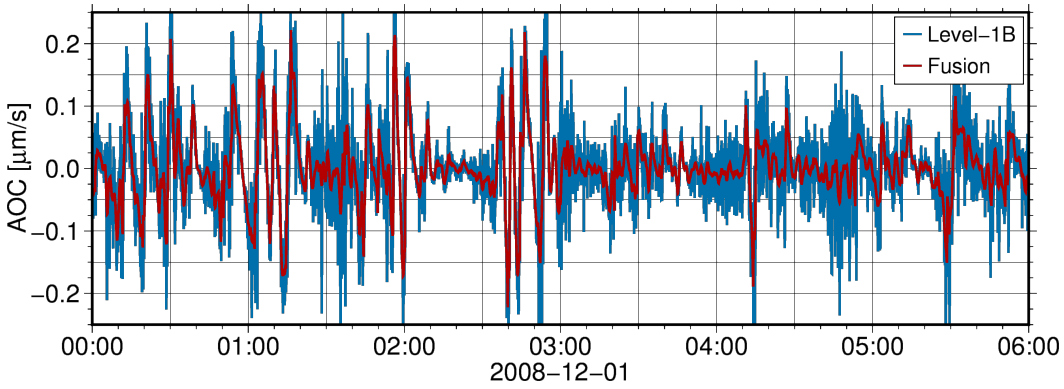

(a) AOC

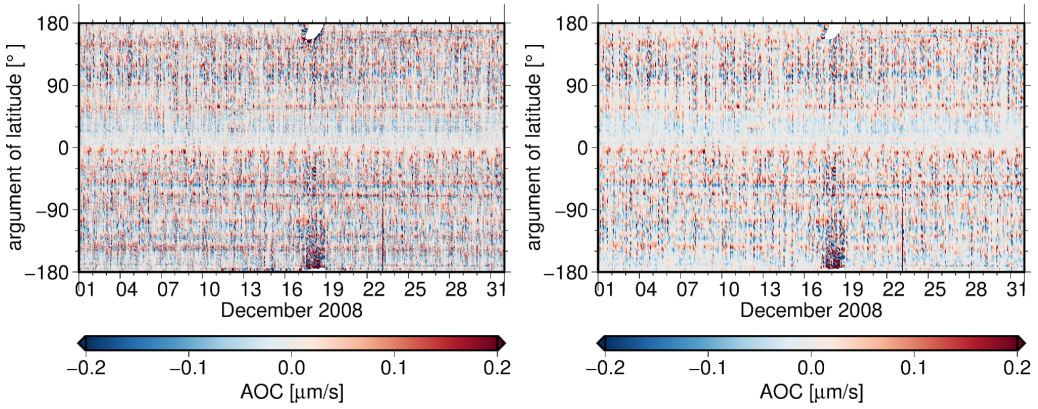

(b) Level-1B

(c) Fusion

Fig. 6.15.: KBR AOCs for range rates: (a) Range rate corrections derived from the RL02 SCA1B (Level-1B) and SCAFusion (Fusion) data product for a 6 h interval on 2008-12-01; (b,c) AOCs (range rates) along the orbit for one month (December 2008), derived from the RL02 SCA1B (b) and the SCAFusion (c) data product. White gaps within (b) and (c) correspond to data gaps.

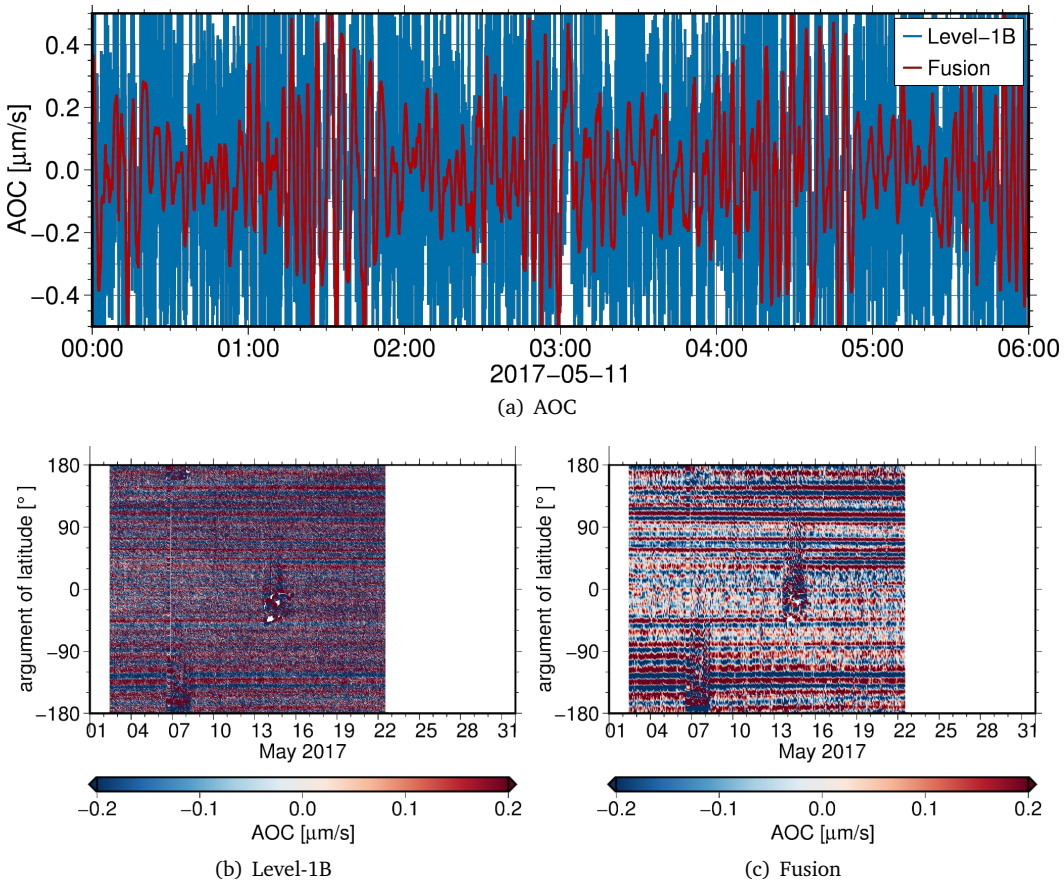

(a) AOC

(b) Level-1B

(c) Fusion

Fig. 6.16.: KBR AOCs for range rates: (a) Range rate corrections derived from the RL02 SCA1B (Level-1B) and SCAFusion (Fusion) data product for a 6 h interval on 2017-05-11; (b,c) AOCs (range rates) along the orbit for one month (May 2017), derived from the RL02 SCA1B (b) and the SCAFusion (c) data product. In May 2017, data was only available between 2017-05-02 and 2017-05-22. Note that since 2017-03-29 the pitch offset was set from $\sim 1^\circ$ to 0° on both spacecraft.

6.3.6 Effect on the ACC observations

The ACC1B data product provides the linear accelerations, representing the non-gravitational accelerations acting upon the spacecraft, with respect to the SRF. However, for the ITSG-Grace gravity field recovery based on the variational equation approach, the linear accelerations need to be rotated from the SRF into the IRF. Thus, the attitude information provided by the SCA1B or SCAFusion data product is directly applied in order to rotate the accelerometer observations. Thus, errors within the attitude data product directly propagate to the rotated linear accelerations, which are used as input for the gravity field recovery.

Figure 6.17 shows the differences in the linear accelerations w.r.t. the IRF, i.e. the differences result from the orientation differences between the SCA1B and SCAFusion data product. For all three axes, the differences reach up $8 \cdot 10^{-9}$m/s^2. For the sensitive along-track and radial axes, the differences clearly exceed the specified measurement accuracy of $1 \cdot 10^{-10}$m/s^2 (cf. Tab. 5.1). But also for the less-sensitive cross-track axis, the differences are repeatedly above the specified measurement accuracy of $1 \cdot 10^{-9}$m/s^2.

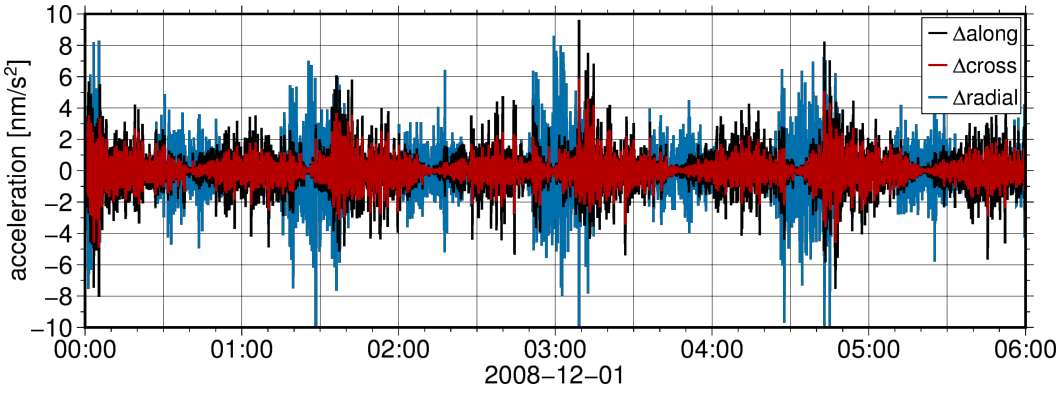

Fig. 6.17.: Linear accelerations differences resulting from the rotation of the ACC1B data product into the IRF based on the RL02 SCA1B and the SCAFusion data product. Linear acceleration differences in along-track (black), cross-track (red), and radial (blue) direction are shown for a 6 h interval on 2008-12-01 for GRACE-A.

These results indicate that the accelerometer measurement accuracy, although it does not meet the accuracy specifications (cf. Section 5.2.2), might not be fully exploited, since the effects caused by the imperfect attitude data repeatedly exceed the measurement accuracy.

In summary, the sensor fusion approach results in a significant reduction of the high-frequency attitude noise, which results in a smoothing of the pointing variations in terms of attitude angles (roll, pitch, yaw), and the AOCs. The effects of the improved attitude data product on the recovered gravity field solutions are analyzed in Section 8.2.

6.4 Further options - Attitude data processing

6.4.1 GRACE

In general, further improvement of the GRACE attitude data is possible, and will be realized by the JPL GRACE Level-1B re-processing campaign (cf. Section 6.2.3). Future SCA1B data products (RL03 and RL04) are based on the combination of star camera and angular accelerometer data using a Kalman filtering approach (Bandikova et al., 2016; Sakumura et al., 2016); and will contain the combined solution. A further refinement of the star camera data processing would also take the measurement accuracy of the star cameras into account, i.e. using a combination method based on the weight matrix instead of assuming a uniform measurement accuracy for all star camera heads.

For non-official processing center, such as the IfG, the improvement of the GRACE attitude data is only possible based on the combination of RL02 SCA1B and ACC1B data products (cf. Section 6), which are publicly available to all processing centers. Since these data products still contain some processing bugs (cf. Section 6.2), the achieved results cannot represent an optimal combination. On the level of the sensor fusion approach, a refined observations weighting or pre-processing, i.e. a revision of the VCE within the sensor fusion approach or a priori filtering of the input data, might also contribute to the improvement of the achieved results. On the level of the gravity field recovery, a more realistic modeling of the star camera noise within the LSA is also feasible. An inclusion of the stochastic information from the satellite orientation (Ellmer and Mayer-Gürr, 2017a) and/or a further reduction of the attitude noise also enables a more stable estimation of the phC vector; contributing to a reduction of the high-frequency noise within the recovered gravity field solutions.

6.4.2 GRACE-FO

Based on the findings of the GRACE attitude determination, GRACE-FO will be equipped with three star camera heads instead of two (cf. Section 2.7), ensuring a combined attitude solution, with the full-accuracy about all three axes, at any time.

For GRACE-FO, the introduced sensor fusion approach can be extended by the incorporation of attitude data from multiple sensors (3 SCA heads, ACC, IMU, LRI). Furthermore, the whole attitude data processing can be reworked by using Level-1A data products instead of Level-1B data products. The use of raw observations (Level-1A) also enables a more detailed analysis of the attitude data. A detailed understanding of possible error sources and systematics (e.g., data outages, Sun/Moon intrusions, temperature variations, etc.) within the attitude data is essential to improve the attitude accuracy by a proper correction and/or consideration of these effects during data processing. Furthermore, a refinement of the star camera data combination can be achieved by taking into account the measurement accuracy of the individual star camera heads by e.g., introducing a weight matrix. An independent attitude determination by different processing centers will also contribute to the quality of the attitude solutions, facilitating a mutual validation and sharing of experiences.

7 Accelerometer data calibration

Both GRACE satellites are equipped with space accelerometers measuring the non-gravitational accelerations acting upon them (Touboul et al., 1999, cf. Section 5.2). These forces are due to atmospheric drag, solar radiation pressure and albedo (cf. Section 3.3). The main observables for the gravity field recovery by GRACE are the inter-satellite ranging measurements, carried out by the onboard KBR system with micrometer precision (Kim, 2000). For the purpose of gravity field recovery, the effects induced by the gravitational and non-gravitational forces need to be separated. For this reason, the accelerometer measurements are essential, as they provide information about the non-gravitational forces acting on the twin satellites. However, the accelerometer measurements cannot be used directly and have to be calibrated, as they are affected by an instrument specific bias and scale.

With increasing lifetime, GRACE is facing additional challenges due to the degraded battery capacity that limits the availability of power-supply in certain orbital configurations (Herman et al., 2012). To extend the batteries' life-time several measures have been taken to reduce the stress on the batteries (cf. Section 2.6), which allow for a mission prolongation. Due to the reduced battery capacity, active thermal control was permanently switched off in April 2011 (Tapley et al., 2015). Since then, temperature variations directly affect the onboard instruments. To avoid a degradation of the recovered monthly gravity field solutions, the effects of thermal variations on the accelerometer measurements have to be modeled during gravity field recovery. The calibration of the accelerometer data is a rather difficult task, since it is not trivial to distinguish distinctly between sensor error and disturbances induced by the satellite environment.

Apart from gravity field recovery, the calibrated accelerometer observations may also be utilized for the analysis of thermospheric models, especially for analyzing problems related to thermospheric density and wind. The atmospheric density is a limiting factor concerning the model accuracy, and neglected horizontal winds in the upper atmosphere lead to mismodeled accelerations, especially for LEOs (Flury et al., 2008; Dornboos et al., 2009). An improved understanding of the GRACE accelerometer data, in particular the unexpected contributions from satellite-internal effects, may prove useful not only for gravity field recovery, but also for atmosphere research.

The main purpose of this Chapter is to present the method used for accelerometer data calibration within the ITSG-Grace2016 release (Mayer-Gürr et al., 2016a; Klinger et al., 2016), and analyze the temperature-dependency of bias and scale factors. The main characteristics of the SuperSTAR accelerometer on-board GRACE are discussed in Section 5.2, and serve as a basis for the analysis presented hereafter. In Section 7.1, the mathematical background of the calibration method, including the calibration equation for bias and scale estimation, is introduced. Since modeled non-gravitational accelerations serve as input for the two-step calibration approach, the modeled forces (cf. Section 3.3) are compared to the accelerometer

measurements in Section 7.1.4. Sections 7.2 and 7.3 further discuss the estimation of biases and scale factors, present the results of the calibration, and analyze the temporal behavior of the calibration parameters. The impact of the calibration parameterization on the recovered gravity field solutions, especially on the low degree coefficients, is discussed in detail in the successive Chapter 8.

7.1 2-step calibration approach

The linear accelerations contained in the ACC1B data product include an instrument scale and bias offset, i.e. the accelerometer measurements are subject to instrument specific scale factors, biases and random noise. A detailed description of the SuperSTAR accelerometers, the ACC1B science data product, and the AHK1B housekeeping data product are given in Section 5.2.

A general recommendation for the initial estimates of the bias and scale parameters, to apply to the linear ACC1B data, is made in the GRACE Technical Note TN-02 (Bettadpur, 2009). For details on the estimation, the reader is referred to Bettadpur (2009). As the recommendations for biases and scale factors are based on the analysis of data between launch and March 2009, the recommendations will progressively worsen as the epoch of the data moves further into the future. Further, the calibration parameters may vary significantly over the satellite's lifetime due to satellite-induced effects or external influencing factors, such as the activations and de-activations of the onboard heater lines, or temperature variations due to the switch-off of the thermal control.

Over the years, several approaches for the GRACE accelerometer data calibration using derived accelerations from POD have been implemented (e.g., Bezděk, 2010). During gravity field recovery, however, different parameterizations for bias and scale parameters and/or empirical parameters are used by the various analysis centers (e.g., Bettadpur, 2012; Dahle et al., 2013; Meyer et al., 2016). Consequently, the estimated calibration parameters and the recovered gravity field solutions can vary a lot, depending on the employed calibration method and the context of data usage.

The proposed calibration method is a two-step approach, making use use of modeled accelerometer data. The approach is schematically depicted in Figure 7.1.

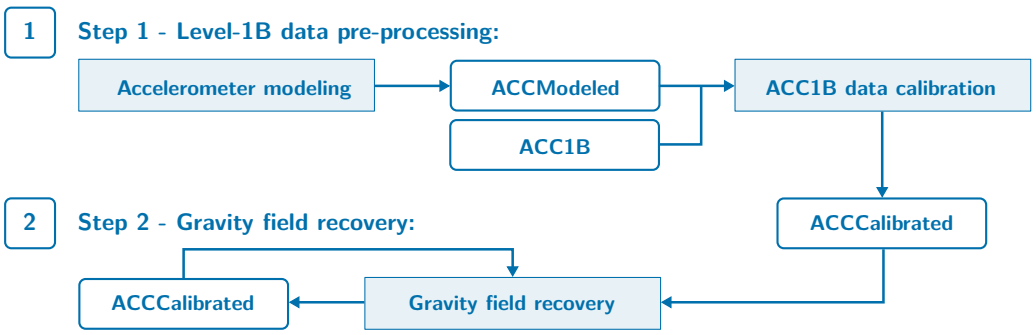

Fig. 7.1.: Schematic overview of the 2-step ACC1B data calibration approach.

In the first step, the modeled non-gravitational accelerations (cf. Section 7.1.4) serve as a reference for the initial calibration of the original ACC1B data, and are also used for data screening purposes. The difference between the modeled and the calibrated accelerometer data is minimized by estimating the calibration parameters (accelerometer biases and scale factors) in a LSA. This in turn enables a data screening step within the Level-1B data pre-processing, as the modeled data serves as reference for a threshold-based outlier detection (cf. Tab. 4.2 in Section 4.3.2). Data which has been affected by thruster firing events (given by the THR1B data product, cf. Section 2.5.2) is not considered during the a priori calibration. Therefore, the thruster-affected data and some additional seconds of data before and after the thruster firing event are excluded. These epochs are excluded from the calibration algorithm to avoid an incorrect calibration and outlier detection, as the thruster firings are not modeled. In the second step, during gravity field recovery, the calibration parameters are re-estimated along with the gravity field parameters. For both steps the same parameterization is applied.

In the following, a short overview of the 2-step calibration approach (cf. Fig. 7.1) is provided. It should be noted that this calibration approach aims at removing effects of instrument imperfections on the gravity field recovery. Thus, the used calibration equation does not guarantee to model these imperfections (e.g., temperature-induced bias drifts, misalignments) in a physical correct way, and are likely to absorb other not-modeled effects.

7.1.1 Calibration equation

As stated in Section 5.2, the linear accelerometer measurements given in the ACC1B data product, are corrupted by unknown scale factors, biases and random noise (Kim, 2000). Within the ITSG-Grace2016 release, both accelerometer biases and scale factors are estimated on a daily basis (cf. Sections 7.1.2 and 7.1.3). The ACC1B data calibration is based on the following calibration equation

$$\mathbf{a}_{\text{cal}} = \mathbf{S}\,\mathbf{a}_{\text{obs}} + \mathbf{b}. \tag{7.1}$$

Herein, $\mathbf{a}_{\text{cal}}$ denotes the calibrated non-gravitational accelerations in the SRF, and $\mathbf{a}_{\text{obs}}$ denotes the original accelerometer measurements (given by ACC1B). The 3x3-scale factor matrix $\mathbf{S}$ multiplies the observed accelerations $\mathbf{a}_{\text{obs}}$, and the bias vector $\mathbf{b}$ is added.

7.1.2 Scale factors

Ideally, the scale factor matrix $\mathbf{S}$ should be an identity matrix with unity main diagonal elements and zero off diagonal elements. But due to small instrument imperfections, which cause a mutual influence of the accelerometer axes among each other, it contains non-unit diagonal elements and non-zero off-diagonal elements. Figure 7.2 illustrates possible accelerometer imperfections. In order to account for these small imperfections, the calibration equation presented in Equation 7.1 uses a fully-populated scale factor matrix. The scale factor matrix

$$\mathbf{S} = \begin{bmatrix} s_x & \alpha+\zeta & \beta-\varepsilon \\ \alpha-\zeta & s_y & \gamma+\delta \\ \beta+\varepsilon & \gamma-\delta & s_z \end{bmatrix} \tag{7.2}$$

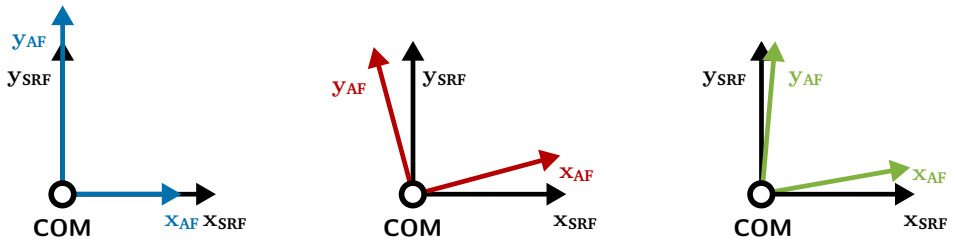

Fig. 7.2.: Illustration of possible accelerometer imperfections, shown for x- and y-axes of the accelerometer (AF): Left: scale factor error (deviation from 1; blue), Middle: misalignment between SRF and AF (red), Right: non-orthogonality of AF axes (cross talk; green).

is composed of both diagonal and off-diagonal elements. The diagonal elements s_x, s_y, s_z influence the magnitude of the observed acceleration components in along-track, cross-track and radial direction, respectively. Based on a small-angle approximation, the off-diagonal elements are composed of a symmetric and a skew-symmetric part: (1) the symmetric shear parameters α, β, γ represent the cross-talk among the axes due to the non-orthogonality of the accelerometer axes, and (2) the skew-symmetric rotation parameters $\zeta, \varepsilon, \delta$ represent the misalignment between SRF and AF, i.e. the accelerometer axes are not fully aligned with the SRF (cf. Fig. 7.2). The initial misalignment originates from the misalignment in installing the accelerometer in the spacecraft (Kim, 2000). As a consequence, the accelerometer axes (AF) do not perfectly coincide with the spacecraft coordinates (SRF).

Before the actual ACC1B data calibration is performed, the GRACE ACC1B data product is initially calibrated according to the GRACE TN-02 (Bettadpur, 2009). Thus, the residuals to the recommended scale factors are estimated, and the scale factor matrix becomes:

$$\mathbf{S} = \begin{bmatrix} s_{x,\text{TN-02}} + \Delta s_x & \alpha + \zeta & \beta - \varepsilon \\ \alpha - \zeta & s_{y,\text{TN-02}} + \Delta s_y & \gamma + \delta \\ \beta + \varepsilon & \gamma - \delta & s_{z,\text{TN-02}} + \Delta s_z \end{bmatrix}, \tag{7.3}$$

with the recommended values $\mathbf{s}_{\text{A, TN-02}} = [0.9595, 09797, 0.9485]^\intercal$ and $\mathbf{s}_{\text{B, TN-02}} = [0.9465, 0.9842, 0.9303]^\intercal$ for GRACE-A and GRACE-B, respectively.

Hitherto, for previous ITSG releases, the off-diagonal elements have been neglected, i.e. the scale factor matrix is assumed to have main diagonal elements only. To account for instrument imperfections, both main diagonal and off-diagonal elements of the scale factor matrix are estimated on a daily basis. Disturbances due to CoM offsets and higher-order scale factors are neglected, but may be a subject to further investigations. At this point, it should be noted that regular CoM calibration maneuvers (cf. Section 4.3.2) are performed to adjust for eccentricities of the accelerometer test mass relative to the satellite's CoM.

7.1.3 Biases

To account for bias drifts due to temperature variations (cf. Fig. 7.6), the biases (cf. Eq. (7.1)) are estimated daily using uniform cubic basis splines (UCBS; De Boor, 2001). UCBS are a special case of basis-splines and are of particular interest due to the simplicity and the efficiency of the induced computations. Uniform means that all knot intervals are equally

spaced, with the basis-splines being shifted copies of each other (cf. Fig. 7.3). On the natural definition domain, there are always 4 non-zero basis functions $b_j (j = 1, \ldots, 4)$ within one knot interval k. The UCBS $N_{i,3}$ are given by

$$N_{i,3} = \begin{cases} b_3 = (1/6)(x^3) & \text{if } x \in [t_i, t_{i+1}[\\ b_2 = (1/6)(-3x^3 + 3x^2 + 3x + 1) & \text{if } x \in [t_{i+1}, t_{i+2}[\\ b_1 = (1/6)(3x^3 - 6x^2 + 4) & \text{if } x \in [t_{i+2}, t_{i+3}[\\ b_0 = (1/6)(-x^3 + 3x^2 - 3x + 1) & \text{if } x \in [t_{i+3}, t_{i+4}] \\ 0 & \text{otherwise} \end{cases} . \tag{7.4}$$

The number of parameters to define a UCBS depends on both the degree $(d = 3)$, and on the number of knot intervals. For the purpose of ACC1B data calibration, the knot interval length is set to 6 hours $(k = 4)$. In sum, 21 parameters $(3(d + k))$ are needed per day and satellite for the bias estimation. This parameterization guarantees continuity of the estimated bias within one day. Compared to higher degree polynomials $(d \geq 6)$, UCBS offer a good alternative with the advantage of a lower (or equal) number of parameters and reduced oscillation effects on the boundaries (cf. Fig. 7.4).

Figure 7.3 illustrates the basic concept of UCBS, and their application for the ACC1B bias estimation.

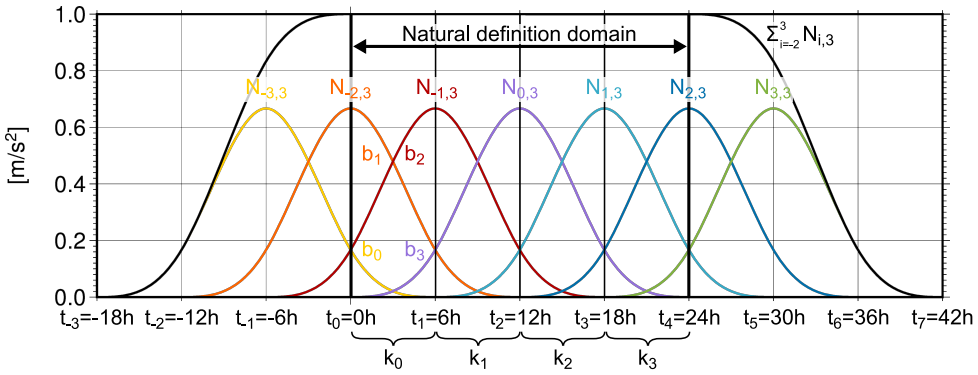

(a) UCBS - Basic definition

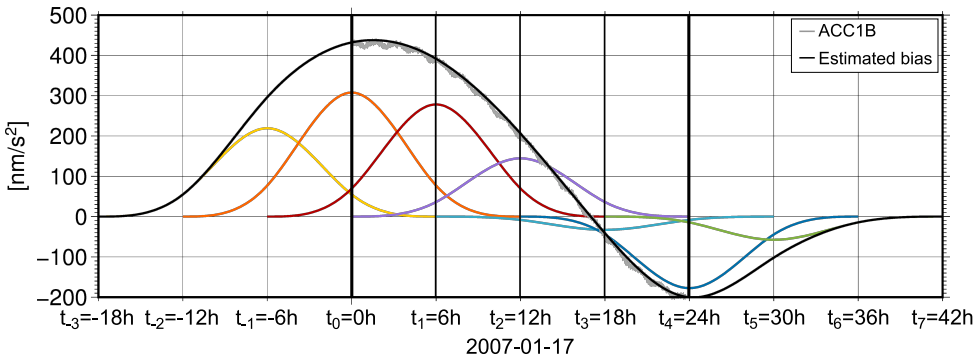

(b) UCBS - ACC1B bias estimation (cross-track)

Fig. 7.3.: Illustration of UCBS: (a) Basic concept: Basis-splines (color) and resulting curve (black) for 4 knot intervals, (b) Estimated basis splines (color) and resultant ACC1B bias (black) w.r.t. the ACC1B cross-track accelerations (gray). The estimated bias refers to one day $(t_0 - t_4)$, i.e. the natural definition domain of the UCBS.

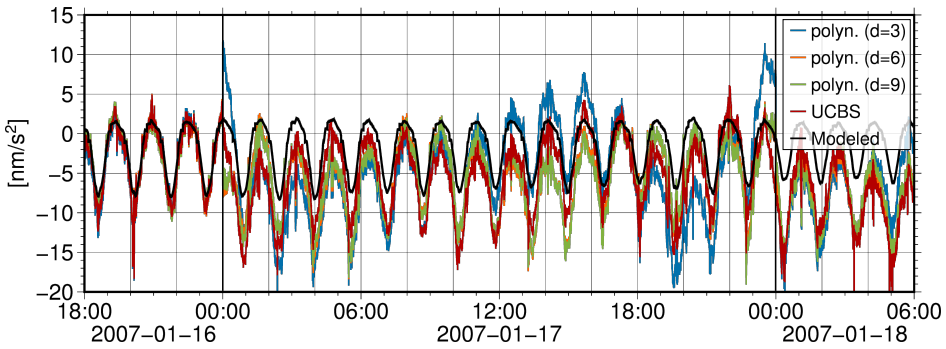

Fig. 7.4.: Bias-reduced cross-track accelerations with the bias estimated based on a polynomial of degree 3 (blue), degree 6 (orange), degree 9 (green), or UCBS (red). For all four solutions, the estimation interval is set to 1 day, and modeled cross-track accelerations (black) serve as reference for the bias estimation. For the UCBS, a knot interval of 6 h is used, guaranteeing continuity within one day.

Figure 7.4 shows a comparison between bias-reduced cross-track accelerations, where the bias estimation is based on either polynomials (estimation interval: 1 day) or UCBS (estimation interval: 1 day with a knot length of 6 h). From this figure it becomes evident, that with UCBS the oscillations at the day-boundaries can be reduced compared to polynomials, and also variations during the day can be reduced w.r.t. the modeled cross-track accelerations.

For the ITSG-Grace gravity field recovery, different knot interval lengths (e.g., 12 h, 6 h, 3 h) were tested and compared. A knot interval length of 6 hours achieves the best results in terms of degree amplitudes, EWH RMS values, and post-fit range rate residuals (cf. Section 8.3, not shown here). Besides, it introduces a reasonable number of additional parameters, not affecting the solvability of the whole normal equation system.

7.1.4 Modeled non-gravitational accelerations

The linear accelerations in along-track, cross-track, and radial direction are modeled according to Section 3.3, and are used as input for the first step of the ACC1B data calibration approach (cf. Section 7.1.1). Figure 7.5 shows the modeled non-gravitational accelerations in along-track, cross-track and radial direction in comparison to the bias-corrected ACC1B accelerometer measurements for two selected 6 h periods on 2007-01-20 and 2015-01-20, respectively. The spikes within the ACC1B accelerometer measurements correspond to epochs with thruster firing events. As both GRACE satellites are identical and show a similar behavior, the analysis is confined to one satellite, namely GRACE-A.

From Figure 7.5 (a, c, e) it becomes obvious, that for higher orbit altitudes (~ 475 km) the bias-corrected ACC1B data shows a good agreement with the modeled accelerations. Whereas, for lower orbit altitudes (~ 410 km, cf. Fig. 7.5 (b, d, f)), the along-track component shows larger inconsistencies. Note that the scaling for the accelerations in Figures 7.5(a) and 7.5(b) is different, due to the increasing magnitude of the along-track accelerations.

With increasing lifetime, the orbital altitude of the GRACE satellites is constantly decreasing (cf. Fig. 7.11(b)). Due to the accompanying increase in atmospheric density (cf. Fig. 7.10(b)), the atmospheric drag also increases accordingly. Consequently, the 65 km altitude decrease (from 2007-01-20 to 2015-01-20) goes along with a significant increase in along-track accel-

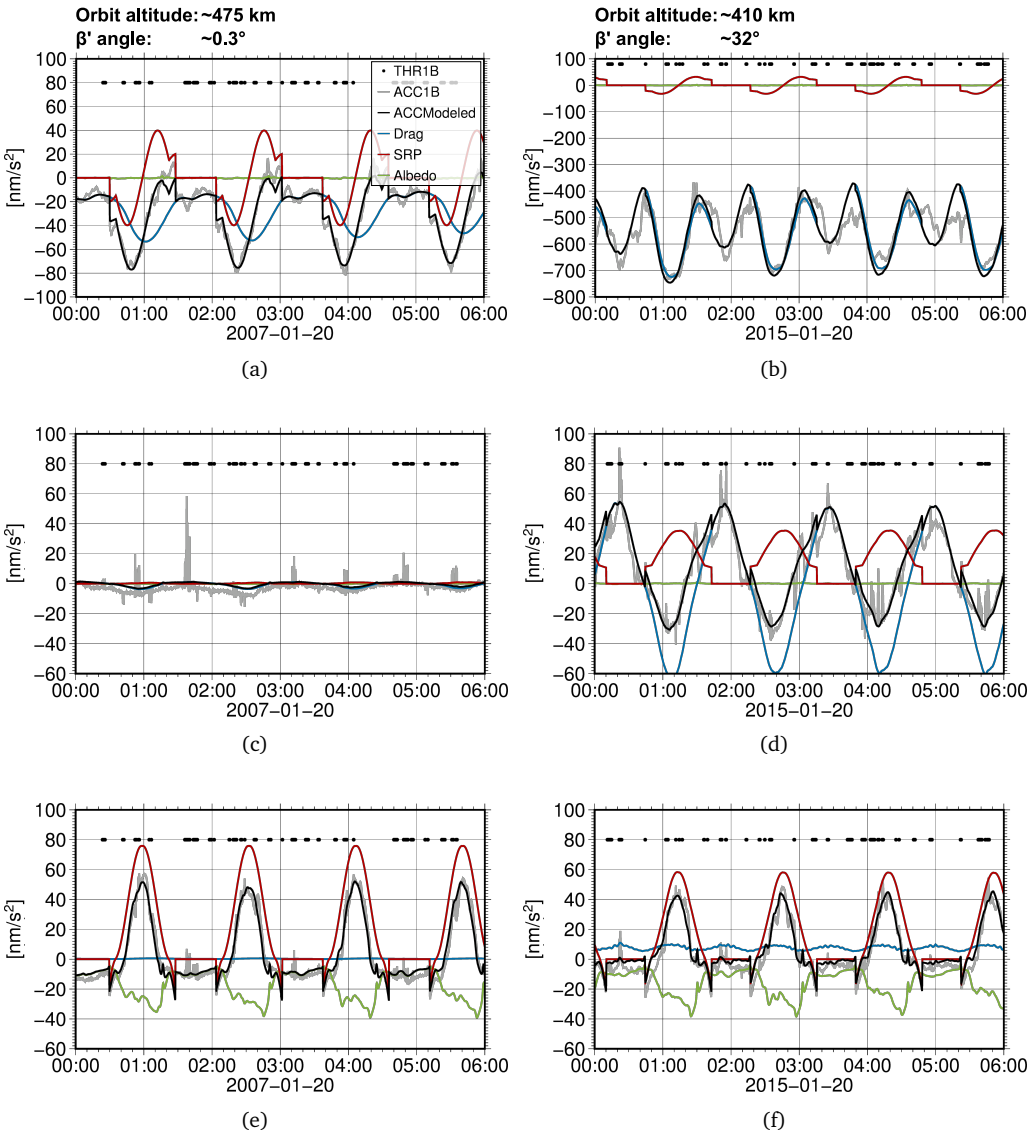

Fig. 7.5.: Modeled non-gravitational accelerations (black) and ACC1B data (gray) in along-track (a, b), cross-track (c, d) and radial direction (e, f). Here, the ACC1B data is bias corrected. The non-gravitational accelerations for GRACE-A are shown for a 6 h segment on 2007-01-20 and 2015-01-20. The individual compartments of the modeled non-gravitational accelerations are shown in color: atmospheric drag (blue), SRP (red), and Albedo (green). Note that the scaling for (a) and (b) is different. The black dots indicate epochs with thruster firings.

erations (cf. Figs. 7.5(a) and 7.5(b)). With decreasing orbit altitude, the comparison with the bias-corrected accelerometer measurements in along-track reveals significant differences between the model (DTM2013) and the measurements (cf. Fig. 7.5(b)), regardless of the used air drag model (not shown here). For 2015-01-20, the DTM2013 model seems to overestimate the amplitudes. In general, even the most recent atmospheric models have consistent errors, which may not be detected by a model inter-comparison ((e.g., geomagnetic storms; Willis et al., 2005)). Possible reasons for the discrepancy in Figure 7.5(b) are that the accelerometer measurements are scaled due to temperature variations and/or the model overestimates the accelerations caused by atmospheric drag, or the drag coefficient, which "scales" the modeled accelerations (cf. Eq. 3.17), is not constant and changes over time. It is

assumed that the problem lies either in the used air density model or the used constant drag coefficient (cf. Tab. 3.1), as the magnitude of the other effects (SRP, albedo) is several orders of magnitude smaller than the effects caused by the atmospheric drag (cf. Fig. 7.5(b)). This topic needs to be investigated further, but is beyond the scope of this thesis.

Beside the orbit altitude, also the orbital configuration with respect to the Sun changes. The mean β' angle for the first period (2007-01-20) is approximately $0.3°$, i.e. the satellite spends nearly half of the revolution time in the Earth's shadow, as the Sun is in its orbital plane. Hence, the accelerations in cross-track direction due to solar radiation pressure are close to zero (cf. Fig. 7.5(c)). For the second period (2015-01-20), the mean β' angle increases to approximately $32°$, with the cross-track accelerations due to solar radiation pressure increasing accordingly (cf. Fig. 7.5(d)). Due to the increase in both atmospheric drag and SRP, the overall modeled accelerations in cross-track direction of the second period are larger as compared to the first period (cf. Figs. 7.5(c) and 7.5(d)). The accelerations in radial direction reveal the smallest differences, mainly caused by a decrease of the incoming solar radiation affecting the rear panel for the later period (cf. Figs. 7.5(e) and 7.5(f)).

In general, the modeled accelerations show a good overall agreement with the bias-corrected measured ACC1B accelerations. Therefore, it seems reasonable to use the modeled accelerations for an a priori calibration of the ACC1B data during the first step of the presented calibration approach (cf. Fig. 7.1, cf. Section 7.1).

7.2 Biases

In the following, the causes of temperature-induced bias drifts are discussed in detail, and the ability of the presented calibration approach to reduce the effects of the bias drifts on the ACC1B data is demonstrated.

7.2.1 Temperature-dependency

In a thermally controlled environment, which keeps the temperature variations below 0.1 K per revolution (Stanton et al., 1998), the GRACE accelerometer are not subject to rapidly changing bias offsets or bias drifts. But, thermal distortions within the satellite environment caused by occasional disabling of heater lines (before April 2011), or by the non-active thermal control (after April 2011), directly affect the accelerometer measurements in terms of temporary bias drifts. From April 2011 onward, when the active thermal control was permanently switched-off, the temperature variations strongly increased (cf. Fig. 2.7), leading to more frequent bias drifts, especially deteriorating the less-sensitive cross-track axis of the accelerometer measurements.

The occurring temperature variations (>5 K/161 d) are highly correlated with the β' angle variations, describing the orbital configuration w.r.t. the Sun (cf. Appendix D.2). The 161-day periodic β' angle variations induce an alternating heating and cooling of the satellite, which directly affects the on-board accelerometer. Approaching full-sun orbit, when the satellite's orbital plane is nearly perpendicular to the Earth-Sun line ($\beta' > 70°$), the heating mainly affects the cross-track component, as the satellite is primarily illuminated at the side panels

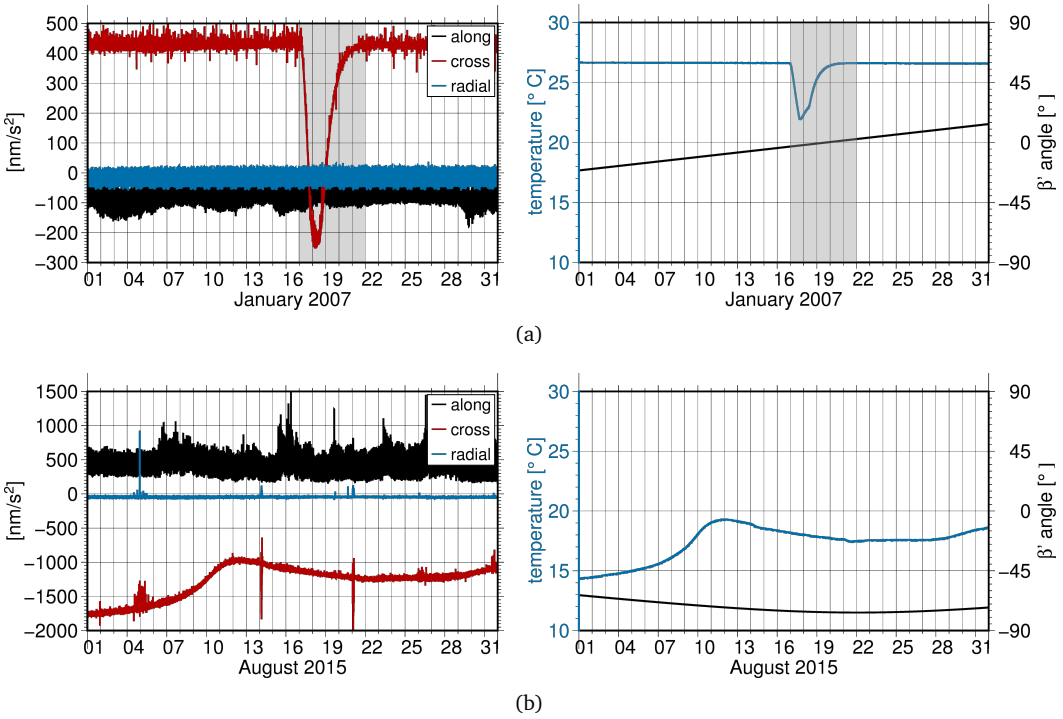

Fig. 7.6.: GRACE-A ACC1B and AHK1B data product for (a) January 2007 and (b) August 2015: Left column: ACC1B accelerometer measurements in along-track (black), cross-track (red), and radial (blue) direction. The accelerometer measurements are calibrated according to the initial recommendations in TN-02 (Bettadpur, 2009). Right column: AHK1B accelerometer housekeeping data in terms of core temperatures (blue), and the corresponding β' angle variations (black).

(cf. Fig. 5.13) (Herman et al., 2012). Following from this, the cross-track axis experiences the strongest bias drifts during these periods.

Figure 7.6 shows the ACC1B accelerometer measurements, and the core temperatures obtained from the AHK1B data product for two different month (January 2007, August 2015), for GRACE-A. As obvious from this figures, the less-sensitive cross-track axis of the accelerometer shows not only a constant bias offset, but also temperature-dependent bias drifts. The latter are caused by different reasons: (1) a cool-down of the accelerometer due to a disabling of the supplemental heater lines (January 2007), and (2) a temperature increase due to the orbital configuration of the satellite (August 2015). Clearly, the bias drifts directly depend on the magnitude of the induced temperature variations. In the case of a single event causing a short-time deviation from a stabilized temperature, the bias drift also shows a temperature-dependent time-lagged behavior, with the relevant periods highlighted in gray in Figure 7.6(a). In the case of an inactive thermal control, the temperature variations are directly correlated to the variations of the β' angle (cf. right panels of Fig. 7.6(a) and Fig. 7.6(b)).

As the temperature variations are well observed with respect to timing and magnitude, the ACC1B accelerometer measurements can be directly compared to the corresponding AHK1B housekeeping data product. Figure 7.7 shows scatter plots of the cross-track accelerations vs. the core temperature, before and after calibration. The mutual comparison of both data sets, before the calibration of the ACC1B data product, illustrates the accelerometers sensitivity to

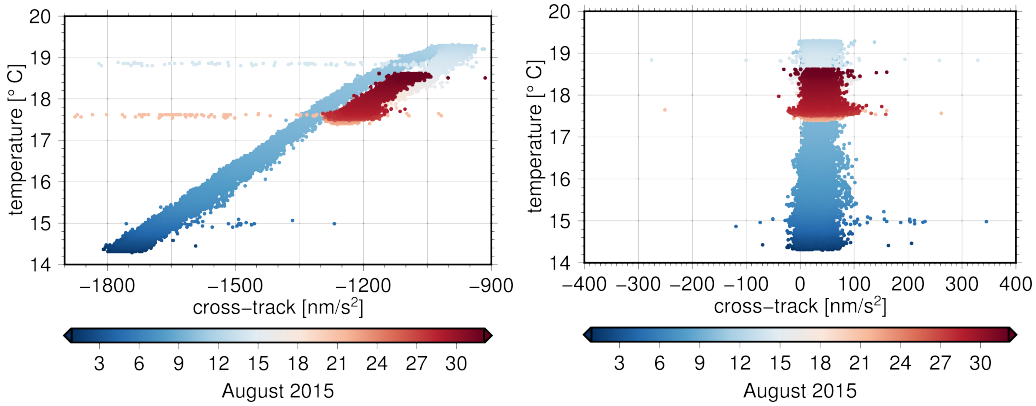

(a) ACC1B (b) Bias-reduced ACC1B

Fig. 7.7.: Scatter plot: GRACE-A ACC1B accelerometer measurements in cross-track direction in direct comparison with the AHK1B core temperatures, for August 2015. The results are shown (a) before, and (b) after the bias reduction according to the ACC1B data calibration approach. The accelerometer measurements in (a) are calibrated according to the initial recommendations in TN-02 (Bettadpur, 2009). The colorbar serves as time-reference, indicating the day of the month.

satellite-internal temperature variations (cf. Fig. 7.7(a)). This proves the difficulty of creating an environment onboard the satellites free from disturbing effects on the accelerometers. After the first step of the ACC1B data calibration (cf. Section 7.1), the diagonal structure in Figure 7.7(a) becomes a vertical structure in Figure 7.7(b), indicating a successful reduction of the temperature-dependent bias drifts.

By comparing the linear accelerations contained within the ACC1B data product (calibrated according to TN-02 (Bettadpur, 2009)) with the calibrated accelerations (cf. Fig. 7.7 and Fig. 7.8), it becomes obvious that the temperature-induced bias drifts can be reduced successfully using daily UCBS (cf. Section 7.1.3). Therefore, these results serve as a validation-basis for the two-step calibration approach introduced in Section 7.1.

Figure 7.8 shows the calibrated ACC1B accelerometer data in along-track, cross-track, and radial direction, for January 2007 and August 2015. The results refer to the first-step of the accelerometer data calibration approach, i.e. the bias-drift is estimated based on the modeled accelerometer data (cf. Section 7.1.4). As expected, the bias offset and bias drift are not present within the a priori calibrated ACC1B data anymore. Especially the temperature-induced effects on the cross-track axis are notably reduced. Within this section only analysis and results for GRACE-A are shown, since very similar results have been obtained for GRACE-B.

The presented analysis is restricted to the analysis of temperature-related bias drifts, based on inter-comparisons between the uncalibrated (ACC1B RL02) and calibrated ACC1B data. It does not contain any values of estimated biases, since they are not directly comparable to the recommended values proposed in the GRACE Technical Note TN-02 (Bettadpur, 2009). The calibration approach described above is based on UCBS. Therefore, the estimated biases are represented by 7 parameters (per axis and day), representing the fit of the UCBS basis functions to the observations. These parameters are not intuitively comprehensible, which makes a direct comparison to other estimates not feasible.

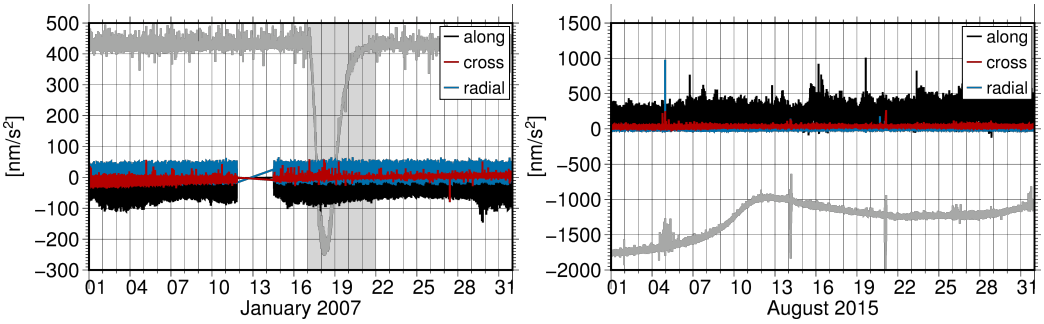

Fig. 7.8.: Calibrated GRACE-A ACC1B data product for (a) Januray 2007 and (b) August 2015: Bias-reduced ACC1B accelerometer measurements in along-track (black), cross-track (red), and radial (blue) direction. As a reference, the original ACC1B cross-track accelerations (calibrated according to TN-02 (Bettadpur, 2009)) are shown in gray.

7.3 Scale factors

Based on the two-step calibration approach introduced in Section 7.1.1, the scale factors are estimated on a daily basis during Level-1B data pre-processing and gravity field recovery (together with the biases). In the following, the results for the main-diagonal and off-diagonal elements of the scale factor matrix are analyzed in detail.

Figure 7.9 shows the estimated elements of the fully-populated scale factor matrix, namely the main-diagonal elements (a, b), and the off-diagonal elements (c, d), for GRACE-A. Evidently, the main-diagonal elements of the cross-track axis (cf. Fig. 7.9(a)) cannot be determined as good as the main-diagonal elements of the along-track and radial axes. This more scattered behavior is most likely due to the reduced sensitivity of the cross-track axis. Additionally, the shear and rotational elements associated with the less-sensitive cross-track axis (cf. Fig. 7.9(c) and 7.9(d)) are non-zero and not constant over time, due to the non-orthogonality of the accelerometer axes and a misalignment between the SRF and AF. Figure 7.9(b) provides a more detailed time series of the main-diagonal elements in along-track and radial direction, which reflects the fact that the high-sensitive axes are both better estimable. Another factor influencing the estimation quality of the scale factors, is the composition and magnitude of the non-gravitational accelerations. Small signals, mainly affecting the cross-track and radial axes, cause singularity problems deteriorating the estimates. However, all estimates show temporal variations not comparable to the constant behavior assumed in TN-02 (Bettadpur, 2009). From Figure 7.9 it becomes evident that after April 2011, the temperature variations are absorbed by the calibration parameters and directly map into the time series of calibration parameters. From Figures 7.9(c) and 7.9(d) it becomes also obvious that the shear and rotational elements of the scale factor matrix are highly correlated, since the non-orthogonality of the accelerometer axes and the misalignment (between SRF and AF) both affect the accelerometer measurements through interference and are closely linked to each other. To some extent the variations of the estimated off-diagonal elements probably reflect the instrument behavior, as a temperature-dependent behavior of the SCA frame was also shown by Harvey (2016). But, most likely they also absorb some other effects, which are not modeled in a physically correct way

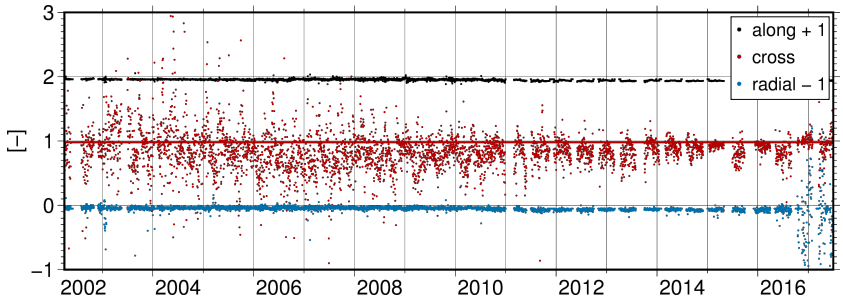

(a) main-diagonal elements (s_x, s_y, s_z)

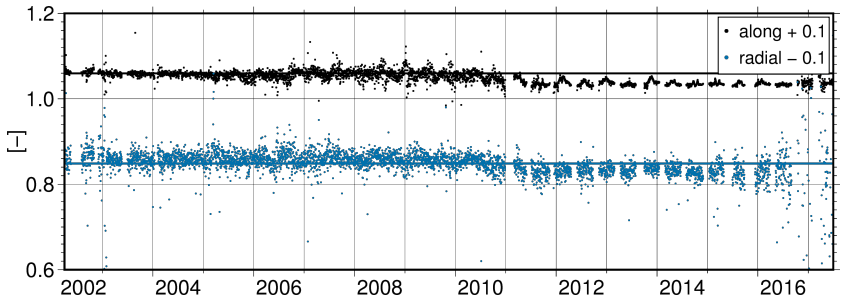

(b) main-diagonal elements (s_x, s_z)

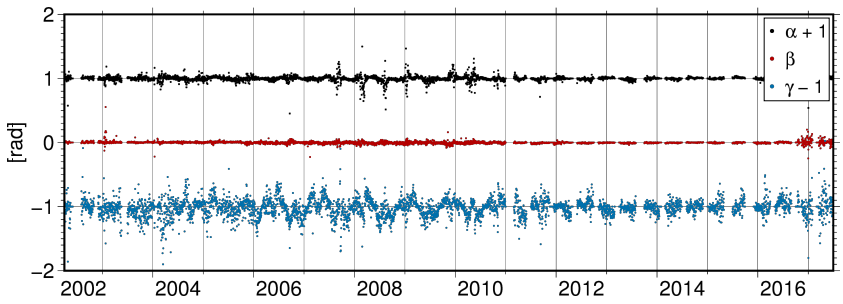

(c) shear elements (α, β, γ)

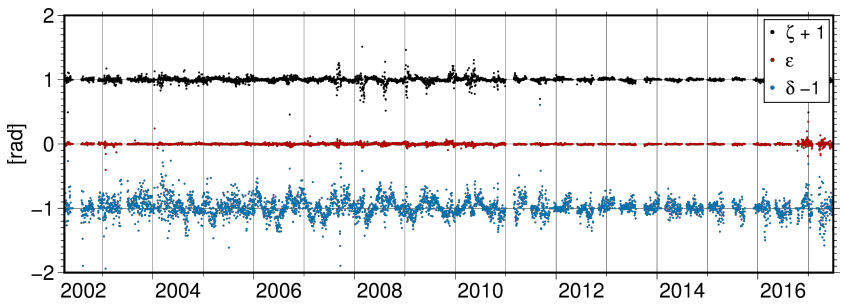

(d) rotational elements $(\zeta, \varepsilon, \delta)$

Fig. 7.9.: Elements of the scale factor matrix: (a) main diagonal elements in along-track (black), cross-track (red), and radial (blue) direction, (b) zoom-in of the main-diagonal elements in along-track and radial direction, (c) shear elements α (black), β (red), γ (blue), and (d) rotational elements ζ (black), ϵ (red) and δ (blue) for GRACE-A. The daily estimates for the whole GRACE mission period (April 2002 to June 2017) are shown. The colored lines in (a) and (b) correspond to to the recommended scale factors from TN-02 (Bettadpur, 2009). For a better illustration, a constant offset of ± 1 (a,c,d) or ± 0.1 (b) is added to the black and blue graphs.

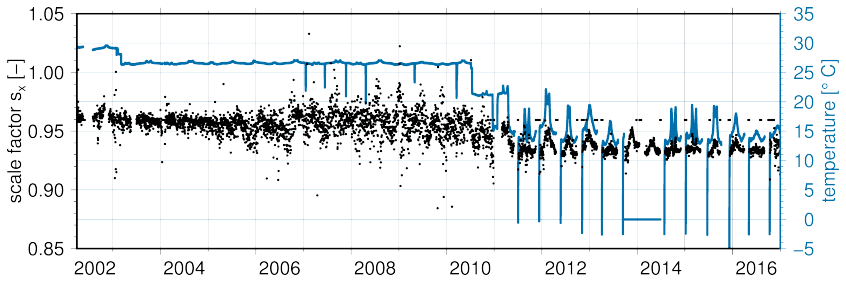

(a) temperature

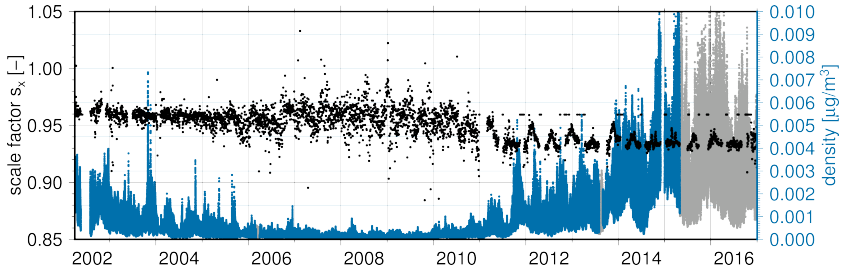

(b) density

Fig. 7.10.: Temporal evolution of estimated scale factors s_x in along-track direction for GRACE-A (black) compared to (a) the accelerometer core-temperature (blue) and (b) the atmospheric densities derived from DTM2013 (blue) and JB08 (gray), for the whole GRACE time period (April 2002 to June 2017). The atmospheric density data from the DTM2013 model is currently only available until 2015-06-20. Note that the magnitude of the atmospheric densities in (b) is given in $\mu g/m^3$.

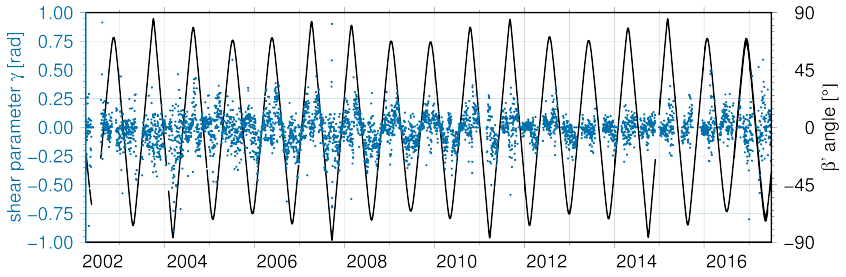

(a) β' angle

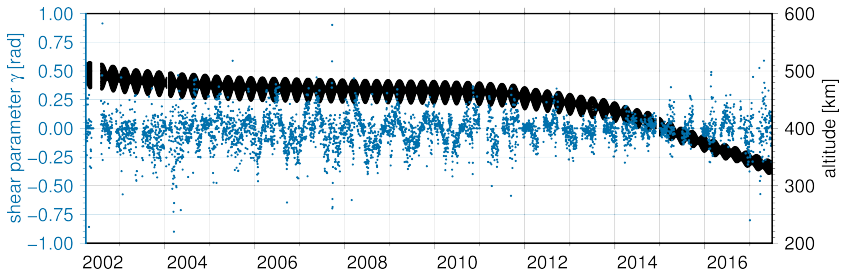

(b) altitude

Fig. 7.11.: Temporal evolution of estimated shear parameter γ (blue) and the corresponding (a) β' prime angle variations (black) and (b) orbital altitude for GRACE-A, for the whole GRACE time period (April 2002 to June 2017). The shear parameter γ represents the cross-talk among the cross-track and radial axes due to the non-orthogonality of the accelerometer axes.

(e.g., temperature variations not captured by the bias model), or which are not modeled at all (cf. Eq. 7.3).

A significant temperature-dependency of the estimated scale factors is demonstrated in Figure 7.10(a), showing the temporal evolution of the estimated scale factors in along-track direction and the accelerometer core-temperatures, for GRACE-A respectively. During active thermal control (from April 2002 to March 2011), the estimated parameters are characterized by a more constant, but scattered behavior. Afterwards, from April 2011 onward, the scale factors show a periodic variability, which is highly correlated to the occurring temperature variations. As aforementioned, the temperature variations themselves depend on the orbital configuration w.r.t. to the Sun, and are related to the β' angle variations (with a 161-day period, cf. Fig. 7.11(a)). From Figure 7.10(b), showing the estimated scale factors in along-track direction and the atmospheric densities derived from the DTM2013 and JB08 model (cf. Section 3.3.5), it is evident that the scale factors are better estimable for periods with higher atmospheric densities (2002 to 2005, 2011 to 2016). This is because, the non-gravitational forces acting in along-track direction grow larger with increasing atmospheric densities (cf. Eq. 3.17), and a larger non-gravitational signal facilitates the scale factor estimation. The variations in the atmospheric density (cf. Fig. 7.10(b)) are closely linked to the solar activity (solar flux) and the geomagnetic activity (Bruinsma, 2014). From 2011 onward, the increasing density is not only related to an increased solar activity, but also to the constantly decreasing orbit altitude of the GRACE satellites (cf. Fig. 7.11(b)).

Figure 7.11(a) shows a direct comparison of the temporal evolution of the estimated shear parameters γ and the β' angle variations. The 161-day periodic signal contained within the time series of the estimated shear elements γ and the rotational elements δ (cf. Figs. 7.9(c) and 7.9(d)) is highly correlated with the β' angle variations, representing different orbit configurations w.r.t. the Sun. This behavior supports the hypothesis that temperature variations due to the orbital configuration cause varying thermal distortions affecting the accelerometer axes. Both parameters, γ and δ, represent the mutual influence among the cross-track and radial axes, due to the non-orthogonality of the AF and due to the misalignment between AF and SRF. Because these instrument imperfections affect the accelerometer measurements through interference from other axis components, their magnitudes are dependent on the magnitude of the actual non-gravitational accelerations (Roesset, 2003). In other words, the misalignment errors grow with increasing non-gravitational accelerations, and are more significant for lower altitudes where larger atmospheric drag is present. Hence, with increasing signal strength of the non-gravitational forces the estimates improve. Higher altitudes and small temperature variations (e.g., during active thermal control; cf. Fig. 7.11(b) and Fig. 7.10(a)) seem to complicate the parameter estimation, leading to a more scattered behavior. However, the 161-day variations within the calibration parameters (γ, δ; cf. Figs. 7.9(c) and 7.9(d)) may also result from the absorption of other spurious signals, which are not modeled, not modeled physically correct, or not accelerometer induced (e.g., CoM offset, attitude errors, etc.). In general, the quality of the estimation results depends on the ability to model the underlying process, which causes the disturbances.

Based on the analysis of the estimated biases and scale factors, it is shown that the three-axis electrostatic accelerometers onboard the GRACE satellites are extremely sensitive to satellite-internal temperature variations. Since April 2011, temperature variations are permanently present due to the switched-off thermal control and directly affect the accelerometer mea-

surements. As a consequence, the temperature-induced accelerometer perturbations have to be modeled adequately during gravity field recovery in order to avoid a corruption of the monthly gravity field solutions. The impact of the ACC1B data calibration on the recovered gravity field solutions is analyzed in Chapter 8.

7.4 Further options - GRACE ACC data processing

The improved understanding of satellite-induced perturbations acting on the GRACE accelerometers is essential not only for increasing the accuracy of present gravity field solutions, but also for the development and evaluation of future gravity field missions, such as GRACE-FO. The presented analysis of the temperature-dependent behavior of the accelerometer scale factors and biases may be seen as a contribution to a step-by-step improvement in the understanding of the complex GRACE accelerometer data. The experience and knowledge gained from GRACE accelerometer data can to some extent be transferred to other missions (e.g., GRACE-FO), as they might be subject to some of the same effects.

Concerning the proposed two-step ACC1B data calibration approach, there are several issues which require further investigation. As previously mentioned, the proposed approach aims at improving the gravity field recovery and does not guarantee a physically correct model. Therefore, it is most important to further analyze the ideal parameterization of the calibration equation, as deficiencies in the modeling are a limiting factor. The setup of calibration parameters is likely to absorb mismodeled or non-accelerometer induced spurious signals that otherwise map into the gravity field coefficients. This further analysis, however, is beyond the scope of this thesis. An intercomparison with POD-derived calibration parameters might also reveal useful insights into the problems and deficiencies of the current calibration approach.

A more realistic modeling of the non-gravitational accelerations, by further improving the atmospheric drag, solar radiation, and albedo modeling (e.g., finite element satellite model, model inter-comparisons, co-estimation of drag coefficients), might contribute to an improvement of the a priori calibration of the ACC1B data (within the first step of the calibration approach). However, it is not assumed that this will have any significant effect on the recovered gravity field solutions.

Progress in the understanding of the complex GRACE accelerometer data may also prove useful for atmosphere research. Apart from the utilization of non-gravitational accelerations for the purpose of gravity field recovery, another possible field of application is empirical atmospheric density modeling, i.e. transforming the accelerations into scientifically valuable thermospheric densities (cf. e.g., Siemes et al. (2016)). The GRACE accelerometer measurements, together with observations from other satellite missions, can be used for the analysis and improvement of current thermospheric models. Particularly later periods of the GRACE mission, might provide invaluable observations of the lower thermosphere. Even the most recent thermospheric models have consistent errors, which cannot be detected by model inter-comparisons only (Willis et al., 2005). One major factor limiting the model accuracy is the atmospheric density. Errors within model-derived densities lead to mismodeled non-gravitational accelerations, especially for LEOs (Flury et al., 2008; Dornboos et al., 2009). Thus, both scientific communities can benefit from collaborations on this topic.

8 Validation - Impact on temporal gravity field solutions

As a consequence of the previously introduced Level-1B data pre-processing methodologies, the following question arises: “What is the impact of the data pre-processing steps, individually and/or in total, on the recovered monthly GRACE gravity field solutions?”. To answer this, the impact of the introduced Level-1B data pre-processing methodologies, including the fully-automated data screening (cf. Section 4.3.2), the sensor fusion approach (cf. Section 6.3), and the ACC1B data calibration (cf. Section 7), on the recovered monthly gravity field solutions is analyzed and validated within this Chapter. The aim is to demonstrate the contribution of the data pre-processing steps to the overall accuracy of the recovered gravity field solutions, and to show the applicability of the introduced methodologies within the gravity field processing chain.

The validation of the recovered gravity field solutions is based on comparisons of spherical harmonic coefficients and post-fit range rate residuals. The recovered spherical harmonic coefficients are analyzed within two domains: (1) in the spectral domain - in terms of degree amplitudes, coefficient triangles, coefficient time series, and (2) in the spatial domain - in terms of EWHs on a global grid. Since the development of the introduced methodologies were originally based on the ITSG-Grace2014 release (Mayer-Gürr et al., 2014), the results are internally validated against the previous and current ITSG releases (ITSG-Grace2014, ITSG-Grace2016). Both releases are a good benchmark to asses any changes within the processing chain. Externally, an overall comparison is done with respect to the latest temporal gravity field models provided by two of the official GRACE processing centers, namely CSR RL05 (Bettadpur, 2012) and GFZ RL05a (Dahle et al., 2013).

In the following, both the effects of the individual pre-processing methodologies as well as their combined effect on the recovered monthly gravity field solutions are analyzed in detail. In Section 8.1, the characteristics of the ITSG-Grace releases used for the internal validation are shortly introduced. In Section 8.2, the impact of the use of a combined star camera data product (SCAFusion) is discussed. In Section 8.3, the effects of both the fully-automated data screening, and the ACC1B data calibration by the two-step calibration approach are analyzed step-by-step in the spectral and spatial domain. Besides, the effect of the accelerometer data calibration on the estimated C20 coefficients is discussed in-depth. In summary, this Chapter is intended to give an overview of the contributions of the individual Level-1B data pre-processing steps, and contain a detailed analysis of their impact on the recovered gravity field solutions. Thus, it provides a detailed evaluation of the methodologies and approaches introduced within this work.

8.1 ITSG-Grace releases

The subsequently presented analysis are based on: (1) the ITSG-Grace2014 release (Mayer-Gürr et al., 2014), and (2) the ITSG-Grace2016 release (Mayer-Gürr et al., 2016b)(cf. Section 4). Both time series of monthly gravity field solutions are publicly available for download at the website of the IfG[1,2] or at the ICGEM website[3].

Table 8.1 gives an overview of the ITSG-Grace2014 and ITSG-Grace2016 processing chains, summarizing some processing details, the used background models, the restored models, the estimated non-gravity parameters, and the used GRACE Level-1B data products.

Tab. 8.1.: ITSG-Grace2014 and ITSG-Grace2016 processing settings.

	ITSG-Grace2014	**ITSG-Grace2016**
Method		
Arc Length	24 h	24 h
Covariance Length	6 h	3 h
Background models		
Earth rotation	IERS 2003 [a]	IERS 2010 [b]
Third body forces	JPL DE421 [c]	JPL DE421
Solid earth tides	IERS 2003	IERS 2010
Pole tides	IERS 2003	IERS2010
Ocean tides	EOT11a [d]	EOT11a
Ocean pole tides	Desai 2004 [e]	Desai 2004
Atmospheric tides	Bode-Biancale 2003 [f]	Van Dam & Ray 2010 [g]
Dealiasing	AOD1B RL05 [h]	AOD1B RL05
Relativistic effects	IERS 2003	IERS 2010
Restored models		
Static field	GOCO03s [i]	GOCO05s [j]
Trend, Annual	ITG-Grace2010 [k]	GOCO05s
Non-gravity parameters		
Satellite state vector	once a day	once a day
Accelerometer bias	polynomial (degree 3)	UCBS (6 h knot interval)
	once a day & axis	once a day & axis
Accelerometer scale	main-diagonal elements	fully-populated
	once a day	once a day
KBR antenna center	once a month	x (once a month)
Data products		
Release	Level-1B RL02	Level-1B RL02
Star camera	SCAFusion [*]	SCAFusion
Kinematic orbits	IfG [**]	IfG

[a]McCarthy and Petit (2003), [b]Petit and Luzum (2010), [c]Folkner et al. (2009), [d]Savcenko et al. (2012), [e]Desai (2002), [f]Biancale and Bode (2006), [g]van Dam and Ray (2010), [h]Flechtner et al. (2015), [i]Mayer-Gürr et al. (2012), [j]Mayer-Gürr et al. (2015), [k]Mayer-Gürr et al. (2010)

[*]Klinger and Mayer-Gürr (2014), [**]Zehentner and Mayer-Gürr (2015)

[1]ITSG-Grace2014: `tugraz.at/institute/ifg/downloads/gravity-field-models/itsg-grace2014/`
[2]ITSG-Grace2016: `ifg.tugraz.at/ITSG-Grace2016`
[3]`icgem.gfz-potsdam.de/series/02_GRACE_monthly_other`

The ITSG-Grace2016 release is the official successor to the ITSG-Grace2014 release. Multiple improvements have been implemented within the gravity field processing chain, including:

- Updated background models,
- A fully automated data screening step (cf. Section 4.3.2),
- Improved accelerometer data calibration (cf. Section 7; Klinger and Mayer-Gürr, 2016),
- Improved covariance function estimation,
- Numerical orbit integration (Ellmer and Mayer-Gürr, 2017b),
- Co-estimation of daily variations (Kvas et al., 2016).

The use of the combined attitude data product (cf. Section 6.3), was already part of the ITSG-Grace2014 processing chain. The improvements not related to the Level-1B data pre-processing are not further discussed here. These processing steps are done partly prior or within the gravity field recovery, and are independent of the pre-processing methodologies introduced here.

In general, the improved processing contributes significantly to the overall accuracy of the monthly gravity field solutions. A noise reduction with respect to ITSG-Grace2014 in the order of 20-40% can be achieved (cf. Fig. 8.1; Horwath et al., 2016; Klinger et al., 2016). An overall comparison of the ITSG releases (ITSG-Grace2014, ITSG-Grace2016) with the monthly gravity field solutions of the official processing centers (CSR RL05 (Bettadpur, 2012), GFZ RL05a (Dahle et al., 2013)) is shown in Figure 8.1. From this comparison, the differences in the accuracy levels between the ITSG releases and between the different processing centers become apparent. Overall, the ITSG-Grace2016 release shows the lowest noise level, which is also a result of the processing chain. The missing month (white lines) are occurring due to missing GRACE instrument data (cf. Section 2.6).

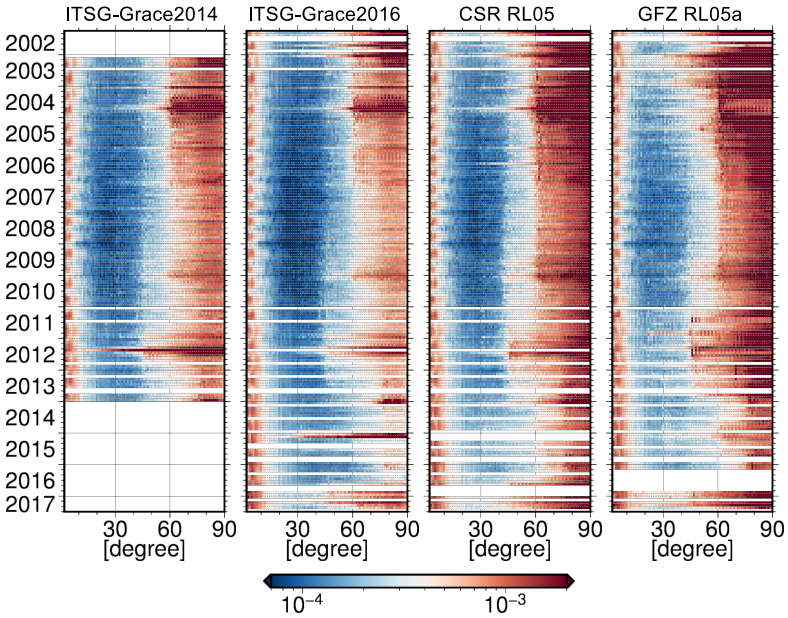

Fig. 8.1.: Degree amplitudes for the whole GRACE mission period (April 2002 to June 2017): ITSG-Grace2014, ITSG-Grace2016, CSR RL05, and GFZ RL05a. The difference degree amplitudes w.r.t. to the GOCO05s (Mayer-Gürr et al., 2015) are shown. Note that the ITSG-Grace2014 release is only available between February 2003 and June 2014.

8.2 Sensor Fusion

The effect of the sensor fusion, i.e. the use of a combined attitude data product (cf. Section 6), on the recovered monthly gravity field solution is analyzed on the basis of the ITSG-Grace2016 release. Therefore, two scenarios are compared, which differ only with respect to the star camera data product used as input for the GRACE gravity field recovery: (1) the original SCA1B RL02 data product, and (2) the combined SCAFusion data product. For the second scenario, the AOCs are computed on the basis of the SCAFusion data product (cf. Section 6.1.1), replacing the Level-1B AOCs. The derived solutions are further denoted as SCA1B RL02, and SCAFusion (ITSG-Grace2016), respectively. The latter corresponds to the official ITSG-Grace2016 release.

Degree amplitudes

In order to get a first impression of the effect of the sensor fusion on the accuracy of the gravity field solutions, the two solutions are compared in terms of difference degree amplitudes w.r.t. to the static GOCO05s (Mayer-Gürr et al., 2015). Here, the analysis is restricted to three sample month (December 2008, April 2014, May 2017). December 2008 represents one of the best month in terms of data quality and data availability, throughout the whole GRACE mission period. Whereas, April 2014 is part of the later GRACE mission phase, which is already affected from temperature variations and power constraints (cf. Tab. 2.2). Finally, May 2017 lies within the last months of the GRACE science operation. This month is characterized not only by a reduced altitude and data availability, but also by a $0°$ pitch offset on both spacecraft (cf. Section 2.2.2). Since March 29, 2017 the pitch angles were set to $0°$ to improve the quality of the transplanted GRACE-B ACC1B product. However, the accelerometer on-board GRACE-B has been switched on again for the last time for the period May 2 until May 24. Table 8.2 summarizes the major differences between December 2008, April 2014, and May 2017 in terms of the orbital configuration, and data availability.

Figure 8.2 shows the degree amplitudes in terms of geoid heights of both solutions (SCA1B RL02, SCAFusion) for the three sample month. For December 2008 and April 2014, the difference degree amplitudes relative to the static reference field are almost identical. The differences between SCA1B RL02 and SCAFusion are in the order of or slightly above the baseline accuracy, i.e. the expected accuracy from pre-launch simulation. The SCAFusion (ITSG-Grace2016) solution is characterized by a slightly reduced error-level between degree 30 and 90 (cf. Fig. 8.2(a) and 8.2(b)). These results might indicate that the current gravity field models are dominated by errors from other sources than the attitude data.

Tab. 8.2.: Orbit and Level-1B science data characteristics for January 2007, December 2008, and April 2014.

Month	Mean orbit altitude	Data availability*	Temperature control	Pitch offset
2008-12	465 km	99.8 %	✓	$\sim 1°$
2014-04	423 km	98.4 %	x	$\sim 1°$
2017-05	336 km	92.5 %	x	$\sim 0°$

*calculation based on the KBR1B data product

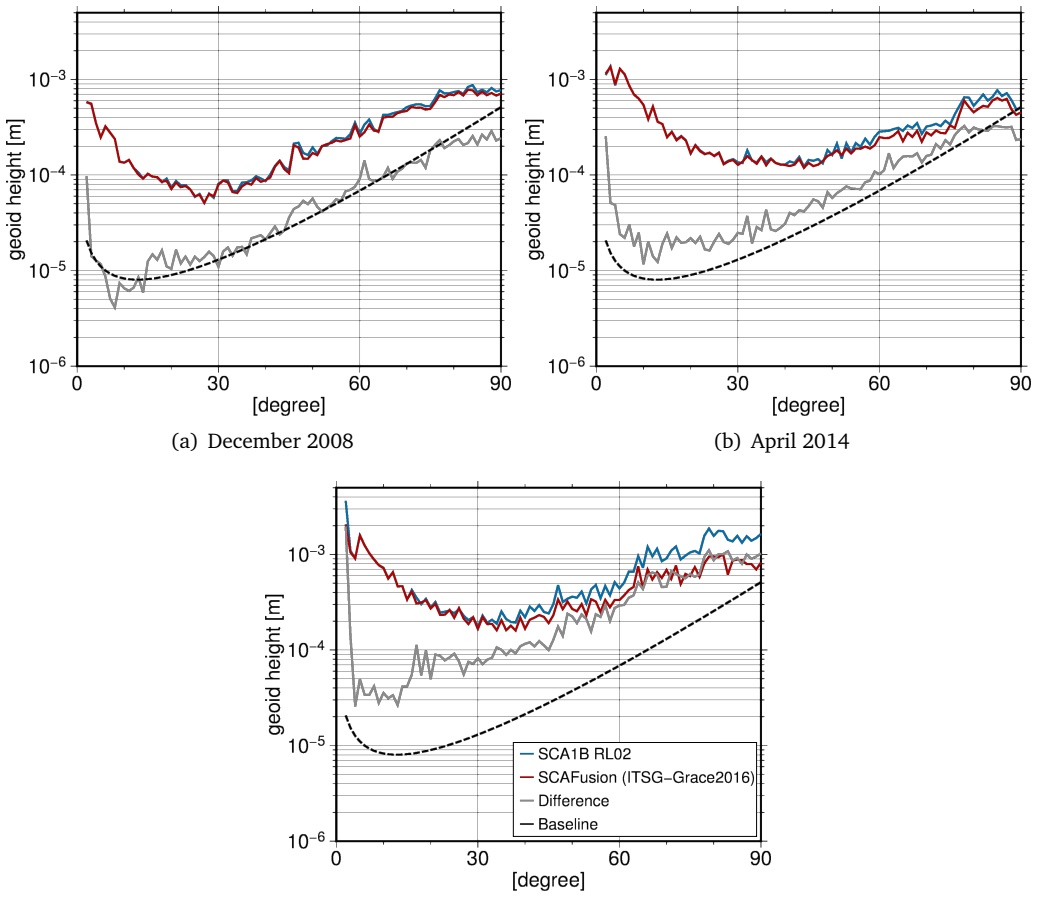

(a) December 2008

(b) April 2014

(c) May 2017

Fig. 8.2.: Difference degree amplitudes: Comparison of the ITSG-Grace2016 (SCA1B RL02) (blue) and the ITSG-Grace2016 (SCAFusion) (red) monthly gravity field solution for three sample month: (a) December 2008, (b) April 2014, and (c) May 2017. The difference degree amplitudes are computed w.r.t. to the GOCO05s. The coefficient differences between ITSG-Grace2016 (SCA1B RL02) and ITSG-Grace2016 (SCAFusion) are shown in gray.

For May 2017, significant differences between both solutions become evident. The error-level of the SCAFusion solution is reduced across the whole spectrum, with the largest improvements occurring for degree 2, and between degree 30 and 90. This effect is caused by the change of the spacecraft formation, i.e. the removal of the pitch offset. The change in the satellites' alignment results in larger AOCs for both spacecraft, directly affecting the KBR ranging observations, which represent a fundamental observation for the GRACE gravity field recovery. By applying the sensor fusion approach, the high frequency noise of the AOC corrections is reduced by the incorporation of the attitude information provided by the accelerometer (cf. Section 6.3.5). This smoothing becomes more effective for periods with larger deviations from the nominal inter-satellite pointing requirements. Thus, the sensor fusion approach contributes to a significant reduction of the error-level for the last month (April to June 2017) of the GRACE science operations, with the satellites flying in a changed formation. The three sample month are are not directly comparable due to the orbital configuration, altitude and data availability (cf. Tab. 8.2). But, they are good examples to demonstrate the effect of the sensor fusion on the basis of different pre-conditions, including varying orbital configurations, satellite health and formation keeping scenarios.

Equivalent water heights

To asses the effect of the sensor fusion in the spatial domain, the estimated spherical harmonic coefficients of the two different scenarios (SCA1B RL02, SCAFusion), and the differences between them are represented in terms of EWHs on a geographic grid. For this representation, the EWHs are computed based on the monthly gravity field solutions, with the static GOCO05s, trend, annual and semiannual signals being removed. Additionally, a 300 km Gaussian filter is applied (cf. Section 3.2.3).

In Figure 8.3, the EWHs of the SCA1B RL02 and SCAFusion solution, as well as the EWH differences between the two solutions for all three sample month (December 2008, April 2014, May 2017) are shown. Table 8.3 summarizes the corresponding grid statistics, containing the global minima, maxima, and the RMS value, respectively. From Figure 8.3(c) it becomes obvious that in case of nominal science operations (December 2008, April 2014), the effect of the fused attitude data on the monthly gravity field solutions is at mm or cm-level in terms of EWH differences. The changes are present primarily as differences in the north-south (NS) striping pattern prevalent in GRACE gravity field solutions, but no significant signal variations are observed in the equivalent water height domain. For both month (December 2008, April 2014) the global RMS values are slightly reduced by introducing the SCAFusion data product instead of the SCA1B RL02 data product. Whereas, in the case of a non-nominal satellite alignment (0° pitch offset; May 2017), the EWH differences show in addition to the NS striping pattern a pronounced horizontal pattern, and are at cm-level (cf. Fig. 8.3(c)). The global RMS is reduced from 7.9 cm (SCA1B RL02) to 6.4 cm (SCAFusion), resulting in a visible reduction of the noise (cf. right column in Fig. 8.3). This confirms that the last month of the GRACE mission are impacted most by the fused attitude data.

In case of a nominal inter-satellite pointing mode, the comparisons between the SCA1B RL02 and the SCAFusion solution in terms of degree amplitudes and EWHs reveal no significant improvement or degradation of the recovered gravity field solutions. However, by comparing the spherical harmonic coefficients in terms of coefficient triangles and in terms of coefficient time series, differences in the zonals and near-zonals become evident.

Tab. 8.3.: EWH grid statistics: Monthly global minimum, maximum and RMS value.

Month	Scenario	Minimum [cm]	Maximum [cm]	RMS [cm]
2008-12	SCA1B RL02	-17.4	23.2	3.6
2008-12	SCAFusion (ITSG-Grace2016)	-15.4	23.5	3.4
2008-12	SCAFusion - SCA1B RL02	-4.7	6.0	0.7
2014-04	SCA1B RL02	-29.3	19.8	4.3
2014-04	SCAFusion (ITSG-Grace2016)	-29.3	20.1	4.2
2014-04	SCAFusion - SCA1B RL02	-6.8	13.3	1.1
2017-05	SCA1B RL02	-45.4	54.4	7.9
2017-05	SCAFusion (ITSG-Grace2016)	-46.5	36.0	6.4
2017-05	SCAFusion - SCA1B RL02	-26.8	31.8	4.1

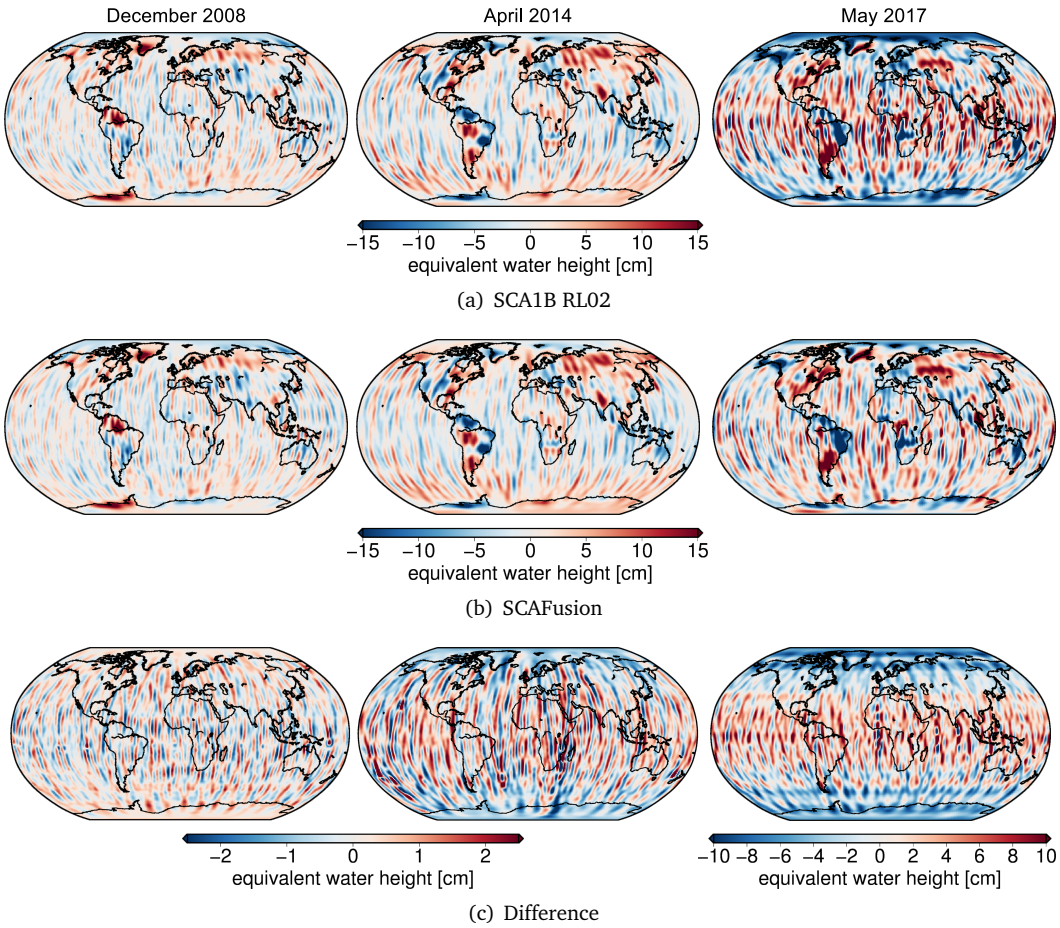

Fig. 8.3.: EWH: (a) SCA1B RL02, (b) SCAFusion (ITSG-Grace2016), and (c) Differences between SCAFusion and SCA1B Rl02 for December 2008 (left column), April 2014 (middle column), and May 2017 (right column). Note that the scaling for (c) is different. The EWHs are given in cm, with the static GOCO05s, trend, annual and semiannual signals removed, and a 300 km Gaussian Filter applied.

Post-fit range rate residuals

Figure 8.4 shows the PSD of the post-fit range rate residuals for both scenarios (SCA1B RL02 and SCAFusion) on a monthly scale (December 2008, April 2014, May 2017), i.e. the differences between adjusted and original KBR observations. The residuals are an estimate for the total errors present within the system, as they absorb measurement errors of all involved instruments and sensors, as well as modeling errors and unparameterized effects. Consequently, a reduction in the high-frequency noise should lead to improved KBR post-fit residuals. As expected, no significant improvements become visible for January 2007. However, the peak around frequencies of 3.3 mHz disappears for the SCAFusion residuals (cf. Fig. 8.4(a)). This peak in power is caused by systematic (pitch) attitude variations, which are related to the dominant frequency of the magnetic torquer rods (Bandikova et al., 2012). For April 2014 and May 2017, the residuals are reduced for the frequencies above 7 mHz due to the sensor fusion approach. The strong reduction in May 2017 is caused by the change in the satellite alignment, which has a strong influence on the AOCs. The signal peaks (0.038 Hz, 0.085 Hz) in the SCAFusion residuals (cf. Fig. 8.4(c)) are probably also related to the removal of the pitch offset, and seem to be amplified by the sensor fusion.

From these results, it can be concluded that the quality of the attitude data products affects both the post-fit range rate residuals and the estimated gravity field parameters. Further improvements within the attitude data processing would most likely lead to a further reduction of the post-fit KBR residuals.

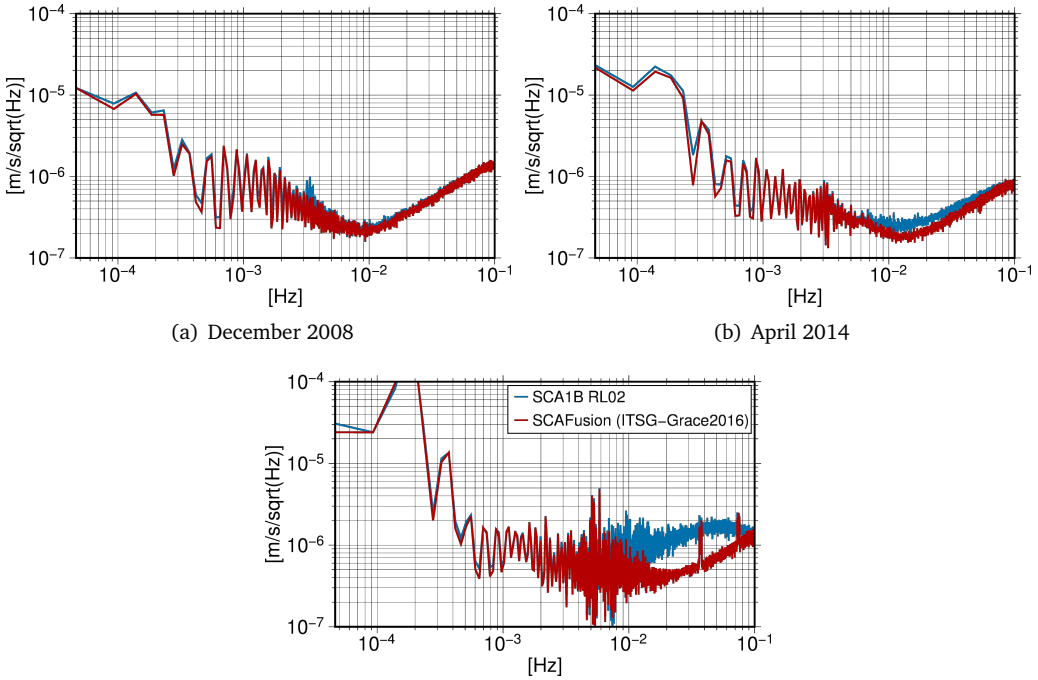

(a) December 2008 (b) April 2014

(c) May 2017

Fig. 8.4.: PSD of SCA1B RL02 (blue) and SCAFusion (red) post-fit range rate residuals: (a) December 2008, (b) April 2014, and (c) May 2017.

Spherical harmonic coefficient - Time series

Figure 8.5 shows the differences between both scenarios (SCA1B RL02, SCAFusion) for all three sample month (December 2008, April 2014, May 2017) in terms of spherical harmonic coefficient triangles. Differences occur for all types of coefficients (zonal, sectoral, tesseral). But, since the most prominent differences occur for the zonal coefficients, time series of selected zonal coefficients (degree 5, 10, 75, 80, 85) are given in Figure 8.6. The coefficient analysis is based on the ITSG-Grace2016 release, and the official CSR RL05 and GFZ RL05a releases. For the year 2008, an additional comparison with the SCA1B RL02 solution is made. As obvious from Figure 8.6, the lower degree zonals of the ITSG-Grace2016 release (except for C20, cf. Section 8.3.1) show the same temporal behavior and amplitude as the zonal coefficients of the other releases (CSR, GFZ). While, the higher degree zonals ($>$ degree 20) are characterized by the same temporal behavior, but with smaller variations. Since the high frequency noise within the attitude data is successfully reduced by the sensor fusion approach (cf. Section 6), also the high-frequent (pitch) pointing jitter is smoothed, resulting in a reduced amplitude of the high-degree zonal coefficients. Errors present in the zonal coefficients manifest themselves as latitudinal banding in the gravity field (cf. Fig. 8.3(c)).

In general, the accuracy of the attitude data product affects all fundamental observations needed for gravity field recovery (linear accelerations, KBR ranging data; cf. Section 6.3.6 and 6.3.5). Therefore, it appears that combined attitude data product slightly reduces the high-frequent noise within the gravity field solutions, especially affecting high-degree zonal spherical harmonic coefficients. During nominal mission operation, no significant improvements become apparent within the spectral and spatial domain. Later, noisier, years in the GRACE mission seem to be impacted more. Overall, the last month of the GRACE science operation are impacted most, due to a drastic change in the GRACE formation.

Another influencing factor for the magnitude of the noise-level reduction is the co-estimation of the KBR phC vector along with the spherical harmonic coefficients during gravity field recovery. By estimating the phC, the noise level can be additionally reduced, but leads to consistently too short estimates for the phC vector (not shown here). This is probably caused by the pointing jitter, complicating a reliable and stable parameter estimation. However, this topic is out of the scope of this thesis, and is not further discussed here.

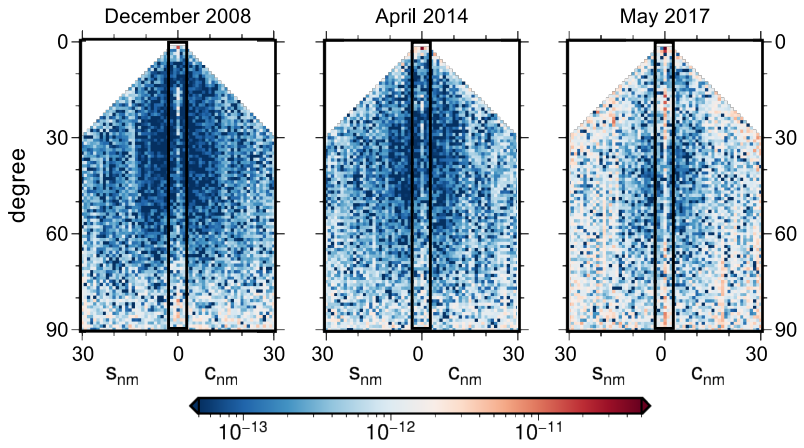

Fig. 8.5.: Spherical harmonics triangle: Absolute differences of spherical harmonic coefficients between SCAFusion and SCA1B RL02 for (a) December 2008, (b) April 2014, and (c) May 2017. The zonal coefficients are highlighted by a black box.

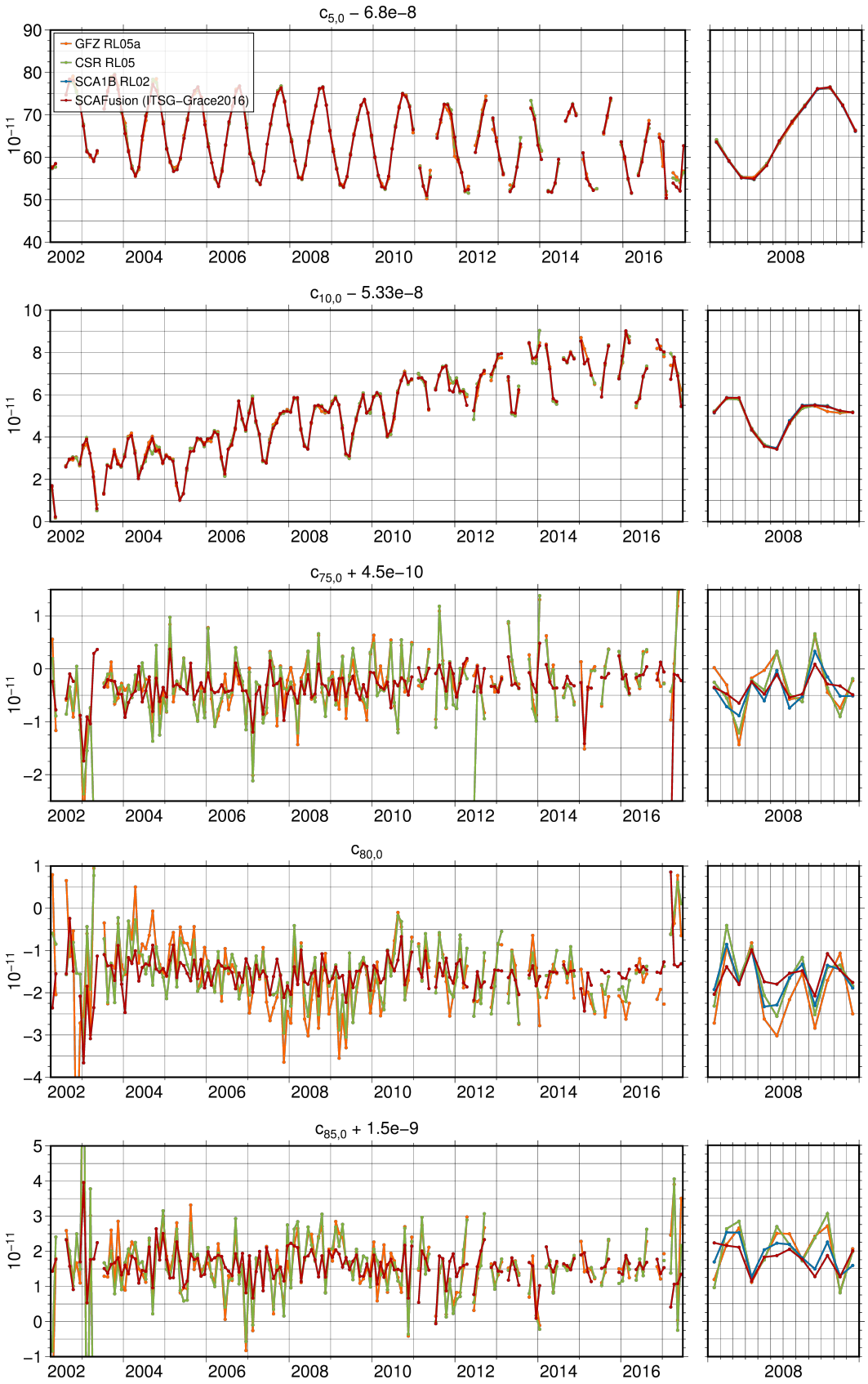

Fig. 8.6.: Time series of GRACE-derived zonal coefficients for the whole GRACE mission period (left column) and for the year 2008 (right column): CSR RL05 (green), GFZ RL05a (orange), SCAFusion (ITSG-Grace2016) (red), and SCA1B RL02 (blue).

8.3 Data screening & Accelerometer data calibration

The data pre-processing methodologies, introduced within this thesis, were originally developed on the basis of the ITSG-Grace2014 release with the aim of improving the recovered gravity field solutions. Therefore, the subsequent analysis are based on the ITSG-Grace2014 release, with the latest ITSG-Grace2016 release serving as a benchmark. By successively introducing the fully-automated data screening step (cf. Section 4.3.2), and then the two-step ACC1B data calibration (cf. Section 7) to the ITSG-Grace2014 processing chain, their effects on the monthly recovered gravity field solutions can be analyzed step-by-step.

Five gravity field recovery scenarios are compared: (1) ITSG-Grace2014, (2) Pre-processing 1, (3) Pre-processing 2, (4) Pre-processing 3, and (5) ITSG-Grace2016. The first and the last one represent official ITSG-Grace releases (with processing settings according to Table 8.1), whereas the others are intermediate processing scenarios. Table 8.4 summarizes the characteristics of the recovered gravity field solutions, including the processing chain used for the gravity field recovery (cf. Tab. 8.1), and the data pre-processing methodologies applied to the processing chain. Pre-processing 2 and Pre-Processing 3 differ only with respect to scale factor matrix (main-diagonal elements vs. fully-populated) used for the ACC1B data calibration. Due to the large number of monthly GRACE gravity field solutions (in total 161), the analysis is restricted to three sample month, namely: (1) January 2007, (2) December 2008, and (3) April 2014. The selected month are characterized by differences with respect to the orbital configuration, the on-board temperature control, and the occurrence of yaw turn and calibration maneuvers (cf. Tab. 8.5). Besides, they represent different phases within the GRACE science mission lifetime (April 2002 to June 2017), and thus offer a good overview of the data pre-processing performance under miscellaneous initial conditions.

Tab. 8.4.: Overview of the gravity field recovery scenarios.

Scenario	Processing chain*	Sensor fusion	Data screening**	ACC1B data calibration
ITSG-Grace2014	ITSG-Grace2014	✓	x	x
Pre-processing 1	ITSG-Grace2014	✓	✓	x
Pre-processing 2	ITSG-Grace2014	✓	✓	main-diagonal elements
Pre-processing 3	ITSG-Grace2014	✓	✓	✓
ITSG-Grace2016	ITSG-Grace2016	✓	✓	✓

*Processing settings according to Tab. 8.1

**Detection and exclusion of outliers, yaw turns, CoM and KBR calibration maneuvers

x = Not applied, ✓ = Applied

Tab. 8.5.: Orbit and Level-1B science data characteristics for January 2007, December 2008, and April 2014.

Month	Orbit altitude	β' angle	Data availability*	Temperature anomalies	Yaw turns
2007-01	468 km	$-21°$ to $+14°$	99.9 %	Disabling of heater lines	x
2008-12	465 km	$+34°$ to $+63°$	99.8 %	x	x
2014-04	423 km	$+62°$ to $+78°$	98.4 %	No active thermal control	✓

*calculation based on the KBR1B data product

Degree amplitudes

Figure 8.7 shows the degree amplitudes in terms of geoid heights of the individual scenarios (cf. Tab. 8.4) for the three sample month (January 2007, December 2008, April 2014). In all three cases, a step-wise reduction of the noise level between degree 20 and 90 can be observed. Depending on the presence of blunders, yaw turns or calibration maneuvers, the inclusion of the data screening step (Pre-Processing 1) leads to more or less large reduction of the error-level (cf. Fig. 8.7(a) vs. Fig. 8.7(b), 8.7(c)). The same holds true for the ACC1B data calibration (Pre-processing 2 & Pre-processing 3). The ACC1B data calibration mainly affects month with (accelerometer) temperature variations, which occur due to the occasional disabling of heater lines (e.g., January 2007) or due to the switched-off thermal control (e.g., April 2014). Since the switch-off of the active thermal control in April 2011, temperature variations recur on a regular basis. The temperature variations are directly related to the orbital configuration w.r.t to the Sun, i.e. the accelerometer temperature variations are linked to the β' angle variations. The impact of the setup of the accelerometer calibration equation on the lower degree coefficients is further discussed in Section 8.3.1. From Figure 8.7 it is evident that the "Pre-processing" scenarios of all three sample month converge towards the ITSG-Grace2016 solution, which serves as a benchmark for internal validation.

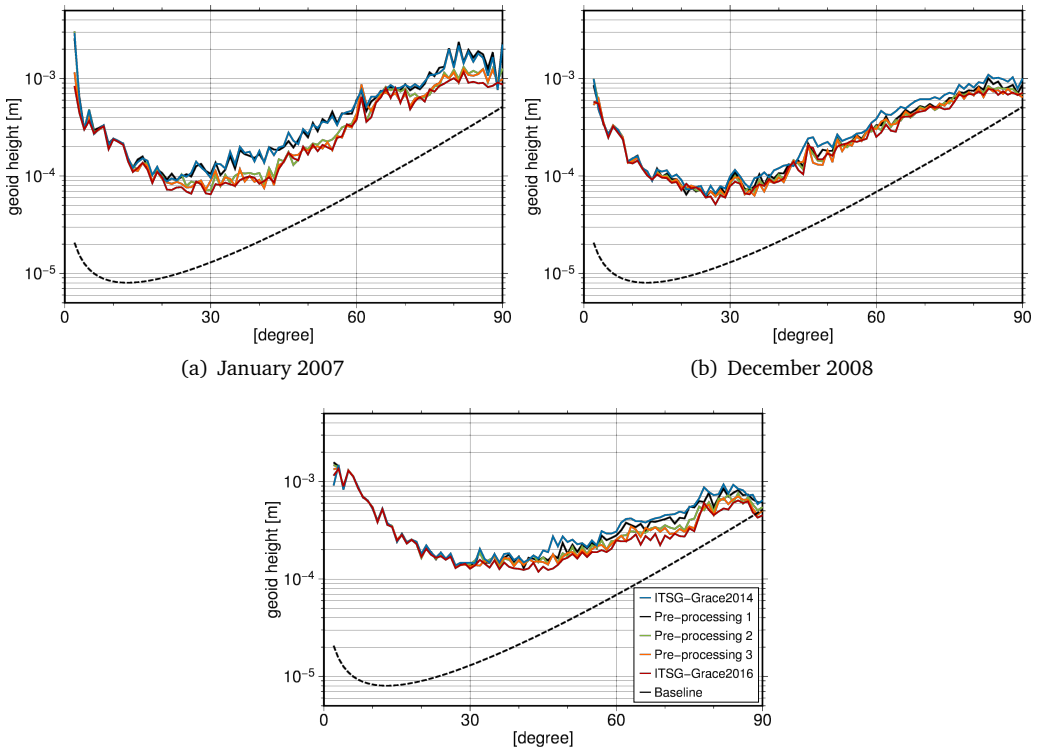

(a) January 2007

(b) December 2008

(c) April 2014

Fig. 8.7.: Difference degree amplitudes: Comparison of the ITSG-Grace2014 (blue), Pre-processing 1 (black), Pre-processing 2 (green), Pre-processing 3 (orange), and ITSG-Grace2016 (red) monthly gravity field solution for three sample month: (a) January 2007, (b) December 2008, and (c) April 2014. The difference degree amplitudes are computed w.r.t to the GOCO05s.

Equivalent water heights

In order to asses the effect of the data screening and ACC1B data calibration in the spatial domain, Figures 8.8, 8.9, and 8.10 display the EWHs of the Pre-processing scenarios and ITSG-Grace2016 scenario w.r.t to the ITSG-Grace2014 scenario for January 2007, December 2008, April 2014, respectively. Table 8.6 summarizes the corresponding grid statistics of the individual solutions.

From the EWH differences w.r.t to the ITSG-Grace2014 release (cf. column on the right in Fig. 8.8, 8.9, and 8.10), it becomes obvious that the successive inclusion of all data pre-processing steps leads to a step-wise reduction of the noise level. The effect on the monthly gravity field solutions is at cm-level in terms of EWH differences. As apparent from the EWH difference plots, a significant reduction of the GRACE-typical NS striping pattern can be achieved for all three sample month within the equivalent water height domain. Besides, the Pre-processing 3 and ITSG-Grace2016 solutions match well together.

The global RMS values are reduced by up to 37 % with respect to the ITSG-Grace2014 solutions, and are close to the RMS values of the ITSG-Grace2016 solutions. The RMS values of the ITSG-Grace2016 solutions are always lowest, which can be expected from the enhanced processing chain, which includes not only the Level-1B data pre-processing methodologies but all updates and improvements w.r.t to the ITSG-Grace2014 release (cf. Section 8.1). Nevertheless, these results confirm the aim of the Level-1B data pre-processing methodologies, now being part of the official ITSG-Grace2016 gravity field processing chain.

Tab. 8.6.: EWH grid statistics: Minimum, Maximum and RMS value.

Month	Scenario	Minimum [cm]	Maximum [cm]	RMS [cm]
2007-01	ITSG-Grace2014	-25.6	26.2	6.5
2007-01	Pre-Processing 1	-28.9	26.1	6.2
2007-01	Pre-Processing 2	-20.0	21.8	5.5
2007-01	Pre-Processing 3	-16.5	23.1	4.1
2007-01	ITSG-Grace2016	-15.3	18.6	3.8
2008-12	ITSG-Grace2014	-19.1	21.0	4.4
2008-12	Pre-Processing 1	-18.2	21.9	4.0
2008-12	Pre-Processing 2	-17.0	21.3	3.9
2008-12	Pre-Processing 3	-16.4	23.4	3.6
2008-12	ITSG-Grace2016	-15.4	23.5	3.5
2014-04	ITSG-Grace2014	-32.2	25.2	5.1
2014-04	Pre-Processing 1	-27.5	22.8	4.7
2014-04	Pre-Processing 2	-29.4	21.6	4.4
2014-04	Pre-Processing 3	-29.0	23.6	4.3
2014-04	ITSG-Grace2016	-29.3	20.1	4.2

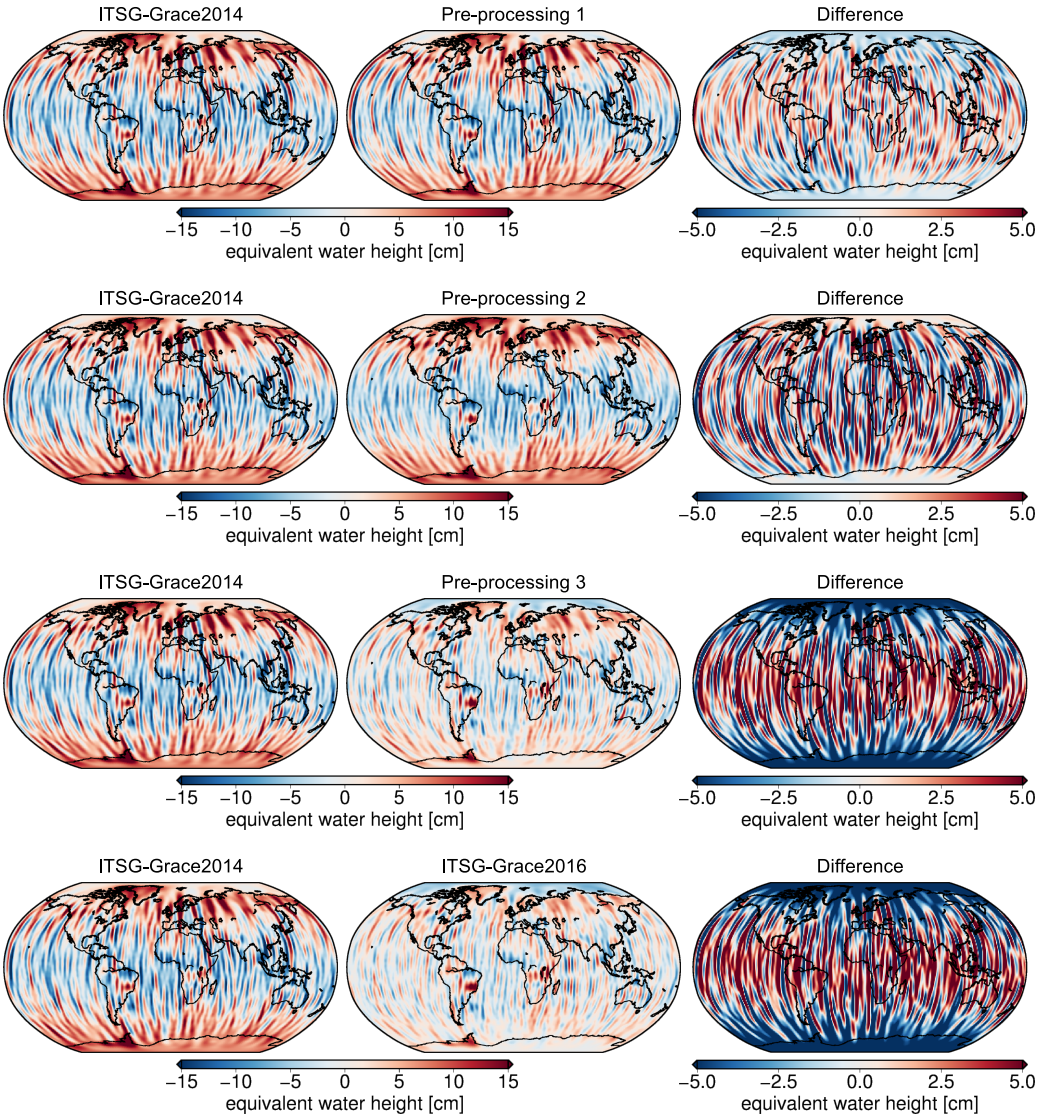

Fig. 8.8.: EWH: Left column: ITSG-Grace2014, Middle column: Pre-processing 1 to ITSG-Grace2016, Right column: Differences between the left (ITSG-Grace2014) and middle (Pre-processing 1 to ITSG-Grace2016) solution, for January 2007. The EWHs are given in cm, with the static GOCO05s, trend, annual and semiannual signals removed, and a 300 km Gaussian Filter applied.

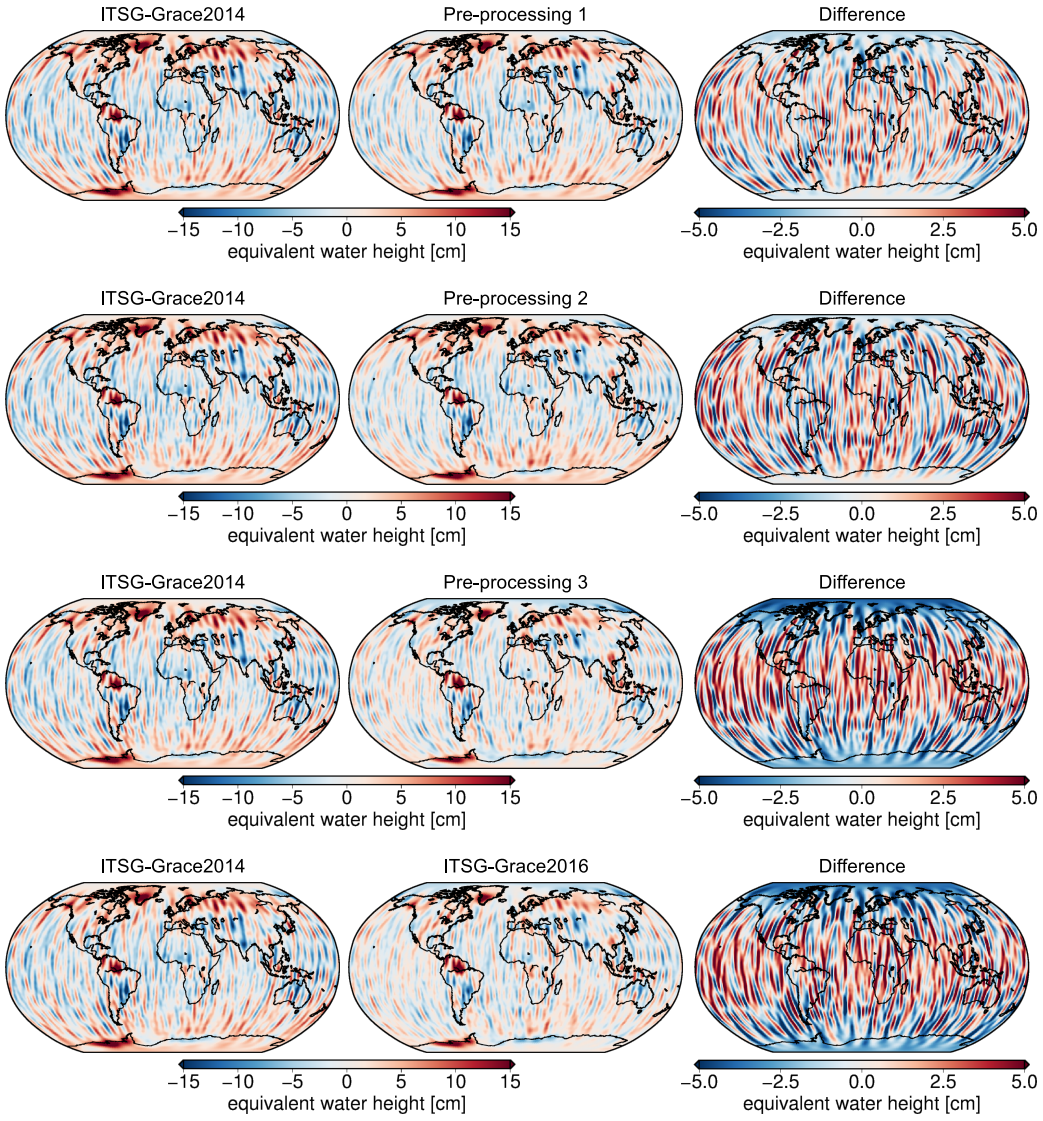

Fig. 8.9.: EWH: Left column: ITSG-Grace2014, Middle column: Pre-processing 1 to ITSG-Grace2016, Right column: Differences between the left (ITSG-Grace2014) and middle (Pre-processing 1 to ITSG-Grace2016) solution, for December 2008. The EWHs are given in cm, with the static GOCO05s, trend, annual and semiannual signals removed, and a 300 km Gaussian Filter applied.

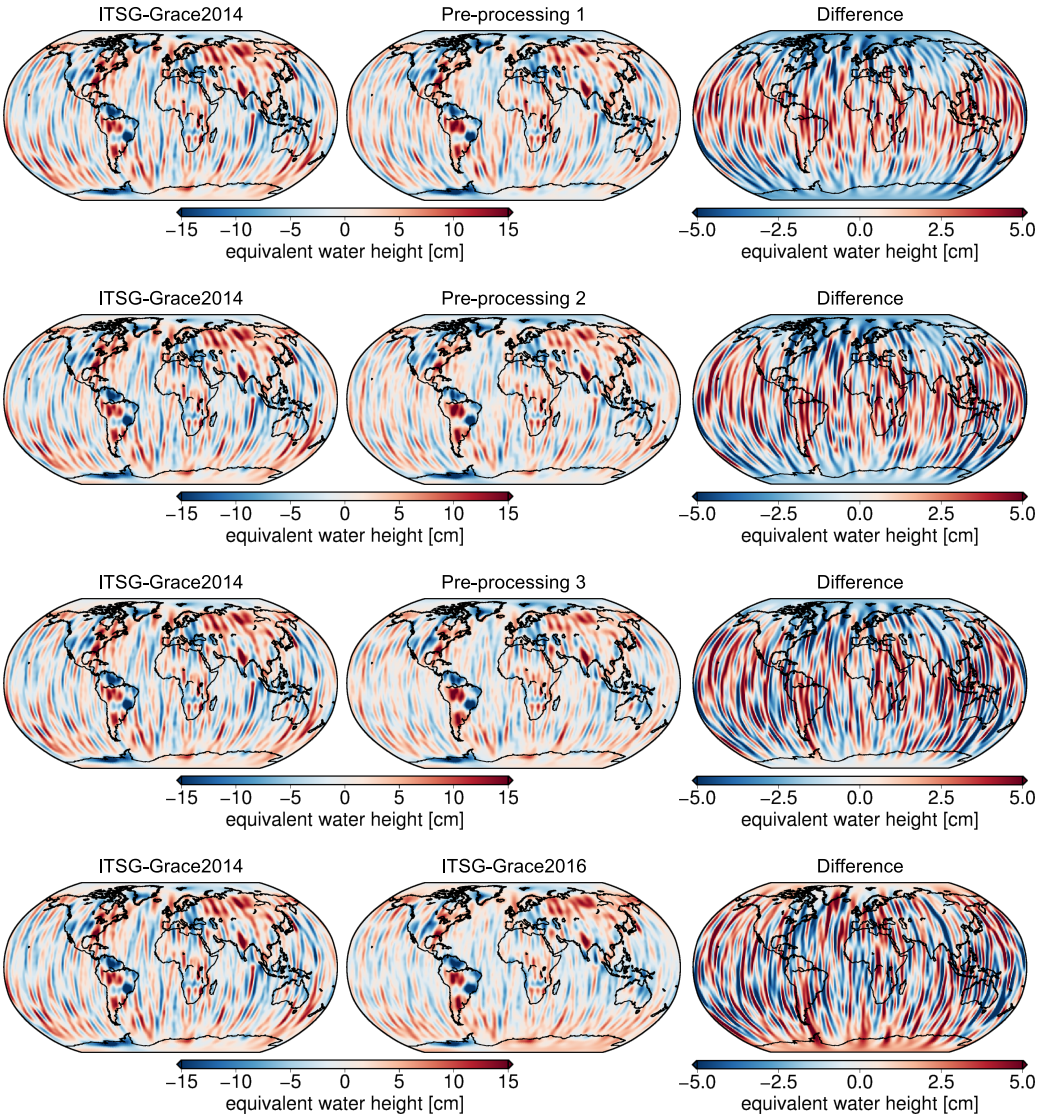

Fig. 8.10.: EWH: Left column: ITSG-Grace2014, Middle column: Pre-processing 1 to ITSG-Grace2016, Right column: Differences between the left (ITSG-Grace2014) and middle (Pre-processing 1 to ITSG-Grace2016) solution, for April 2014. The EWHs are given in cm, with the static GOCO05s, trend, annual and semiannual signals removed, and a 300 km Gaussian Filter applied.

Post-fit range rate residuals

Another method to validate the quality of gravity field solutions, is to assess the post-fit KBR residuals. Figure 8.11 shows the post-fit range rate residuals of the recovered gravity field solutions (ITSG-Grace2014, Pre-processing 1, Pre-processing 2, Pre-processing 3, ITSG-Grace2016) on a monthly scale (January 2007, December 2008, April 2014). In theory, a reduction in the high-frequency noise should lead to improved KBR post-fit residuals. As expected, the post-fit range-rate residuals of all three scenarios show a slight to moderate improvement, and are on the level of the ITSG-Grace2016 solutions (cf. Fig. 8.11; no further analysis shown here). In agreement with the noise reduction visible within the difference degree amplitudes (cf. Fig. 8.7) and the EWHs (cf. Figs. 8.8, 8.9, 8.10), the largest reduction of the post-fit range rate residuals occurs for January 2007, followed by April 2014.

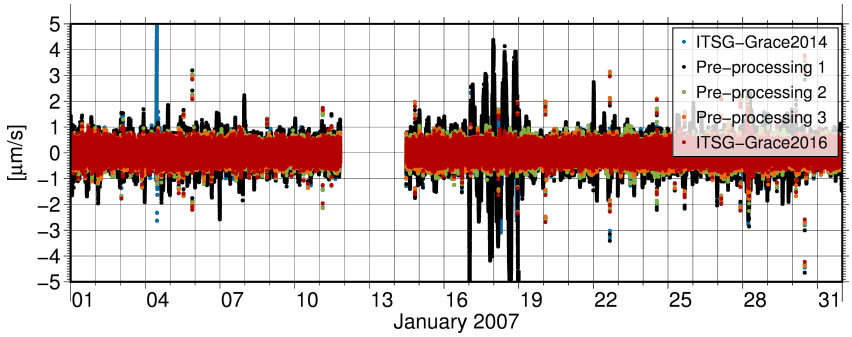

(a)

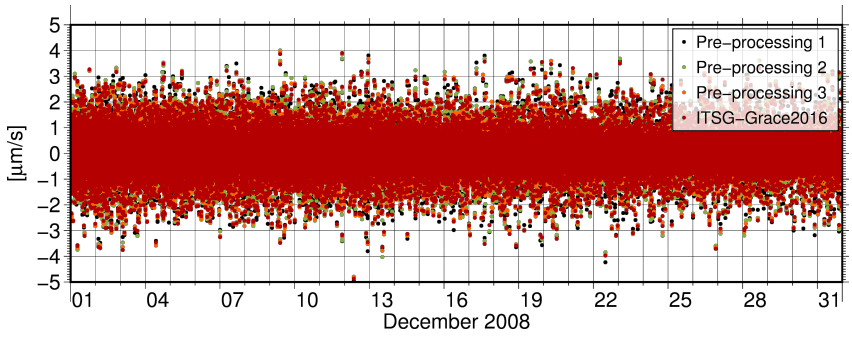

(b)

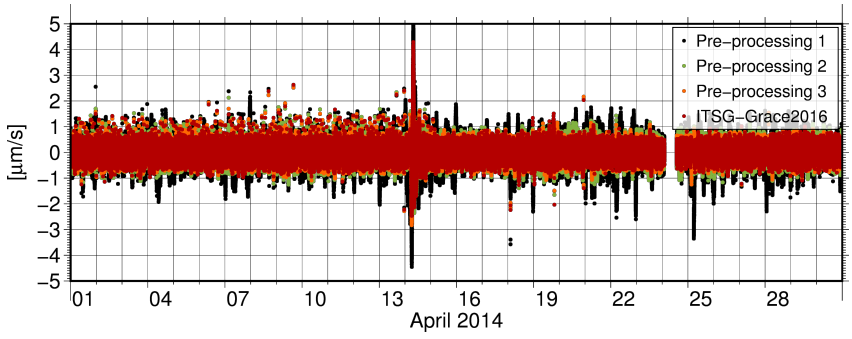

(c)

Fig. 8.11.: Time series of post-fit KBR range rate residuals for (a) January 2007, (b) December 2008, and (c) April 2014. Comparison of the ITSG-Grace2014 (blue), Pre-processing 1 (black), Pre-processing 2 (green), Pre-processing 3 (orange), and ITSG-Grace2016 (red) scenario.

8.3.1 Impact on C20 coefficients

In the following, the impact of the use of a fully-populated scale factor matrix within the ACC1B data calibration (cf. Section 7.1.2) on the monthly gravity field solutions, in particular the effect on the C20 coefficients, is analyzed in detail. For this purpose, two different variations of the ITSG-Grace2016 release are compared: (1) the official ITSG-Grace2016 release, and (2) the preliminary ITSG-Grace2016 release. The latter is further denoted as ITSG-Grace2016 (prelim), and differs only with respect to the scale factor matrix. Instead of the fully-populated scale factor matrix (as in the case of ITSG-Grace2016), solely the main diagonal elements of the scale factor matrix were estimated within the gravity field recovery (cf. Eq. (7.2)).

The largest spherical harmonic coefficient C20 is due to the flattening of the Earth, and reflects the Earth's dynamic oblateness. The C20 coefficient exhibits a secular decrease (cf. Fig. 8.13), which is mainly caused by the glacial isostatic adjustment (Cheng et al., 2013).

The C20 coefficients determined from GRACE data alone always have been corrupted by a strong 161-day periodic signal. Therefore - for science applications of the GRACE monthly solutions - the GRACE-only estimates of the C20 coefficients are typically replaced by C20 estimates derived from the analysis of Satellite Laser Ranging (SLR) data. The ~ 160-day signal appearing in the GRACE C20 time series has sometimes been referred to as a tide-like variation (e.g., Chen et al., 2009), since the period is close to the perturbation period on the GRACE orbits due to the spherical harmonic coefficient pair C22/S22 of the S2 ocean tide. According to Cheng and Ries (2017), errors in the S2 tide model used in GRACE data processing could produce a significant perturbation to the GRACE orbits, but cannot contribute to the ~ 160-day signal appearing in the C20 time series. Consequently, the anomalous signal in the GRACE C20 estimates cannot be attributed to aliasing from the errors in the S2 tide.

Based on the analysis presented within this Section, the following hypothesis is postulated: "Non-gravitational accelerations have strong tone signals (cf. Fig. 8.12), such as 1-cycle-per-revolution (cpr) and 2-cpr, with frequency characteristics similar to the accelerations caused by the resonant gravity field coefficients (Kim, 2000). Hence, accelerometer errors

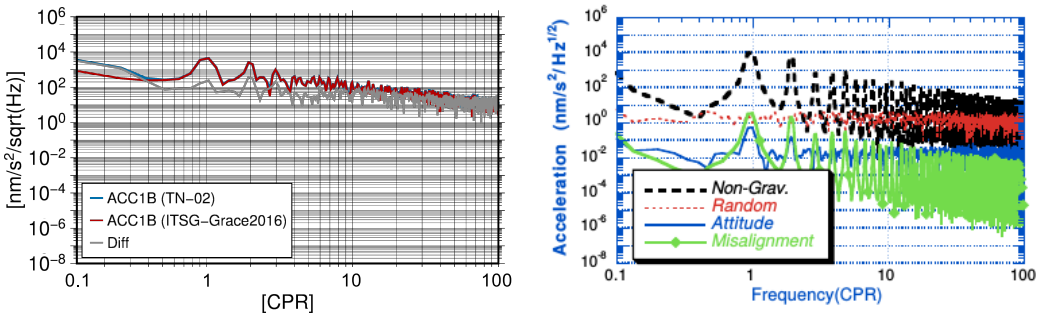

Fig. 8.12.: Left: PSD of ACC1B (TN-02) (blue), ACC1B (ITSG-Grace2016) (red), and the difference (gray) between both. Right: PSD of individual accelerometer errors at 450 km (Source: Kim (2000)). ACC1B represents the original Level-1B data calibrated according to TN-02, and ACC1B (ITSG-Grace2016) represents the calibrated accelerometer data according to the ITSG-Grace2016 settings, for one day on 2007-01-17.

and disturbances due to e.g., misalignment or thermal variations can degrade the estimation of the C20 coefficients significantly." This hypothesis is also supported by Cheng and Ries (2017), whose preliminary analysis of the cross-track forces acting on GRACE and the cross-track component of the accelerometer data suggests that a non-geophysical, temperature-dependent systematic error in the accelerometer data could be a cause for the ~ 160-day signal present in the GRACE-derived C20 time series.

Results from the ITSG-Grace2016 release, applying the ACC1B data calibration approach (cf. Section 7), strongly support the use of a fully-populated scale factor matrix within the gravity field recovery. The analysis of the recovered spherical harmonic coefficients reveals a large influence on the low degree and order coefficients, especially on the C20 coefficients (cf. Fig. 8.14).

Figure 8.13 compares the monthly estimates of C20 derived from GRACE and SLR data over the period from April 2002 to June 2017. Here, the SLR Tellus time series[4] (2001 to present), which provides C20 estimates obtained from the analysis of SLR observations to five geodetic satellites (LAGEOS-1 and 2, Starlette, Stella, and Ajisai; Cheng et al., 2011), is used as an independent benchmark. The estimates for the C20 coefficients of the preliminary solution ITSG-Grace2016 (prelim) and the CSR RL05 solution (Bettadpur, 2012) match quite well. Remarkably, the ITSG-Grace2016 estimates for the C20 coefficients show significantly better agreement with the independent SLR solution. In general, the ITSG-Grace2016 series agrees well with the SLR series. Figure 8.13 shows that a gain in consistency is achieved by the use of the fully-populated scale factor matrix. Compared to the ITSG-Grace (prelim) solution, the bias of the ITSG-Grace2016 solution to the SLR Tellus solution can be visibly reduced; most evidently for the period from 2008 to 2014. The differences in the trend between ITSG-Grace2016 and SLR Tellus for the period of 2002 to 2008 cannot be explained sufficiently. The inconsistency for periods later then 2014 might be related to the reduced availability and quality of the GRACE data, as all GRACE-derived solutions show above average variations and gaps.

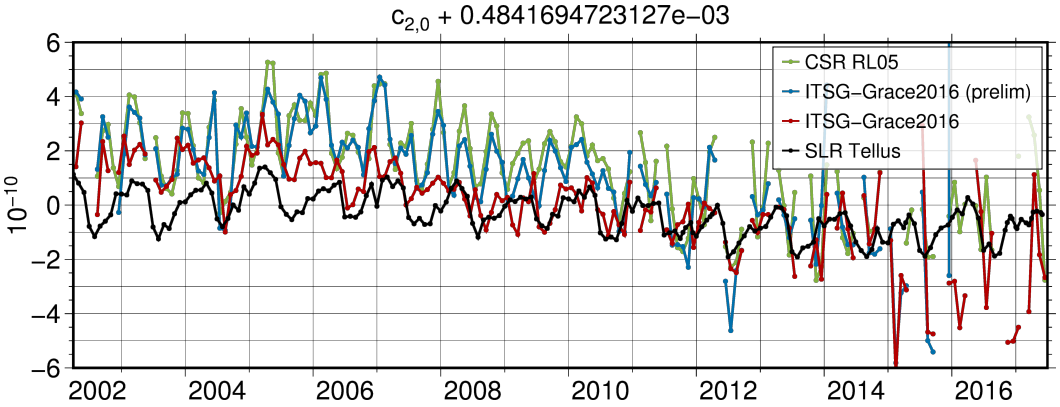

Fig. 8.13.: Comparison of C20 estimates from GRACE-only monthly gravity field solutions (CSR RL05 (green), ITSG-Grace2016 (prelim) (blue), ITSG-Grace2016 (red) and from SLR analysis (SLR Tellus (black)). The C20 estimates for the whole GRACE mission period (April 2002 to June 2017) are displayed.

[4] grace.jpl.nasa.gov/data/get-data/oblateness

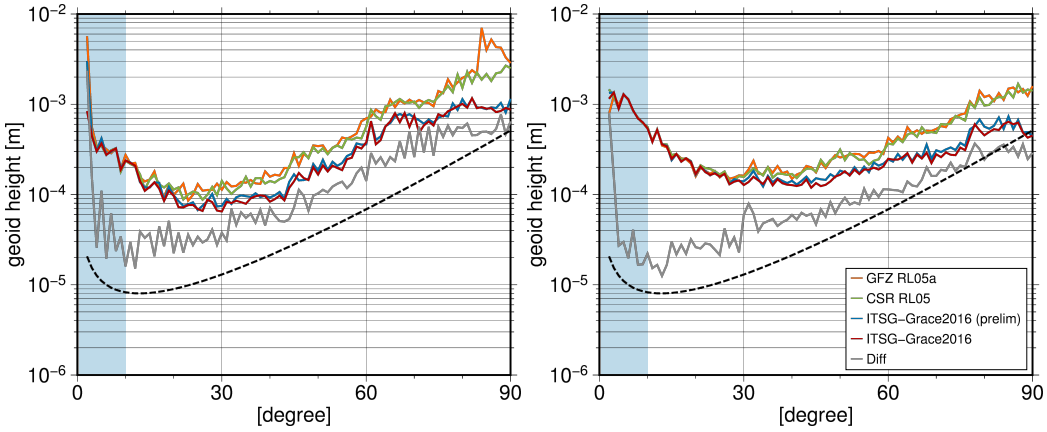

(a) January 2007 (b) April 2014

Fig. 8.14.: Difference degree amplitudes: Comparison of the GFZ RL05a (orange), CSR RL05 (green), the ITSG-Grace2016 (prelim) (blue), and the ITSG-Grace2016 (red) monthly gravity field solution for (a) January 2007 and (b) April 2014. The difference degree amplitudes are computed w.r.t to the GOCO05s. The coefficient differences between ITSG-Grace2016 and ITSG-Grace2016 (prelim) are shown in gray. The lower spherical harmonic degrees (0 to 10) are highlighted by a blue background.

Figure 8.14 exemplarily shows the difference degree amplitudes for two month (January 2007 and April 2014) with respect to the static gravity field GOCO05s (Mayer-Gürr et al., 2015) for the CSR RL05 solution, the ITSG-Grace2016 (prelim) solution, the ITSG-Grace2016 solution, and the differences between the official and the preliminary ITSG-Grace2016 solution. Compared to the preliminary solution, ITSG-Grace2016 performs better over the whole spectrum, but the largest differences are visible in the lowest degrees (cf. Fig 8.14). For degree 2, the difference is several orders of magnitude larger than for the other degrees. This significant difference in the C20 coefficient can be attributed to the use of the fully-populated scale factor matrix (cf. Section 7.1.2). Consequently, Figure 8.14 clearly demonstrates the ability to improve the C20 estimates within the latest ITSG-Grace2016 release, by applying the two-step calibration approach.

Based on the presented results and findings, the Level-1B data pre-processing methodologies are assumed to be an important contributing factor to the improvement from ITSG-Grace2014 to ITSG-Grace2016.

9 Conclusions and Outlook

Until now, efforts are still ongoing to further improve the accuracy of GRACE temporal gravity field models, as there still remains almost an order of magnitude between the error-level of present gravity field solutions and the so-called GRACE baseline (cf. Fig. 1.1), a predicted accuracy from a pre-mission simulations (Kim and Tapley, 2002; Stanton et al., 1998). How can this gap be further minimized to approach the baseline? - Since there are several contributors to the GRACE error budget, there also exists no definite answer to this question. In general, the accuracy of GRACE gravity field models is primarily limited by: (1) unmodeled noise and errors within the GRACE Level-1B data (inter-satellite ranging, attitude, accelerometer, orbit) - including errors in the original instrument data as well as in the corrections and calibration parameters, and (2) aliasing effects due to spatial and temporal undersampling, and uncertainties within the background models. On the one hand, imperfections within the background models need to be further reduced in order to diminish aliasing effects. On the other hand, the satellite observations, i.e. the science data products, need to be improved and the anisotropic accuracy characteristics of GRACE instruments need to be taken into account during gravity field recovery. Since any uncorrected errors or disturbances within the instrument data directly propagate to the recovered gravity field solution.

With the last instrument data in June 2017, GRACE has ended science mission. To continue GRACE's legacy, the GRACE-FO mission (Flechtner et al., 2017) - a quasi-replica of GRACE carrying an almost identical payload - will pursue the objectives of the GRACE mission. A successful launch in early 2018, will guarantee a continuation of the observation of Earth's gravity field from space. By this the GRACE time series of highly-accurate monthly gravity field models can be extended, and further improved. For future gravity field missions, such as GRACE-FO, the GRACE mission serves as a lesson learned. A profound understanding and knowledge of the GRACE instrument characteristics and accuracies, and possible error sources and disturbances prevalent within the GRACE instrument data is fundamental in order to fully exploit the observations provided by future gravity field missions. At the same time, it enables the improvement of the current GRACE data processing algorithms and thus gravity field recovery.

The importance and potential of Level-1B data pre-processing methodologies to reduce the GRACE error-level was demonstrated on the basis of the ITSG-Grace processing chain. Based on the transition from the ITSG-Grace2014 (Mayer-Gürr et al., 2014) to the ITSG-Grace2016 (Mayer-Gürr et al., 2016b) release, which includes multiple updates within the processing chain, the contribution of individual updates to the overall accuracy improvement was highlighted. In particular, the effects and benefits of (1) a fully-automated data screening, (2) an enhanced attitude determination on the basis of the sensor fusion approach, and (3) a new approach for the accelerometer data calibration were analyzed in detail within this study.

9.1 Conclusions

This PhD study primarily aimed at improving the GRACE temporal gravity field models by introducing Level-1B data pre-processing methodologies, as part of the ITSG-Grace gravity field processing chain. The major findings of this thesis can briefly be summarized as:

- Enhanced data screening methodologies, on the basis of Level-1B science and housekeeping data products, prove beneficial to identify erroneous observations and time periods with reduced data quality.
- The sensor fusion, i.e. combination of Level-1B angular accelerometer and star camera data, contributes to a reduction of the high-frequency attitude noise, prevalent within the original SCA1B data product.
- The ACC1B data calibration avoids a degradation of the recovered gravity field solutions due to temperature-induced bias and scale factor variations.
- The use of a fully-populated scale factor matrix within the ACC1B data calibration furthermore helps to improve GRACE C20 estimates.
- Based on the presented results and findings, the Level-1B data pre-processing methodologies are assumed to be an important contributing factor to the noise-level reduction from ITSG-Grace2014 to ITSG-Grace2016.

The importance of data screening

For GRACE gravity field recovery, the data screening of the Level-1B data products is often done on a manually basis, which is rather time-consuming, labour-intensive, and error-prone; or sometimes it is neglected at all. Within this work, a fully-automated data screening step was implemented within the ITSG-Grace processing chain. The inclusion of a fully-automated a priori data screening step, i.e. selectively discarding data as part of the Level-1B data pre-processing, enables a more sophisticated detection of large blunders and outliers within the Level-1B science data products, and allows for the identification of epochs with erroneous observations and/or time periods with reduced data quality. For the purpose of data screening, both Level-1B science data products and additional housekeeping data products (e.g., SOE) are used. The former enable a threshold-based outlier detection tailored to the characteristics of the different science data products. Whereas, the latter provide an additional source of information, which facilitates the automatic identification of satellite and sensor events, which may affect the Level-1B science data quality. Based on the implemented data screening methodologies, either single observations or time periods of anomolous data (e.g., yaw turns, CoM calibration maneuvers, KBR calibration maneuvers) are excluded from the further gravity field processing. By this means, it is avoided that outliers within the observations propagate to the temporal gravity field models. In the case of outliers or observations with reduced data quality, the inclusion of the a priori data screening successfully reduces the noise-level of the recovered monthly solutions.

Attitude improvements - Benefits of the sensor fusion

The full exploitation of the primary inter-satellite ranging observations, provided by the KBR system, is only possible with highly-accurate attitude data. Hitherto, the GRACE attitude determination during SM was based solely on the combination of the attitude quaternions, provided by the two star cameras on-board each satellite. The official SCA1B RL02 data product shows a significantly higher noise level than expected and does not carry the full accuracy, due to an implementation error in the Level-1A to Level-1B processing scheme.

Besides the absolute attitude information provided by the star cameras, the accelerometer provides additional relative attitude information in terms of angular accelerations. To exploit this additional information for the purpose of attitude estimation, the so-called sensor fusion approach was introduced to the ITSG-Grace processing chain. The sensor fusion approach is based on the combination of the Level-1B star camera and angular accelerometer data (SCA1B, ACC1B) within a LSA. By applying the principles of VCE in combination with a robust estimator within the iterative LSA, a sophisticated weighting of the observation groups and the detection of blunders within the data sets are enabled. As expected, the combined attitude solution benefits from the different noise characteristics of the star camera and the angular accelerometer. The fused attitude information consists of the low-frequency information provided by the star camera, and the high-frequent information provided by the angular accelerometer. We could show that the fused attitude data product is characterized by a significantly reduced high-frequency noise. This reduced attitude noise, directly affects the ranging and accelerometer data, which represent fundamental observations needed for the GRACE gravity field recovery. In case of good data quality and availability, the sensor fusion contributes to marginal improvements within the recovered gravity field models. Whereas, in the case of a changed satellite alignment or reduced data quality, the sensor fusion contributes to a noise-level reduction within the higher degrees (> 60). However, some limitations occur to the sensor fusion approach, since already pre-processed Level-1B data products are used as input for the senor fusion - the combined attitude estimation. Errors or noise present within the ACC1B and SCA1B data products cannot be eliminated by combining both data sets. Yet, the high-frequent noise of the SCA1B data product can be reduced significantly.

Findings from various studies by e.g., Bandikova and Flury (2014), Inácio et al. (2015), Harvey et al. (2016), and Klinger and Mayer-Gürr (2014) initiated a Level-1B data re-processing campaign at JPL, aiming at improving the attitude data processing. For the new SCA1B RL03 data product, the SDS also decided to change the official SCA1B algorithm in order to combine star camera and angular accelerometer data using a Kalman filtering approach (Bandikova et al., 2016; Sakumura et al., 2016).

The importance of ACC1B data calibration

The processing of GRACE accelerometer data has proven to be more challenging than expected, since the acceleration measurements suffer from a variety of disturbances (Hudson, 2003; Fackler, 2004; Frommknecht, 2008; Peterseim et al., 2012). The most prominent disturbance within the ACC1B data product arise from temperature-induced bias and scale factor variations (Klinger and Mayer-Gürr, 2016). The high temperature sensitivity was not expected to be a limiting factor to GRACE gravity field recovery, as the on-board thermal control was supposed to regulate the temperature. But, as a result of reduced battery

capacity, the active thermal control was permanently switched-off in April 2011. Since then, temperature variations directly affect the on-board accelerometers, impacting the quality of the ACC1B data product. Thus, more intense data pre-processing efforts are required to account for these operation anomalies. To avoid a degradation of the recovered gravity field solution due to temperature-induced accelerometer perturbations, a two-step ACC1B data calibration approach was implemented within the ITSG-Grace processing chain. Especially for month with temperature variations, the ACC1B data calibration significantly contributes to a reduction of the noise-level of the recovered gravity field models (ITSG-Grace2016). Besides, the C20 estimates can be significantly improved, i.e. clearly benefiting from the use of a fully-populated scale factor matrix. Therefore, we suggest the presence of non-zero off-diagonal elements in the accelerometer scale factor matrix and recommend the use of a fully-populated scale factor matrix to account for instrument imperfections.

From the experience with other missions, like CHAMP, GOCE or Swarm, it is known that accelerometers are sensitive to temperature variations. Based on the analysis of the estimated biases and scale factors, GRACE proofs just another example that accelerometers are highly sensitive instruments, which must be protected, in particular against temperature variations.

GRACE Level-1B data pre-processing

In summary, this work highlights the importance and potential of GRACE Level-1B data pre-processing methodologies as part of the gravity field recovery. The presented findings and research results also emphasize the independent validation of the official Level-1B data products, and support the public release of all data products (Level-1A and Level-1B) to all processing centers. Even today, every once in a while new findings and results revolutionize our understanding of GRACE instruments, and how errors or disturbances within the observation data impact the recovered gravity field solutions.

9.2 Outlook

The extension of the presented research and its application to the future GRACE-FO mission (cf. Section 2.7) is a major future objective and strong motivation for further investigations. In the following, some of the potential extensions and applications are briefly introduced.

9.2.1 GRACE

Further improvement of the Level-1B data pre-processing methodologies

On the basis of Level-1B data products, a further refinement of the sensor fusion approach and ACC1B data calibration approach is possible by further improving the parameterization of the data combination and calibration equation, respectively. For future ITSG-Grace releases, the sensor fusion represents a promising area of research, especially with regard to the stochastic modeling, i.e. the inclusion of stochastic information from the satellite orientation.

9.2.2 GRACE-FO

Independent Level-1A to Level-1B data processing

The investigations so far have focused on the pre-processed Level-1B data products, which are provided by JPL and form the data basis for the GRACE gravity field recovery. But, for GRACE-FO (cf. Section 2.7), both the Level-1A and Level-1B data products will be publicly available to all processing centers. This allows not only for an independent Level-1A to Level-1B data processing, but also for a more detailed analysis of the individual instrument data sets (e.g., noise behavior, thermal effects, interference from other instruments or sensors). Furthermore, a re-work and possible improvement of the presented data pre-processing methodologies is envisaged. Redundant Level-1A (to Level-1B) data processing reduces the dependency on official processing centers, but more importantly also allows for cross-checks among different ACs, triggering further improvements within the data processing algorithms.

Extension and revision of the sensor fusion approach

The satellite's orientation is a core piece of information needed for gravity field recovery. In view of GRACE-FO data processing, the attitude data fusion can be extended to several sensors. The goal is to adapt our sensor fusion approach to the specifics of GRACE-FO. For this purpose, algorithms for an enhanced sensor fusion of the star camera attitude data with accelerometer data, IMU data, and the LRI attitude data (yaw and pitch angles from the beam steering control loop), need to be developed and tested. The use of Level-1A data products additionally allows for a refinement of the star camera data combination by taking into account the different performance of the star cameras.

These future GRACE-FO research topics will be part of the project MAGIC (Mass redistributions from GRACE-FO using Laser Interferometry and Microwave ranging based on tailored data processing), funded by the Austrian Research Promotion Agency (FFG) in the frame of the Austrian Space Applications Programme Phase 13 (ASAP 13, Project 859736).

GRACE Reference Frames

A

For GRACE, several reference frames are used to define the various science data products (cf. Section 2.4). All Level-1B science and housekeeping data products refer to the Science Reference Frame (SRF), a body-fixed reference frame (c.f. Section A.2). In the following, the definitions of the most important GRACE reference frames, used in the framework of this thesis, are summarized. A more detailed description of all GRACE reference frames is given in Case et al. (2010) and Bettadpur (2010). Figure A.1 depicts three of the most common reference frames.

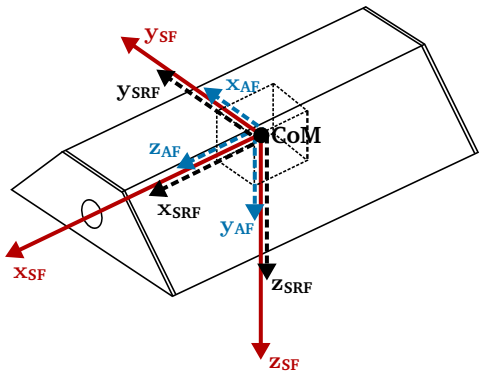

Fig. A.1.: GRACE reference frames: accommodation of the Satellite Frame (SF) (red), Science Reference Frame (SRF) (black), and Accelerometer Frame (AF) (blue). The x_{SF}-axis is pointing to the other satellite, and towards the KBR antenna phase center.

A.1 Satellite Frame (SF)

The Satellite Frame (SF) was used as basis for the satellite assembly and the payload alignment on ground (Bettadpur, 2010). The origin of the SF is at the target location of the CoM of the accelerometer proof mass. The SF coordinate axes are defined as follows:

$$
\begin{aligned}
\mathbf{x}_{\mathrm{SF}} &= \text{pointing from the origin} \\
&\quad \text{to the target location of the KBR antenna phase center (roll axis)}, \\
\mathbf{y}_{\mathrm{SF}} &= \text{forms a right handed triad with } \mathbf{x}_{\mathrm{SF}} \text{ and } \mathbf{y}_{\mathrm{SF}} \text{ (pitch axis)}, \\
\mathbf{z}_{\mathrm{SF}} &= \text{normal to the } \mathbf{x}_{\mathrm{SF}}\text{-axis and to the plane of the main equipment platform (yaw axis)}.
\end{aligned}
\tag{A.1}
$$

In orbit, the GRACE satellites have a nadir-pointing yaw axis orientation, with the roll axis in anti-flight and in-flight direction for the leading and trailing satellite, respectively.

A.2 Science Reference Frame (SRF)

By definition, the origin of the Science Reference Frame (SRF) is located at the CoM of the satellite. The SRF axes are directed parallel to the measurement axes of the accelerometer (cf. Appendix A.3)

$$\begin{aligned} \mathbf{x}_{\mathrm{SRF}} &= \mathbf{z}_{\mathrm{ACC}}, \\ \mathbf{y}_{\mathrm{SRF}} &= \mathbf{x}_{\mathrm{ACC}}, \\ \mathbf{z}_{\mathrm{SRF}} &= \mathbf{y}_{\mathrm{ACC}}. \end{aligned} \tag{A.2}$$

The origin of the SRF is maintained by regularly performed CoM calibration and trim maneuvers. The instruments onboard GRACE utilize several different coordinate systems. But, for consistency all Level-1B data products are specified w.r.t. the SRF.

A.3 Accelerometer Frame (AF)

The origin of the Accelerometer Frame (AF) is at the CoM of the accelerometer, which is aligned with the satellite's CoM regularly (by CoM calibration maneuvers). The AF coordinate axes are directed as follows:

$$\begin{aligned} \mathbf{x}_{\mathrm{AF}} &= \mathbf{y}_{\mathrm{SF}}, \\ \mathbf{y}_{\mathrm{AF}} &= \mathbf{z}_{\mathrm{SF}}, \\ \mathbf{z}_{\mathrm{AF}} &= \mathbf{x}_{\mathrm{SF}}. \end{aligned} \tag{A.3}$$

A.4 Star Camera Frame (SCF)

Each GRACE satellite is equipped with two star camera heads (cf. Section 2.3.1), which are rigidly attached to the accelerometer. The star camera heads are mounted with a zenith offset of $\pm 45°$, pointing towards the port and starboard panels of the spacecraft (cf. Fig. A.2).

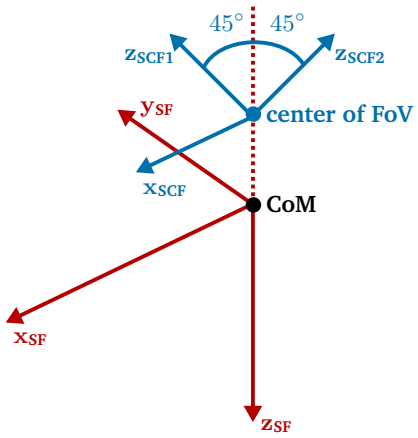

Fig. A.2.: Accommodation of the GRACE Star Camera Frame (SCF) (blue), based on the Satellite Frame (SF) (red).

The Star Camera Frame (SCF) is a sensor frame, i.e. a coordinate system defined with respect to the star camera itself. The origin of each SCF is the center of FoV, i.e. the intersection of the optical axis (boresight) with the mounting plane for the star camera head. The z-axis is aligned with the boresight of the star camera and is perpendicular to the FoV. The cross-boresight axes (x- and y-axis) are co-planar to the FoV. Consequently, the axes are directed as follows:

$$\begin{aligned}
\mathbf{x}_{\mathrm{SCF}} &= \mathbf{x}_{\mathrm{SF}}, \\
\mathbf{y}_{\mathrm{SCF}} &= \mathbf{x}_{\mathrm{SCF}} \times \mathbf{z}_{\mathrm{SCF}}, \\
\mathbf{z}_{\mathrm{SCF}} &= \text{optical axis of the star camera (boresight),} \\
&\qquad \text{pointing nominally at } \pm 45^{\circ} \text{from the } \mathbf{z}_{\mathrm{SF}} \text{ direction.}
\end{aligned} \tag{A.4}$$

The rotation between the SCF and the SRF is obtained through calibration procedures, and is provided in the quaternion product QSA1B (Case et al., 2010).

A.5 K-Band Frame (KF)

The origin of the K-Band Frame (KF) coincides with the origin of the SRF. The KF axes are directed as follows:

$$\begin{aligned}
\mathbf{x}_{\mathrm{KF}} &= \text{pointing from the satellite CoM} \\
&\qquad \text{to the calibrated KBR APC (phC vector),} \\
\mathbf{y}_{\mathrm{KF}} &= \mathbf{z}_{\mathrm{KF}} \times \mathbf{x}_{\mathrm{KF}}, \\
\mathbf{z}_{\mathrm{KF}} &= \mathbf{x}_{\mathrm{KF}} \times \mathbf{y}_{\mathrm{SRF}}.
\end{aligned} \tag{A.5}$$

A.6 LOS Frame (LOSF)

The origin of the LOS Frame (LOSF) coincides with the origin of the SRF, with the x-axis pointing towards the other satellite's CoM. The LOS axes are directed as follows:

$$\begin{aligned}
\mathbf{x}_{\mathrm{LOS}_j} &= \mathbf{e}_{ij} = \frac{\mathbf{r}_j - \mathbf{r}_i}{|\mathbf{r}_j - \mathbf{r}_i|} \\
\mathbf{y}_{\mathrm{LOS}_j} &= \mathbf{x}_{\mathrm{LOS}_j} \times \frac{\mathbf{r}_i}{|\mathbf{r}_i|}, \\
\mathbf{z}_{\mathrm{LOS}_j} &= \mathbf{x}_{\mathrm{LOS}_j} \times \mathbf{y}_{\mathrm{LOS}_j} = \mathbf{e}_{ij} \times \left(\mathbf{x}_{\mathrm{LOS}_j} \times \frac{\mathbf{r}_i}{|\mathbf{r}_i|} \right).
\end{aligned} \tag{A.6}$$

Therein, parameters with the indices $i, j = A, B$ $(i \neq j)$ refer to GRACE-A or GRACE-B, and the vector $\mathbf{r}$ represents the position of one satellite w.r.t. the inertial frame.

In the case of a perfect inter-satellite alignment, the LOS Frame and the KF coincide, i.e. the phc vector is perfectly aligned with the LOS.

A.7 Inertial Reference Frame (IRF)

Within this thesis, the Inertial Reference Frame (IRF) refers to the International Celestial Reference Frame (ICRF), realized by the J2000.0 equatorial coordinates.

The ICRF is a quasi-inertial reference system with its origin located at the Earth's CoM. The z-axis points towards the North Pole and corresponds to the rotation axis of the Earth. The x-axis points towards the vernal equinox for the epoch J2000.0. The right-handed coordinate system is completed by the y-axis, which is perpendicular to the xz-plane. For the exact definitions, the reader is referred to IAU (2000), McCarthy and Petit (2003), and Petit and Luzum (2010).

A.8 Terrestrial Reference Frame (TRF)

Within this thesis, the Terrestrial Reference Frame (TRF) refers to the International Terrestrial Reference Frame (ITRF). The ITRF is defined and maintained by the IERS, and adopted as standard global TRF within the IERS conventions 2010 (Petit and Luzum, 2010). For details on the definitions, the reader is referred to e.g., McCarthy and Petit (2003) and Petit and Luzum (2010). The current realization of the ITRF is the ITRF2014 (Altamimi et al., 2016).

Transformations between the ICRF and the ITRF are performed based on the transformation parameters provided by the IERS (McCarthy and Petit, 2003; Petit and Luzum, 2010).

GRACE Macro Model

B

The GRACE Macro Model is a 9-plate model describing the surface properties and geometry of the satellites. As the GRACE mission consists of two identical satellites (GRACE-A, GRACE-B), only one Macro Model valid for both satellites is provided. At launch, both satellites had an identical mass of 487.2 kg. Updated mass values are provided in the MAS1B housekeeping data products (cf. Section 2.5.2).

Figure B.1 shows the GRACE Macro Model, i.e. an engineering drawing of a GRACE satellite in front view and in side view.

For each surface element (plate), the area, the normal vector (in the SRF), the type of material, and its emissivity, absorptivity, and reflectivity coefficients are provided (Bettadpur, 2010); summarized in Table B.1.

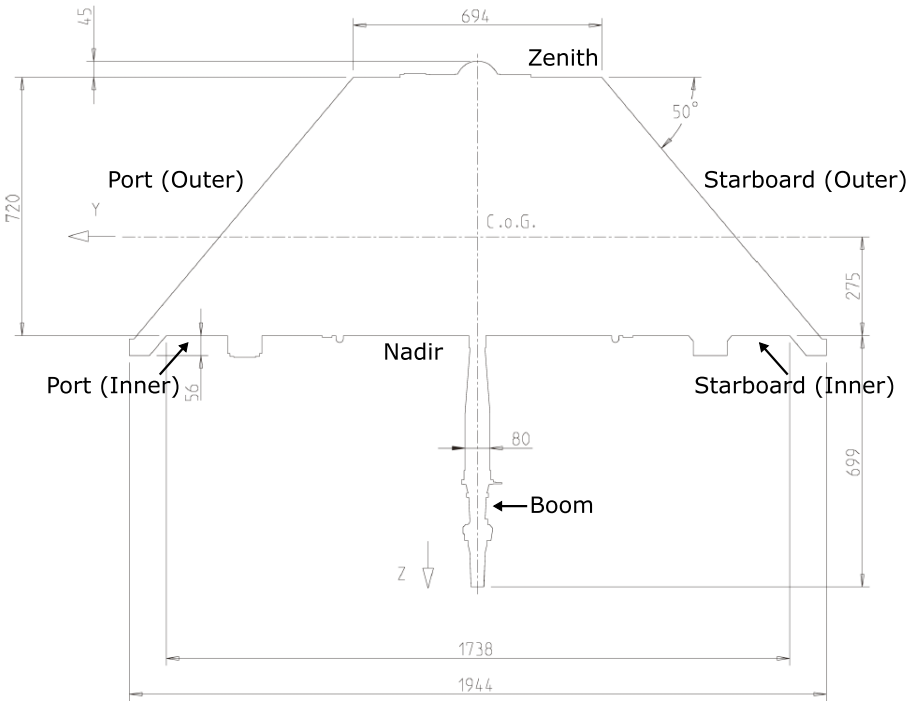

(a) Front view

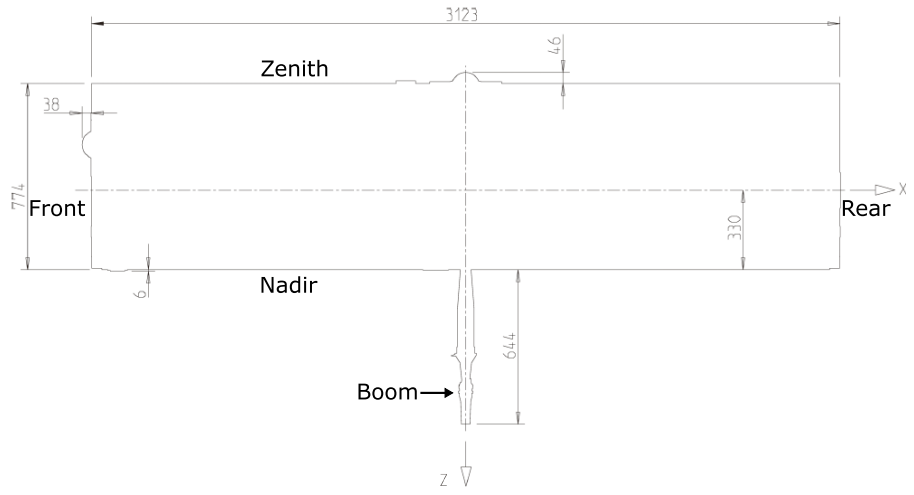

(b) Side view

Fig. B.1.: GRACE Macro Model: 9-plate model of a GRACE satellite in front view (a) and side view (b), with dimensions in mm. Source: Bettadpur (2010).

Tab. B.1.: GRACE Macro Model: surface properties according to Bettadpur (2010).

#	Panel	Area [m^2]	Unit normal [x,y,z]	Material	Emiss (IR)	Absorp (Vis)	Refl (Vis)		Refl (IR)	
1	Front	0.96	$\begin{bmatrix}+1.00\\+0.00\\+0.00\end{bmatrix}$	SiOx/Kapton	0.62	0.34	0.40	0.26	0.23	0.15
2	Rear	0.96	$\begin{bmatrix}-1.00\\+0.00\\+0.00\end{bmatrix}$	SiOx/Kapton	0.62	0.34	0.40	0.26	0.23	0.15
3	Starboard (Outer)	3.16	$\begin{bmatrix}+0.00\\+0.77\\-0.64\end{bmatrix}$	Si Glass (Solar Array)	0.81	0.65/0.72*	0.05	0.30	0.03	0.16
4	Starboard (Inner)	0.23	$\begin{bmatrix}+0.00\\-0.77\\+0.64\end{bmatrix}$	SiOx/Kapton	0.62	0.34	0.40	0.26	0.23	0.15
5	Port (Outer)	3.16	$\begin{bmatrix}+0.00\\-0.77\\-0.64\end{bmatrix}$	Si Glass (Solar Array)	0.81	0.65/0.72*	0.05	0.30	0.03	0.16
6	Port (Inner)	0.23	$\begin{bmatrix}+0.00\\+0.77\\+0.64\end{bmatrix}$	SiOx/Kapton	0.62	0.34	0.40	0.26	0.23	0.15
7	Nadir	6.07	$\begin{bmatrix}+0.00\\+0.00\\+1.00\end{bmatrix}$	Teflon	0.75	0.12	0.68	0.20	0.19	0.06
8	Zenith	2.17	$\begin{bmatrix}+0.00\\+0.00\\-1.00\end{bmatrix}$	Si Glass (Solar Array)	0.81	0.65/0.72	0.05	0.30	0.03	0.16
9	Boom	0.05	–	SiOx/Kapton	0.62	0.34	0.40	0.26	0.23	0.15

*non-operating solar array

C Quaternions

In 1843, Sir William Rowan Hamilton, an Irish physicist, astronomer, and mathematician, introduced quaternions. Quaternions can be seen as hyper-complex numbers of rank 4 (Kuipers, 1999). An important precursor to the work of Hamilton was Olinde Rodrigues' parameterization of general rotations by four parameters (1840).

In the context of GRACE, quaternions are used to represent the satellites' attitude within the Level-1A and Level-1B star camera data products (cf. Section 4.1). Therefore, quaternions are essential for any star camera data processing or analysis.

In the following, only the fundamentals of quaternion algebra are introduced, based on the theory and the definitions given by Kuipers (1999) and Diebel (2006). A complete and comprehensive overview of the extensive body of quaternion mathematics is far beyond the scope of this thesis.

C.1 Quaternion basics

A quaternion $\mathbf{q}$ may be represented as a 4-tuple of real numbers (Kuipers, 1999)

$$q = (q_0, q_1, q_2, q_3)\,, \tag{C.1}$$

where $q_0,\ q_1,\ q_2,\ q_3$ are real numbers or scalars. Or alternatively, quaternions may also be represented as a vector

$$q = q_0 + \mathbf{q} = q_0 + \mathbf{i}q_1 + \mathbf{j}q_2 + \mathbf{k}q_3, \tag{C.2}$$

where q_0 represents the scalar part, $\mathbf{q} = [q_1, q_2, q_3]^\intercal$ represents the vector part, and $\mathbf{i},\ \mathbf{j},\ \mathbf{k}$ denote the standard orthonormal basis of $\mathbb{R}^3$. The scalars $q_0,\ q_1,\ q_2,\ q_3$ are denoted as quaternion components. In this vector-like notation, the quaternion can be represented by its 4 components:

$$\mathbf{q} = [q_0, q_1, q_2, q_3]^\intercal = \begin{bmatrix} q_0 \\ \mathbf{q}_{1:3} \end{bmatrix},\ \mathbf{q}_{1:3} \in \mathbb{R}^3. \tag{C.3}$$

As a consequence, quaternions are always denoted by some lower-case bold-faced letters (e.g., $\mathbf{q},\ \mathbf{p}$), like ordinary vectors in three-dimensional space (Kuipers, 1999).

The complex conjugate, norm, and inverse of a quaternion $\mathbf{q}$ are defined as

$$q^* = [q_0, -q_1, -q_2, -q_3]^\intercal = \begin{bmatrix} q_0 \\ -\mathbf{q}_{1:3} \end{bmatrix}, \tag{C.4}$$

$$|\mathbf{q}| = \sqrt{\mathbf{q}^*\mathbf{q}} = \sqrt{q_0^2 + q_1^2 + q_2^2 + q_3^2}, \tag{C.5}$$

$$\mathbf{q}^{-1} = \frac{\mathbf{q}^*}{|\mathbf{q}|}. \tag{C.6}$$

By the definition of the inverse, the following condition holds true:

$$\mathbf{q}^{-1}\mathbf{q} = \mathbf{q}\mathbf{q}^{-1} = 1. \tag{C.7}$$

Quaternions are primarily used as rotation operators to represent three-dimensional (3D) rotations. Any finite rotation (from a reference frame A to a reference frame B) may be achieved by a single rotation about an appropriately chosen axis (cf. Fig. C.1). Therefore, it is possible to parameterize the attitude of a body with and angle $\psi \in \mathbb{R}$ and a unit vector $\mathbf{n} \in \mathbb{R}^3$ (Diebel, 2006). The unit quaternion that arises from a rotation ψ about an axis $\mathbf{n}$ is given by

$$\begin{aligned} q_0 &= \cos(\psi/2), \\ q_1 &= \sin(\psi/2)\cos\alpha, \\ q_2 &= \sin(\psi/2)\cos\beta, \\ q_3 &= \sin(\psi/2)\cos\gamma, \end{aligned} \tag{C.8}$$

where $cos\alpha$, $cos\beta$, $cos\gamma$ are the direction cosines of the rotation axis $\mathbf{n}$.

A unit quaternion is a quaternion with unity norm

$$|\mathbf{q}| = 1. \tag{C.9}$$

For any unit quaternion $\mathbf{q}$, the inverse of the quaternion is equal to the complex conjugate

$$\mathbf{q}^{-1} = \mathbf{q}^*. \tag{C.10}$$

Throughout this work, quaternions which are used to represent the attitude of a satellite, are assumed to be unit quaternions.

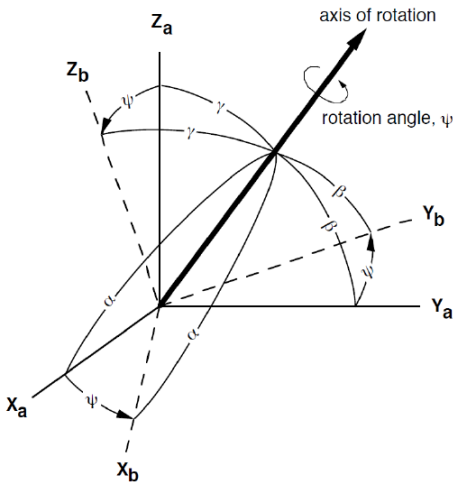

Fig. C.1.: Axis-angle representation of a 3D frame rotation. Source: Wu et al. (2006).

C.2 Quaternion operations

C.2.1 Addition & Scalar multiplication

Both, quaternion addition and scalar multiplication, are inherited from the vector space. Therefore, the sum of two quaternions $\mathbf{q}$ and $\mathbf{p}$ is defined by adding the quaternions component-by-component

$$\mathbf{q} + \mathbf{p} = \begin{bmatrix} q_0 + p_0 \\ q_1 + p_1 \\ q_2 + p_2 \\ q_3 + p_3 \end{bmatrix}. \tag{C.11}$$

Accordingly, the product of a scalar c and a quaternion $\mathbf{q}$ is given by

$$c\mathbf{q} = \begin{bmatrix} cq_0 \\ cq_1 \\ cq_2 \\ cq_3 \end{bmatrix}. \tag{C.12}$$

C.2.2 Multiplication

The product of two quaternions $\mathbf{q}$ and $\mathbf{p}$ in matrix notation is defined as

$$\mathbf{qp} = \underbrace{\begin{bmatrix} +q_0 & -q_1 & -q_2 & -q_3 \\ +q_1 & +q_0 & -q_3 & +q_2 \\ +q_2 & +q_3 & +q_0 & -q_1 \\ +q_3 & -q_2 & +q_1 & +q_0 \end{bmatrix}}_{\mathbf{Q}(\mathbf{q})} \begin{bmatrix} p_0 \\ p_1 \\ p_2 \\ p_3 \end{bmatrix}. \tag{C.13}$$

The multiplication of two quaternions, as defined in Equation C.13, gives as result a quaternion $\mathbf{s} = \mathbf{qp}$. Quaternion multiplication is associative ($\mathbf{q}(\mathbf{ps}) = (\mathbf{qp})\mathbf{s}$), but not commutative ($\mathbf{qp} \neq \mathbf{pq}$).

C.2.3 Rotation of a vector by a quaternion

In matrix form, the rotation of a vector $\mathbf{v}$ by the rotation matrix $\mathbf{R}$ is given by the equation:

$$\mathbf{w} = \mathbf{R}\mathbf{v}. \tag{C.14}$$

Equivalently, the rotation of a vector $\mathbf{v}$ by using a quaternion $\mathbf{q}$ as rotation operation, is then given by

$$\begin{aligned} \mathbf{w} &= \mathbf{q}^* \mathbf{v} \mathbf{q} \\ &= (2q_0 - 1)\mathbf{v}_A + 2(\mathbf{v}_A \cdot \mathbf{q}_{1:3})\mathbf{q}_{1:3} + 2q_0(\mathbf{v}_A \times \mathbf{q}_{1:3}). \end{aligned} \tag{C.15}$$

Therein, the vector $\mathbf{v}$ is considered as a "pure quaternion", i.e. a quaternion with a zero scalar part ($v = 0 + \mathbf{v}$). Geometrically, the rotation operator $\mathbf{q}^* \mathbf{v} \mathbf{q}$ can be seen as a reference frame rotation, i.e. rotating a fixed vector $\mathbf{v}$ in a reference frame A into a reference frame B, resulting in vector $\mathbf{w}$.

C.2.4 Unit quaternion ⇒ rotation matrix

The transformation from a unit quaternion $\mathbf{q}$ to a rotation matrix $\mathbf{R}$ is explicitly defined by

$$\mathbf{R}(\mathbf{q}) = \begin{bmatrix} q_0^2 + q_1^2 - q_2^2 - q_3^2 & 2q_1q_2 + 2q_0q_3 & 2q_1q_3 - 2q_0q_2 \\ 2q_1q_2 - 2q_0q_3 & q_0^2 - q_1^2 + q_2^2 - q_3^2 & 2q_2q_3 + 2q_0q_1 \\ 2q_1q_3 + 2q_0q_2 & 2q_2q_3 - 2q_0q_1 & q_0^2 + q_1^2 - q_2^2 + q_3^2 \end{bmatrix}. \tag{C.16}$$

C.2.5 Rotation matrix ⇒ unit quaternion

The inverse transformation from a rotation matrix to a unit quaternion is not explicit

$$\begin{aligned} q_0 &= \pm \frac{1}{2}\sqrt{1 + R_{11} + R_{22} + R_{33}}, \\ q_1 &= (R_{23} - R_{32})/4q_0, \\ q_2 &= (R_{31} - R_{13})/4q_0, \\ q_3 &= (R_{12} - R_{21})/4q_0, \end{aligned} \tag{C.17}$$

where R_{ij} denotes the matrix elements, with the indices i, j referring to the rows and columns of the rotation matrix. For more details, the reader is referred to Diebel (2006).

C.2.6 Unit quaternion ⇒ Euler angles (1-2-3)

The mapping from a unit quaternion to a set of Euler angles (or Cardan angles, cf. Appendix D.1) with the Euler angle sequence (1-2-3), is given by

$$\begin{aligned} \phi &= \arctan\left(\frac{2(q_2q_3 + q_0q_1}{q_0^2 - q_1^2 - q_2^2 + q_3^2}\right) = \arctan\left(\frac{R_{23}}{R_{33}}\right), \\ \theta &= -\arcsin\left(2(q_1q_3 - q_0q_2)\right) = -\arcsin\left(R_{13}\right), \\ \psi &= \arctan\left(\frac{2(q_1q_2 + q_0q_3}{q_0^2 + q_1^2 - q_2^2 - q_3^2}\right) = \arctan\left(\frac{R_{12}}{R_{11}}\right). \end{aligned} \tag{C.18}$$

C.2.7 Unit quaternion ⇒ Angular velocity

The quaternion rates $\dot{\mathbf{q}}$ are related to the angular velocity $\boldsymbol{\omega}$ (in body fixed coordinates) through (Diebel, 2006)

$$\boldsymbol{\omega}(\mathbf{q}, \dot{\mathbf{q}}) := 2\mathbf{W}(\mathbf{q})\dot{\mathbf{q}}. \tag{C.19}$$

Therein, the quaternion rate matrix $\mathbf{W}$ maps a unit quaternion and its temporal derivative to the angular velocity. The time derivative of the unit quaternion is given by the vector of

quaternion rates, which can be computed by numerical differentiation. The quaternion rate matrix $W(\mathbf{q})$ is defined as

$$\mathbf{W} = \begin{bmatrix} -q_1 & +q_0 & +q_3 & -q_2 \\ -q_2 & -q_3 & +q_0 & +q_1 \\ -q_3 & +q_2 & -q_1 & +q_0 \end{bmatrix}. \tag{C.20}$$

C.2.8 Unit quaternion $\Rightarrow$ Angular acceleration

Following from Equation (C.20), the angular acceleration $\dot{\boldsymbol{\omega}}$, expressed in a body-fixed reference frame, may also be related to the time derivatives of the quaternion components by

$$\dot{\boldsymbol{\omega}} := 2\mathbf{W}(\mathbf{q})\ddot{\mathbf{q}}. \tag{C.21}$$

The second derivative of the unit quaternion may be approximated by numerical differentiation or a second order difference quotient (cf. Section 6.3.2).

Auxiliary computations

D

D.1 Roll, pitch, yaw - Cardan angles

Any rotation matrix $\mathbf{R}$ can be decomposed as a product of three elemental rotation matrices

$$\mathbf{R} = \mathbf{R}_1(\phi)\mathbf{R}_2(\theta)\mathbf{R}_3(\psi), \tag{D.1}$$

where $\mathbf{R}_{1-3}$ are the elementary rotations about the x-, y-, z-axes. The angles associated with the sequence (1-2-3) are also denoted as Cardan Angles (or simply as Euler angles), which are commonly used in aerospace engineering. The angles ϕ, θ, and ψ are known as roll, pitch, and yaw, respectively. The individual rotation matrices are defined as follows:

$$\mathbf{R}_1 = \begin{bmatrix} 1 & 0 & 0 \\ 0 & \cos\phi & \sin\phi \\ 0 & -\sin\phi & \cos\phi \end{bmatrix}, \tag{D.2}$$

$$\mathbf{R}_2 = \begin{bmatrix} \cos\theta & 0 & -\sin\theta \\ 0 & 1 & 0 \\ \sin\theta & 0 & \cos\theta \end{bmatrix}, \tag{D.3}$$

$$\mathbf{R}_3 = \begin{bmatrix} \cos\psi & \sin\psi & 0 \\ -\sin\psi & \cos\psi & 0 \\ 0 & 0 & 1 \end{bmatrix}. \tag{D.4}$$

Evaluating Equation (D.1) yields

$$\mathbf{R} = \begin{bmatrix} \cos\theta\ \cos\psi & \cos\theta\ \sin\psi & -\sin\theta \\ \sin\phi\ \sin\theta\ \cos\psi - \cos\phi\ \sin\psi & \sin\phi\ \sin\theta\ \sin\psi + \cos\phi\ \cos\psi & \sin\phi\ \cos\theta \\ \cos\phi\ \sin\theta\ \cos\psi + \sin\phi\ \sin\psi & \cos\phi\ \sin\theta\ \sin\psi - \sin\phi\ \cos\psi & \cos\phi\ \cos\theta \end{bmatrix}. \tag{D.5}$$

The inverse mapping, which expresses the Cardan angles as a function of the rotation matrix, is given by

$$\begin{aligned} \phi &= \arctan\left(\frac{R_{23}}{R_{33}}\right), \\ \theta &= -\arcsin\left(R_{13}\right), \\ \psi &= \arctan\left(\frac{R_{12}}{R_{11}}\right), \end{aligned} \tag{D.6}$$

where R_{ij} denotes the matrix elements, with the indices i, j referring to the rows and columns of the matrix $\mathbf{R}$ (cf. Eq. (D.5)).

D.2 Beta prime angle

The β' angle is a quantity primarily used in spaceflight, describing the orbital configuration w.r.t. the Sun. It determines the amount of time an object, such as a LEO, spends in direct sunlight, absorbing solar energy by the solar panels. The β' angle is defined as the angle between the orbital plane of the spacecraft and the Earth-Sun line (cf. Figure D.1)

$$\beta' = \arccos\left(\frac{\mathbf{n} \cdot \mathbf{r}_\odot}{|\mathbf{n}| \cdot \mathbf{r}_\odot}\right) - 90°, \tag{D.7}$$

where $\mathbf{n}$ is the vector cross product between the satellite's position and velocity vector w.r.t. to the inertial frame ($\mathbf{n} = -(\mathbf{r} \times \dot{\mathbf{r}})$), i.e. it denotes the normal vector of satellite's orbit. $\mathbf{r}_\odot$ denotes the position vector of the Sun w.r.t. to the inertial frame, representing the Earth-Sun line. Theoretically, the β' angle of a near-polar LEO varies between $\pm 90°$, as depicted in Figure D.1.

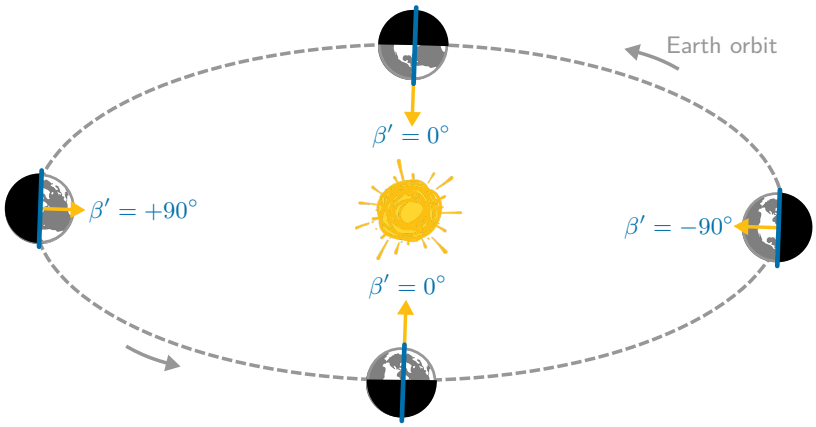

Fig. D.1.: Illustration of the β' angle variations of a near-polar LEO: the orbital plane is depicted in blue, with the normal vector or angular momentum vector being perpendicular to the instantaneous orbital plane. The position vector of the Sun, i.e. the Earth-Sun line is depicted as yellow vector.

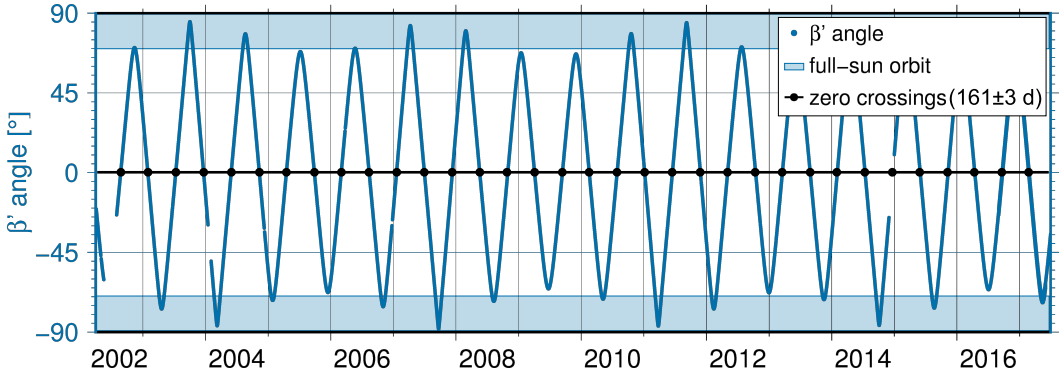

Fig. D.2.: β' angle variations of GRACE-A for the GRACE mission period from April 2002 to June 2017.

Figure D.2 shows the β' angle variations of GRACE-A for the whole GRACE mission period from April 2002 to June 2017. Since the two GRACE satellites follow each other in the same orbit, only results for GRACE-A are shown.

Every 161 days, at $\beta' = 0°$ crossings, the Sun is in the orbital plane of the satellites. During this period, the spacecraft spend nearly half their revolution time in the Earth's shadow, and thus rely on their batteries for power. As a consequence, the GRACE instruments are shut down for small β' angles (since April 2011). In between, when the satellite is in full-sun orbit ($\beta' > 70°$), the Sun is visible to the satellite at all time and primarily illuminates the side panels (Herman et al., 2012).

In the case of GRACE, the β' angle does not reach exactly $\pm 90°$ due to the drift of the ascending node of the orbit, which causes a precession of the orbital plane ($\sim 1.1°$ day) with a 322 day period in the inertial frame.

D.3 Argument of latitude

The argument of latitude u represents the position of the satellite along the orbit, describing the angle between the ascending node and the satellite (cf. Fig. D.3). Thus, its values vary between $0°$ and $360°$ ($\pm 180°$), as depicted in Figure D.4. The argument of latitude is defined as

$$u = \omega + \nu, \tag{D.8}$$

where ω denotes the argument of perigee, and ν denotes the true anomaly. Further evaluating Equation (D.8) gives (Montenbruck and Gill, 2001)

$$u = \arctan\left(\frac{z/\sin i}{x\cos\Omega + y\sin\Omega}\right) = \arctan\left(\frac{z}{-xh_y + yh_x}\right), \tag{D.9}$$

with

$$\mathbf{h} = \frac{\mathbf{r}\times\dot{\mathbf{r}}}{|\mathbf{r}\times\dot{\mathbf{r}}|} = \begin{bmatrix} h_x \\ h_y \\ h_z \end{bmatrix}. \tag{D.10}$$

Therein, $\mathbf{h}$ denotes the normalized areal velocity vector, derived from the satellite's position $\mathbf{r} = [x, y, z]^\intercal$ and velocity $\dot{\mathbf{r}} = [\dot{x}, \dot{y}, \dot{z}]^\intercal$.

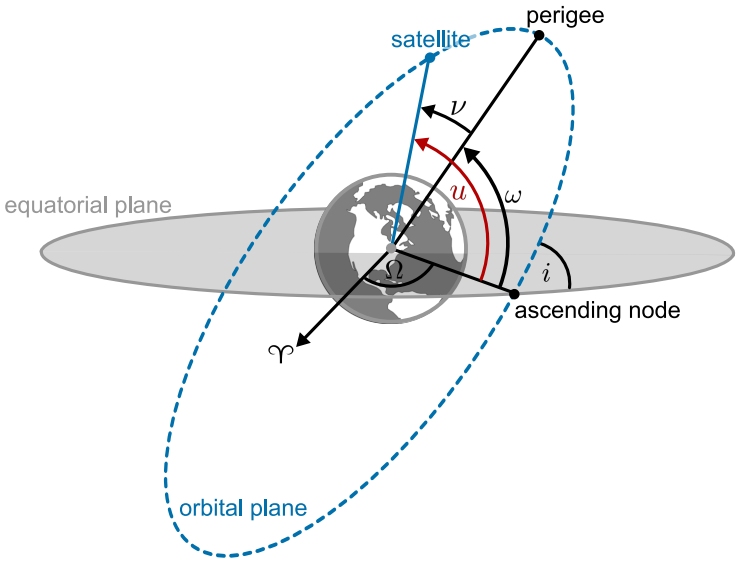

Fig. D.3.: Keplerian elements (inclination i, right ascension of the ascending node Ω, argument of perigee ω, true anomaly ν) and argument of latitude u (red).

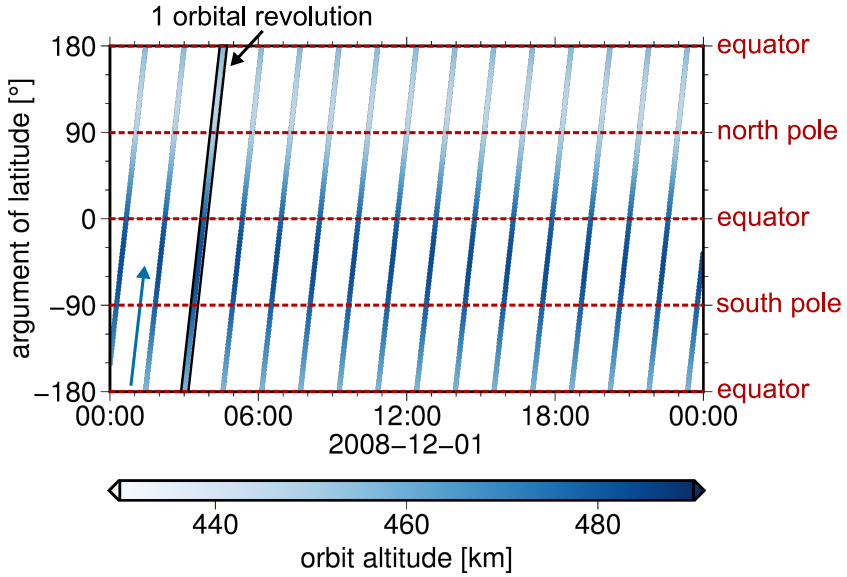

Fig. D.4.: Plotting along the orbit: Argument of latitude plot illustrating the GRACE-A orbit altitude as a function of the argument of latitude and time for one day (2008-12-01; ≈ 15.5 orbital revolutions). The direction of flight is indicated by the blue arrow. The color indicates the orbit altitude.

Bibliography

Altamimi, Z., Rebischung, P., Métivier, L., and Collilieux, X. (2016). *ITRF2014: A new release of the International Terrestrial Reference Frame modeling nonlinear station motions*. Journal of Geophysical Research: Solid Earth 121 (8), 6109–6131. DOI: 10.1002/2016JB013098.

Arbinger, C., Amico, S., Feucht, U., and Finzi, A. (2003). *The GRACE formation: science mode pointing performance analysis*. In: 3rd International Workshop on Satellite Constellations and Formations. Pisa, Italy.

Asmar, S. W. (1997). *Characteristic Trends of Ultrastable Oscillators for Radio Science Experiments*. TDA Progress Report, 42-129. URL: https://ipnpr.jpl.nasa.gov/progress_report/42-129/129F.pdf.

Bandikova, T. (2015). *The role of attitude determination for inter-satellite ranging*. PhD thesis. Fakultät für Bauingenieurwesen und Geodäsie, Wilhelm Leibniz Universität Hannover. URL: https://dgk.badw.de/fileadmin/user_upload/Files/DGK/docs/c-758.pdf.

Bandikova, T. and Flury, J. (2014). *Improvement of the GRACE star camera data based on the revision of the combination method*. Advances in Space Research 54, 1818–1827. DOI: 10.1016/j.asr.2014.07.004.

Bandikova, T., Flury, J., and Ko, U.-D. (2012). *Characteristics and accuracies of the GRACE inter-satellite pointing*. Advances in Space Research 50, 123–135. DOI: 10.1016/j.asr.2012.03.011.

Bandikova, T., Harvey, N., Sakumura, C., and McCullough, C. (2016). *RL03 - data processing and improved features*. Poster presentation at: GRACE Science Team Meeting 2016, Potsdam, Germany.

Bandikova, T., McCullough, C., and Kruizinga, G. (2017). *Improved GRACE accelerometer data transplant due to thruster spike modeling*. Poster presentation at: GRACE Science Team Meeting 2017, Austin, Texas.

Behzadpour, S., Mayer-Gürr, T., Flury, J., and Goswami, S. (2017). *Estimation of GRACE observation error covariance in wavelet domain*. Presented at: EGU General Assembly 2017, Vienna, Austria. Geophysical Research Abstracts Vol. 19, EGU2017-12512.

Bettadpur, S. (2009). *Recommendation for a-priori Bias & Scale Parameters for Level-1B ACC Data (Version 2)*. GRACE TN-02. Center for Space Research, The University of Texas at Austin. URL: ftp://podaac.jpl.nasa.gov/allData/grace/docs/TN-02_ACC_CalInfo.pdf.

Bettadpur, S. (2010). *Gravity Recovery and Climate Experiment: Product Specification Document*. Technical Report GRACE 307-720. Center for Space Research, The University of Texas at Austin. URL: ftp://podaac.jpl.nasa.gov/allData/grace/docs/ProdSpecDoc_v4.6.pdf.

Bettadpur, S. (2012). *UTCSR Level-2 Processing Standards Document For Level-2 Product Release 0005*. GRACE 327-742. Center for Space Research, The University of Texas at Austin. URL: ftp://podaac.jpl.nasa.gov/allData/grace/docs/L2-CSR0005_ProcStd_v4.0.pdf.

Bettadpur, S. and McCullough, C. (2017). *The Classical Variational Approach*. In: Global Gravity Field Modeling from Satellite-to-Satellite Tracking Data. Ed. by M. Naeimi and J. Flury. Cham: Springer International Publishing, 81–95. ISBN: 978-3-319-49941-3.

Beutler, G., Jäggi, A., Mervart, L., and Meyer, U. (2010). *The celestial mechanics approach: theoretical foundations*. Journal of Geodesy 84 (10), 605–624. DOI: 10.1007/s00190-010-0401-7.

Bezděk, A. (2010). *Calibration of accelerometers aboard GRACE satellites by comparison with POD-based nongravitational accelerations*. Journal of Geodynamics 50, 410–423. DOI: 10.1016/j.jog.2010.05.001.

Biancale, R. and Bode, A. (2006). *Mean annual and seasonal atmospheric tide models based on 3-hourly and 6-hourly ECMWF surface pressure data*. Scientific Technical Report STR, 06/01. GeoForschungsZentrum Potsdam. DOI: 10.2312/GFZ.b103-06011.

Biancale, R., Lemoine, J.-M., Balmino, G., Bruinsma, S., Perosanz, F., Marty, J.-C., Loyer, S., Bourgogne, S., and Gégout, P. (2014). *CNES/GRGS gravity field models RL03-v3*. GFZ Data Services.

Bowman, B. R., Tobiska, W. K., Marcos, F. A., Huang, C. Y., Lin, C. S., and Burke, W. J. (2008). *A New Empirical Thermospheric Density Model JB2008 Using New Solar and Geomagnetic Indices*. In: AIAA/AAS Astrodynamics Specialist Conference. Honolulu, Hawaii. URL: http://sol.spacenvironment.net/jb2008/pubs/AIAA_2008-6438_JB2008_Model.pdf.

Bruinsma, S. (2014). *The DTM-2013 thermosphere model*. Journal of Space Weather and Space Climate 5. DOI: 10.1051/swsc/2015001.

Case, K., Kruizinga, G., and Wu, S.-C. (2010). *GRACE Level 1B Data Product User Handbook*. Technical Report JPL D-22027. Jet Propulsion Laboratory. URL: ftp://podaac.jpl.nasa.gov/allData/grace/docs/Handbook_1B_v1.3.pdf.

Chen, J. L., Wilson, C. R., and Seo, K.-W. (2009). *S2 tide aliasing in GRACE time-variable gravity solutions*. Journal of Geodesy 83 (7), 679–687. DOI: 10.1007/s00190-008-0282-1.

Cheng, M. and Ries, J. (2017). *The unexpected signal in GRACE estimates of C_{20}*. Journal of Geodesy 91 (8), 897–914. DOI: 10.1007/s00190-016-0995-5.

Cheng, M., Ries, J. C., and Tapley, B. D. (2011). *Variations of the Earth's figure axis from satellite laser ranging and GRACE*. Journal of Geophysical Research 116 (B01409). DOI: 10.1029/2010JB000850.

Cheng, M., Tapley, B. D., and Ries, J. C. (2013). *Deceleration in the Earth's oblateness*. Journal of Geophysical Research 118, 704–747. DOI: 10.1002/jgrb.50058.

Christophe, B., Boulanger, D., Foulon, B., Huynh, P.-A., Lebat, V., Liorzou, F., and Perrot, E. (2015). *A new generation of ultra-sensitive electrostatic accelerometers for GRACE Follow-on and towards the next generation gravity missions*. Acta Astronautica 117, 1–7. DOI: 10.1016/j.actaastro.2015.06.021.

Dahle, C., Flechtner, F., Gruber, C., König, D., König, R., Michalak, G., and Neumayer, K.-H. (2013). *GFZ GRACE Level-2 Processing Standards Document for Level-2 Product Release 0005*. Scientific Technical Report STR12/02 - Data. GeoForschungsZentrum Potsdam. URL: ftp://rz-vm152.gfz-potsdam.de/grace/DOCUMENTS/Level-2/GRACE_GFZ_L2_Processing_Standards_Document_for_RL05.pdf.

De Boor, C. (2001). *A Pracitcal Guide to Splines*. Revised edition. Berlin Heidelberg New York: Springer. ISBN: 978-0-387-95366-3.

Desai, S. D. (2002). *Observing the pole tide with satellite altimetry*. Journal of Geophysical Research: Oceans 107 (C11), 7–1–7–13. DOI: 10.1029/2001JC001224.

Diebel, J. (2006). *Representing Attitude: Euler Angles, Unit Quaternions, and Rotation Vectors*. Stanford University. URL: https://www.astro.rug.nl/software/kapteyn/_downloads/attitude.pdf.

Dobslaw, H., Bergmann-Wolf, I., Forootan, E., Dahle, C., Mayer-Gürr, T., Kusche, J., and Flechtner, F. (2017). *Modeling of present-day atmosphere and ocean non-tidal de-aliasing errors for future gravity mission simulations*. Journal of Geodesy 90 (5), 423 –436. DOI: 10.1007/s00190-015-0884-3.

Dornboos, E., Förster, M., Fritsche, B., Helleputte, T. van, Ijssel, J. van den, Koppenwallner, G., Lühr, H., Rees, D., Visser, P., and Kern, M. (2009). *Air density models derived from multi-satellite drag observations*. ESA study, ESTEC contract 21022/07/NL/HE, DEOS/TU Delft scientic report.

Ellmer, M. and Mayer-Gürr, T. (2017a). *Estimation of GRACE K-Band antenna phase center coordinates using an error-in-variables approach*. Presented at: EGU General Assembly 2017, Vienna, Austria. Geophysical Research Abstracts Vol. 19, EGU2017-6415.

Ellmer, M. and Mayer-Gürr, T. (2017b). *High precision dynamic orbit integration for spaceborne gravimetry in view of GRACE Follow-on*. Advances in Space Research 60 (1), 1 –13. DOI: 10.1016/j.asr.2017.04.015.

ESA (1999). *The Four Candidate Earth Explorer Core Missions - Gravity Field and Steady-State Ocean Circulation Mission*. ESA SP-1233. URL: http://earth.esa.int/goce04/Documents/goce_sp1233_1.pdf.

Fackler, U. (2004). *GRACE - Analyse von Beschleunigungsmessungen*. MA thesis. Institut für Astronomische und Physikalische Geodäsie, Technische Universität München. URL: http://www.iapg.bgu.tum.de/mediadb/9833/9834/iapg_fesg_rpt_20.pdf.

Flechtner, F., Dobslaw, H., and Fagiolini, E. (2015). *AOD1B Product Description Document for Product Release 05*. Tech. rep. URL: ftp://podaac.jpl.nasa.gov/allData/grace/docs/AOD1B_PDD_v4.4.pdf.

Flechtner, F., Neumayer, K.-H., Dahle, C., Dobslaw, H., Fagiolini, E., Raimondo, J.-C., and Güntner, A. (2016). *What can be expected from the GRACE-FO Laser Ranging Interferometer for Earth Science Applications*. Surveys in Geophysics 37 (2), 453–470. DOI: 10.1007/s10712-015-9338-y.

Flechtner, F., Landerer, F., Webb, F., Watkins, M., Dahle, C., Massmann, F.-H., Bettadpur, S., and Save, H. (2017). *Status of the GRACE Follow-On Mission*. Presented at: GRACE Science Team Meeting 2017, Austin, Texas. URL: http://www2.csr.utexas.edu/grace/GSTM/2017/proceedings.html.

Flury, J., Bettadpur, S., and Tapley, B. (2008). *Precise accelerometry onboard the GRACE gravity field satellite mission*. Adv. Space Res. 42, 1414–1423. DOI: 10.1016/j.asr.2008.05.004.

Folkner, W. M., Williams, J. G., and Boggs, D. H. (2009). *The Planetary and Lunar Ephemeris DE 421*. IPN Progress Report 42-178, pp. 1–34. URL: https://ipnpr.jpl.nasa.gov/progress_report/42-178/178C.pdf.

Förstner, W. (1979). *Ein Verfahren zur Schätzung von Varianz- und Kovarianzkomponenten*. Allgemeine Vermessungsnachrichten 11-12, 446–453.

Frommknecht, B. (2008). *Integrated sensor analysis of the GRACE mission*. PhD thesis. Fakultät für Bauingenieur- und Vermessungswesen, Technische Universität München. URL: http://mediatum.ub.tum.de/doc/630607/454947.pdf.

Goswami, S. and Flury, J. (2016). *Identification and Separation of GRACE Sensor Errors in Range-rate Residuals*. Presented at: GRACE Science Team Meeting 2016, Potsdam, Germany.

Harvey, N. (2016). *GRACE star camera noise*. Advances in Space Research 58, 408–414. DOI: 10.1016/j.asr.2016.04.025.

Harvey, N., Dunn, C., Kruizinga, G., and Young, L. (2016). *Triggering Conditions for GRACE Ranging Measurement Signal-to-Noise Ratio Dips*. Journal of Spacecraft and Rockets 54 (1), 327–330. DOI: 10.2514/1.A33578.

Heiskanen, W. A. and Moritz, H. (1967). *Physical Geodesy*. San Francisco: W. H. Freeman. ISBN: 978-3-211-33545-1.

Herman, J. and Steinhoff, M. (2012). *Balancing, Turning, Saving Special AOCS Operations to extend the GRACE Mission*. In: 12th International Conference on Space Operations, Stockholm, Sweden. DOI: 10.2514/6.2012-1275114.

Herman, J., Presti, D., Codazzi, A., and Belle, C. (2004). *Attitude Control For GRACE - The First Low-Flying Satellite Formation*. URL: http://www.issfd.org/ISSFD_2004/papers/P0106.pdf.

Herman, J., Davis, A., Chin, K. B., Kinzler, M., Scholz, S., and Steinhoff, M. (2012). *Life with a weak Heart: Prolonging the Grace Mission despite degraded Batteries*. In: 12th International Conference on Space Operations, Stockholm, Sweden. URL: http://elib.dlr.de/76288/1/id1275101-Paper-002.pdf.

Hofmann-Wellenhof, B., Lichtenegger, H., and Wasle, E. (2008). *GNSS — Global Navigation Satellite Systems*. Wien New York: Springer. DOI: 10.1007/978-3-211-73017-1.

Horwath, M., Lemoine, J.-M., Biancale, R., and Bourgogne, S. (2011). *Improved GRACE science results after adjustment of geometric biases in the Level-1B K-Band ranging data*. Journal of Geodesy 85 (1), 23–38. DOI: 10.1007/s00190-010-0414-2.

Horwath, M., Groh, A., and EGSIEM Team, the (2016). *Evaluation of recent GRACE monthly solution series with an ice sheet perspective*. Poster presentation at: EGU General Assembly 2016, Vienna, Austria. Geophysical Research Abstracts Vol. 18, EGU2016-9728.

Huber, P. J. (1981). *Robust Statistics*. New York: Wiley.

Hudson, D. (2003). *In-Flight Characterization and Calibration of the SuperSTAR Accelerometer*. MA thesis. Center for Space Research, The University of Texas at Austin.

IAU (2000). *Resolution No. B1.3, Definition of barycentric celestial reference system and geocentric celestial reference system*. URL: http://www.iau.org/administration/resolutions/general_assemblies/.

Inácio, P., Ditmar, P., Klees, R., and Farahani, H. H. (2015). *Analysis of star camera errors in GRACE data and their impact on monthly gravity field models*. Journal of Geodesy 89 (6), 551–571. DOI: 10.1007/s00190-015-0797-1.

IPCC (2013). *Climate Change 2013: The Physical Science Basis. Contribution of Working Group I to the Fifth Assessment Report of the Intergovernmental Panel on Climate Change [Stocker, T.F., D. Qin, G.-K. Plattner, M. Tignor, S.K. Allen, J. Boschung, A. Nauels, Y. Xia, V. Bex and P.M. Midgley (eds.)]* Cambridge, United Kingdom and New York, NY, USA: Cambridge University Press, p. 1535. DOI: 10.1017/CBO9781107415324.

Jekeli, C. (1981). *Alternative Methods to Smooth the Earth's Gravity Field*. Technical Report, 327. Department of Geodesy and Science and Surveying, Ohio State University. URL: https://earthsciences.osu.edu/sites/earthsciences.osu.edu/files/report-327.pdf.

Johannessen, J. A., Balmino, G., Leprovost, C., Rummel, R., Sabadini, R., Sünkel, H., Tscherning, C. C., Visser, P., Woodworth, P., Hughes, C. W., Legrand, P., Sneeuw, N., Perosanz, F., Aguirre-Martinez, M., Rebhan, H., and Drinkwater, M. R. (2003). *The European Gravity Field and Steady-State Ocean Circulation Explorer Satellite Mission: Its Impact on Geophysics*. Surveys in Geophysics 24, 339–386. DOI: 10.1023/B:GEOP.0000004264.04667.5e.

Jørgensen, J. L. (2000). *In Orbit Performance of a Fully Autonomous Star Tracker*. In: Proceedings of 4th ESA International Conference on Spacecraft Guidance, Navigation and Control Systems. ESA SP-425. ESTEC, Noordwijk, The Netherlands, 103 –110.

Jørgensen, J. L. and Pickles, A. (1998). *Fast and robust pointing and tracking using a second generation star tracker*. In: Proceedings of SPIE - The International Society for Optical Engineering. Vol. 3351, 3351 –3351 –11. DOI: 10.1117/12.308838.

Kaula, W. M. (1966). *Theory of Satellite Geodesy - Applications of Satellites to Geodesy*. Dover Publications.

Kim, J. (2000). *Simulation Study of A Low-Low Satellite-to-Satellite Tracking Mission*. PhD thesis. The Universtiy of Texas at Austin. URL: http://citeseerx.ist.psu.edu/viewdoc/download?doi=10.1.1.460.4923&rep=rep1&type=pdf.

Kim, J. and Tapley, B. (2002). *Error analysis of a low-low satellite-to-satellite tracking mission*. Journal of Guidance, Control, and Dynamics 25 (6), 1100–1106. DOI: 10.2514/2.4989.

Kirschner, M., Montenbruck, O., and Bettadpur, S. (2001). *Flight Dynamics Aspects of the GRACE Formation Flying*. In: 2nd International Workshop on Satellite Constellations and Formation Flying. Haifa, Israel. URL: http://citeseerx.ist.psu.edu/viewdoc/download?doi=10.1.1.556.3828&rep=rep1&type=pdf.

Kirschner, M., Montenbruck, O., and D'Amico, S. (2004). *Safe Switching of the GRACE Formation Using an Eccentricity/Inclination Vector Separation*. In: Proceedings of the 18th International Symposium on Space Flight Dynamics (ESA SP-548). Munich, Germany, 315–319. URL: http://www.issfd.org/ISSFD_2004/papers/P1067.pdf.

Klinger, B. and Mayer-Gürr, T. (2014). *Combination of GRACE star camera and angular acceleration data: impact on monthly gravity field models*. Presented at: GRACE Science Team Meeting 2014, Potsdam, Germany.

Klinger, B. and Mayer-Gürr, T. (2016). *The role of accelerometer data calibration within GRACE gravity field recovery: Results from ITSG-Grace2016*. Advances in Space Research 58, 1597–1609. DOI: 10.1016/j.asr.2016.08.007.

Klinger, B., Mayer-Gürr, T., Behzadpour, S., Ellmer, M., Kvas, A., and Zehentner, N. (2016). *The new ITSG-Grace2016 release*. Presented at: EGU General Assembly 2016, Vienna, Austria. Geophysical Research Abstracts Vol. 18, EGU2016-11547. URL: https://pure.tugraz.at/portal/files/3643450/2016_04_Klinger_etal_EGU2016_ITSG_Grace2016.pdf.

Knocke, P. C., Ries, J. C., and Tapley, B. D. (1988). *Earth radiation pressure effects on satellites*. Proceedings of the AIAA/AAS Astrodynamics Conference, 88-4292-CP, 577–587. DOI: 10.2514/6.1988-4292.

Ko, U.-D., Wang, F., and Eanes, R. J. (2015). *Improvement of Earth Gravity Field Maps after Pre-processing Upgrade of the GRACE Satellite's Star Trackers*. Korean Journal of Remote Sensing 31 (4), 353–360. DOI: 10.7780/kjrs.2015.31.4.8.

Koch, K.-R. (1999). *Parameter Estimation and Hypothesis Testing in Linear Models*. 2nd, updated and enlarged edition. Berlin Heidelberg: Springer. ISBN: 978-3-662-03976-2.

Koch, K.-R. and Kusche, J. (2001). *Regularization of geopotential determination from satellite data by variance components*. Journal of Geodesy 76 (5), 259–268. DOI: 10.1007/s00190-002-0245-x.

Krarup, T., Juhl, J., and Kubik, K. (1980). *Götterdämmerung over Least Squares Adjustment*. 14th Congress ISP Hamburg, International Archives of Photogrammetry, XXIII, B3, Commission III: 369-378. URL: http://www.isprs.org/proceedings/XXIII/congress/part3/369_XXIII-B3.pdf.

Kruizinga, G. (2004). *SOE Sequence of Events File format description*. GRACE TN-03. Jet Propulsion Laboratory, California Institute of Technology. URL: ftp://podaac.jpl.nasa.gov/allData/grace/docs/TN-03_SOE_format.txt.

Kruizinga, G., Bertiger, W., Boening, C., Byun, S., Finch, C., Harvey, N., Kuang, D., Strekalov, D., Yuan, D.-N., Bettadpur, S., and Wang, F. (2015). *GRACE Level-1 Data Processing Status*. Presented at: GRACE Science Team Meeting 2015, Austin, Texas.

Kruizinga, G., Bandikova, T., Bertiger, W., Boening, C., Byun, S., Finch, C., Harvey, N., Kuang, D., Sakumura, C., Strekalov, D., Yuan, D.-N., Bettadpur, S., and Wang, F. (2016). *GRACE Level-1 Data Processing Status*. Presented at: GRACE Science Team Meeting 2016, Potsdam, Germany.

Kruizinga, G., Bandikova, T., Bertiger, W., Boening, C., Byun, S., Finch, C., Harvey, N., Kuang, D., Sakumura, C., Strekalov, D., Yuan, D.-N., Bettadpur, S., Save, H., and Wang, F. (2017). *GRACE Science Data System Level-1 Processing Status*. Presented at: GRACE Science Team Meeting 2017, Austin, Texas.

Kubik, K., Weng, W., and Frederikse, P. (1985). *Oh, gross errors!* Australian Journal of Geodesy, Photogrammetry and Surveying 42, 1–18.

Kuipers, J. B. (1999). *Quaternions and rotation sequences: a primer with applications to orbits, aerospace, and virtual reality*. 3rd edition. Princeton, NJ: Princeton University Press. ISBN: 9780691102986.

Kurtenbach, E. (2011). *Entwicklung eines Kalman-Filters zur Bestimmung kurzzeitiger Variationen des Erdschwerefeldes aus Daten der Satellitenmission GRACE*. PhD thesis. Institut für Geodäsie und Geoinformation 9, University of Bonn. URL: https://dgk.badw.de/fileadmin/user_upload/Files/DGK/docs/c-683.pdf.

Kusche, J. (2007). *Approximate decorrelation and non-isotropic smoothing of time-variable GRACE-type gravity field models*. Journal of Geodesy 81 (11), 733–749. DOI: 10.1007/s00190-007-0143-3.

Kusche, J., Schmidt, R., Petrovic, S., and Rietbroek, R. (2009). *Decorrelated GRACE Time-Variable Gravity Solutions by GFZ, and their Validation using a Hydrological Model*. Journal of Geodesy 83 (10), 903–913. DOI: 10.1007/s00190-009-0308-3.

Kvas, A., Klinger, B., Behzadpour, S., Ellmer, M., Zehentner, N., and Mayer-Gürr, T. (2016). *ITSG-Grace2016 – Daily Gravity Field Solutions from GRACE*. Presented at: GRACE Science Team Meeting 2016, Potsdam, Germany.

Liebe, C. C. (2002). *Accuracy Performance of Star Trackers – A Tutorial*. IEEE Transactions on Aerospace and Electronic Systems 38 (2), 587–599. DOI: 10.1109/TAES.2002.1008988.

Mayer-Gürr, T. (2006). *Gravitationsfeldbestimmung aus der Analyse kurzer Bahnbögen am Beispiel der Satellitenmission CHAMP und GRACE*. PhD thesis. Institut für Geodäsie und Geoinformation 9, University of Bonn. URL: http://hss.ulb.uni-bonn.de/2006/0904/0904.pdf.

Mayer-Gürr, T. (2007). *ITG-Grace03s: The latest GRACE gravity field solution computed in Bonn*. Presented at: Joint International GSTM and DFG SPP Symposium, Potsdam, Germany.

Mayer-Gürr, T., Kurtenbach, E., and Eicker, A. (2010). *ITG-Grace2010: the new GRACE gravity field release computed in Bonn*. Presented at: EGU General Assembly 2010, Vienna, Austria. Geophysical Research Abstracts Vol. 12, EGU2010-2446.

Mayer-Gürr, T., Pail, R., Gruber, T., Fecher, T., Rexer, M., Schuh, W.-D., Kusche, J., Brockmann, J.-M., Krasbutter, I., Becker, S., Eicker, A., Schall, J., Rieser, D., Zehentner, N., Baur, O., Höck, E., Hausleitner, W., Maier, A., Krauss, S., Jäggi, A., Meyer, U., and Prange, L. (2012). *The combined satellite only model GOCO03s*. Presented at: International Symposium on Gravity, Geoid and Height Systems 2012, Venice, Italy. URL: http://www.bernese.unibe.ch/publist/2012/pres/Pres_GGHS2012_mayer-guerr_etal.pdf.

Mayer-Gürr, T., Zehentner, N., Klinger, B., and Kvas, A. (2014). *ITSG-Grace2014: a new GRACE gravity field release computed in Graz*. In: GRACE Science Team Meeting 2014. Potsdam, Germany. DOI: 10.13140/RG.2.1.5098.2805.

Mayer-Gürr, T., Pail, R., Gruber, T., Fecher, T., Rexer, M., Schuh, W.-D., Kusche, J., Brockmann, J.-M., Rieser, D., Zehentner, N., Kvas, A., Klinger, B., Baur, O., Höck, E., Krauss, S., and Jäggi, A. (2015). *The combined satellite gravity field model GOCO05s*. Presented at: EGU General Assembly 2015, Vienna, Austria. Geophysical Research Abstracts Vol. 17, EGU2015-12364.

Mayer-Gürr, T., Klinger, B., Kvas, A., Zehentner, N., Ellmer, M., and Behzadpour, S. (2016a). *Insights into the ITSG-Grace2016 processing*. Presented at: International Symposium on Gravity, Geoid and Height Systems 2016, Thessaloniki, Greece.

Mayer-Gürr, T., Behzadpour, S., Ellmer, M., Kvas, A., Klinger, B., and Zehentner, N. (2016b). *ITSG-Grace2016 - Monthly and Daily Gravity Field Solutions from GRACE*. GFZ Data Services. DOI: 10.5880/icgem.2016.007.

McCarthy, D. D., ed. (1996). *IERS conventions*. IERS Technical Note No. 21. Central Bureau of IERS - Observatoire de Paris, Paris, 97 pp.

McCarthy, D. D. and G. Petit, eds. (2003). *IERS conventions*. IERS Technical Note No. 32. erlag des Bundesamts für Kartographie und Geodäsie, Frankfurt am Main, 127 pp. ISBN: 3-89888-884-3.

Meissl, P. (1982). *Least Squares Adjustment - A Modern Approach*. Mitteilungen der Geodätische Institute der Technischen Universität Graz, Folge 43, Graz, Austria. URL: ftp://skylab.itg.uni-bonn.de/schuh/Separata_Meissl/Meissl_1982_Least_Squares_Adjustment_A_Modern_Approach.pdf.

Meyer, U., Jäggi, A., Jean, Y., and Beutler, G. (2016). *AIUB-RL02: an improved time series of monthly gravity fields from GRACE data*. Geophysical Journal International. DOI: 10.1093/gji/ggw081.

Mohr, P. J, Newell, D. B., and Taylor, B. N. (2016). *CODATA recommended values of the fundamental physical constants: 2014*. Reviews of Modern Physics 88 (3), 035009–1–035009–73. DOI: 10.1103/RevModPhys.88.035009.

Montenbruck, O. and Gill, E. (2001). *Satellite Orbits - Models, Methods, and Applications*. 2nd corrected edition. Berlin Heidelberg New York: Springer. ISBN: 978-3-642-58351-3.

NASA (2002). *GRACE Launch Press Kit*. URL: https://www.jpl.nasa.gov/news/press_kits/gracelaunch.pdf.

Niemeier, W. (2008). *Ausgleichsrechnung - Statistische Auswertemethoden*. 2nd edition. Berlin: de Gruyter. ISBN: 978-3110190557.

Peterseim, N. (2014). *TWANGS - High-Frequency Disturbing Signals in 10 Hz Accelerometer Data of the GRACE Satellites*. PhD thesis. Institut für Astronomische und Physikalische Geodäsie, Technische Universität München. URL: https://mediatum.ub.tum.de/doc/1197563/1197563.pdf.

Peterseim, N., Flury, J., and Schlicht, A. (2012). *Magnetic torquer induced disturbing signals within GRACE accelerometer data*. Advances in Space Research 49, 1388–1394. DOI: 10.1016/j.asr.2012.02.013.

Petit, G. and B. Luzum, eds. (2010). *IERS Conventions*. IERS Technical Note No. 36. Verlag des Bundesamts für Kartographie und Geodäsie, Frankfurt am Main, 179 pp. ISBN: 3-89888-989-6.

Picone, J. M., Hedin, A. E., Drob, D. P., and Aikin, A. C. (2002). *NRLMSISE-00 empirical model of the atmosphere: Statistical comparisons and scientific issues*. Journal of Geophysical Research: Space Physics 107 (A12), SIA 15–1–SIA 15–16. DOI: 10.1029/2002JA009430.

Reigber, C. (1989). *Gravity field recovery from satellite tracking data*. In: Theory of Satellite Geodesy and Gravity Field Determination. Ed. by F. Sansò and R. Rummel. Berlin, Heidelberg: Springer Berlin Heidelberg, 197–234. ISBN: 978-3-540-48223-9. DOI: 10.1007/BFb0010552.

Reigber, C., Schwintzer, P., and Lühr, H. (1999). *The CHAMP geopotential mission*. Bollettino di Geofisica Teorica ed Applicata 40 (3-4), 285–289.

Rodríguez-Solano, C. J., Hugentobler, U., and Steigenberger, P. (2009). *Impact of albedo radiation on GPS satellites*. In: Geodesy for Planet Earth. Ed. by S. Kenyon, M. C. Pacino, and U. Marti. International Association of Geodesy Symposia. Vol. 136. Springer, 113–119. DOI: 10.1007/978-3-642-20338-1_14.

Roesset, P. (2003). *A Simulation Study Of The Use Of Accelerometer Data In The GRACE Mission*. PhD thesis. The Universtiy of Texas at Austin. URL: https://repositories.lib.utexas.edu/handle/2152/888.

Rummel, R. (1979). *Determination of short-wavelength components of the gravity field from satellite-to-satellite tracking of satellite gradiometry - an attempt to an identification of problem areas*. Manuscripta Geodetica 4 (2), 107–148.

Sakumura, C., Harvey, N., Bandikova, T., and McCullough, C. (2016). *Parametertization, alignment, and gravity field results*. Poster presentation at: GRACE Science Team Meeting 2016, Potsdam, Germany.

Savcenko, R., Bosch, W., Dettmering, D., and Seitz, F. (2012). *EOT11a - Global Empirical Ocean Tide model from multi-mission satellite altimetry, with links to model results*. Supplement to: Savcenko, Roman; Bosch, Wolfgang (2012): EOT11a - Empirical Ocean Tide Model from Multi-Mission Satellite Altimetry. Deutsches Geodätisches Forschungsinstitut (DGFI), München, 89, 49 pp, hdl:10013/epic.43894.d001. DOI: 10.1594/PANGAEA.834232.

Save, H. (2016). *GRACE Battery Status and Science Impact*. Presented at: GRACE Science Team Meeting 2016, Potsdam, Germany.

Schneider, M. (1968). *A General Method of Orbit Determination*. Library Translation. Band 1279, Royal Aircraft Establishment, Ministry of Technology, Farnborough, England.

Sheard, B. S., Heinzel, G., Danzmann, K., Shaddock, D. A., Klipstein, W. M., and FOlner, W. M. (2012). *Intersatellite laser ranging instrument for the GRACE follow-on mission*. Journal of Geodesy 86 (12), 1083–1095. DOI: 10.1007/s00190-012-0566-3.

Siemes, C. (2011). *GOCE gradiometer calibration and Level 1b data processing*. ESA Working Paper EWP-2384. URL: https://earth.esa.int/c/document_library/get_file?folderId=85857&name=DLFE-1312.pdf.

Siemes, C., Encarnação, J. de Teixeira da, IJssel, J., Kraus, J., Pereštý, R., Grundwaldt, L., Apelbaum, G., Flury, J., and Olsen, P. E. H. (2016). *Swarm accelerometer data processing from raw accelerations to thermospheric neutral densities*. Planets and Space 68 (1), 92. DOI: 10.1186/s40623-016-0474-5.

Stanton, R., Bettadpur, S., Dunn, C., Renner, K.-P., and Watkins, M. (1998). *GRACE Science & Mission Requirements Document*. Technical Report 327-200, Jet Propulsion Laboratory, University of Texas Center for Space Research, GeoForschungsZentrum Potsdam.

Stummer, C. (2012). *Gradiometer Data Processing and Analysis for the GOCE Mission Analysis*. PhD thesis. Institut für Astronomische und Physikalische Geodäsie, Technische Universität München. URL: https://mediatum.ub.tum.de/doc/1111698/362238.pdf.

Stummer, C., Fecher, T., and Pail, R. (2011). *Alternative method for angular rate determination within the GOCE gradiometer processing*. Journal of Geodesy 85, 858–596. DOI: 10.1007/s00190-011-0461-3.

Tapley, B., Bettadpur, S., Watkins, M., and Reigber, C. (2004). *The gravity recovery and climate experiment: Mission overview and early results*. Geophysical Research Letters 31 (9). DOI: 10.1029/2004GL019920.

Tapley, B., Flechtner, F., Watkins, M., and Bettadpur, S. (2015). *GRACE Mission: Status and Prospects*. Presented at: GRACE Science Team Meeting 2015, Austin, Texas.

Thomas, J. (1999). *An Analysis of Gravity-Field Estimation Based on Intersatellite Dual-1-Way Ranging*. Technical Report JPL 98-15, Jet Propulsion Laboratory.

Touboul, P., Foulon, B., and Willemenot, E. (1999). *Electrostatic space accelerometers for present and future missions*. Acta Astronautica 45 (10), 605–617. DOI: 10.1016/S0094-5765(99)00132-0.

Touboul, P., Foulon, B., Rodrigues, M., and Marque, J. P. (2004). *In orbit nano-g measurements, lessons for future space missions*. Aerospace Science and Technology 8 (5), 431–441. DOI: 10.1016/j.ast.2004.01.006.

van Dam, T. and Ray, R. D. (2010). *S1 and S2 Atmospheric Tide Loading Effects for Geodetic Applications*. URL: http://geophy.uni.lu/ggfc-atmosphere/tide-loading-calculator.html.

Wahr, J., Molenaar, M., and Bryan, F. (1998). *Time variability of the Earth's gravity field: Hydrological and oceanic effects and their possible detection using GRACE*. Journal of Geophysical Research: Solid Earth 103 (B12), 30205–30229. DOI: 10.1029/98JB02844.

Wang, F. (2003). *Study on center of mass calibration and K-brand ranging system calibration of the GRACE mission*. PhD thesis. The Universtiy of Texas at Austin.

Wang, F., Bettadpur, S., Save, H., and Kruizinga, G. (2010). *Determination of Center-of-Mass of Gravity Recovery and Climate Experiment Satellites*. Journal of Spacecraft and Rockets 47 (2), 371–379. DOI: 10.2514/1.46086.

Watkins, M. M. and Yuan, D.-N. (2014). *JPL Level-2 Processing Standards Document For Level-2 Product Release 05.1*. GGRACE 327-744 (v 5.1). Jet Propulsion Laboratory, California Institute of Technology. URL: ftp://podaac.jpl.nasa.gov/allData/grace/docs/L2-JPL_ProcStds_v5.1.pdf.

Wickert, J., Michalak, G., Schmidt, T., Beyerle, G., Cheng, C. Z., Healy, S. B., Heise, S., Huang, C. Y., Jakowski, N., Köhler, W., Mayer, C., Offiler, D., Ozawa, E., Pavelyev, A. G., Rothacher, M., Tapley, B., and Arras, C. (2009). *GPS radio occultation: results from CHAMP, GRACE and FORMOSAT-3/COSMIC*. Terrestrial Atmospheric and Oceanic Sciences 20 (1), 35–50. DOI: 10.3319/TAO.2007.12.26.01(F3C).

Wielicki, A. and Barkstrom, B. R. (1996). *Clouds and the Earth's Radiant Energy System (CERES) - Algorithm Theoretical Basis Document*. Atmospheric Sciences Division, NASA Langley Research Center, Hampton, Virginia 23681-000. URL: https://ceres.larc.nasa.gov/documents/ATBD/pdf/r2_1/ceres-atbd2.1-over.pdf.

Willis, P., Deleflie, F., Barlier, F., Bar-Seve, Y. E., and Romans, L. J (2005). *Effects of thermosphere total density perturbations on LEO orbits during severe geomagnetic conditions (Oct-Nov 2003) using DORIS and SLR data*. Advances in Space Research 36 (3), 522–533. DOI: 10.1016/j.asr.2005.03.029.

Witkowski, M. and Massmann, F. H. (2012). *Status GRACE mission operations*. Presented at: GRACE Science Team Meeting 2012, Potsdam, Germany.

Wu, S.-C., Kruizinga, G., and Bertiger, W. (2006). *Algorithm Theoretical Basis Document for GRACE Level-1B Data Processing V1.2*. Technical Report GRACE 327-741, Jet Propulsion Laboratrory. URL: ftp://podaac.jpl.nasa.gov/allData/grace/docs/ATBD_L1B_v1.2.pdf.

Zehentner, N. and Mayer-Gürr, T. (2015). *Precise orbit determination based on raw GPS measurements*. Journal of Geodedy 90 (3), 275–286. DOI: 10.1007/s00190-015-0872-7.

List of Acronyms

AC	Analysis Center
ACC	Accelerometer
ACC1B	Accelerometer Data Product
AF	Accelerometer Frame
AHK1B	Accelerometer Housekeeping Data Product
AIUB	Astronomical Institute of the University of Bern
AOC	Antenna Offset Correction
AOCS	Attitude and Orbit Control System
APC	Antenna Phase Center
ASAP	Austrian Space Applications Programme
ATH	Attitude Thrusters
CCD	Charged Coupled Device
CCI	Climate Change Initiative
CEES	Coarse Earth/Sun Sensor
CERES	Clouds and Earth's Radiant Energy System
CFRP	Carbon Fiber Reinforced Plastic
CHAMP	CHAllenging Minisatellite Payload
CNES/GRGS	Le Centre national d'études spatiales/Le Groupe de Recherche de Géodésie Spatiale
CoM	Center of Mass
CPV	Common Pressure Vessel
cpr	cycles-per-revolution
CSR	Center for Space Research at the University of Texas at Austin
DLR	German Aerospace Center
DTM2013	Drag Temperature Model 2013
DTU	Technical University of Denmark
ESA	European Space Agency
ESSP	Earth System Science Pathfinder
EWH	Equivalent Water Height
FFG	Austrian Research Promotion Agency
GFZ	German Research Centre for Geosciences
GNSS	Global Navigation Satellite System

GNV1B	GPS Navigation Data Format Record
GOCE	Gravity field and steady-state Ocean Circulation Explorer
GPS	Global Positioning System
GRACE	Gravity Recovery and Climate Experiment
GRACE-FO	Gravity Recovery and Climate Experiment Follow-On
GROOPS	Gravity Recovery Object Oriented Programming System
GRGS	Le Groupe de Recherche de Géodésie Spatiale
GSOC	German Space Operations Center
GUI	Graphical User Interface
hl-SST	High-Low Satellite-to-Satellite Tracking
IAG	International Association of Geodesy
ICGEM	International Centre for Global Earth Models
ICRF	International Celestial Reference Frame
ICU	Interface Control Unit
ID	Identification Number
IERS	International Earth Rotation and Reference System Service
IfG	Institute of Geodesy at the Graz University of Technology
IFGS	International Gravity Field Service
IMU	Inertial Measurement Unit
IPCC	Intergovernmental Panel on Climate Change
IPCC-AR5	Fifth Assessment Report of the Intergovernmental Panel on Climate Change
IPU	Instrument Processing Unit
IRF	Inertial Reference Frame
ISDC	Information System and Data Center
ITSG	Former Institute of Satellite Geodesy and Theoretical Geodesy at the Graz University of Technology
ITRF	International Terrestrial Reference Frame
JB2008	Jacchia-Bowman 2008
JPL	Jet Propulsion Laboratory
KBR	K-Band Ranging
KBR1B	KBR Data Format Record
KF	K-Band Frame
LEO	Low Earth Orbiter
ll-SST	Low-Low Satellite-to-Satellite Tracking
LOS	Line-Of-Sight
LOSF	LOS Frame
LRI	Laser Ranging Interferometer
LRR	Laser Retro Reflector
LSA	Least Squares Adjustment
MAG	Magnetometer
MAS1B	Spacecraft Mass Data Format Record

MOS	Mission Operation System
MTE	Mass Trim Electronics
MTM	Mass Trim Mechanism
MTQ	Magneto-Torquers
NASA	National Aeronautics and Space Administration
NGGM	Next-Generation Gravity Missions
NiH	Nickle-Hydrogen
OBDH	Onboard Data Handler
ONERA	Office National d'Études et de Recherches Aérospatiales
OTH	Orbit Thrusters
PCDU	Power Conditioning and Distribution Unit
phC	phase center
POD	Precise Orbit Determination
PODAAC	Physical Oceanography Distributed Active Archive Center
PSD	Power Spectral Density
RDC	Raw Data Center
RFEA	Radio-Frequency Electronics Assembly
RL	Release
RX	Receiver
SAT	Satellite System
SCA	Star Camera
SCA1B	Star Camera Data Product
SCF	Star Camera Frame
SDS	Science Data System
SF	Satellite Frame
SH	Spherical Harmonic
SIS	Science Instrument System
SLR	Satellite Laser Ranging
SM	Science Mode
SNR	Signal-to-Noise Ratio
SOE	Sequence of Events
SRF	Science Reference Frame
SRP	Solar Radiation Pressure
SSL	Space Systems/Loral
SST	Satellite-to-Satellite Tracking
SU	Sensor Unit
SZA TX/RX	S-Band Zenith Transmitter and Receiver Antenna
THR1B	Thrusters Data Format Record
TN	Technical Note
TNK1B	Cold Gas Tank Data Format Record
TOF	(Time of flight)
TRF	Terrestrial Reference Frame

TX	Transmitter
UCBS	Uniform Cubic Basis Splines
USO	Ultra-Stable Oscillator
VCE	Variance Component Estimation
VKB1B	Vector Product
w.r.t.	with respect to
XML	Extensible Markup Language

List of Figures

List of Tables